2011

The Effect of the Heart on the Brain Function

Chokchai Chutakositkanon
Lehigh University

The Effect of the Heart on the Brain Function

by

Chokchai Chutakositkanon

Presented to the Graduate and Research Committee
of Lehigh University
in Candidacy for the Degree of
Doctor of Philosophy

in

Mechanical Engineering

Lehigh University

May 2011

This dissertation is accepted and approved in partial fulfillment of the requirements for the Degree of Doctor of Philosophy.

_____
Date

_____
Dr. Alistair K. Macpherson, Dissertation Advisor

_____
Accepted Date

_____
Dr. Sudhakar Neti, Dissertation Advisor

Committee Members:

_____
Dr. Jacob Y. Kazakia, Committee Member

_____
Dr. Eric P. Salathe, Committee Member

_____
Dr. Marcus Averbach, Committee Member

Acknowledgments

I would like to express my sincere gratitude and appreciation to those who have contributed to the success of this dissertation, especially my advisors, Dr. Alistair K. Macpherson, Dr. Sudhakar Neti, for their extensive guidance and assistance during my studies and Dr. Marcus Averbach from Radiology Department, St.Lukes Hospital for the heart patients' experimental data and guidance. It would have been impossible for me to achieve this success without their expertise, continuous support and encouragement.

I would like to express my gratitude to Dr. Jacob Y. Kazakia, Professor in Mechanical Engineering and Mechanics for being a member of my PhD research committee and suggestions on my dissertation and Dr. Eric P. Salathe, Professor in Department of Mathematical, and Director of the Institute for Biomedical Engineering and Mathematical Biology for being a member of my dissertation defense committee and suggestions on my dissertation. I also would like to thank Dr. Peter Macpherson, Professor in Department of Applied Technology, Rogers State University, Dr. Henggui Zhang, Physics Department, the University of Manchester, and Dr. Michael O. Chaney, Lilly Research Laboratories, Eli Lilly and Company, for helping and give me idea to simulation modeling.

I would like to thank all patients for their dedication and volunteering spirit, which resulted in invaluable data that could lead to the improvement or development of better strategies for other cardiac patients and fellow human beings in general. I am also thankful to the Royal Thai Government Scholarship program that provided continued sponsorship and support for my studies at Lehigh University

I am especially grateful to my parents and siblings for their encouragement at every aspect of my life, and thank all my friends, who provided continuous encouragement and support during my study.

Table of Contents

List of Figures

ABSTRACT

The interaction between the heart and brain activity has been widely studied extensively in the past. This present work deals with the interaction between the heart and brain activity of patients treated with dobutamine. During dobutamine infusion, the heart rate increases, but there is a negligible increase in blood pressure. For this study, brain activity (EEG) is monitored while patients are undergoing dobutamine infusion. This study comprises of three main parts. The movement of the myocardium recorded as part of the echocardiogram test was used in blood flow model. Blood flow results for several successive heart eats were found to be consistent. In the first part of the work, the generation of the electrical signal in the Sinus Nodes (SA nodes) was modeled. The process starts with the docking of dobutamine into the β_1 adrenergic receptor using AutoDock4 software. The SA node model was simulated by 200 molecules docking with four different dosages of dobutamine 10, 20, 30, and 40 mics (or milligrams per kg per minute). Assumptions were made concerning the number of ion channels opened by the dobutamine docking and the potential passed to the AV nodes and the Purkinji fibers calculated using mathematical models of cardiac action potentials. The relationship of these with the electrocardiograph output (ECG) the electrical potential of the heart was investigated. In the second part of this work, the effect of the electrical signals transmitted to the brain were examined using fast Fourier transforms as a spectral tool for analysis in combination with the brain wave data from EEG and ECG records. In all patients a resonance peaks around 10Hz were found. The resonant EEG transform signals are generally located at the back and top

of the head. Wavelet analysis was also used to determine whether the source of the Fourier transform resonance was related to the heart activity. It was found that a frequency in the heart beat was similar to that in the brain. Sensitivity of blood flow simulations of two successive beats on the heart wall modeling is consistent (6.05:5.87 N/m^2) between the first and second beats. The third part of this work studied the quantitative correlations between heart and brain signals. In addition to the wavelet correlations further correlations were examined to see if other sources were responsible for the triggering of the resonance (~10 Hz) mentioned above. There are three sets of correlations presented; correlation of EKG and EEG with heart stress, correlation of wavelet transform of EEG with EKG, and correlation of EEG with electrical signal generated. All larger probabilities for the occurrence of correlation coefficients greater than 0.5 between heart and brain data were higher at the front of the head. By shifting the time between the EEG and EKG signals (emulating phase shifting), the reaction time were found to be between 0.2 and 0.4 sec. Correlation of EEG with electrical signal generated, the Ca^{2+} ion had better correlation with EEG than other ions at Purkinji fiber. It is hoped that the data presented here representing the effect of heart functions and heart rate on the brain can lead to more research activity in this area.

CHAPTER 1

Introduction

1.1 Motivation

The heart is an important organ for the maintenance of life because it is the main part of the blood circulatory system that drives blood flow to all parts of the body. In order for blood flow to occur, the heart must perform several complex activities to result in a successful circulatory system. At the present time, we know a lot about heart physiology and functions; yet many of heart's processes are still in a state of controversy and remain undiscovered and unexplained. For example, the relation between the blood circulatory system and respiratory system; the manner in which the heart rate will increase as we breath faster. The interaction between the brain and the heart also has received much attention where some heart ailments are ascribed to brain functions, primarily the effect worries and related stresses on the heart. Understanding this not only raising inquiring questions about heart failure problems, but is also leading to the improvement of strategies to treat the cardiac patients. The effect of the heart on the brain function forms the core of the present work. It is suspected that heart functions do affect brain behavior and this is led many researchers investigate the topic. For instance the flow patterns of blood in the heart, related forces and stresses on the myocardium are suspected in playing a role of waves generated by the brain. A better appreciation of such behavior can lead to better

strategies for the design and implantion of artificial hearts, artificial heart valves and pacemakers and elated medicines.

Much of the work presented here is computational modeling and analysis of the heart-brain interaction though using patient data. The advantage of computational simulation is that it is inexpensive and obviously safety. This dissertation work utilizes engineering methodologies and analyses to study the relation between brain wave signals from the electroencephalograph (EEG) and properties of heart behavior calculated from Echocardiograms (echos) and the associated Electrocardiograms (ECG). Some of the cardiac functions and properties used for the analyses include the myocardial shear and normal stresses in the left ventricle (LV), flow behavior in LV, heart rate and Electro Cardo Gram EKG. The patient datasets analysed here include, electroencephalograph (EEG) and echocardiogram with electrocardiogram (ECG) will record from same patient and also simultaneous. The study is start with the echocardiogram because heart part is more understand than brain part. Furthermore, the heart rate is more facile control than brain signal. Dobutamine, a sympathomimetic drug used for increase the heart rate in heart patients, is major of changing in heart and brain properties in this dissertation. The Effect of Heart-Brain Interaction by Dobutamine, research is utilized engineering methodologies and analysis to study the relation between brain signal from the electroencephalograph (EEG) and some properties of heart calculated from the echocardiogram examination of the heart. The simulated quantities were the variation of electric potential with heart rate, the shear force in the left ventricle and the pressure inside heart.

1.2 Scope and Description of the Dissertation

The overall objective of this research program is to simulate and investigate techniques for the relation between the heart and brain. The study of three topics main goals will be followed throughout the program.

1. Simulate the docking of Dobutamine with the heart β_1-adrenergic receptor and correlate Dobutamine dosage with change of heart rate. Calculate the electro-chemical currencies generated by Dobutamine. Analyze the electrical potentials that cause the atrium and ventricles myocytes to contract

2. Computational model of echocardiogram's of the left ventricle chamber of the human heart and simulations neural activities from brain EEG's patterns.
3. Analyze the relation of heart-brain activity. Calculate shear stress in heart and correlate shear stress with brain activity parts.

1.3 Dissertation Outline

The chapters of this dissertation are organized in the following manner. Chapter 2 presents a description of past literature. Chapter 3 includes an introduction of echocardiograms, modeling of blood flow in the left ventricle model and evaluation of heart stress. Heart physical properties from blood flow model in chapter 3 are used in chapter 4 to evaluate the docking of dobutamine onto the β_1 adrenergic receptor. Chapter 4 includes an introduction to dobutamine use, β_1 adrenergic receptors, and simulation methods resulting in the effects of dobutamine on SA node. In chapter 5, electrical signals generated by the action potentials are described and calculation

results are in three parts; those related to sinoatrial node, atrioventricular node, and Purkinji fiber. Chapter 6 and chapter 7 are about brain wave analyses. Electroencephalogram records, fast Fourier transforms, and wavelet transform methods are illustrated. Chapter 8 includes the introduction of correlation coefficients and correlation analysis. Here heart behavior and properties are related to the brain wave analysis using data from previous chapters. Chapter 9 and chapter 10 are discuss all the dissertation results ending with a summary and recommendations for future work.

CHAPTER 2

Literature Survey

2.1 The Anatomy of the Cardiac Conduction System

During the 19th century, there were many research studies related to the anatomy of the cardiac conducting system. In 1839, Jan E. Purkyně was credited with the discovery of Purkinje fibers, the fibrous tissue that conducts electrical impulses to all parts and ventricles of the heart. However, matters remained controversial as to whether the cardiac impulse was conducted through heart muscle or nerves. With his experiments in 1852, by tying a ligature as a constriction between the sinus venosus and the atrium in the frog, Hermann F. Stannius showed that heart impulses were conducted across the atrioventricular junction through the myocardium. Even that did not quite settle the mysteries related to the transmission of the impulse in human hearts. In 1893, Wilhelm His Jr., a cardiologist and anatomist discovered the His bundle, the specialized tissue in the heart that transmits the electrical impulses and helps synchronize contraction. In 1907, Keith and Flack gave a detailed histological description of various mammalian right atriums including human hearts and structure which they called sinuauricular node that they interpreted as the place where the heart beat originates. In 1909, Thorel suggested the existence of discrete morphological pathways between the sinoatrial and atrioventricular nodes within the atrial walls. More recently in 2009, Anderson et al [2-1] used immunohistochemical techniques to essentially confirm the above findings for rat, mouse, and guinea pig hearts. Cardiac

anatomy, physiology, morphology and pathology are now thought to be well known with some of the details shown in Figure 2-1.

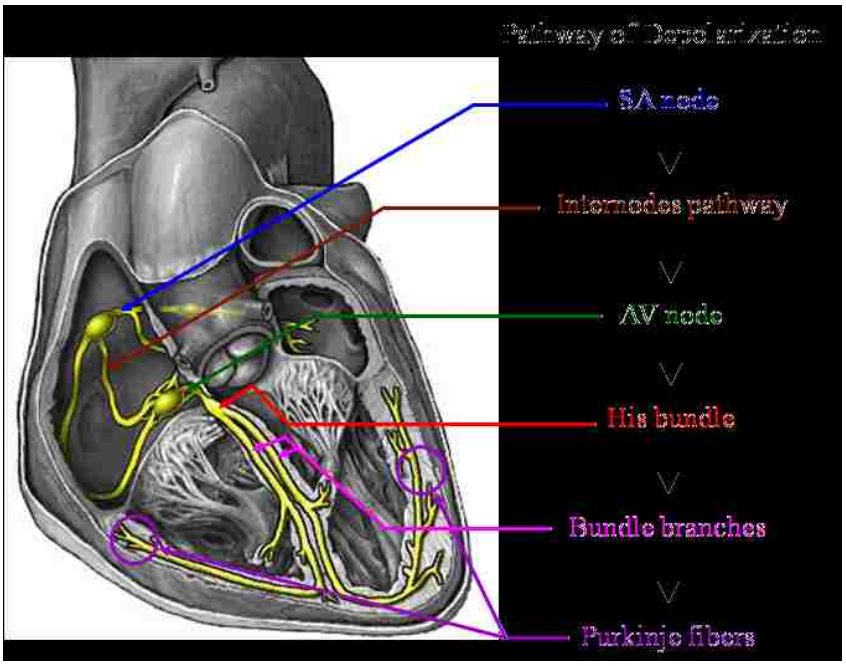

Figure 2-1 Electrical conduction in the heart
[http://www.healthcentral.com/heart-disease/more-images-6996-146.html]

2.2 Flows with Collapsible Boundaries

There are many practical problems are that are governed by flows in flexible pipes or passages; e.g., flows in flexible hoses; flows in blood vessels, arteries, veins, valves, flows in urinary passages and bronchial airways. Fluid flow through collapsible passages is a complex problem to solve due to the interaction between the changing boundary and the flowing fluid. Many previous theoretical works on flow in collapsible tubes have tried to simplify analysis by reducing the spatial dimension of the problem. Bertram [2-2] predicted behavior of the dynamics of flow in collapsible tubes numerically (see Figure 2-2). Soon after Armitstead, Bertram and et. al., [2-3]

used a mathematical model to describe the bifurcation behavior of a model of flow through a collapsible tube.

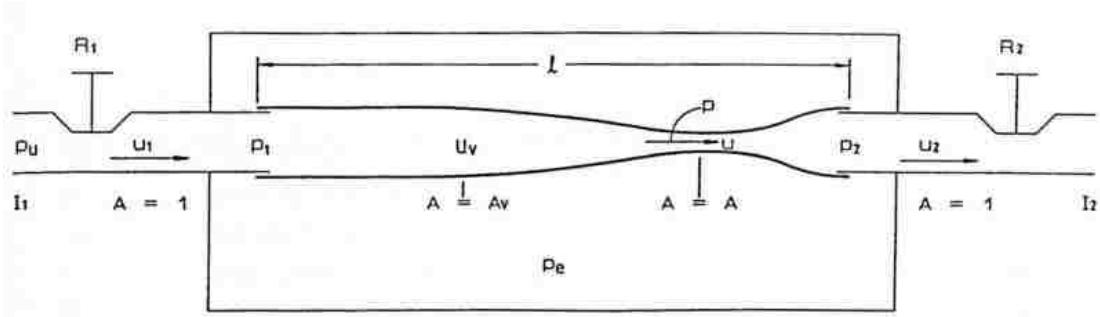

Figure 2-2 The starling resistor

Buxton and Clarke [2-4] developed an efficient a three-dimensional computer simulation of the dynamics of a vein valve. They coupled the solid mechanics of both the vein wall, and the valve leaflets, with the hydrodynamics of the blood flow. In particular, they applied a pressure gradient across the system and simultaneously let the solid mechanics evolve and fluid hydrodynamics towards equilibrium. The vein wall shown in Figure 2-3 is considered to have a Young's modulus of 1,000 kN m^2 and a thickness of 0.05 cm. The density of blood is taken to be 1,060 kg m^3 and the blood viscosity to be 0.0027 N-s/ m^2.

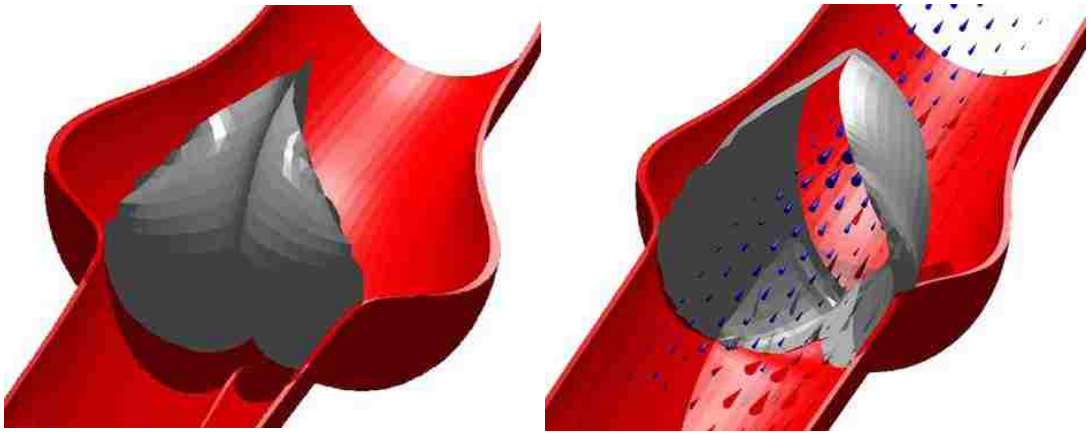

Figure 2-3 Model of the vein valve at closed and open states

The pressure difference across the valve of 13.8 kPa pushes the valve cusps together, occluding the flow of blood, and 'inflates' the valve. Additionally, the fluid pressure causes the valve sinuses to 'balloon' out. These simulation results illustrate the basic physics of valve: restricting the reverse flow of blood and ensuring unidirectional blood flow through the vein valve.

Peskin and Printz [2-5, 2-6] improved the divergence of finite difference procedure by using the immersed boundary method for the study of flow patterns around heart valves. For the numerical analysis of blood flow in the heart, the Navier-Stokes equation and continuity equation was used to solve the problems.

$$\rho\left(\frac{\partial \mathbf{u}}{\partial t}+\mathbf{u}.\nabla\mathbf{u}\right)+\nabla p=\mu\nabla^2\mathbf{u}+\mathbf{F} \tag{2.1}$$

$$\nabla.\mathbf{u}=0 \tag{2.2}$$

The equation of motion in this case is between the fluid and non-fluid regions. Therefore the force density $\mathbf{F}(x,t)$ should be applied on the surface of the non-fluid regions. The calculation of the boundary force density of the system may be written as:

$$\mathbf{F}(\mathbf{x},t)=\int_0^L \mathbf{f}(s,t)\delta(\mathbf{x}-\mathbf{X}(s,t))\,ds \tag{2.3}$$

The computational algorithm used in this work can be summarized as follows:

1) Find the boundary force $\mathbf{f}^n$ for the boundary configuration $\mathbf{X}^n$.

2) Apply the force $\mathbf{f}^n$ to the grid of fluid computation:

3) Update the fluid velocity under the influence of the force density $\mathbf{F}^n$.

4) Interpolate the new velocity to the old boundary positions and move the boundary points.

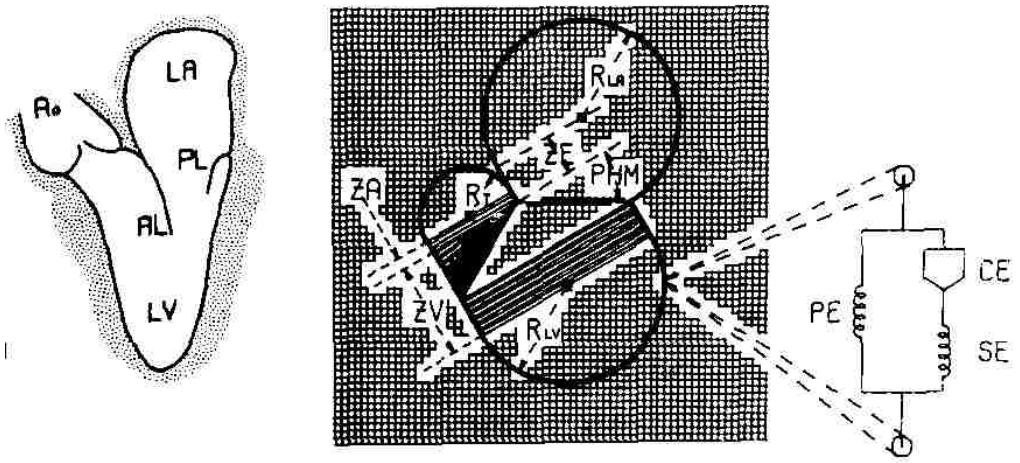

Figure 2-4 Left Side of Heart model

The results from this new two dimensional immersed boundary method was compare to the old two dimensional immersed boundary method with $\mathbf{D}=(D_x,D_y)$ given by central differences with same overall algorithms but with **D** constructed from δ_h by the $(D_x\phi)(x,y)=\sum_{x'y'}\phi(x',y')\gamma(x-x')\omega(y-y')$ and

$$(D_y\phi)(x,y)=\sum_{x'y'}\phi(x',y')\omega(x-x')\gamma(y-y').$$

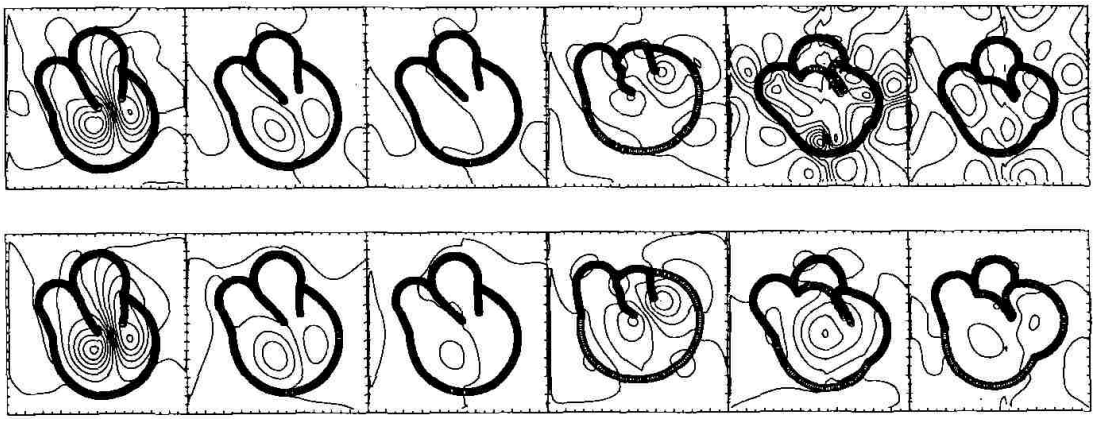

Figure 2-5 Computed streamline, top row: old method bottom row: new method

The diameter of the mitral annulus initially is 1.9 cm. The entire computational domain measures 7.36 cm × 7.36 cm, cover by 64×64 mesh. Therefore mesh width is 0.115 cm. The time step 0.7ms duration of the cardiac cycle is 0.7s of which 0.45s diastole and 0.25s systole. Blood density is $1g/cm^3$ with kinematic viscosity 0.04 cm^2/s. The computed average velocity of flow through the mitral valve has the maximum value of about 40 cm/s, and the maximum pressure during systole is about 6 $\times 10^4$ $dynes/cm^2$. The improvement achieved through the use of the new method can be measured by the ratio of the old volume error to the new volume error. In the two cases, the improvement factors are about 67 and 225. With the new immersed boundary method the result is more accurate. Moreover this improvement in methodology is useful in the case of the blood flow in the contraction of the heart chambers.

David M. McQueen and Charles S. Peskin [2-7] have constructed of the model heart in 3-D from study of the fiber architecture of the hearts of dogs and hogs were bathed in a substance that dissolves the connective tissue between the muscle fibers.

They computed the blood flow in the model. The model requires specifying update heart anatomy and then repeated application of the immersed boundary method. This involves a finite difference solution on a 128x128x128 grid repeated approximately 57,000 times to model a single beat of the heart. Such a computation takes about 250 CPU hours.

2.3 Docking of Molecule

There are many experimental studies of the docking of a ligand to the receptor. Using computational software is cheaper and much quicker. Badry D Bursulaya, Maxim Totrov, and et al. [2-8] had performed a comparative assessment of several algorithms for flexible molecular docking by several programs: DOCK 4.0, FlexX 1.8, AutoDock 3.0, GOLD 1.2 and ICM 2.8. Two different studies, involving docking experiments on a data set of 37 protein–ligand complexes and screening a library containing 10,037 entries against 11 different proteins, was completely employed. The docking accuracy of the methods was judged base on the corresponding rank-one solutions. They have found that the fraction of molecules docked with acceptable accuracy is 0.47, 0.31, 0.35, 0.52 and 0.93 for, respectively, AutoDock, DOCK, FlexX, GOLD and ICM. Thus ICM provided the highest accuracy in ligand docking against these receptors. The results from the other programs are found to be less accurate and of approximately the same quality. A speed comparison demonstrated that FlexX was the fastest and AutoDock was the slowest among the tested docking programs. They have estimated that in virtual database screening, 50% of the potentially active compounds will be found among 1.5% of the top scoring solutions

found with ICM and among 9% of the top scoring solutions produced by DOCK and FlexX. Robin J. Rosenfeld, David S. Goodsell, and et al. [2-9] found the W191G cavity of cytochrome c peroxidase, was a useful model system for introducing small molecule oxidation in an artificially created cavity. They docked these set of ligands and a set of non-binders in the W191G cavity using AutoDock 3.0. They compared the docking predictions with experimentally determined binding energies and X-ray crystal structure complexes. For the ligands, the predicted binding energies differed from measured values about ± 0.8 kcal/mol. For general ligands, the docking simulation clearly predicted a single binding mode that matched the crystallographic binding mode within 1.0 Å RMSD. For two ligands, where the docking procedure yielded an ambiguous result, solutions matching the crystallographic result could be obtained by including an additional crystallographically observed water molecule in the protein model. In summary, AutoDock 3.0 appears to be useful in predicting key structural and energetic features of ligand binding in the W191G cavity.

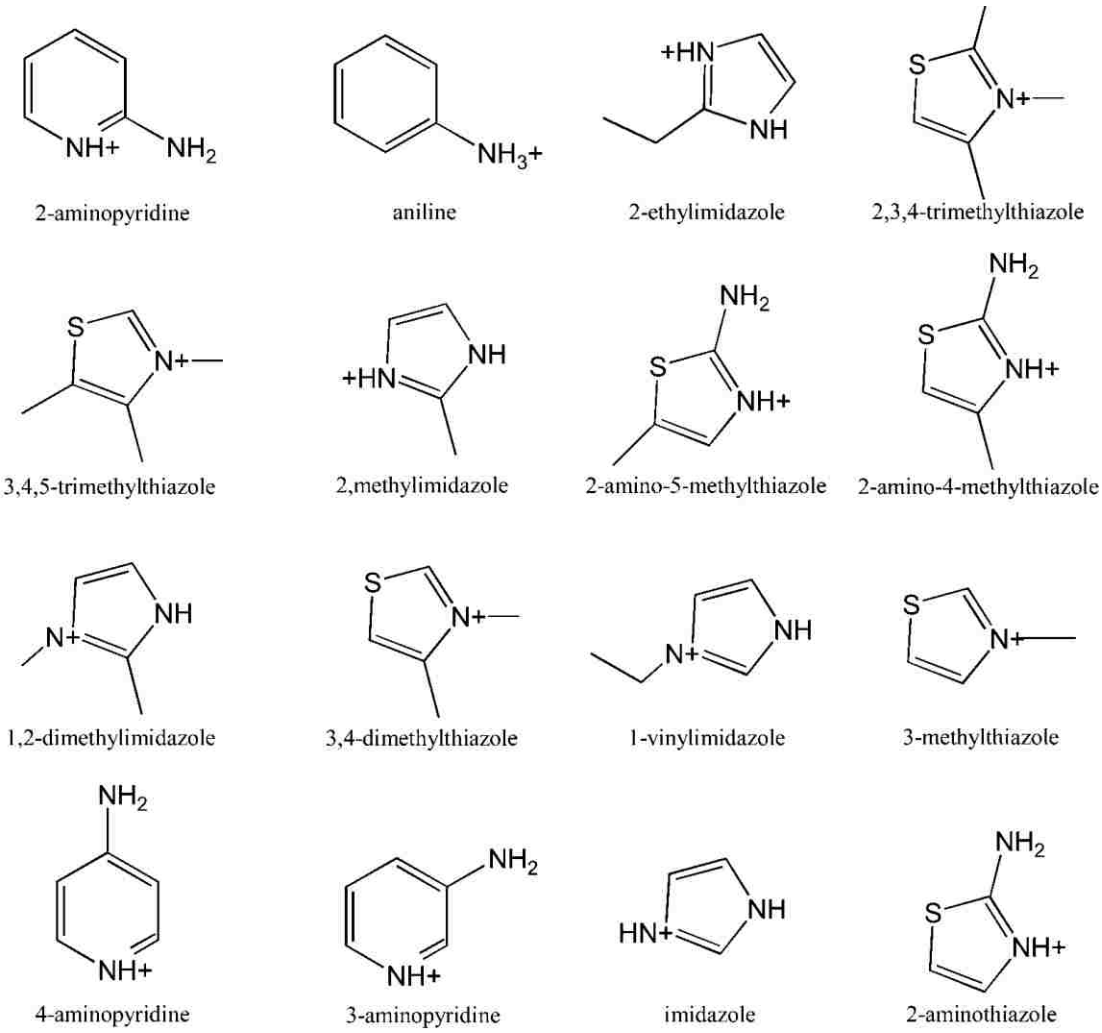

Figure 2-6 The set of ligands docked to the W191G cavity in R.J. Rosenfeld study

Macpherson, Neti, et al [2-10, 2-15] predicted the blocking of the hormone angiotensin II and the effect of the drug losartan on the heart. They simulated docking of losartan with to the myocardial cells. As the hormone will be absorbed by the heart wall during the filling in the ventricle, the blood flow into the left ventricle was calculated for the period of the diastole stage. The full model of drug docking analysis included multi-scale models in three length scale levels: continuum scale, blood cell scale, and scales of the order of angiotensin II interactions with receptors know as

ATR_1 interactions. In continuum scale, the calculation of blood flow in the left ventricle was done to obtain the blood velocity interaction with the ventricle walls. There was done by using the Pesking method described earlier but the boundary conditions were established from patient echocardiograms. The velocity closest to the heart wall of blood flow was used as the velocity flow input to the blood cell scale calculation. The Monte Carlo method was used for the calculations in the scale of blood cell. The blood was considered to be composed of water, erythrocyte, albumin, angiotensin II and losartan. The solution starts with the Landau equation, which in the test particle form below has been described as a generalized diffusion equation in velocity space by Chandrasekhar. Expressed in a non-dimensional form it becomes

$$\partial\phi_\tau = \partial_{v_r}(-F_r + 0.5\partial_s T_{rs})\phi \tag{2.4}$$

The solution is obtained in terms of the drag force F_r and a random force T_{rs}.

$$F_r = -8v^{-1}G(v)v_r \tag{2.5}$$

$$T_{rs} = 2v^{-1}H(v)\delta_{rs} + 2v^{-3}E(v)v_r v_s \tag{2.6}$$

For ATR_1 interactions,since the movements of components in blood are sufficiently far apart, they can be assumed to be due the collisions between the components predicted by molecular dynamics. They evaluated absorption of the drug and angiotensin II through receptors in the diastole cycle. The rate depends on the heart shape as the convective velocity is a function of the changing shape. Receptor density is taken as a function of the amount of neurotransmitters. The result indicate flow velocities up to 7 cm/sec towards the membrane and up to 3 cm/sec away from the membrane. In figure 2-6 there are 15 receptors blocked due to losartan and 6 due

to angiotensin II at the end of the calculation period. It is thought that there are approximately 100 times as many drug and angiotensin II molecules as receptors in the left ventricle.

Figure 2-7 Flowcharts of the three stages of simulation

The atrium and mitral valve have been assumed to be fixed in position and hence they cause locally unrealistic disturbances in the flow.

The result of flow velocity is up to 7 cm/sec towards the membrane and up to 3 cm/sec away from the membrane. In the simulation a drug molecule docks with a receptor and after sometime it is removed. In figure 2-9 there are 15 receptors blocked due to losartan and 6 due to angiotensin II at the end of the calculation period. There are approximately 100 times as many drug and angiotensin II molecules as receptors in the left ventricle.

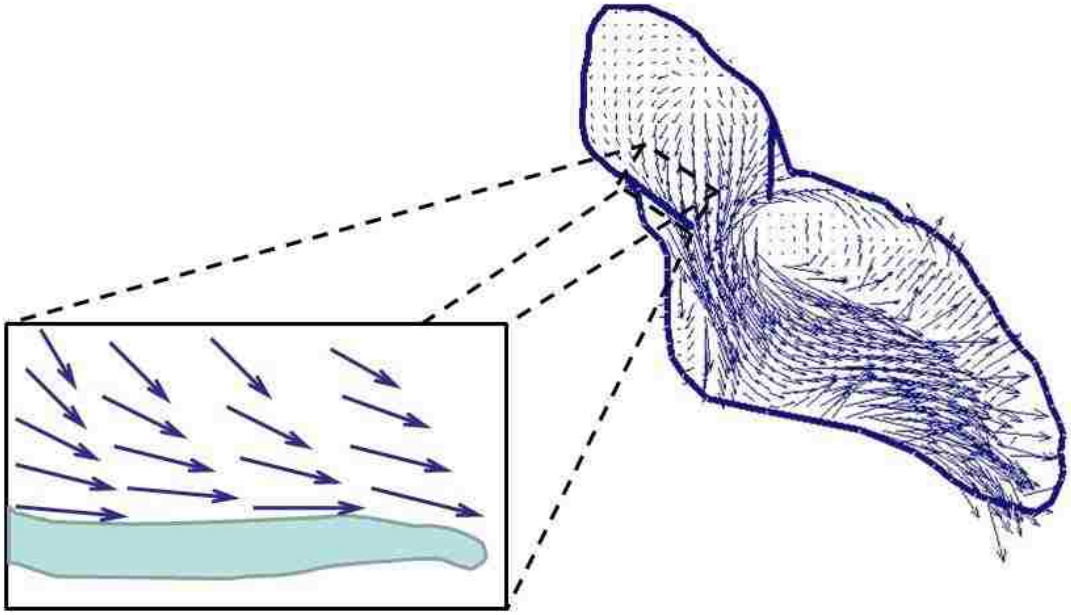

Figure 2-8 Flow velocity closest to the heart wall during diastole

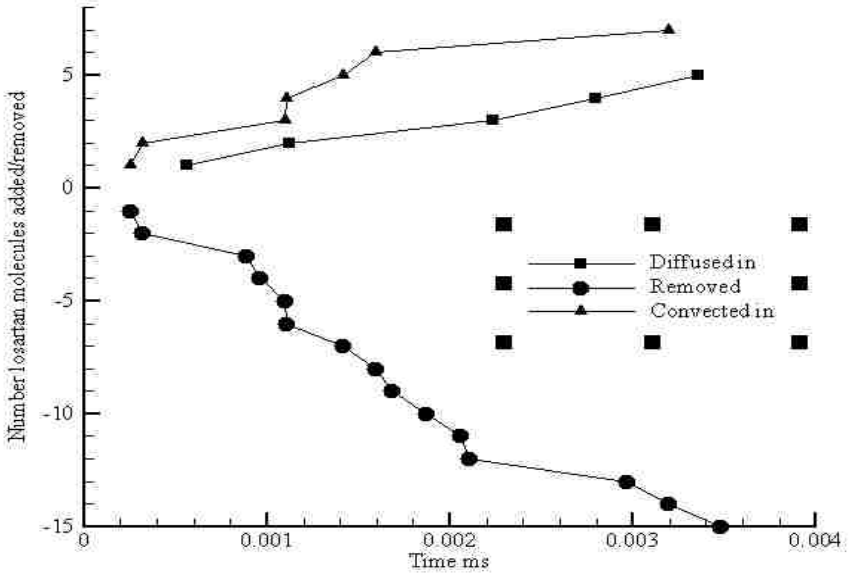

Figure 2-9 The docking of losartan with convective velocity 1cm/sec

When the normal velocity is 10 cm/sec the convective velocity dominates the process (Figure 2-9). Diffusion domination was rare when more than twice the number of receptors were blocked at low flow velocities (1cm/sec).

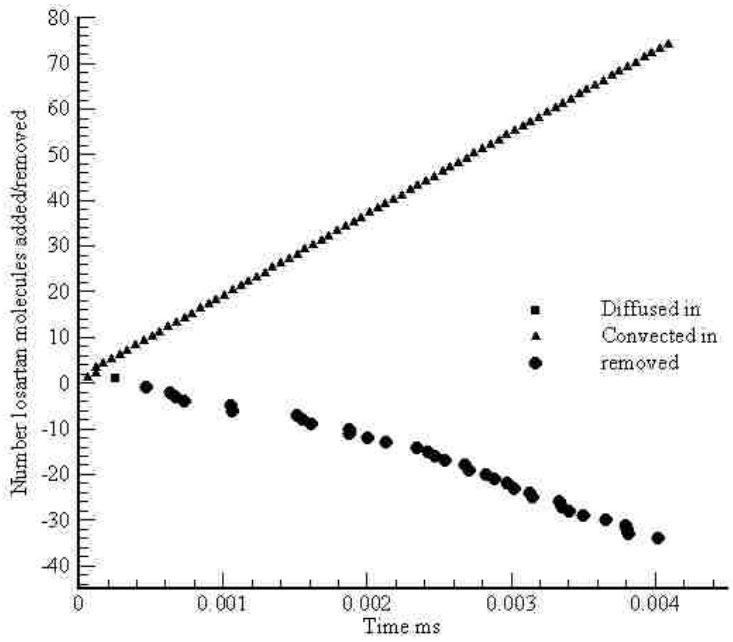

Figure 2-10 The docking of losartan with convective velocity 10cm/sec

The number of angiotensin receptor sites that were blocked was around 28 compared to 38 for losartan and the difference appears to be greater than due to statistical variations. Thus it again appears that with large convective velocities the drug docks (and blocks) more readily than the angiotensin II.

2.4 Mathematical Models of the Action Potential

Zhang, Holden, et al. [2-16 to 2-18] have developed mathematical models of the action potential in the periphery and center of the rabbit sinoatrial (SA) node, rabbit atrioventricular (AV) node, and the human Purkinje fiber cells. These results of these mathematical models were compared with experimental data. Mathematical

simulation models performed reasonably well compared to some experimental in responses to Na^+ current, L- and T-type Ca^{2+} currents, K^+ currents.

Mathematical models of the action potential in cells of the rabbit SA node at 37°C were developed using experimental data from rabbit SA node preparations. The rabbit SA node measures ~8 mm×~10 mm. The new formulations for a number of ionic currents were SA node cells: i_{Na}, $i_{Ca,L}$, $i_{Ca,T}$, i_{to}, 4-AP-sensitive sustained outward current (i_{sus}), $i_{K,r}$, $i_{K,s}$, and i_f. The models also include formulations for background currents ($i_{b,Na}$, $i_{b,Ca}$, and $i_{b,K}$), i_p, and i_{NaCa}. The membrane potential is calculated using equation 2.7 where as i_{tot} calculated using equation 2.8.

$$\frac{dV}{dt} = -\frac{1}{C_m} i_{tot} \tag{2.7}$$

$$i_{tot} = i_{Na} + i_{Ca,L} + i_{Ca,T} + i_{to} + i_{sus} + i_{K,r} + i_{K,s} + i_f + i_{b,Na} + i_{b,Ca} + i_{b,K} + i_{NaCa} + i_p \tag{2.8}$$

To solve for the action potentials i.e., ordinary differential equations, the fourth-order Runge-Kutta-Merson numerical integration method was employed. The chosen time and space steps were 0.1 ms, which gives a stable solution of the equations and maintains the accuracy of the computation of membrane current and potential. One-dimensional partial differential equations were solved by an explicit Euler method with a three-node approximation of the Laplacian operator, with a time step of 0.1 ms and a space step of 0.1 mm for SA node tissue and 0.32 mm for atrial muscle.

The action potentials generated using the models at 37°C from the SA node of the rabbit at fast and slow time modes. For comparison, figure 2-11 [2-16] also shows action potentials recorded experimentally from rabbit SA node preparations:

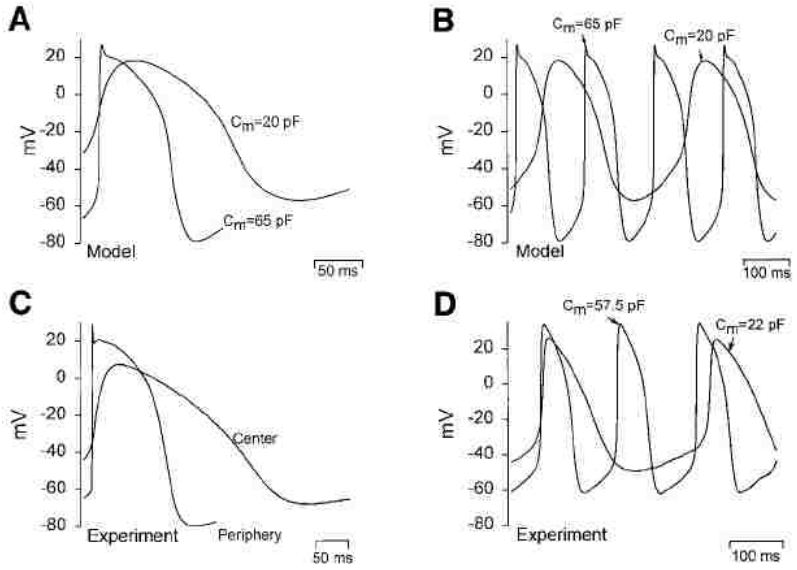

Figure 2-11 Comparison the action potentials simulation result with experiment, A and C fast time base, B and D slow time base

The effect on the action potentials in blocking i_{Na}, $i_{Ca,L}$, $i_{Ca,T}$, and i_K of the models behave in the same way as the effect on the action potentials recorded from the rabbit SA node tissue. However the takeoff potential and maximum upstroke velocity on the action potentials of the models was different from the action potentials recorded from the rabbit SA node tissue. For example, effect of blocking of i_{Na}, in figure 2-12, experimental data the maximum upstroke velocity was reduced from 100 to 5 V/s but in the simulation it reduced from 60 to 8 V/s.

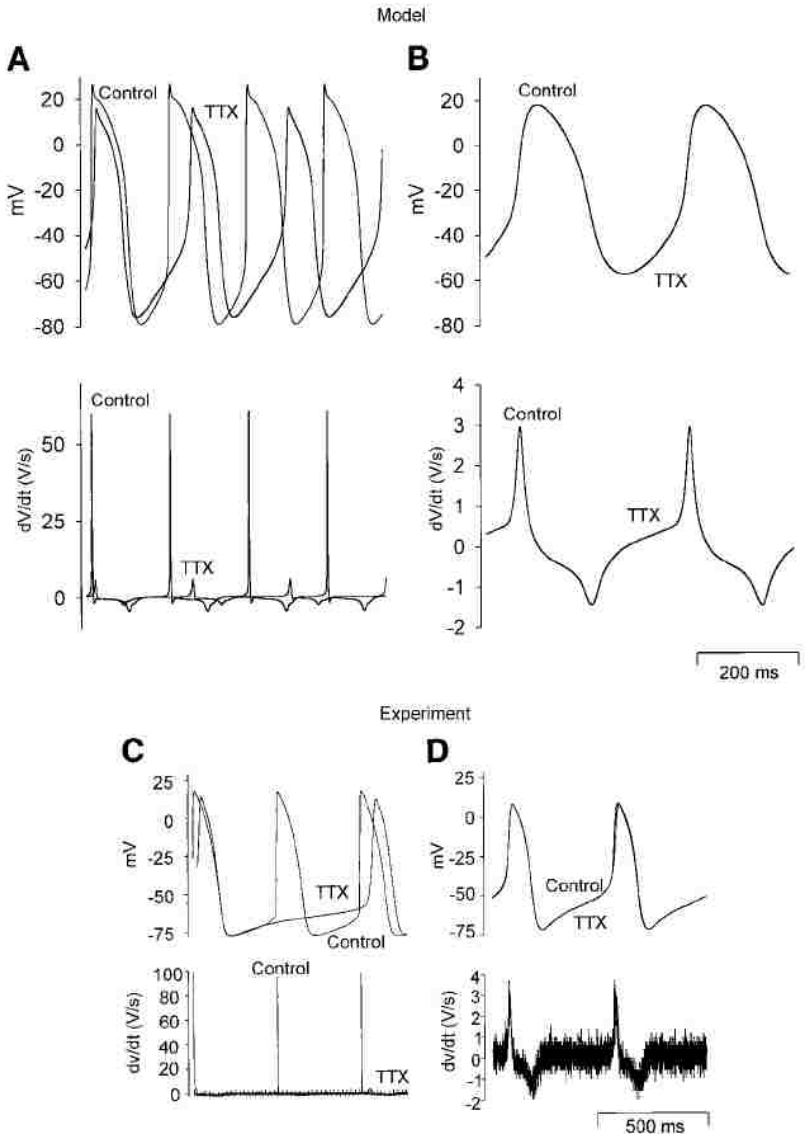

Figure 2-12 Effect of block of i_{Na} SA node action potentials

Comparing the previous models, the models developed have a structure similar to previous SA node models. However, because of recent experimental findings, the new models have been able to update from the previous models in many ways. Such as, 4-AP sensitive current (i_{to} and i_{sus}), and the two components of i_K ($i_{K,r}$ and $i_{K,s}$). Therefore the developed models agree better with experiments. The limitations of the present models include, for example lack of information about the relationship

between the densities of some ionic currents, uncertainty about the accuracy of the experimental source data, and lack of intracellular Na^{+} and Ca_2^{+} regulation.

2.5 Heart-Brain Interaction

Andrew [2-20], illustrated the concept of a functional "heart brain" interaction in 1991. He discovered that the heart has a complex fundamental nervous system sufficiently sophisticated to qualify as a "little brain" in its own right called the intrinsic cardiac nervous system, or heart's brain. The heart's brain is a complex network of several types of neurons, neurotransmitters, proteins and support cells like those found in the brain proper. Its sophisticated circuitry enables it to act independently of the cranial systems / brain. This enables 'heart' to learn, remember, and even feel and sense. He also provided a comprehensive overview of the function of the heart's intrinsic nervous system and the role of central and peripheral autonomic neurons in the regulation of cardiac function. The nervous system pathways between the heart and brain are shown in Figure 2-13. There are around 40,000 neurons in heart's nervous system, called sensory neurites, which detect circulating hormones and neurochemicals and sense heart rate and pressure information. Hormonal, chemical, rate and pressure information is translated into neurological impulses by the heart's nervous system and send from the heart to the brain through several afferent pathways (parasympathetic). The afferent nerve pathways enter the brain pass through paths located in the brain stem called the medulla. At this location the signals have a regulatory role over many of the autonomic nervous system signals and flow out of the brain to the heart, blood vessels and other glands and organs.

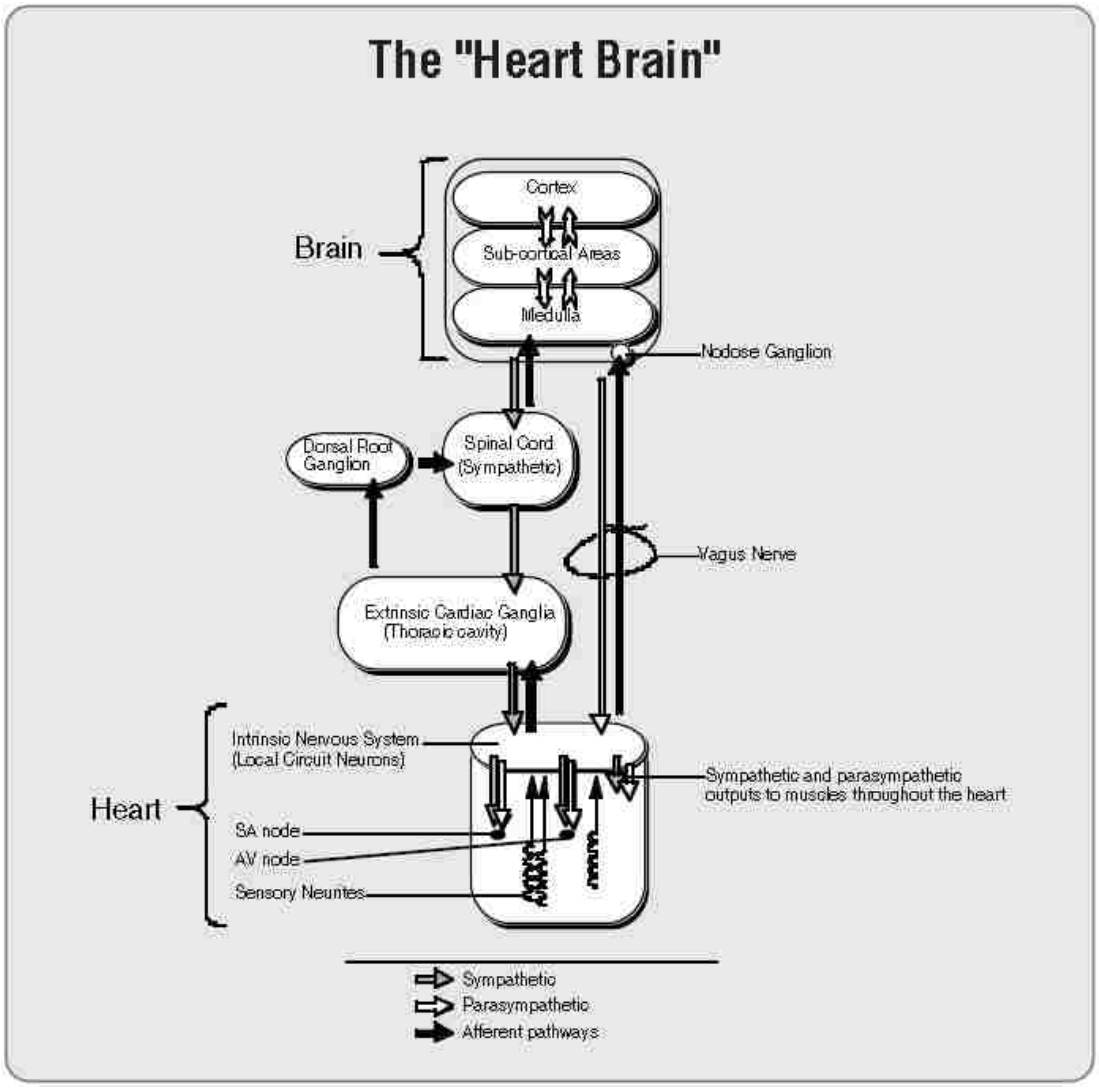

Figure 2-13 The heart's intrinsic cardiac nervous system

Armour has explained that the heart nervous system interacts in parallel with neuronal processing centers but as a separate processing system. The heart has its own intrinsic nervous system that operates and processes information independent of the brain or nervous system. This is what permits a heart transplantation to work. Normally, the heart communicates with the brain via nerve fibers running through the vagus nerve and the spinal column. In a heart transplant, these nerve connections do

not reconnect for an extended period of time, if at all; however, the transplanted heart is able to function in its new host through the capacity of its intact, intrinsic nervous system.

The intrinsic cardiac nervous system, or heart's brain, is made up of complex ganglia, containing afferent local circuit (receiving inter-neurons) and efferent (transmitting) sympathetic and parasympathetic neurons Armour [2-20]. Multifunctional sensory neurites, which are distributed throughout the heart, are sensitive to many types of sensory input originating from within the heart itself. The intrinsic cardiac ganglia integrate messages from the brain and other processing centers throughout the body with information received from the cardiac sensory neurites. Once information has been processed by the heart's intrinsic neurons, the appropriate signals are sent to the sinoatrial (SV) and atrioventricular (AV) nodes and on to the muscles in the heart. Thus, under normal physiological conditions, the heart's intrinsic nervous system plays an important role in much of the routine control of cardiac function, independent of the central nervous system. The heart's intrinsic nervous system is very important for the maintenance of cardiovascular stability and efficiency, and without it, the heart cannot function properly.

Traditionally, the study of communication pathways between the head and heart has been approached from a rather one-sided perspective, with scientists focusing primarily on the heart's responses to the brain's commands. However, Armour's research has now proven that communication between the heart and brain is

actually a dynamic, ongoing, two-way dialogue, with each organ continuously influencing the other's function. Research has shown that the heart communicates to the brain in four major ways: neurological communication or nervous system (via the transmission of nerve impulses), biochemical communication (via hormones and neurotransmitters), biophysical communication or (baro) pulse waves (via pressure waves), and energetic communication (through electromagnetic field interactions). Communication along all these conduits significantly affects the brain's activity. Moreover, the research shows that messages that the heart sends the brain can significantly affect performance.

Alkire [2-21], explained the relationship between anesthetic-induced changes in the electroencephalogram (EEG) and the concurrent cerebral metabolic changes caused by anesthesia. Using positron emission tomography (PET) data of cerebral metabolism obtained in volunteers during anesthesia were correlated retrospectively with various concurrently measured EEG descriptors. An EEG signal was obtained using gold cup electrodes applied to the scalp with cream and located according to the international 10 - 20 electrode system. Skin impedance was maintained at $< 5\ k\Omega$. The following leads were recorded: left and right frontal-mastoid (FP1-A1, FP2-A2, channels 1 and 2), left and right frontal-CZ (FP1-CZ, FP2-CZ, channels 3 and 4), plus a ground electrode placed at the center of the forehead. He found the percentage of absolute cerebral metabolic reduction, evident during anesthesia, trended median frequency ($r = -0.46$, $P = 0.11$), and the spectral edge ($r = -0.52$, $P = 0.07$), and correlated with anesthetic type ($r = -0.70$, $P < 0.05$), relative β power ($r = -0.60$, $P <$

0.05), total power ($r = 0.71$, $P < 0.01$), and bispectral index ($r = - 0.81$, $P < 0.001$). After controlling for anesthetic type, only bispectral index ($r = 0.40$, $P = 0.08$) and α power ($r = 0.37$, $P = 0.10$) approached significance for explaining residual percentage of absolute cerebral metabolic reduction prediction error. Some EEG descriptors correlated linearly with the magnitude of the cerebral metabolic reduction caused by propofol and isoflurane anesthesia. These data suggest that a physiologic link exists between the EEG data and cerebral metabolism during anesthesia that is mathematically quantifiable.

Musizza, Stefanovska, et al.[2-22] hypothesized interactions that occur between cardio-respiratory and neuronal oscillations. To prove the hypothesized, they have applied stochastic non-linear dynamics techniques to the analysis of time-varying hysiological oscillations recorded from rats under anaesthesia. The cardiac and respiratory oscillations were extracted from ECG and respiration signals. The time evolutions of individual neuronal oscillations were extracted from the EEG by means of the wavelet transform, with particular attention being paid to δ-waves (0.5–3.5 Hz) and θ-waves (3.5–7.5 Hz). They found the presence of strong δ-oscillations and θ-oscillations in the EEG as both the respiratory and cardiac frequencies remain relatively stable. From their results, that imply the existanc causal relationship between cardiac, respiratory and brain oscillatory processes. Lacey and Lacey [2-23] have presented a series of biochemical processes, of repetitive membrane depolarization and repolarization, results in repetitive transmission along the heart's own conductive tissue system, which, in turn, results in cyclic contraction and

relaxation of the cardiac muscle. The heart is slowed and speeded by the vagal (pressure, baro-sensor) and sympathetic cardiac efferents. Sensitive interceptors feed back to the central nervous system information about the timing, force, volume, and pressure of each, heartbeat. They have shown the relation between the whole-nerve electroneurogram of the right carotid sinus nerve with pressure within the carotid sinus produced.

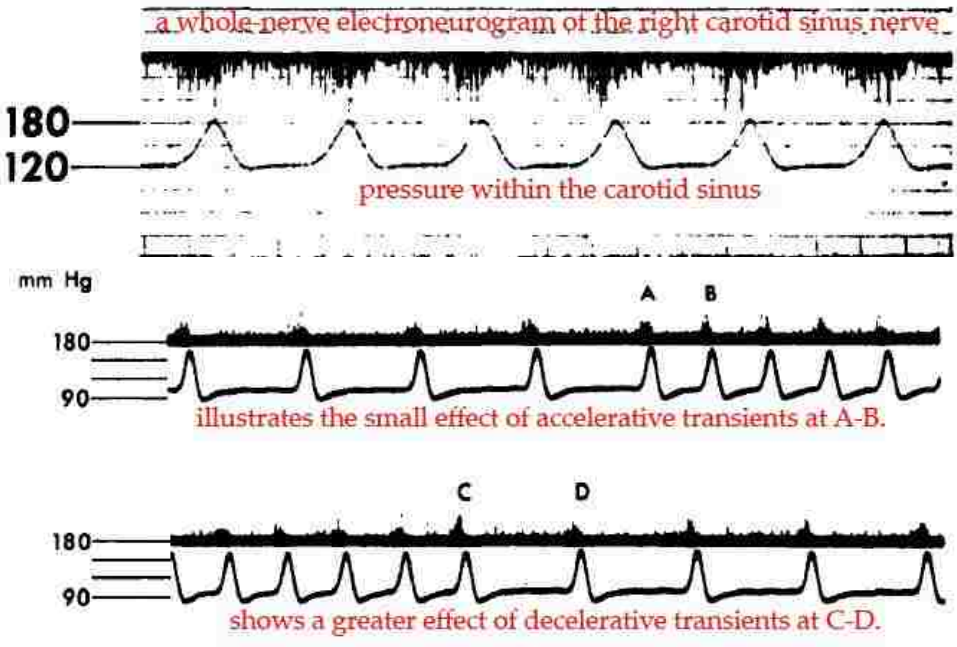

Figure 2-14 Relation between electoneurgram and pressure

Akin [2-24] has compared the use of Fourier transform method and Wavelet transform method of EEG for detecting brain diseases. In his study, two EEG signals for both healthy (normal) and pathological (abnormal) cases were recorded from subjects under relaxation, with their eyes closed. These signals analyzed by Fourier transform method and Wavelet transform method. Small changes could not be detected using Fourier transforms. The wavelet transform in 3D representation of

signals as amplitude, frequency, and time was found to be more useful. The 3D representation is more convenient for pathological cases.

The current work focuses on the effect of the heart on brain function for patients with paced hearts. Patient echocardiograms are used for analyzing the heart blood flow and myocardial stresses. Patient ECG and EEH signal analyses are used to relate the heart paced performance on the EEG and brain function. Details pertaining these analyses are presented in the following chapters.

CHAPTER 3

Docking of Dobutamine

As a result of the injection of Dobutamine and the uptake of Dobutamine by the patient, the patient's heart rate increases. This Chapter describes the first step in the process of the absorption of Dobutamine by the patient and it involves the docking of Dobutamine to an appropriate receptor on the cell. The Dobutamine attaches to the sinoatrial (SA) node cells at particular sites on the membrane surface. These sites are known as β_1 adrenergic receptors. As there are no experimental results available for this docking procedure this chapter describes the calculations involved in estimating the rate of docking on the cells.

3.1 Dobutamine and β_1 Receptor

Dobutamine is a sympathetic nervous system drug used for treating people who have problems with heart failure and cardiogenic shock. Dobutamine ($C_{18}H_{23}NO_3$), has a 2 minute half-life in the human body, and is a drug that provides direct stimulation to the β_1 adrenergic receptor. However dobutamine also has a small effect in the stimulation of β_2 and α_1 receptors. The average molecular weight and monoisotopic molecular weight of dobutamine is 301.3801 and 301.1678. The docking of dobutamine to these receptors occurs at the sinoatrial (SA) node cell wall that is a small mass of specialized tissue located in the right atrium of the heart.

Beta receptor is a class of G-protein-coupled receptors. There are three known types of beta receptor, β_1, β_2, and β_3. β_1-Adrenergic receptors (ADRB1) are located mainly in the heart and in the kidneys.

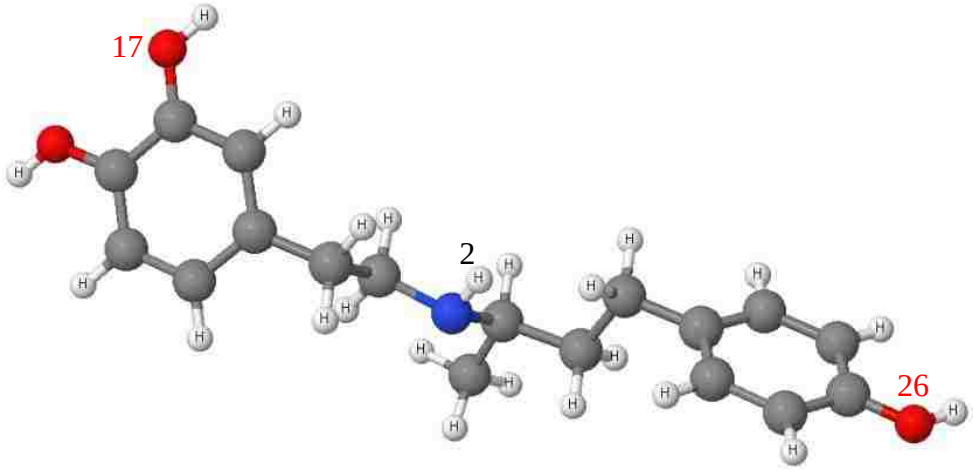

Figure 3-1 The chemical structure of dobutamine [http://pdb.rcsb.org/pdb/ligand/ligandsummary.do?hetId=Y00&sid=2Y01]

3.2 Using AutoDock4

The AutoDock4 software is a computer program available under the GNU General Public License, and is designed to predict the interaction of ligands to a set of grids describing the target protein. AutoDock4 has been widely used in many academic, governmental and non-profit institutions around the world because AutoDock4 not only saves time and cost in modeling the chemistry and managing the experiments but also provides high quality predictions. To utilizeAutoDock4 software there are four major steps: preparation of coordinate system, pre-calculation of atomic affinities, docking of ligands, and analysis of results.

In coordinate preparation step, the Protein Data Bank (PDB) of the ligand and the target protein are used. The extended PDB format provides standard representation for macromolecular structure data that includes polar hydrogen atoms, but not hydrogen atoms bonded to carbon atoms. AutoDock4 software converts PDB format to PDBQT coordinate files including atomic partial charges, atom types and information on the torsional degrees of freedom.

The pre-calculation of atomic affinities step, involves using the AutoGrid procedure whereby the protein is embedded in a three-dimensional grid and a probe atom is placed at each grid point. The energy of interaction of this single atom with the protein is assigned to the grid point.

The docking of ligands step is carried out using one of several search methods. The most efficient method is a Lamarckian Genetic Algorithm (LGA), For typical systems, AutoDock is run several times to obtain several docking conformations/ Analysis of the predicted energy and the consistency of results are combined to identify the best solution.

The last step involves the analysis of results. AutoDockTools includes a number of methods for analyzing the results of docking simulations. These include tools for clustering results by conformational similarity, visualizing conformations, visualizing interactions between ligands and proteins, and visualizing the affinity potentials created by AutoGrid.

Each docking by AutoDock4 requires at least four input files. (1) a PDBQT file for the ligand, dobutamine data file from PDB file, (2) a PDBQT file for the receptor, β_1 adrenergic receptor data file from PDB file, (3) a grid parameter file (GPF) for the AutoGrid calculation, and (4) a docking parameter file (DPF) for AutoDock4 calculation.

3.3 Docking Positions of Dobutamine Atoms

The results for docking of dobutamine into the β_1 adrenergic receptor by the AutoDock4 program are given in terms of ten interactions. The possible docking positions of the dobutamine atoms specified in cartesian coordinates. Docking is assumed to be assured when the length between bonded atoms is less than 2.5×10^{-10} m. That is if the dobutamine atom is within 2.5×10^{-10} m of the atoms of β_1 adrenergic receptor, then bonding is assumed to have taken place. Therefore, the nearest atom between the β_1 receptor and each atom of dobutamine can be calculated from

$$d_{min} = \sqrt{(x_b - x_d)^2 + (y_b - y_d)^2 + (z_b - z_d)^2} \qquad (3.1)$$

Where as d_{min} is the least distance between dobutamine and β_1 receptor atom, (x_b, y_b, z_b) is the position of β_1 atom, and (x_d, y_d, z_d) is the position of dobutamine atom.

In all cases the dobutamine had at least one O-bond connected to the β_1 adrenergic receptor. The result of the calculated docking positions for dobutamine is shown in figure 3-2. The most likely configurations of all ten possible docking

positions are the first and the fourth docked positions, figure 3-2, involving 3 O-bonds on the β_1 adrenergic receptor.

The results for docking of the dobutamine into the β_1 adrenergic receptor, also included was given the estimated an estimate of the free energy of binding. The eEstimated free energy of binding by software AutoDock is included obtained from intermolecular energy, internal energy, torsion free energy, and unbound system energy. The intermolecular energy combines with the van der Waals energy, hydrogen bond energy, dissolution energy, and electrostatic energy. The first possible docking position result shown in figure 3-3 is the best position of docking dobutamine with the β_1 adrenergic receptor because this position provides the lowest estimated free energy of binding. The estimated free energy of binding is 10.49 kcal/mol as shown in figure 3-3.

dobutamine atom		beta I atom	docking									
number	name		1	2	3	4	5	6	7	8	9	10
1	N	d_{min} (A)	2.030879	2.227681	1.898663	1.576158	2.454867	2.200735	2.238256	2.108333	1.845344	2.227313
		number	3513	3513	3447	1379	3513	3447	3513	3513	1379	3513
		name	H	H	H	H	H	H	H	H	H	H
2	C	d_{min} (A)	2.677225	2.583053	2.013816	2.338299	2.402119	1.862699	2.573506	2.671232	2.867135	2.570462
		number	4013	4068	1377	745	4068	699	4068	4068	1377	4068
		name	O	O	H	O	O	H	O	O	H	O
3	C	d_{min} (A)	1.944167	2.134034	1.594833	2.231108	2.085795	1.609373	2.117294	2.007401	2.00139	2.11445
		number	3518	4017	1441	696	4017	1441	3518	3518	699	3518
		name	H	H	H	H	H	H	H	H	H	H
4	C	d_{min} (A)	1.539398	1.590693	1.932249	2.207014	1.669642	1.916372	1.596855	1.55737	1.763982	1.617808
		number	4058	4058	1379	1379	4058	1379	4058	4058	1379	4058
		name	H	H	H	H	H	H	H	H	H	H
5	C	d_{min} (A)	1.621223	1.602072	1.535142	1.566899	1.554165	1.63029	1.677494	1.647287	2.333864	1.638116
		number	4060	4060	1377	733	4060	1377	4060	4060	696	4060
		name	H	H	H	H	H	H	H	H	H	H
6	C	d_{min} (A)	2.165752	2.196894	1.794599	2.802463	2.250478	1.957262	2.24155	2.191733	2.062712	2.23033
		number	4058	4058	4058	1379	4058	4058	4058	4058	1379	4058
		name	H	H	H	H	H	H	H	H	H	H
7	NH	d_{min} (A)	2.288844	2.567856	2.234437	2.24444	2.869532	2.498398	2.621016	2.418747	1.795337	2.581187
		number	3513	3513	4057	745	3513	4057	3513	3513	3451	3513
		name	H	H	H	O	H	H	H	H	H	H
8	C	d_{min} (A)	2.170715	2.246317	2.582906	2.495677	2.345294	2.383681	2.247627	2.188144	2.629409	2.257475
		number	4057	4057	3513	795	4057	1379	4057	4057	3513	4057
		name	H	H	H	H	H	H	H	H	H	H
9	C	d_{min} (A)	2.958106	2.87004	2.008759	2.311648	2.885334	2.190704	2.812965	2.904862	1.938495	2.829062
		number	696	696	1379	3518	696	3513	696	696	1344	696
		name	H	H	H	H	H	H	H	H	H	H
10	C	d_{min} (A)	1.860613	1.818934	2.696378	1.748065	1.887303	2.273451	1.822039	1.857809	2.286053	1.790515
		number	696	696	1344	4027	696	3518	696	696	1344	696
		name	H	H	H	H	H	H	H	H	H	H
11	C	d_{min} (A)	1.821568	1.756665	2.28425	2.59943	1.744243	2.172315	1.72938	1.794543	2.246716	1.759987
		number	4109	4109	795	4031	4109	795	4109	4109	795	4109
		name	H	H	H	H	H	H	H	H	H	H
12	C	d_{min} (A)	2.54318	2.512944	2.451141	2.275417	2.488342	2.402601	2.537733	2.528501	2.558469	2.497912
		number	4057	4057	3518	1326	1441	795	4057	4057	4017	4057
		name	H	H	H	H	H	H	H	H	H	H
13	C	d_{min} (A)	1.512946	1.567118	2.679387	2.440869	1.555964	2.177795	1.568651	1.519822	2.730006	1.580801
		number	3447	3447	3513	795	3447	1379	3447	3447	3513	3447
		name	H	H	H	H	H	H	H	H	H	H
14	C	d_{min} (A)	1.475312	1.433906	2.190991	1.763739	1.428864	2.059255	1.448871	1.474129	1.948739	1.455699
		number	4109	4109	795	852	4109	795	4109	4109	4027	4109
		name	H	H	H	H	H	H	H	H	H	H
15	H	d_{min} (A)	1.428794	1.399358	2.643142	1.481419	1.446255	2.044915	1.431993	1.438138	1.691545	1.475687
		number	4109	4109	795	4031	4109	1326	4109	4109	4027	4109
		name	H	H	H	H	H	H	H	H	H	H
16	O	d_{min} (A)	2.134419	2.103551	1.965254	1.465858	1.994417	1.661771	2.072198	2.08517	1.821955	2.111291
		number	3444	3444	4017	1326	1441	1327	3444	3444	4017	3444
		name	H	H	H	H	H	H	H	H	H	H
17	OH	d_{min} (A)	2.120306	2.169942	1.705083	1.85392	1.962373	1.658157	2.106909	2.103151	1.99951	2.193864
		number	3382	3382	4027	1275	3444	796	3382	3382	4066	3382
		name	O	O	H	H	H	H	O	O	H	O
18	C	d_{min} (A)	1.970847	2.321681	1.978692	2.489798	2.149166	1.793044	2.404331	2.151246	1.590392	2.345011
		number	3518	3518	4109	746	795	704	3518	3518	1441	3518
		name	H	H	H	O	H	H	H	H	H	H
19	C	d_{min} (A)	2.348851	2.042652	2.011218	2.240003	1.88545	1.960554	2.046179	2.169074	2.247458	2.057044
		number	795	795	4109	4109	795	4109	795	795	3444	795
		name	H	H	H	H	H	H	H	H	H	H
20	C	d_{min} (A)	1.63237	1.591364	2.2235	2.010432	2.734474	2.106401	1.630084	1.579186	1.682649	1.585354
		number	795	795	4109	704	1327	4109	795	795	4057	795
		name	H	H	H	H	H	H	H	H	H	H
21	C	d_{min} (A)	2.492761	2.227842	2.273213	1.750646	2.027591	2.065505	2.170675	2.311158	2.344815	2.224597
		number	795	738	4057	1441	1379	4057	738	738	4057	738
		name	H	H	H	H	H	H	H	H	H	H
22	C	d_{min} (A)	2.191487	2.384114	2.353264	1.911312	2.214161	2.456784	2.377623	2.404786	2.613967	2.396655
		number	1379	1379	4057	1441	1379	4057	1379	1379	3382	1379
		name	H	H	H	H	H	H	H	H	O	H
23	C	d_{min} (A)	1.951145	1.999663	2.610412	2.317097	2.292541	2.577731	1.901815	2.000821	1.486098	1.974797
		number	1379	1379	4057	3444	738	4107	1379	1379	3390	1379
		name	H	H	H	H	H	O	H	H	H	H
24	C	d_{min} (A)	2.367853	2.664385	2.465423	1.905485	1.70999	1.951352	2.653151	2.544194	1.716079	2.624299
		number	1332	1332	3390	4057	795	3390	1332	1332	3390	1332
		name	H	H	H	H	H	H	H	H	H	H
25	O	d_{min} (A)	1.992535	2.021996	1.880573	1.868062	1.99621	2.05256	1.918517	1.979128	2.43563	1.943889
		number	732	733	4088	3391	732	4088	733	732	3380	733
		name	H	H	H	H	H	H	H	H	H	H
26	OH	d_{min} (A)	1.925967	1.93669	1.856748	1.720646	2.024015	1.917644	1.845033	1.866101	1.954102	1.88807
		number	1378	733	4050	3444	1378	4088	733	733	4162	733
		name	O	H	O	H	O	H	H	H	H	H

Figure 3-2 Minimum distance docking of dobutamine atom on β_1 receptor

```
Run:    1 / 10
Date:   Tue Aug 25 16:10:19 2009
Output level is set to 1.

        FINAL LAMARCKIAN GENETIC ALGORITHM DOCKED STATE
        _______________________________________________

DOCKED: MODEL        1
DOCKED: USER    Run = 1
DOCKED: USER    DPF = C:\cygwin\home\Chokchai\Dobutamine.dpf
DOCKED: USER
DOCKED: USER    Estimated Free Energy of Binding    =  +10.49 kcal/mol  [=(1)+(2)+(3)-(4)]
DOCKED: USER
DOCKED: USER    (1) Final Intermolecular Energy     =   +7.50 kcal/mol
DOCKED: USER        vdW + Hbond + desolv Energy     =   +7.92 kcal/mol
DOCKED: USER        Electrostatic Energy            =   -0.41 kcal/mol
DOCKED: USER    (2) Final Total Internal Energy     =   +1.76 kcal/mol
DOCKED: USER    (3) Torsional Free Energy           =   +2.98 kcal/mol
DOCKED: USER    (4) Unbound System's Energy         =   +1.76 kcal/mol
DOCKED: USER
DOCKED: USER
DOCKED: USER    NEWDPF move Dobutamine.pdbqt
DOCKED: USER    NEWDPF about 0.236500 1.039700 -0.458800
DOCKED: USER    NEWDPF tran0 -0.715172 -3.745308 -0.505443
DOCKED: USER    NEWDPF quaternion0 0.468049 0.027926 -0.355870 -0.808398
DOCKED: USER    NEWDPF axisangle0 0.795141 0.047441 -0.604566 -72.120674
DOCKED: USER    NEWDPF quat0 0.795141 0.047441 -0.604566 -72.120674 # deprecated
DOCKED: USER    NEWDPF dihe0 -156.41 52.32 -6.91 158.58 -126.67 56.81 -150.84 142.14 -24.99 66.43
DOCKED: USER
DOCKED: REMARK  10 active torsions:
DOCKED: REMARK  status: ('A' for Active; 'I' for Inactive)
DOCKED: REMARK    1  A    between atoms: N_1  and  C_15
DOCKED: REMARK    2  A    between atoms: N_1  and  C_3
DOCKED: REMARK    3  A    between atoms: C_3  and  C_5
DOCKED: REMARK    4  A    between atoms: C_5  and  C_6
DOCKED: REMARK    5  A    between atoms: C_6  and  C_7
DOCKED: REMARK    6  A    between atoms: C_10  and  O_13
DOCKED: REMARK    7  A    between atoms: C_15  and  C_16
DOCKED: REMARK    8  A    between atoms: C_16  and  C_17
DOCKED: REMARK    9  A    between atoms: C_19  and  O_23
DOCKED: REMARK   10  A    between atoms: C_20  and  O_25
DOCKED: USER                              x       y       z     vdW  Elec       q    Type
DOCKED: USER                           _______ _______ _______ _____ _____    _____   ____
DOCKED: ROOT
DOCKED: ATOM      1  N   UNK     0      -1.161  -3.116  -0.258 -0.64 -0.03    +0.087 N
DOCKED: ATOM      2  H   UNK     0      -0.264  -3.453  -0.611 -0.11 -0.12    +0.316 HD
DOCKED: ENDROOT
DOCKED: BRANCH   1   3
DOCKED: ATOM      3  C   UNK     0      -2.140  -4.156  -0.640 +0.73 -0.15    +0.274 C
DOCKED: BRANCH   3   4
DOCKED: ATOM      4  C   UNK     0      -2.614  -3.962  -2.101 +1.53 -0.01    +0.068 C
DOCKED: BRANCH   4   5
DOCKED: ATOM      5  C   UNK     0      -2.647  -2.510  -2.426 -0.58 +0.01    -0.054 A
DOCKED: ATOM      6  C   UNK     0      -2.284  -2.057  -3.715 +0.46 -0.00    +0.010 A
DOCKED: ATOM      7  C   UNK     0      -2.200  -0.681  -3.994 -0.50 -0.03    +0.040 A
DOCKED: ATOM      8  C   UNK     0      -2.498   0.265  -2.993 -0.13 -0.04    +0.098 A
DOCKED: ATOM      9  C   UNK     0      -2.883  -0.171  -1.708 +0.12 -0.02    +0.099 A
DOCKED: ATOM     10  C   UNK     0      -2.969  -1.553  -1.436 +0.08 -0.01    +0.046 A
DOCKED: BRANCH   8  11
DOCKED: ATOM     11  O   UNK     0      -2.411   1.492  -3.251 +1.87 +0.20    -0.358 OA
DOCKED: ATOM     12  H   UNK     0      -2.278   2.075  -2.606 +0.75 -0.02    +0.218 HD
DOCKED: ENDBRANCH   8  11
DOCKED: BRANCH   9  13
DOCKED: ATOM     13  O   UNK     0      -3.134   0.663  -0.800 +0.94 +0.06    -0.358 OA
DOCKED: ATOM     14  H   UNK     0      -2.720   0.625  -0.023 +0.20 -0.08    +0.218 HD
DOCKED: ENDBRANCH   9  13
DOCKED: ENDBRANCH   4   5
DOCKED: ENDBRANCH   3   4
DOCKED: ENDBRANCH   1   3
DOCKED: BRANCH   1  15
DOCKED: ATOM     15  C   UNK     0      -0.982  -2.889   1.203 +0.16 -0.07    +0.216 C
DOCKED: ATOM     16  C   UNK     0      -1.907  -3.811   2.051 +4.02 -0.04    +0.042 C
DOCKED: BRANCH  15  17
DOCKED: ATOM     17  C   UNK     0      -1.279  -1.394   1.525 -0.18 -0.02    +0.040 C
DOCKED: BRANCH  17  18
DOCKED: ATOM     18  C   UNK     0      -1.907  -1.135   2.925 +1.00 -0.05    +0.040 C
DOCKED: BRANCH  18  19
DOCKED: ATOM     19  C   UNK     0      -1.066  -1.725   4.000 -0.48 +0.04    -0.058 A
DOCKED: ATOM     20  C   UNK     0       0.193  -1.164   4.320 -0.07 -0.00    +0.010 A
DOCKED: ATOM     21  C   UNK     0       0.975  -1.694   5.363 +0.15 -0.00    +0.037 A
DOCKED: ATOM     22  C   UNK     0       0.512  -2.797   6.106 -0.59 -0.01    +0.065 A
DOCKED: ATOM     23  C   UNK     0      -0.738  -3.366   5.794 +0.14 -0.02    +0.037 A
DOCKED: ATOM     24  C   UNK     0      -1.518  -2.835   4.750 -0.43 -0.01    +0.010 A
DOCKED: BRANCH  22  25
DOCKED: ATOM     25  O   UNK     0       1.217  -3.263   7.036 -0.46 +0.06    -0.361 OA
DOCKED: ATOM     26  H   UNK     0       0.901  -3.895   7.559 -0.09 -0.06    +0.217 HD
DOCKED: ENDBRANCH  22  25
DOCKED: ENDBRANCH  18  19
DOCKED: ENDBRANCH  17  18
DOCKED: ENDBRANCH  15  17
DOCKED: ENDBRANCH   1  15
DOCKED: TORSDOF 10
DOCKED: TER
DOCKED: ENDMDL
        _______________________
```

Figure 3-3 The first possible docking position from Autodock predictions

The bonding results for the dobutamine atom from AutoDock were compared with results for the similar bonding obtained using MOE software as simulated by Cheney [3-7] and are shown in figure 3-4. MOE (molecular operating environment) software is a comprehensive molecular simulation system that integrates visualization, molecular modeling, protein modeling and bioinformatics, cheminformatics and QSAR Quantitative structure-activity relationship, high throughput discovery, pharmacophore modeling and structure based design. MOE software is expensive (not public domain) and is generally run on supercomputers. Both AutoDock and MOE provide the similar bonding information about dobutamine atom. The MOE software is considered to be more accurate than results obtained Auotodock. Thus with regard to the docking of dobutamine onto the sinoatrial node, we will use the result from the MOE as presented below [3-7]. In figure 3-2 for dobutamine atom number 26, the first O_2 atom is at a distance of 1.925967 Å. From figure 3-4, which are the results from MOE computations, the corresponding first location of O_2 atom is are 1.52 Å which are relatively similar. Since the number representations used by Autodock and MOE are different, it is difficult relate the positions referred to by the two different computational systems. But the locations of the two O_2 atoms referred to above are the same. For example the atom number 26 is at the bottom right hand corner extreme in figure 3-1, where as it is the right hand top corner in figure 3-4.

Interaction Data

Ligand: hum_beta1-dobutamine_08_28_09.pdb: RECEPTOR
Receptor: hum_beta1-dobutamine_08_28_09.pdb: RECEPTOR

Heavy atoms: ligand = 22, receptor = 2960

ligand	receptor	residue	chain	type	score	distance
H 4475	O 899	GLY 98	hum_ 1	H-don	31.7%	1.52
H 4453	OD 1266	ASP 121	hum_ 1	H-don	25.3%	1.23
O 4440	OG 2706	SER 212	hum_ 1	H-don	98.2%	2.43
O 4437	OG 2755	SER 215	hum_ 1	H-don	26.0%	2.69
H 4452	OD 3947	ASN 329	hum_ 1	H-don	49.3%	1.63
O 4440	OG 2706	SER 212	hum_ 1	H-acc	98.2%	2.43
O 4437	OG 2755	SER 215	hum_ 1	H-acc	26.0%	2.69
C 4473	O 899	GLY 98	hum_ 1	weak	0.0%	3.37
C 4473	C 898	GLY 98	hum_ 1	weak	0.0%	4.35
O 4474	C 898	GLY 98	hum_ 1	weak	0.0%	3.67

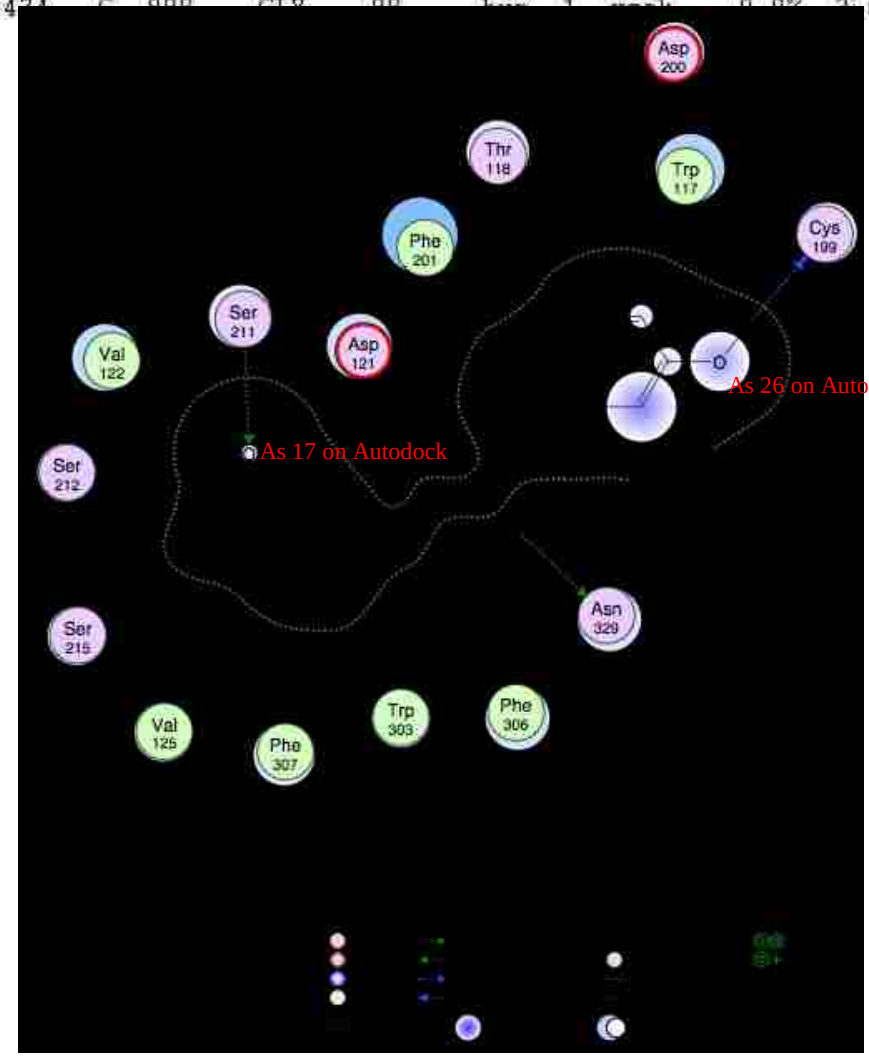

Figure 3-4 MOE bonding results of dobutamine on β_1 adrenergic receptor [3-7]

3.4 Docking of Dobutamine onto the Sinoatrial Node Model

It can be seen in figure 3-2 there are five possible sites on the dobutamine molecule that docking can occur. The motion of the Dobutamine from the blood to the cell membrane was analyzed in three scales. The flow in the region most distant from the surface was a continuum region, the interaction at the blood cell size level was a Monte Carlo process and the interactions with the receptors was undertaken using a direct simulation method known as molecular dynamics.

3.4.1 Continuum Scale

The two dimensional Navier Stokes equation is

$$\rho\left(\frac{\partial \hat{u}}{\partial t} + \hat{u} \bullet \nabla \hat{u}\right) + \nabla p = \mu \nabla^2 \hat{u} + \hat{F} \tag{3.1}$$

The blood flow velocity closest to the membrane was used as the bulk flow input to the blood cell scale calculation.

3.4.2 Blood Cell Scale

The Monte Carlo method was used. The blood is considered to be composed of water, erythrocyte, albumin, angiotensin II and dobutamine. The solution starts with the Landau equation which in the test particle form below has been described as a generalized diffusion equation in velocity space, Chandrasekhar, (1942). Expressed in a non-dimensional form it becomes

$$\partial \boldsymbol{\varphi}_{\boldsymbol{\tau}} = \partial_{v_r}(-\mathbf{F_r} + 0.5\partial_s \mathbf{T_{rs}})\boldsymbol{\varphi} \tag{3.2}$$

where $\boldsymbol{\varphi}$ is the velocity distribution, the v_r differentiation is with respect to non-dimensional velocity $\mathbf{v}/2k\mathbf{T}$, subscript $\boldsymbol{\tau}$ is differentiation with respect to the non-dimensional time defined below.

$$\mathbf{F_r} = -8\mathbf{v}^{-1}\mathbf{G(v)}\mathbf{v_r} \tag{3.3}$$

$$\mathbf{T_{rs}} = 2\mathbf{v}^{-1}\mathbf{H(v)}\boldsymbol{\delta}_{\mathbf{rs}} + 2\mathbf{v}^{-3}\mathbf{E(v)}\mathbf{v_r}\mathbf{v_s} \tag{3.4}$$

and **H**,**G** and **E** are tabulated Chandrasekhar, 1942 [3-1]. The non-dimensional [3-2] time is Balescu 1975

$$\mathbf{t} = \frac{\boldsymbol{\beta}^{3/2}\mathbf{B}n}{m^{1/2}}\boldsymbol{\tau} \tag{3.5}$$

where m is the mass, n the number density, $\boldsymbol{\beta}$ =1/k**T** and **B** is defined as

$$\mathbf{B} = 8\pi^5 \int_0^{l_m} l^3 \mathbf{V}_l dl \tag{3.6}$$

The movement of the blood components assumes they are sufficiently far apart so that collisions between the components will not occur. This is the usual assumption made for the application of the Landau equation. Under these circumstances the force on an ion will consist of a drag due to **G**(**v**) and a random force due to **H**(**v**). The time scale is as defined in equation (3.5).

3.4.3 Molecular Dynamics Scale

The interaction time scale is as defined in equation (3.6). The convective step is then implemented. This is achieved by choosing a short length of time ΔT. The particles then move with the velocity **v** attained at the end of time ΔT for a distance $\mathbf{v}\Delta T$. New cells are then formed and the process repeated. The boundary conditions as

described above are applied at the end of each time step ΔT. The value of ΔT was determined as follows [3-3]. Within a cell containing N particles the particle with the largest total interaction cross section σ_i is chosen for collision where

$$\sigma_i = \sum_{j=1}^{N} \frac{|c_i - c_j|}{c_i} \sigma_{oij} \tag{3.7}$$

The cross section is very difficult to calculate in the present case as the particles are so large. Thus two possible interactions were considered. In one case the particles were considered to carry a charge and the collision cross section σ_{oij} is given in terms of the deflection angle χ_m. In the other case the particles were considered to be hard spheres. The two cases were compared to judge the importance of the cross sectional approximation. The procedure then continues by choosing two colliding particles and time t calculated by

$$t_i = -\xi \times \frac{n}{\sigma_i N} \tag{3.8}$$

Where ξ is a random number between 0 and 1, n is the number of molecules in the cell, N is the number density. This process is repeated for all cells. The geometry for the calculation of the diffusion of the dobutamine in the sinoatrial node is complex as shown in figure 3-5 from [3-4]. The arrows point to capillaries. The length of the centre arrow is approximately 50 μm long. The distance between the capillaries is then 48μm and 81μm. An accurate calculation of a docking process would require detailed knowledge concerning the cell structure, the location of the interstitial fluid,

the capillary lengths, the number of capillaries normally active etc. Within the limits discussed below the diffusion equation (3.9) can be approximately solved.

$$\frac{\partial C_N}{\partial t} = D\frac{\partial^2 C_N}{\partial^2 x} \tag{3.9}$$

Although the diffusion process is three dimensional [3-5], due to the uncertainties in the present case only a one dimensional solution will be considered. The molecular dynamics region was the region above the surface and below the Monte Carlo region. The β_1 adrenergic receptor molecule raises approximately 50Å above the cell surface. Thus the lower surface of the Monte Carlo region was placed at 57Å above the cell surface. If a dobutamine molecule entered the molecular dynamics region it was allowed to proceed at its current velocity to the cell surface. The density of β_1 adrenergic receptors of β_1 adrenergic receptors was obtained from [3-6] as 7.7 pmol/mL. Assuming that 30% of the receptors would be activated at a given time a random number was generated and if it was greater than the probability of hitting a receptor a collision was considered to occur. An arbitrary impact parameter was chosen for the dobutamine molecule as well as an arbitrary rotational angle. The molecule was then allowed to proceed through the molecular dynamics region until it intercepted the receptor. If the appropriate atoms on the dobutamine were within 3Å of a docking site, as shown in figure 3-2, then a docking was considered to occur. At this time the receptor was removed from the cell as thus the density of receptors in the cell was reduced. New dobutamine molecule was introduced at the midpoint of the region of interest.

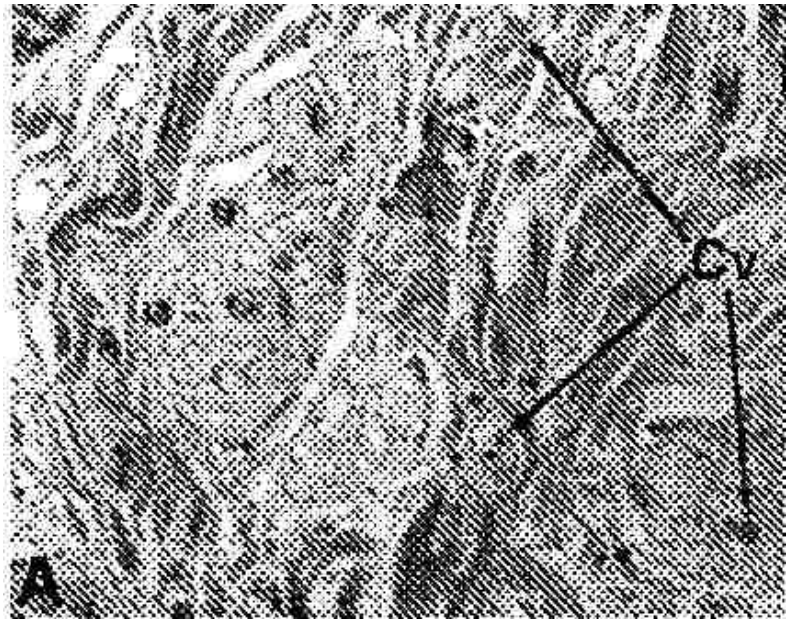

Figure 3-5 Sinoatrial node histologic section [3-4]

3.5 Docking of Dobutamine Model Result

The docking of dobutamine model was undertaken for four different dosages of dobutamine 10, 20, 30, and 40 mics. Because this model required extensive CPU time, each simulation dosage was run until 200 molecules of dobutamine docked into the β_1 adrenergic receptor. This was considered sufficient time as based on the dosage time probably the dobutamine would be released by the receptor in this time. All dosages results look like the linear curve are linear except 10 mics. For 10 mics dosage, the curve is beginning to look exponential. If simulated this model long enough all curve should be exponential.

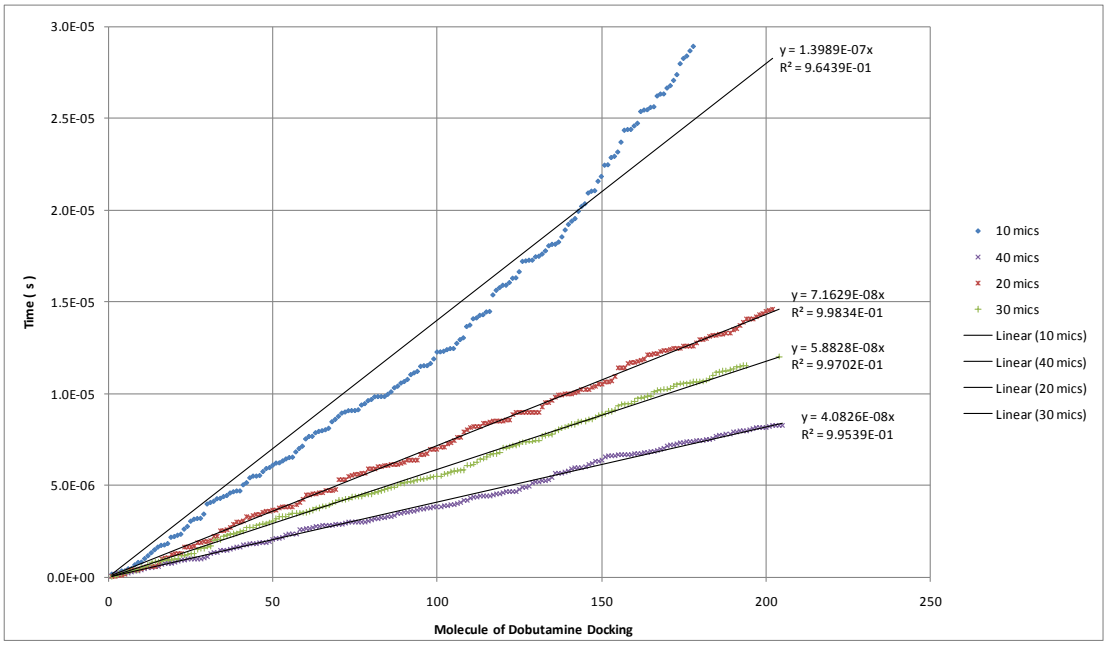

Figure 3-6 Number dobutamine molecules docking with time

3.6 Summary

The locations of dobutamine atoms that docked into the β_1 adrenergic receptor were found by the AutoDock4 software. The best position for docking is the lowest free energy level. The Autodock software was used here since it is a public domain software but more accurate results from Chaney [3-7] obtained using MOE software were used for the best positions of dobutamine docking. The data from MOE results corresponding to the pairs of bonding atoms were used as the parameters for simulation docking of dobutamine model. The quantity of dobutamine molecules docking for each dosage as a function of time period was determined using the procedures described above.

CHAPTER 4

Electrical Signal Generated

In this chapter, the generated electrical signals which lead to heart contractions were simulated. The electrical signal generated by the docking of a combination of the patient's neurotransmitters and the dobutamine dosages. There are three models for each part of the generated signal: sinoatrial (SA) node, atrioventricular (AV) node, and Purkinji fiber (PF). The simulation results from the previous chapter were used as input to this section. The sinoatrial node generates an electrical stimulus that travels down through the conduction pathways and causes both right and left ventricles to contract and pump out blood. The right and left atria are stimulated first and then contract a short period of time before the right and left ventricles. The electrical impulse travels from the sinoatrial node to the atrioventricular (AV) node, where impulses are delayed for a very short period, and then the electrical impulse continues down the conduction pathway into both right and left ventricles.

4.1 Mechanism of Action Potential

The three neuronal parts are activated and inhibited by neurotransmitters or neuron-mimic drug. Drugs that bind to a receptor and produce a response similar to the normal activation of that receptor is called agonist, while drugs that bind to a receptor but are unable to activate that receptor are called antagonist. Dobutamine is a synthetic neuron-mimic drug that acts like the dopamine neurotransmitter group, but predominantly activates the β_1 receptor. Most receptors in the sinoatrial node are the

β_1 adrenergic receptors which are excited by natural neurotransmitters and synthetic neuron-mimic drug such as dobutamine. While the naturally activated neurotransmitters on the dobutamine dock onto the β_1 adrenergic receptors, the sinoatrial node cell membrane potential will increase. The increase of potential is achieved by the admittance of positive on figure 4-3. The increase in positive potential is known as depolarization of the sinoatrial node cell membrane. In the case of the β_1 adrenergic receptors they are stimulated for the second time before the first stimulus has died away, the second stimulated potential adds to the previous one and creates a greater depolarization than from one docked of neurotransmitters or dobutamine alone. This is called temporal summation. In the case of both neurotransmitters and dobutamine they are stimulated simultaneously. This also results in summates in the sinoatrial node cell membrane potential. This is called spatial summation. The increase in potential will continue to occur until a threshold potential is achieved.

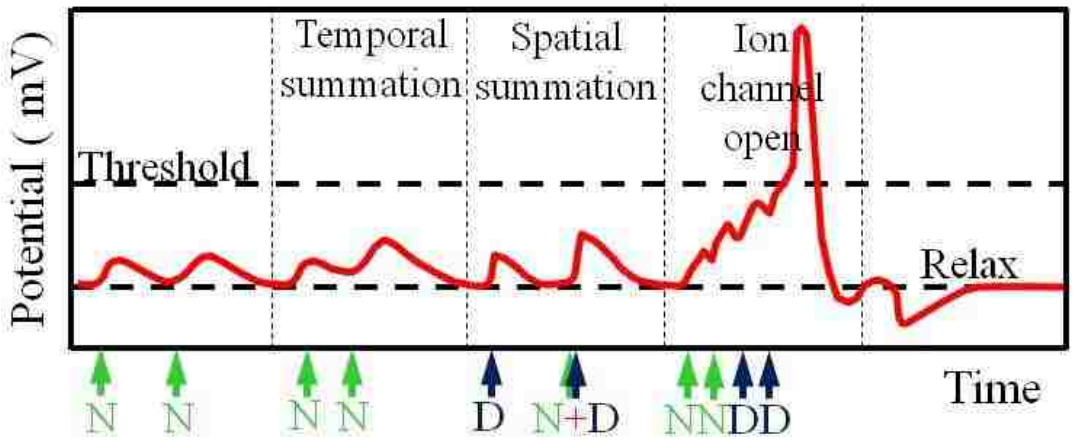

Figure 4-1 Activations of membrane potential
[Vander Human Physiology 8th Ed McGraw.Hill P201]

4.2 Mathematical Model of Cardiac Action Potentials

The action potentials in the heart producing electrical signals to stimulate heart muscle contraction are calculated separately into three parts sinoatrial (SA) node, atrioventricular (AV) node, and Purkinji fiber (PF). The electrical signals in the heart are generated by the flow in and flow out of ions passing through the selected ion gates at the heart neuron cell membrane. They are conducted through the depolarization pathway which combines SA node, internode pathway, AV node, AV bundle, bundle branches, and Purkinje fibers. The three significant ions of heart electrical signal are sodium ionic Na^{+}, calcium ionic Ca^{2+}, and potassium ionic K^{+}. Moreover there are some insignificant ions involved in the generated heart electrical signal that could provide for more accuracy of the mathematical model.

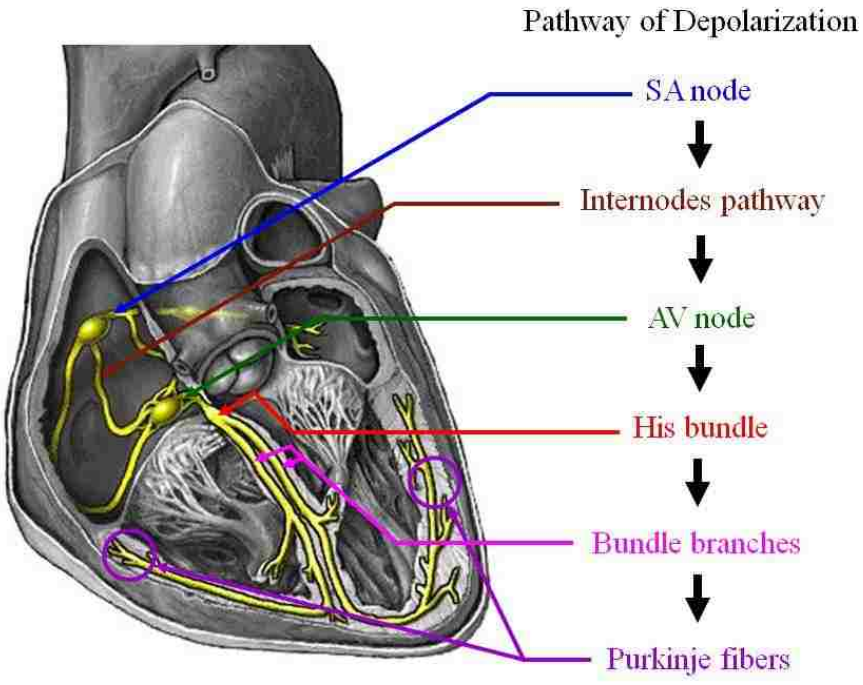

Figure 4-2 Pathway of depolarization

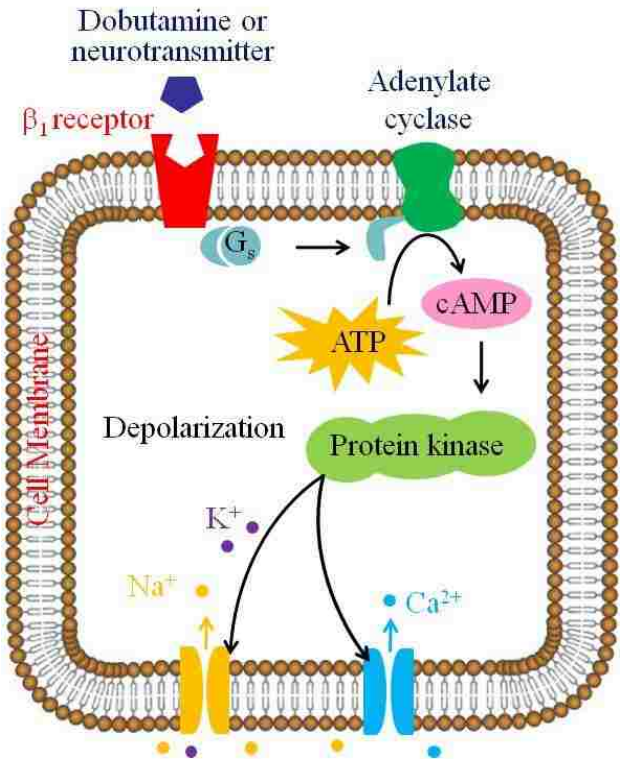

Figure 4-3 Ions flows pass though the cell membrane

4.2.1 Sinoatrial Node Electrical Signal Generation

According to H. Zhang [2-16] study, the sinoatrial node action potentials is combined with eight types of current: Na^+ sodium ionic current (i_{Na}), L-type Ca^{2+} calcium ionic current ($i_{Ca,L}$), T-type Ca^{2+} calcium ionic current ($i_{Ca,T}$), 4-AP-sensitive currents (i_{to} and i_{sus}), rapid delayed rectifying K^+ potassium ionic current ($i_{K,r}$), slow delayed rectifying K^+ potassium ionic current ($i_{K,s}$), hyperpolarization-activated current (i_f), background, pump, and exchanger currents. The action potentials (V) in the sinoatrial node were calculated from the total ionic currents in a cell (i_{tot}) and cell capacitance (C_m).

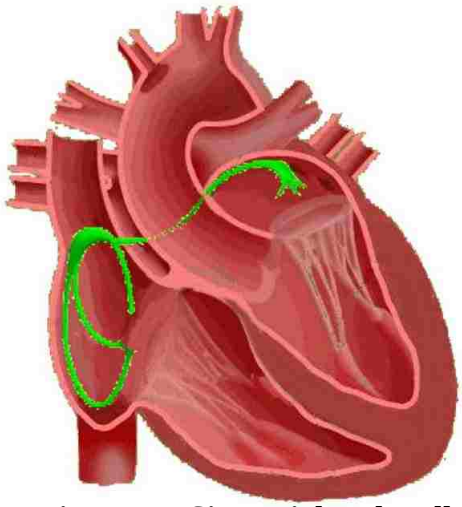

Figure 4-4 Sinoatrial node cell

$$i_{tot} = i_{Na} + i_{Ca,L} + i_{Ca,T} + i_{to} + i_{sus} + i_{K,r} + i_{K,s} + i_f + i_{b,Na} + i_{b,Ca} + i_{b,K} + i_{NaCa} + i_p \quad (4.1)$$

$$\frac{dV}{dt} = -\frac{1}{C_m} i_{tot} \quad (4.2)$$

Equilibrium potentials for Na^+, Ca^{2+}, and K^+ are find from

$$E_{Na} = \frac{RT}{zF} \ln\left(\frac{[Na^+]_o}{[Na^+]_i}\right) \quad (4.3)$$

$$E_{Ca} = \frac{RT}{zF} \ln\left(\frac{[Ca^{2+}]_o}{[Ca^{2+}]_i}\right) \quad (4.4)$$

$$E_K = \frac{RT}{zF} \ln\left(\frac{[K^+]_o}{[K^+]_i}\right) \quad (4.5)$$

Whereas $[Na^+]_i, [Ca^{2+}]_i, [K^+]_i$ are intracellular Na^+, Ca^{2+}, and K^+ concentrations. $[Na^+]_o, [Ca^{2+}]_o, [K^+]_o$ are extracellular Na^+, Ca^{2+}, and K^+ concentrations. T is

absolute temperature, R is universal gas constant, F is Faraday's constant, and z is valency of ion.

The formulation for TTX-sensitive Na^+ sodium ionic current,

$$i_{Na} = g_{Na} m^3 h [Na^+]_o \frac{F^2}{RT} \frac{e^{(V-E_{Na})F/RT} - 1}{e^{F/RT} - 1} V \tag{4.6}$$

The formulation for L-type Ca^{2+} calcium ionic current,

$$i_{Ca,L} = g_{Ca,L} \left[f_L d_L + \frac{0.006}{1 + e^{-(V+14.1)/6}} \right] (V - E_{Ca,L}) \tag{4.7}$$

The formulation for T-type Ca^{2+} calcium ionic current,

$$i_{Ca,T} = g_{Ca,T} f_T d_T (V - E_{Ca,T}) \tag{4.8}$$

The formulations for transient and sustained components of 4-AP-sensitive currents,

$$i_{to} = g_{to} q r (V - E_K) \tag{4.9}$$

and

$$i_{sus} = g_{sus} r (V - E_K) \tag{4.10}$$

The formulation for rapid delayed rectifying K^+ potassium ionic current,

$$i_{K,r} = g_{K,r} p_a p_i (V - E_K) \tag{4.11}$$

The formulation for slow delayed rectifying K^+ potassium ionic current,

$$i_{K,s} = g_{K,s} x_s^2 (V - E_K) \tag{4.12}$$

The formulation for hyperpolarization-activeted current,

$$i_f = g_{f_{Na}} y(V - E_{Na}) + g_{f_K} y(V - E_K) \tag{4.13}$$

And the formulations background Na^+, Ca^{2+}, and K^+ currents,

$$i_{b\,Na} = g_{b\,Na}(V - E_{Na}) \tag{4.14}$$

$$i_{b\,Ca} = g_{b\,Ca}(V - E_{Ca}) \tag{4.15}$$

and

$$i_{b\,K} = g_{b\,K}(V - E_K) \tag{4.16}$$

Na^+/Ca^{2+} exchanger current,

$$i_{NaCa} = k_{NaCa} \frac{[Na^+]_i^3 [Ca^{2+}]_0 e^{0.03743V\gamma_{NaCa}} - [Na^+]_0^3 [Ca^{2+}]_i e^{0.03743V(\gamma_{NaCa}-1)}}{1 + d_{NaCa}\left([Na^+]_i^3 [Ca^{2+}]_0 + [Na^+]_0^3 [Ca^{2+}]_i\right)} \tag{4.17}$$

Na^+- K^+ pump current,

$$i_p = \bar{i}_p \left(\frac{[Na^+]_i}{K_{m,Na} + [Na^+]_i} \right)^3 \left(\frac{[K^+]_0}{K_{m,K} + [K^+]_0} \right)^2 \frac{1.6}{1.5 + e^{-(v+60)/40}} \tag{4.18}$$

4.2.2 Atrioventricular Node Electrical Signal Generation

The conduction procedure between sinoatrial node and atrioventricular node, involve two pathways of the atrioventricular node action potential, fast pathway and slow pathway. Therefore the mathematical model has two pathways. The action potentials (V) in the sinoatrial node were calculated from,

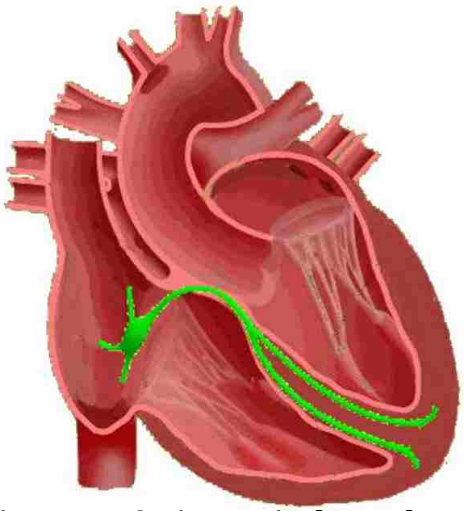

Figure 4-5 Atrioventricular node cell

$$i_{tot} = \begin{cases} i_{Na} + i_{Ca,L} + i_{to} + i_{K,r} + i_f + i_{st} + i_{K,l} + i_{NaCa} + i_p + i_b & (AN, N, NH) \\ i_{Na} + i_{Ca,L} + i_{Ca,T} + i_{to} + i_{K,r} + i_{K,s} + i_f + i_b + i_{NaK} + i_{NaCa} + i_{CaP} & (AM, N) \end{cases} \quad (4.19)$$

$$\frac{dV_i}{dt} = -\frac{1}{C_{m,i}}\left(i_{tot} + \sum_j g_{i,j}[V_i - V_j]\right) \quad (4.20)$$

The formulation for Na^+ sodium ionic current,

$$i_{Na} = g_{Na} m^3 h_{tot} V \frac{e^{(V-E_{Na})F/RT} - 1}{e^{VF/RT} - 1} \quad (4.21)$$

The formulation for Ca^{2+} calcium ionic current,

$$i_{Ca,L} = g_{Ca,L} d_L [0.675 f_{L,fast} + 0.325 f_{L,slow}](V - E_{Ca,L}) \quad (4.22)$$

The formulations for transient outward currents,

$$i_{to} = g_{to} r[0.45 q_{fast} + 0.55 q_{slow}](V - E_K) \quad (4.23)$$

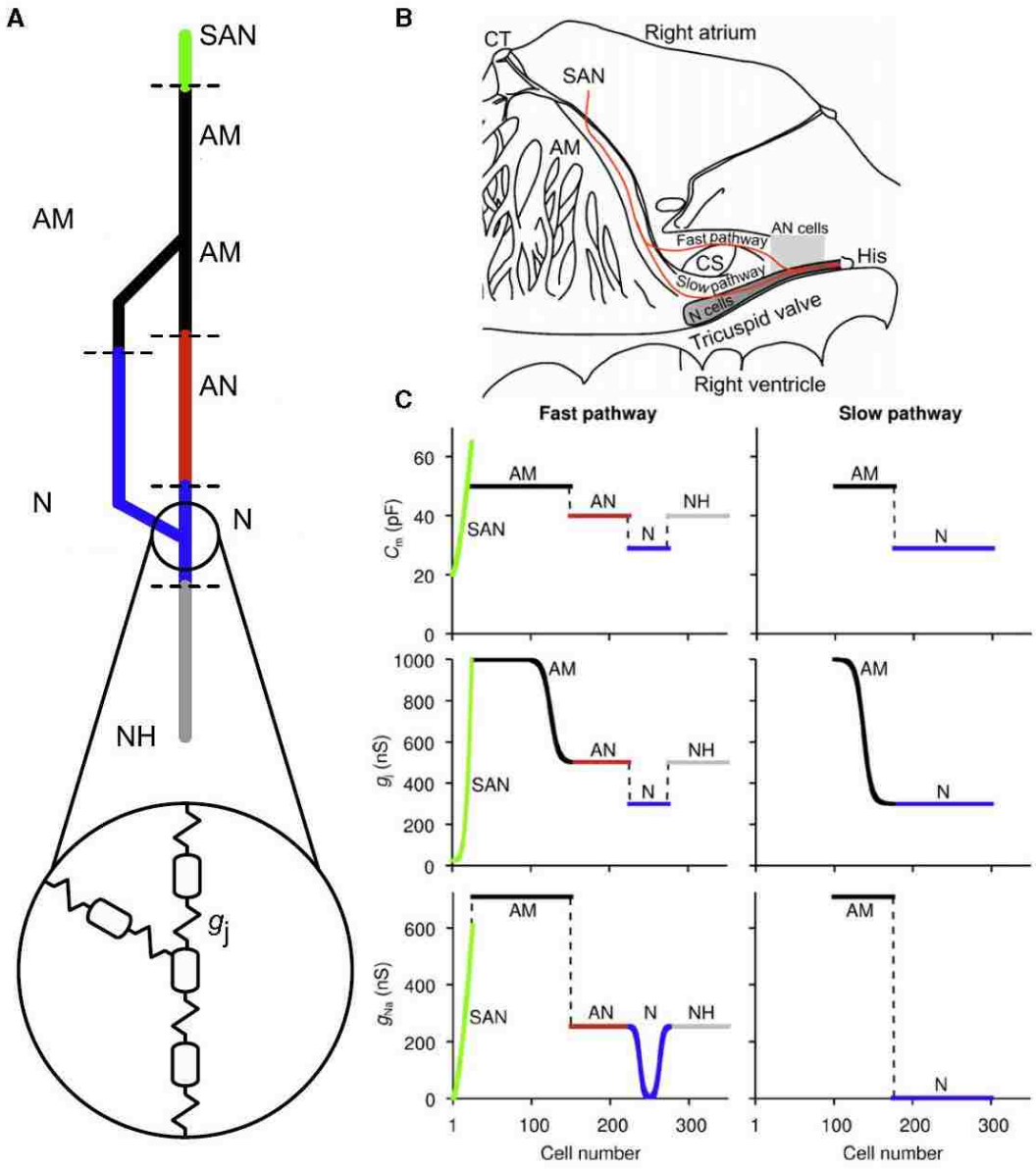

Figure 4-6 Pathway of atrioventricular node action potential [Biophysical Journal Volume 97 October 2009 2117–2127]

The formulation for rapid delayed rectifying K^+ potassium ionic current,

$$i_{K,r} = g_{K,r}[0.9p_{a,fast} + 0.1p_{a,slow}]p_i(V - E_K) \tag{4.24}$$

The formulation for hyperpolarization-activeted current,

$$i_f = g_f y(V-(-30)) \tag{4.25}$$

The formulation for steady state current,

$$i_{st} = g_{st} q_a q_i (V - E_{st}) \tag{4.26}$$

The formulation for inward rectifier K^+ potassium ionic current,

$$i_{K,l} = g_{K,l}\left(\frac{[K^+]_o}{[K^+]_o + 0.59}\right)^3 \left(0.5 + \frac{0.5}{1+e^{-\frac{(V+30)}{5}}}\right)\frac{V+81.9}{1+e^{1.393(V+85.5)(F/RT)}} \tag{4.27}$$

The formulation for Na^+/Ca^{2+} exchanger current,

$$i_{NaCa} = k_{NaCa}\frac{[Na^+]_i^3[Ca^{2+}]_0 e^{0.03743V\gamma_{NaCa}} - [Na^+]_0^3[Ca^{2+}]_i e^{0.03743V(\gamma_{NaCa}-1)}}{1+d_{NaCa}\left([Na^+]_i^3[Ca^{2+}]_0 + [Na^+]_0^3[Ca^{2+}]_i\right)} \tag{4.28}$$

The formulation for pump current,

$$i_p = \bar{i}_p\left(\frac{[Na^+]_i}{K_{m,Na}+[Na^+]_i}\right)^3\left(\frac{[K^+]_0}{K_{m,K}+[K^+]_0}\right)^2 \frac{1.6}{1.5+e^{-(v+60)/40}} \tag{4.29}$$

And the formulations background current,

$$i_b = g_b(V - E_b) \tag{4.30}$$

4.2.3 Purkije Fiber Electrical Signal Generation

The action potential in the Purkinje fiber are described by the following differential equation

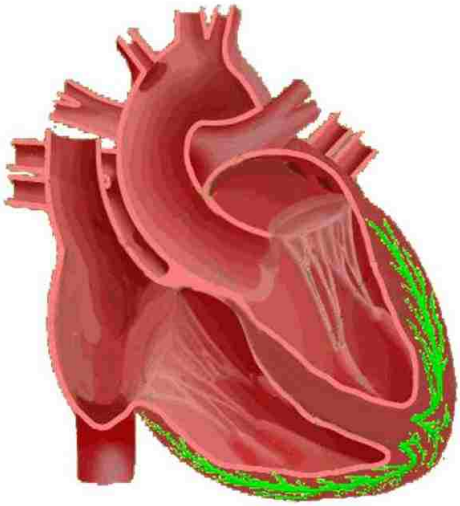

Figure 4-7 Purkinje fiber

$$i_{ion} = i_{K,r} + i_{K,s} + i_{K,l} + i_{to} + i_{sus} + i_{Na} + i_{b,Na} + i_{Ca,L} + i_{b,Ca} + i_{NaK} + i_{NaCa} + i_{p,Ca} + i_{p,K} + i_f \quad (4.31)$$

$$\frac{dV}{dt} = -\frac{1}{C_m}\left(i_{ion} + _{stim}\right) \quad (4.32)$$

Whereas i_{sim} is an externally applied stimulus current.

The formulation for inward rectifier K^+ potassium ionic current,

$$i_{K,l} = g_{K,l}\left(\frac{1}{1+e^{0.1(V+75.44)}}\right)((V-8)-E_K) \quad (4.33)$$

The formulations for transient outward current,

$$i_{to} = g_{to}\left(\frac{1}{1+e^{(20-V)/13}}\right)\left(\frac{1}{1+e^{(V+27)/13}}\right)(V-E_K) \tag{4.34}$$

The formulations for sustained current,

$$i_{sus} = g_{sus}\left(\frac{1}{1+e^{(5-V)/17}}\right)(V-E_K) \tag{4.34}$$

The formulation for hyperpolarization-activeted current,

$$i_f = g_{f,K}\left(\frac{1}{1+e^{(V+80.6)/6.8}}\right)(V-E_K) + g_{f,Na}\left(\frac{1}{1+e^{(V+80.6)/6.8}}\right)(V-E_{Na}) \tag{4.35}$$

The formulation for fast Na^+ sodium ionic current,

$$i_{Na} = g_{Na}m^3h\left(\frac{1}{(1+e^{(V+71.55)/7.43})^2}\right)(V-E_{Na}) \tag{4.36}$$

The formulation for L-type Ca^{2+} calcium ionic current,

$$i_{Ca,L} = g_{Ca,L}dff_2f_{class}4\frac{(V-15)F^2}{RT}\left[\frac{0.25[Ca^{2+}]_{ss}e^{2(V-15)F/RT}-[Ca^{2+}]_o}{e^{2(V-15)F/RT}-1}\right] \tag{4.37}$$

The formulation for slow delayed rectifying K^+ potassium ionic current,

$$i_{K,s} = g_{K,s}\left(\frac{1}{1+e^{(-5-V)/14}}\right)^2(V-E_K) \tag{4.38}$$

The formulation for rapid delayed rectifying K^+ potassium ionic current,

$$i_{K,r} = g_{K,r}\sqrt{\frac{[K^+]_o}{5.4}}\left(\frac{1}{1+e^{(-26-V)/7}}\right)\left(\frac{1}{1+e^{(V+88)/24}}\right)(V-E_K) \tag{4.39}$$

The formulation for Na^+/Ca^{2+} exchanger current,

$$i_{NaCa} = k_{NaCa}\frac{e^{\gamma VF/RT}[Na^+]_i^3[Ca^{2+}]_o - e^{(\gamma-1)VF/RT}[Na^+]_o^3[Ca^{2+}]_i\alpha}{(K_{mNa_i}^3+[Na^+]_o^3)(K_{mCa}+[Ca^{2+}]_o)\left(1+k_{sat}e^{(\gamma-1)VF/RT}\right)} \tag{4.40}$$

The formulation for Na^+- K^+ pump current,

$$i_{NaK} = \frac{P_{NaK}[K^+]_o[Na^+]_i}{(K_{mK}+[K^+]_o)(K_{mNa}+[Na^+]_i)\left(1+0.1245e^{-0.1VF/RT}+0.0353e^{-VF/RT}\right)} \tag{4.41}$$

$$i_{pCa} = g_{pCa}\frac{[Ca^{2+}]_i}{(K_{pCa}+[Ca^{2+}]_i)} \tag{4.42}$$

$$i_{pK} = g_{pK}\frac{V-E_K}{1+e^{(25-V)/5.98}} \tag{4.43}$$

The formulations background current,

$$i_b = g_{bNa}(V-E_{bNa})+g_{bCa}(V-E_{bCa}) \tag{4.44}$$

And the Ca^{2+} calcium dynamics current,

$$i_{leak} = V_{leak}\left([Ca^{2+}]_{sr}-[Ca^{2+}]_i\right) \tag{4.45}$$

$$i_{up} = \frac{V_{maxup}}{1+K_{up}^2/[Ca^{2+}]_i} \tag{4.46}$$

$$i_{rel} = V_{rel} \frac{k_1 [Ca^{2+}]_{ss}^2 \overline{R}}{k_3 + k_1 [Ca^{2+}]_{ss}^2} \left([Ca^{2+}]_{sr} - [Ca^{2+}]_{ss} \right) \tag{4.47}$$

$$i_{xfer} = V_{xfer} \left([Ca^{2+}]_{ss} - [Ca^{2+}]_{i} \right) \tag{4.48}$$

4.3 Action Potentials Result

To match the action potential at various heart rates, the sodium ionic Na^+ current, calcium ionic Ca^{2+} current, potassium ionic K^+ current, total current, and the action potential of sinoatrial node, atrioventricular node, and Purkinji fiber were calculated and plotted in same various peak span of heart rate. The minimum heart rate of all patients is HR67 which equal to 0.89552 sec, and the maximum heart rate of all patients is HR137 which equal to 0.437956 sec. Therefore the range of the peak span of action potentials (one heart beat) must be in between 0.4 to 0.9 sec, to determine the correlation with others properties.

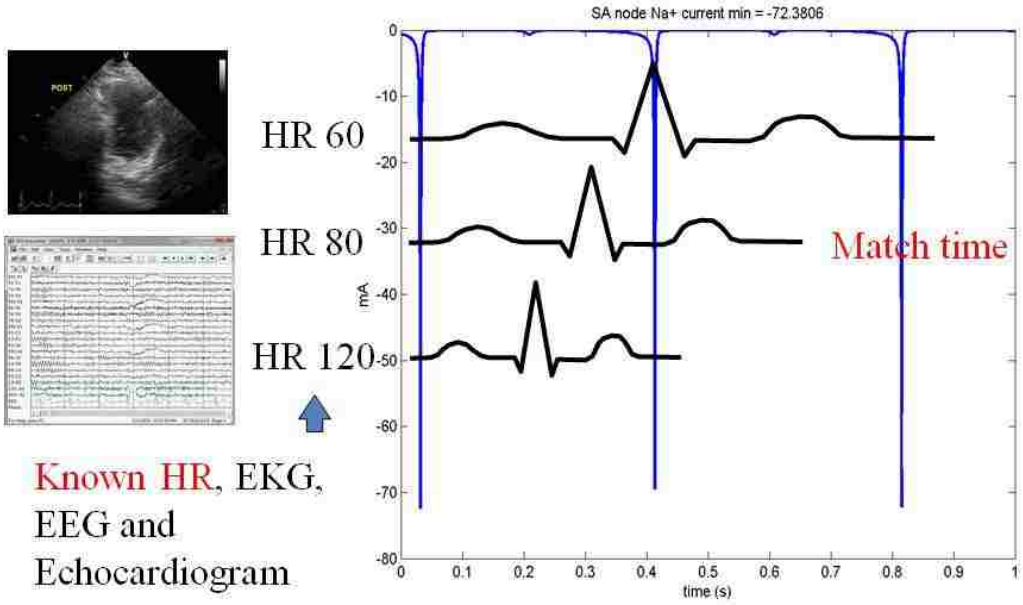

Figure 4-8 Matching action potential with others properties

The results from the action potential in the sinoatrial node model is in between 0.4 to 0.9 sec period provided the maximum sodium ionic Na^+ current 88.1 mA, maximum calcium ionic Ca^{2+} current 33.7 mA, maximum potassium ionic K^+ current 8.6 mA, maximum total ionic current 100.2 mA, and maximum action potential voltage 147.0 mV.

The results from the action potential in the atrioventricular node model lies between 0.4 to 0.9 sec periods provided the maximum sodium ionic Na^+ current 70.6 mA, maximum calcium ionic Ca^{2+} current 27.1 mA, maximum potassium ionic K^+ current 0.26 mA, maximum total ionic current 67.7 mA, and maximum action potential voltage 70.8 mV.

The results from action potential in Purkinji fiber model lies between 0.4 to 0.9 sec period provided the maximum sodium ionic Na^+ current 283.3 mA, maximum calcium ionic Ca^{2+} current 12.9 mA, maximum potassium ionic K^+ current 0.36 mA, maximum total ionic current 282.7 mA, and maximum action potential voltage 63.7 mV.

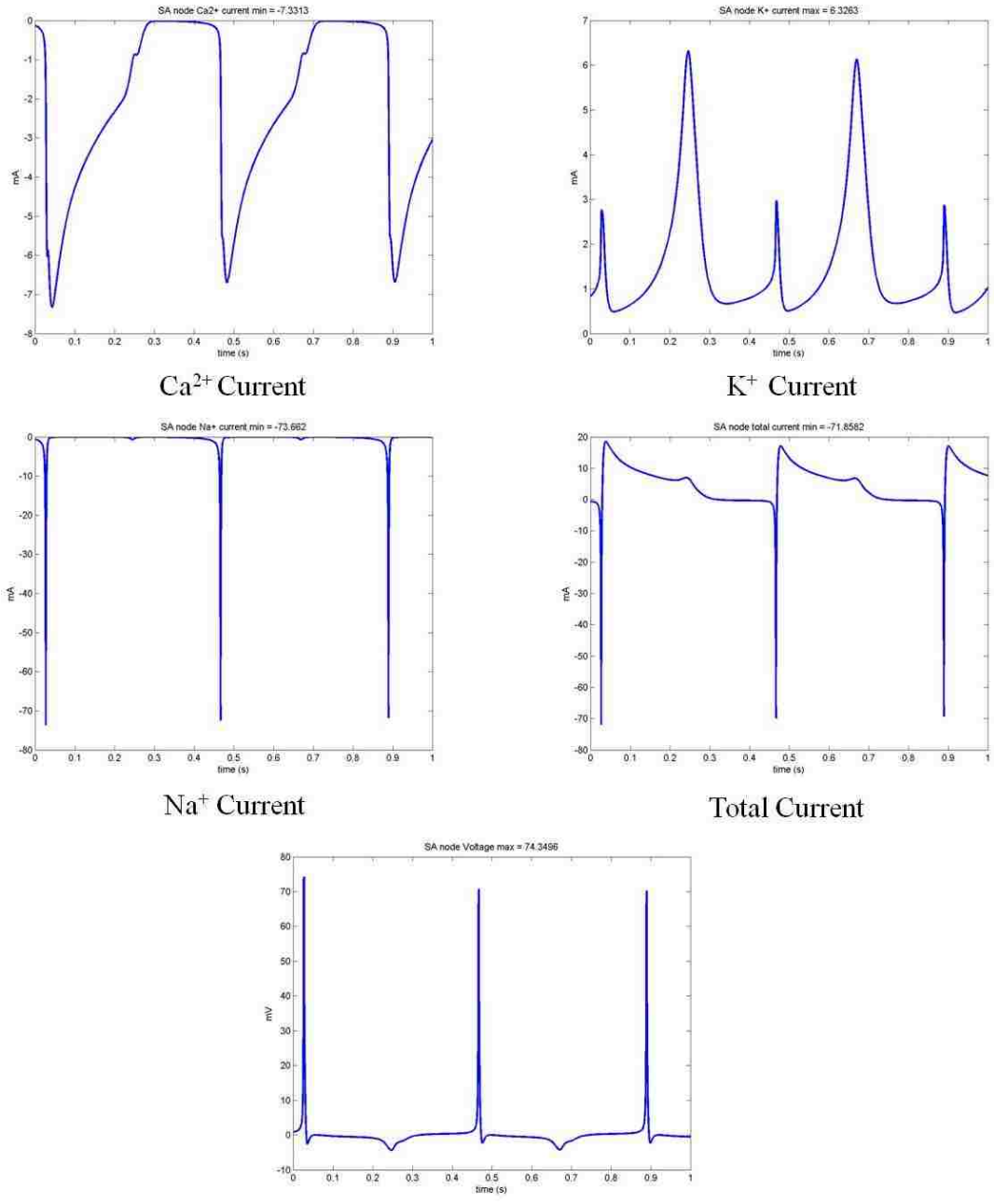

Ca^{2+} Current

K^{+} Current

Na^{+} Current

Total Current

Action Potential Voltage

Figure 4-9 Sinoatrial node currents and action potential results

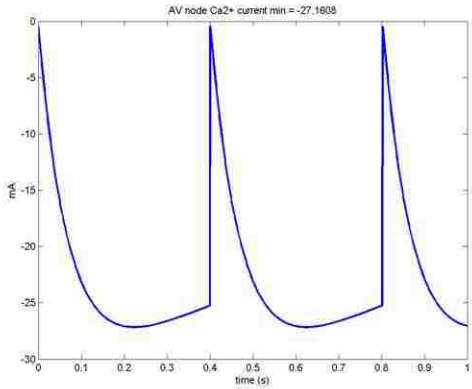

Ca^{2+} Current

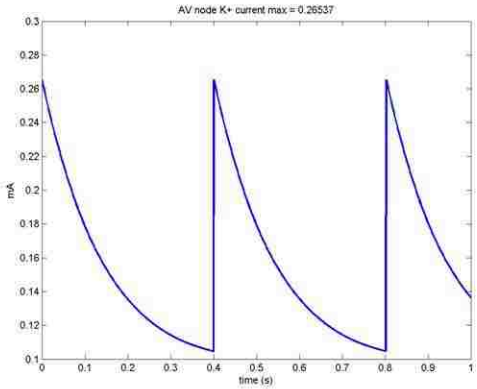

K^{+} Current

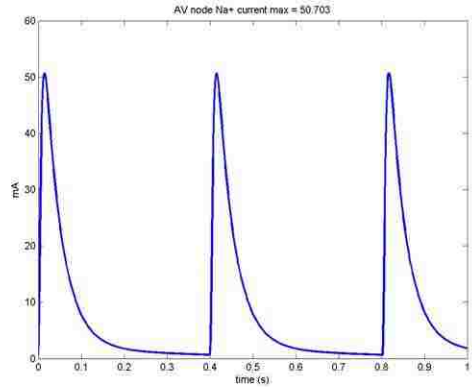

Na^{+} Current

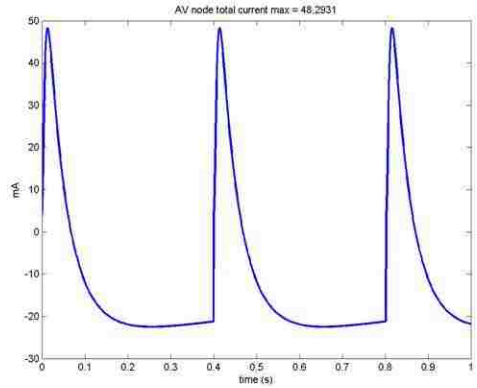

Total Current

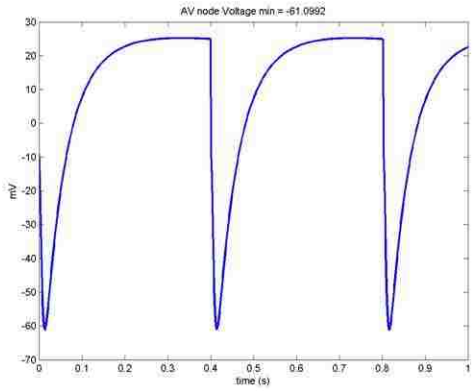

Action Potential Voltage

Figure 4-10 Atrioventricular node currents and action potential results

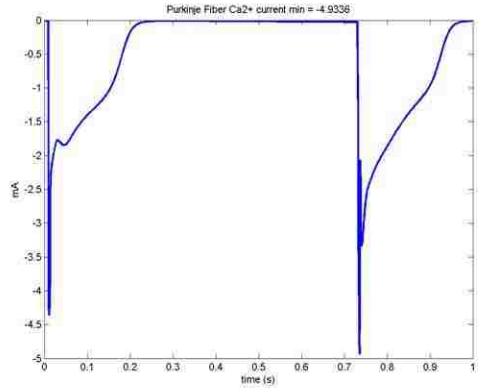

Ca^{2+} Current

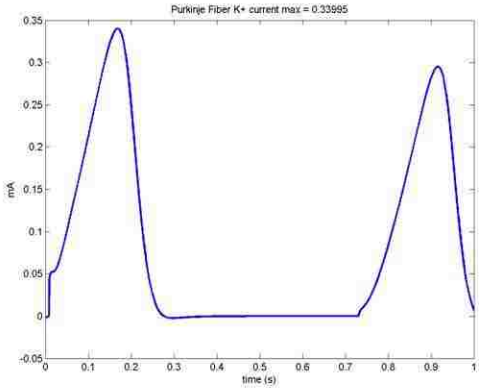

K^{+} Current

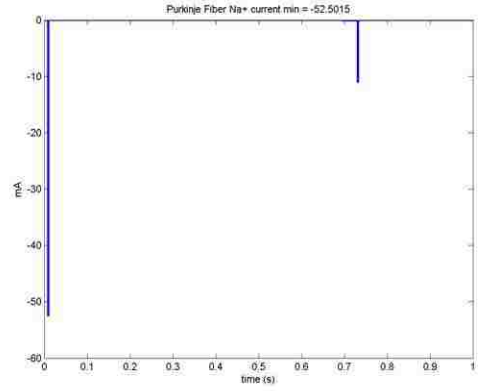

Na^{+} Current

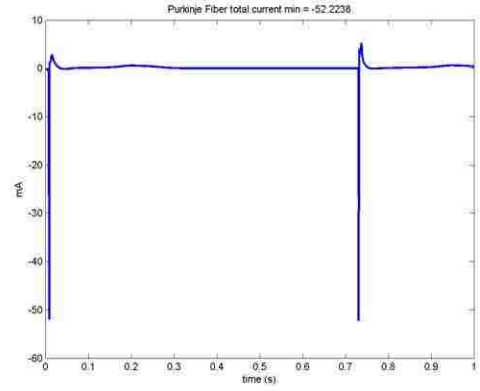

Total Current

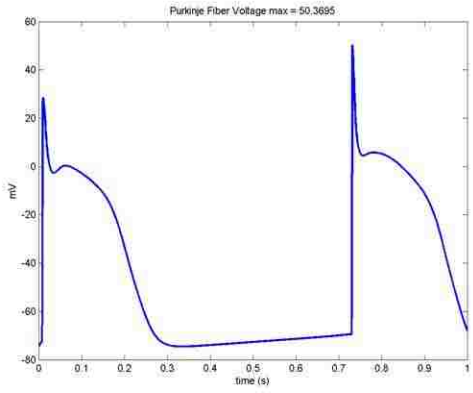

Action Potential Voltage

Figure 4-11 Purkinji fiber currents and action potential results

4.4 Summary

Mathematical models of cardiac action potentials were divided in three parts of the heart neuron system sinoatrial node, atrioventricular node, and Purkinji fiber. Ionic currents and action potentials for all models were found in between 0.4 to 0.9 sec period, to match with heart rate, heart stress, echocardiogram, and brain wave record for determine the correlations in next simulations.

CHAPTER 5

Blood Flow and Stresses in the Left Ventricle

Calculations of the flow patterns of the blood in the left ventricle used a modification of the moving immersed boundaries numerical method. The difference was that the velocity of the heart wall endocardium was used as the boundary condition. The position of the endocardium as a function of time was measured from the echocardiograms of five patients. The shear stress, and normal stress from these blood flow calculation were correlated with brain wave.

Data from five patients has been analyzed in this work. The data includes echocardiograms and ECG and EEG data obtained during a Dobutamine stress test. Patients were administered 10 to 40 mics (milligrams per kg of body weight per minute) Dobutamine and the echo, ECG and EEG data were obtained while the heart was paced as part of the stress test. Patient data is included in the Table below.

Table 5-1 Patient Data and Clinical Condition

Patient No.	Age	Sex	Clinical Condition
1	68	F	Normal HR 20 – 40 mics of Dobutamine, no ischemia
2	77	F	HR 134 with 40 mics of Dobutamine and 5 mcg of Atropine, no ischemia
3	58	F	Normal systolic function, no ischemia
4	58	F	Normal Dobutamine echocardiographic study
5	79	F	90% HR at 30 mics of Dobutamine, patient on O_2 during test, LV hypertrophy

5.1 Echocardiogram

An echocardiogram, often referred to in the medical community as a cardiac echo or simply an echo, is a sonogram of the heart. It uses standard ultrasound techniques to create moving images of two-dimensional slices of the heart. The echocardiogram allows doctors to see the heart beating, and to see many of the structures of the heart. There are three types of echocardiography involved with heart research transthoracic echocardiography, stress echocardiography, and transesophageal echocardiography. Ordinarily, the echocardiogram test and electrocardiogram test, a test that records the electrical activity of the heart, are recorded at the same time.

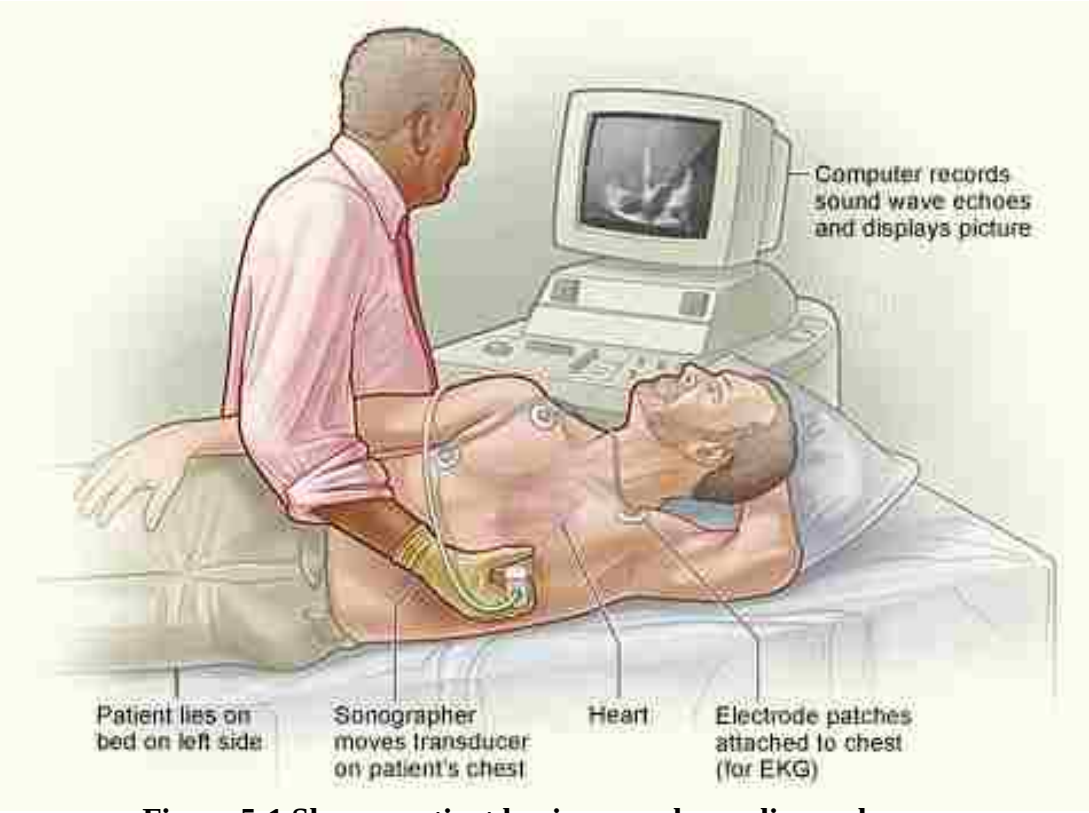

Figure 5-1 Show a patient having an echocardiography
[U.S. Department of Health & Human Services]

5.2 Prepare Model's Input Data

To generate the data for the immersed boundaries, two-dimensional slices of the left side of the heart are taken from the echocardiogram. For the simulation model there are six steps shown in figure 5-2, in each heart beat: Starting with time T_0 when the heart mitral valve and aortic valve both are closed and the ventricle chambers are relaxing. The next step is time T_1 where the mitral valve is at the fully open position and the aortic valve is still closed. Blood flows from the left atrium to fill the left ventricle. The left atrium contracts to force the blood into the ventricle. Therefore at end of this step the atrium chamber has fully contracted and the ventricle chamber fully expanded. At step T_2 the mitral valve starts to close while the aortic valve is still closed, and the left ventricle chamber expands to the maximum volume. Step T_3, the mitral valve is completely closed and the aortic valve starts to open. The ventricle chamber starts to contract and blood flows out. At time step T_4 blood flows through aortic valve and ventricle chamber wall boundary contracts. Step T_5 the aortic valve is at the maximum open position. The process then is repeated for the next heart beat. The ventricle chamber wall boundary is now fully contracted. The steps T0-T3 when the atrium is contracted is called diastole and steps T_3-T_6 when the ventricle is contracted is called systole.

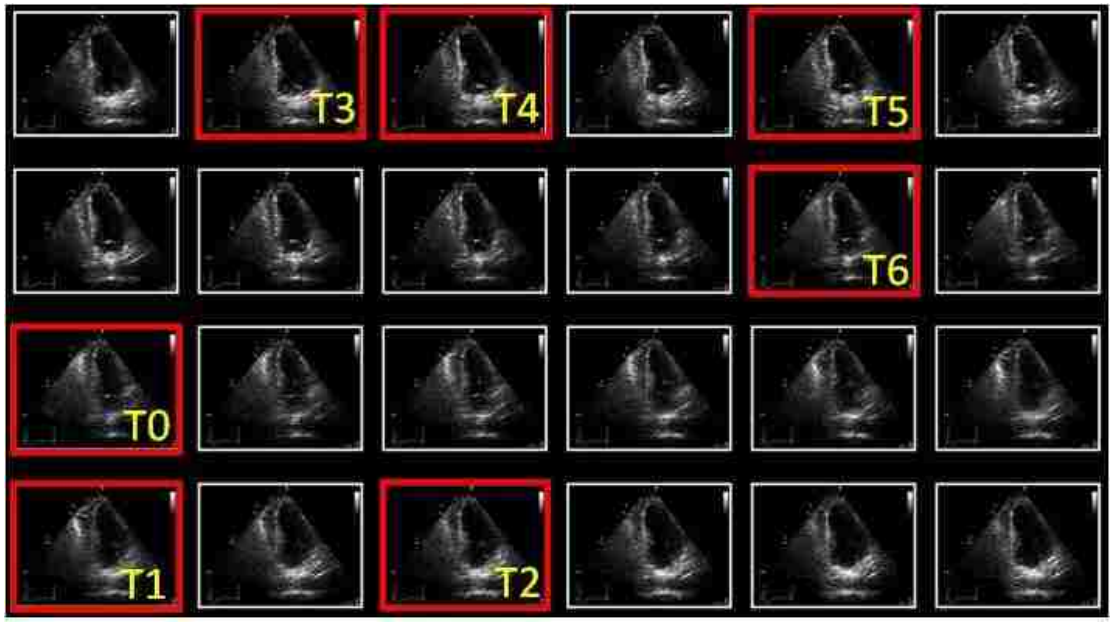

Figure 5-2 Shows selected individual steps of echocardiography

An echocardiogram image was selected at each time step as shown in figure 5-3. The appropriate atrium model was attached as shown in figure 5-4. The edge was traced and used as the boundary value for the calculation. This was repeated at each time step.

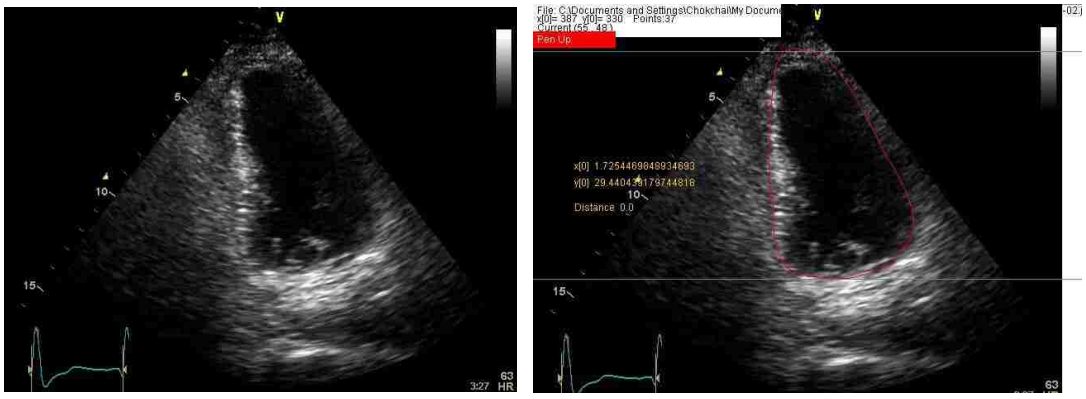

Figure 5-3 Show the left ventricle edge detection form echocardiogram

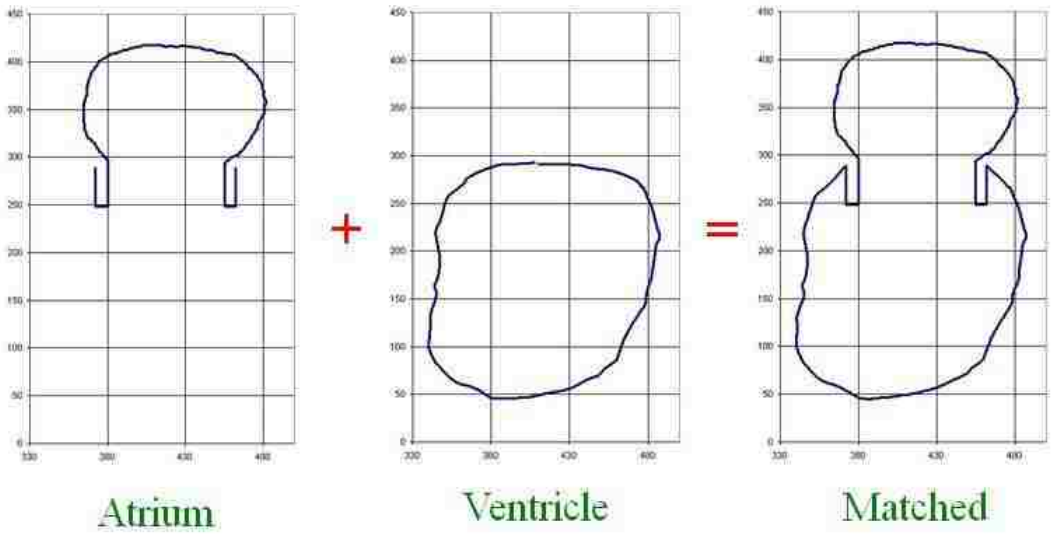

Figure 5-4 Matched between left ventricle and left atrium

To make sure that at each step the heart wall edges are correctly positioned , the position of the mitral valve was fixed at the same x-y coordinate as shown in figure 5-5 In the lower left corner of the electrocardiogram the heart rate is shown as beats per minute.

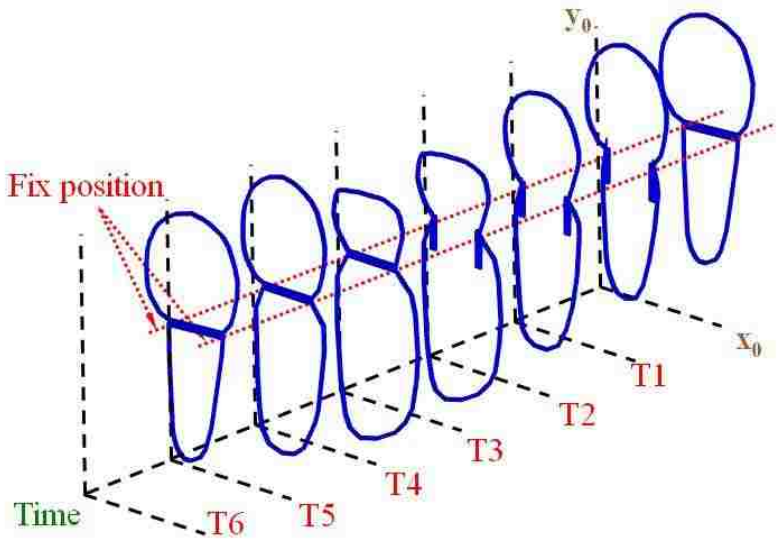

Figure 5-5 Fixed position of individual steps of echocardiography

5.3 Modeling and Algorithm

Because the heart wall is an elastic tissue, the calculation of the flow in the left side of heart has to have updated boundaries in correspondence with the moving of the heart wall. The mathematical formulation for immersed boundary method will follow in topic 5.3.1.

5.3.1 Mathematical Modeling and Algorithm

The equation of motion in a closed elastic curve immersed in a two-dimensional incompressible fluid can be explained by the Navier-Stokes equation on the x-y Cartesian [2-6] co-ordinate system as

$$\rho\left(\frac{\partial \hat{u}}{\partial t} + \hat{u} \bullet \nabla \hat{u}\right) + \nabla p = \mu \nabla^2 \hat{u} + \hat{F} \tag{5.1}$$

$$\nabla \bullet \hat{u} = 0 \tag{5.2}$$

The equation of motion in this case is between the fluid and non-fluid regions. Therefore the force density $\mathbf{F}(x, t)$ should be applied at the surface of the non-fluid regions. The calculation of the boundary force density of the system may be written as:

$$\mathbf{F}(\mathbf{x}, t) = \int_0^L \mathbf{f}(s, t)\delta(\mathbf{x} - \mathbf{X}(s, t))\, ds \tag{5.3}$$

Where as $$\frac{\partial \mathbf{X}(s, t)}{\partial t} = \int \mathbf{u}(x, t)\delta(\mathbf{x} - \mathbf{X}(s, t))\, d\mathbf{x} \tag{5.4}$$

Here $\mathbf{u}(x, t)$ is the fluid velocity, $p(x, t)$ is the fluid pressure, ρ is the constant blood density and μ is the constant blood viscosity. The function $\mathbf{f}(x, t)$ is the force on the

boundary element at point s. The value of calculating f(s,t) on (2.5) was to assume an equation of state for the heart material. In the present case the function f(s,t) can be obtained in finite difference form from the equation (2.5)

$$\mathbf{x}_k^* = [\mathbf{x}_k^n + \Delta t \mathbf{u}_k^n] + \lambda f_k(\mathbf{x}_1^* L \mathbf{x}_n^*) \tag{5.5}$$

The superscript * indicates next time step.

where $\mathbf{x}$ is defined on the Cartesian system and $\mathbf{X}$ is the point on the Lagrangian system. The solution is obtained using a discrete time step n so that $\mathbf{u}^n(\mathbf{x}) = \mathbf{u}(\mathbf{x}, n\Delta t)$.

1) Find the boundary force $\mathbf{f}^n$ for the boundary configuration $\mathbf{X}^n$:

2) Apply the force $\mathbf{f}^n$ to the grid of fluid computation:

$$\mathbf{F}^n(x) = \sum_s \mathbf{f}^n(s)\delta_h(\mathbf{x} - \mathbf{X}^n(s))\Delta s \qquad ; \mathbf{x} = (x, y) \tag{5.6}$$

$$\delta_h(\mathbf{x}) = \delta_h(x)\delta_h(y) \quad \text{and} \quad \delta_h(x) = \begin{cases} \frac{1}{4h}\left(1 + \cos\frac{\pi x}{2h}\right) & |x| \le 2h \\ 0 & |x| \ge 2h \end{cases} \tag{5.7}$$

3) Update the fluid velocity under the influence of the force density $\mathbf{F}^n$. Solve the following systems successively for $\mathbf{u}^{n+1,0}, \mathbf{u}^{n+1,1}, \mathbf{u}^{n+1,2}, \mathbf{u}^{n+1,3}, \ldots (\mathbf{u}^{n+1}, p^{n+1})$:

$$\rho \frac{\mathbf{u}^{n+1,0} - \mathbf{u}^n}{\Delta t} = \mathbf{F}^n \tag{5.8}$$

$$\rho\left(\frac{\mathbf{u}^{n+1,1} - \mathbf{u}^{n+1,0}}{\Delta t} + u_x^n D_x^0 \mathbf{u}^{n+1,1}\right) = \mu D_x^+ D_x^- \mathbf{u}^{n+1,1} \tag{5.9}$$

$$\rho\left(\frac{\mathbf{u}^{n+1,2}-\mathbf{u}^{n+1,1}}{\Delta t}+u_y^n D_y^0 \mathbf{u}^{n+1,2}\right)=\mu D_y^+ D_y^- \mathbf{u}^{n+1,2} \tag{5.10}$$

$$\rho\left(\frac{\mathbf{u}^{n+1}-\mathbf{u}^{n+1,2}}{\Delta t}\right)+D_x^0 D_y^0 p^{n+1}=0 \tag{5.11}$$

$$D_x^0 D_y^0 \mathbf{u}^{n+1}=0 \tag{5.12}$$

4) Interpolate the new velocity to the old boundary positions and move the boundary points:

$$\mathbf{X}^{n+1}(s)=\mathbf{X}^n(s)+\Delta t\sum_s \mathbf{u}^{n+1}(\mathbf{x})\delta_h(\mathbf{x}-\mathbf{X}^n(s))h^2 \tag{5.13}$$

Here D^+, D^-, D^0 the forward, backward, and centered divided difference operator.

As the system is closed it is necessary to supply the blood from a source and the outflow is simulated by sinks as shown in figure 5-6 let $Q(t)$ be the volume flow rate. From the continuity equation $\nabla.\mathbf{u}=0$ the source can be written as:

$$\nabla.\mathbf{u}=\psi(\mathbf{x},t)=Q(t)\psi_0(\mathbf{x}) \tag{5.19}$$

Because blood flow in left side of heart is the periodic domain, the integral of $\nabla.\mathbf{u}$ is identically zero, $\nabla.\mathbf{u}=\int\psi_0(\mathbf{x})dv=0$. Therefore, the sinks must match the source.

$$\psi_0(\mathbf{x})=w_a(\mathbf{x}-\mathbf{X}_a)-w_e(\mathbf{x}) \tag{5.20}$$

where $\mathbf{X}_a$ is a point the middle of the left atrium, w_a and w_e the spatial distribution of the source and sink.

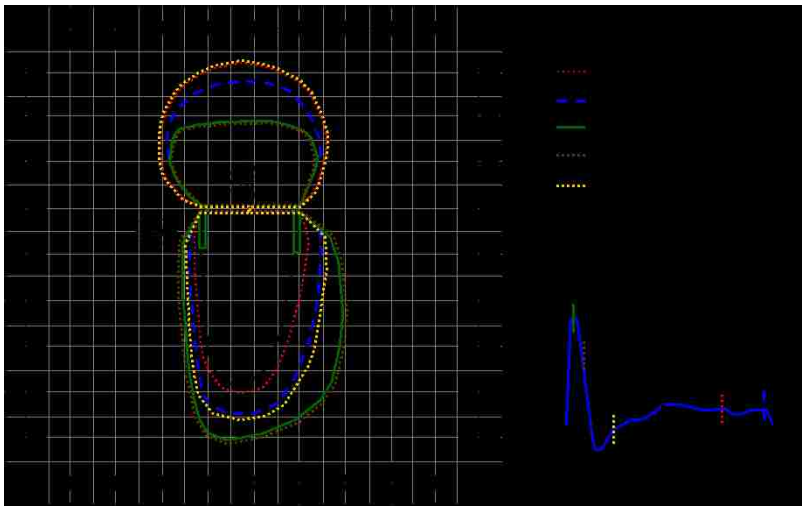

Figure 5-6 Show the blood flow simulation model of heart's left side

The continuity equation, the mass input is equal to the mass output; is satisfied.

5.3.2 Sensitivity of Models Checked

An estimate of the accuracy of the measurement of the endocardium position was made, by using echocardiograms which have two completed beats connected together. The check compared the amplitude and shape of shear stress from individual successive beat simulation. As the two beats are consecutive the amplitude and shape of shear stress should not be significantly different. The sensitivity check showed that, the amplitude in dyne/cm^2 results of both beats are close to each other. Typical values were for the two beats left ventricle 60.5337:58.7328, mitral valve 52.7328:48.3120, endocardium 8.2077:7.7669, septum 40.3563:35.9228, and apex 5.5196:4.2342 for first : second beat respectively. Moreover both beats also give almost same shear stress characteristic curve results.

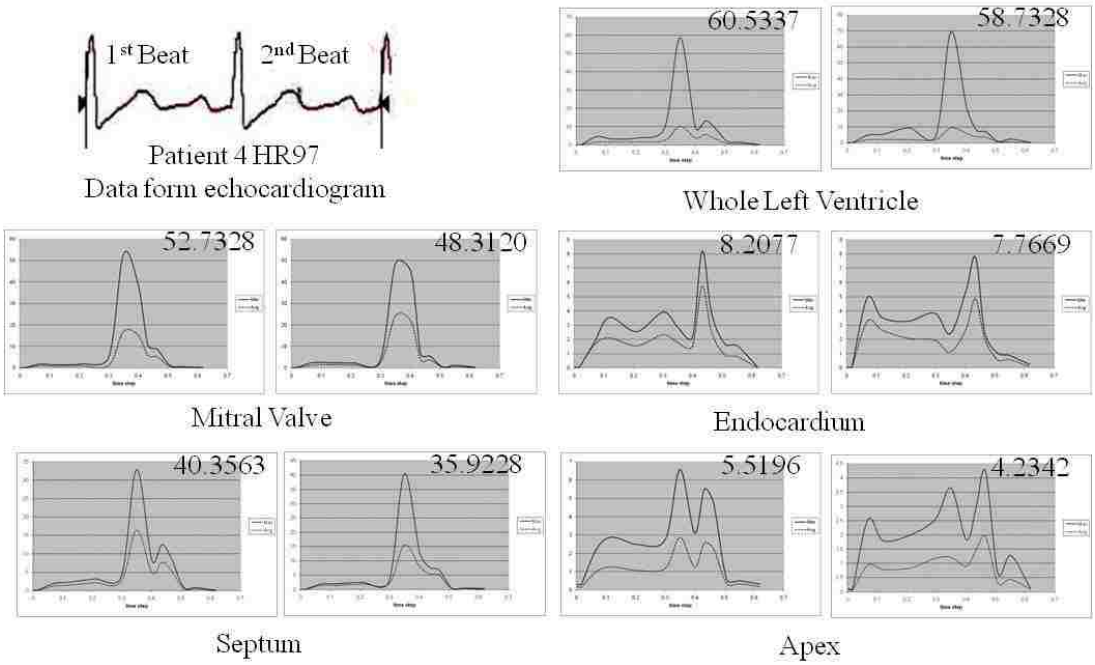

Figure 5-7 Sensitivity of simulation checked

For this numerical model, changing of boundary edge one pixel, the shear stress changed from 5.1647 to 5.0221 dyne/cm^2. In a more extreme case assuming ten pixels difference, the shear stress changed to 3.8635 dyne/cm^2, as shown in figure 5-8.

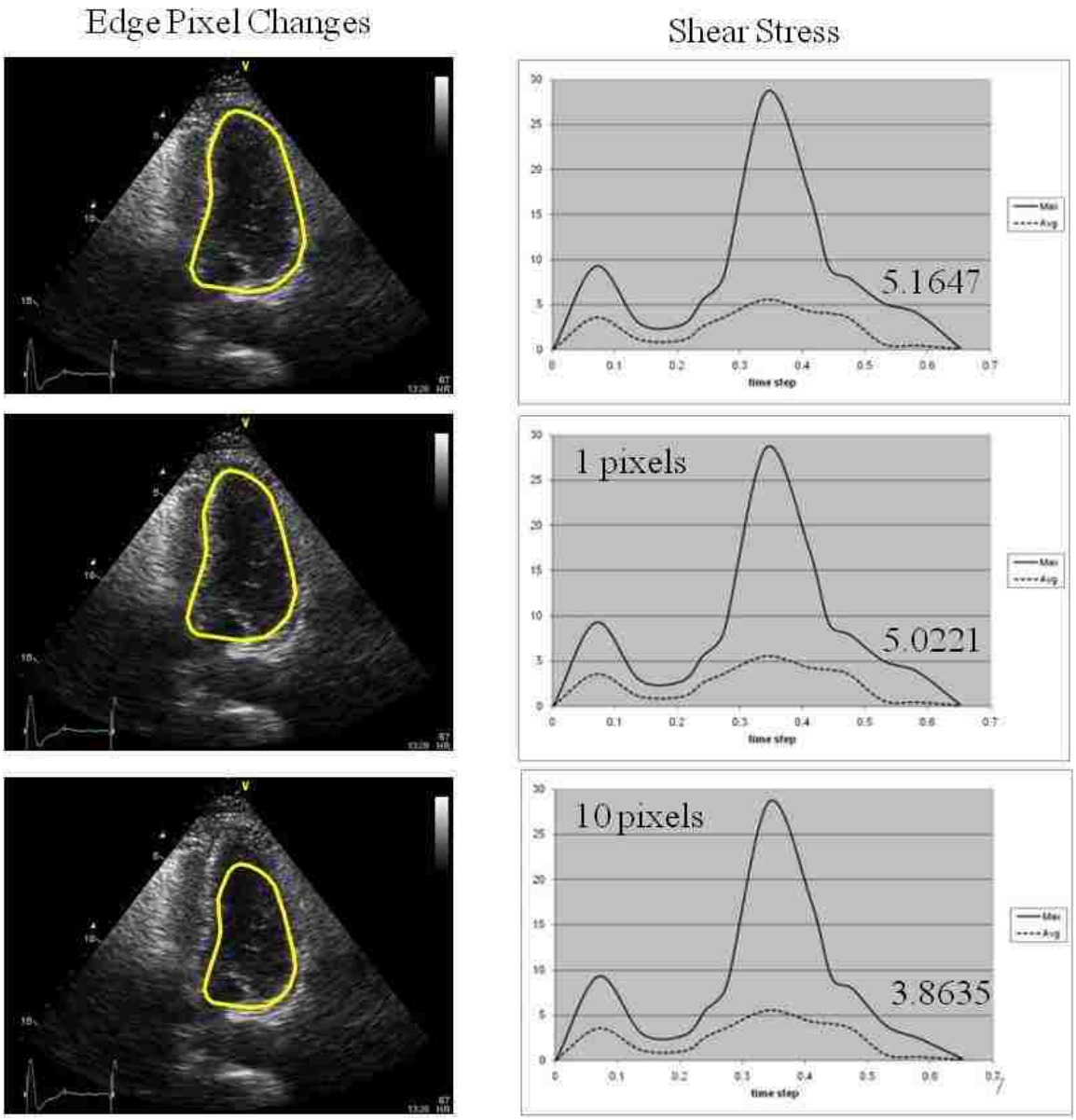

Figure 5-8 Sensitivity of edge pixel changed

5.4 Result

The numerical models of blood flow in the left ventricle provide the systolic-diastolic volume change, blood velocity pattern, blood pressure, and computed normal stress also wall shear stress.

5.4.1 Systolic-Diastolic Volume Change

The systolic-diastolic volume change was determined from the area difference between the maximum expansion contour and minimum contraction contour of the left ventricle wall edge detection. This is the maximum volume change of the one heart beat.

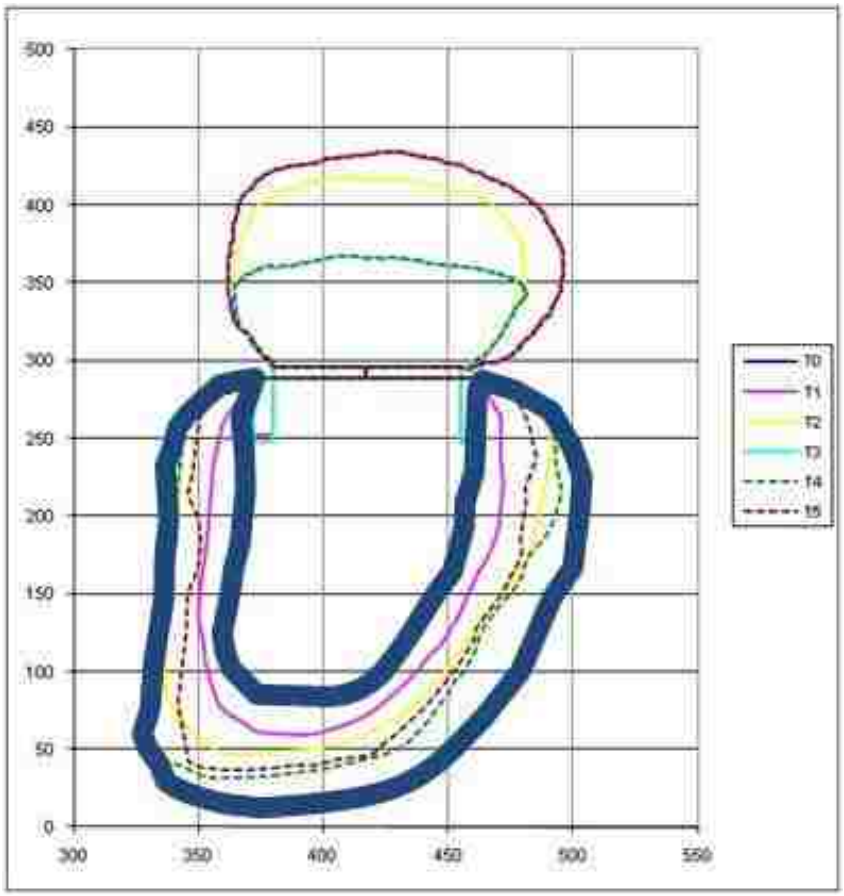

Figure 5-9 Left ventricle volume (area unit^2) change

When the dosage of dobutamine was increased the systolic-diastolic volume also increased until a maximum value was achieved. As shown in figure 5-10.

mics	Patient1	Patient2	Patient3	Patient4	Patient5
0	13119.5000	9162.5000	15982.5000	16190.0000	10150.3750
10	22278.0000		22334.0000	16762.5000	14527.2500
20	21262.0000	8288.9161	18779.2500	16819.1535	12161.5000
30		7390.6655		15341.0000	10482.8750
35	14589.7500				
40		9348.7500	12339.5000	11563.5000	

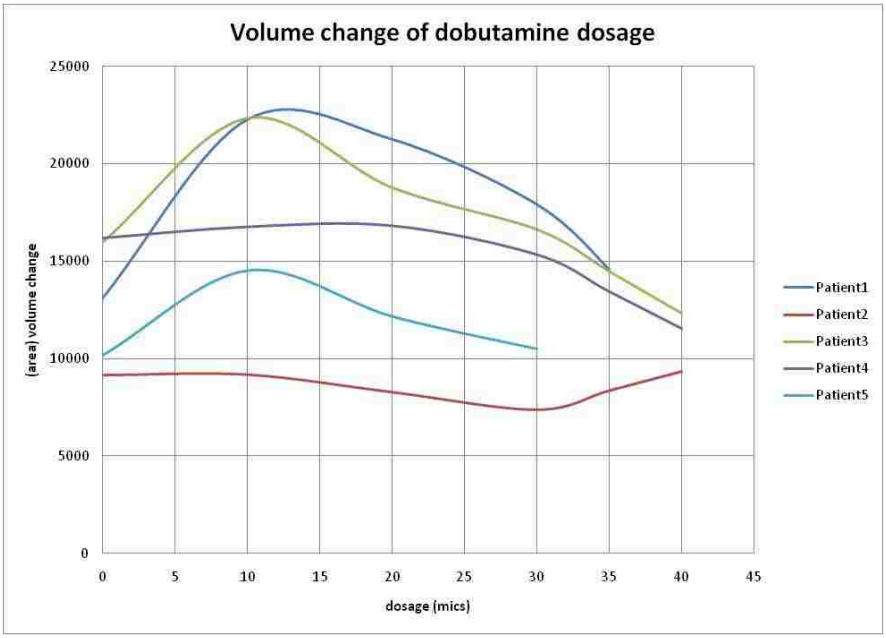

Figure 5-10 Left ventricle volume (area) change of dobutamine dosage

5.4.2 Heart Wall Stress

At each step time the velocity profile in the left ventricle was plotted and used for the calculation of the heart wall stress. The shear stress was calculated in the fluid as close to the wall as the data allowed. It was assumed that the stress was continuous at the wall boundary. Velocity profiles in the left ventricle were plotted with the boundary change to confirm that the left ventricle shape change according to the heart beat cycle and also to confirm that the flow direction correlated with boundary changed.

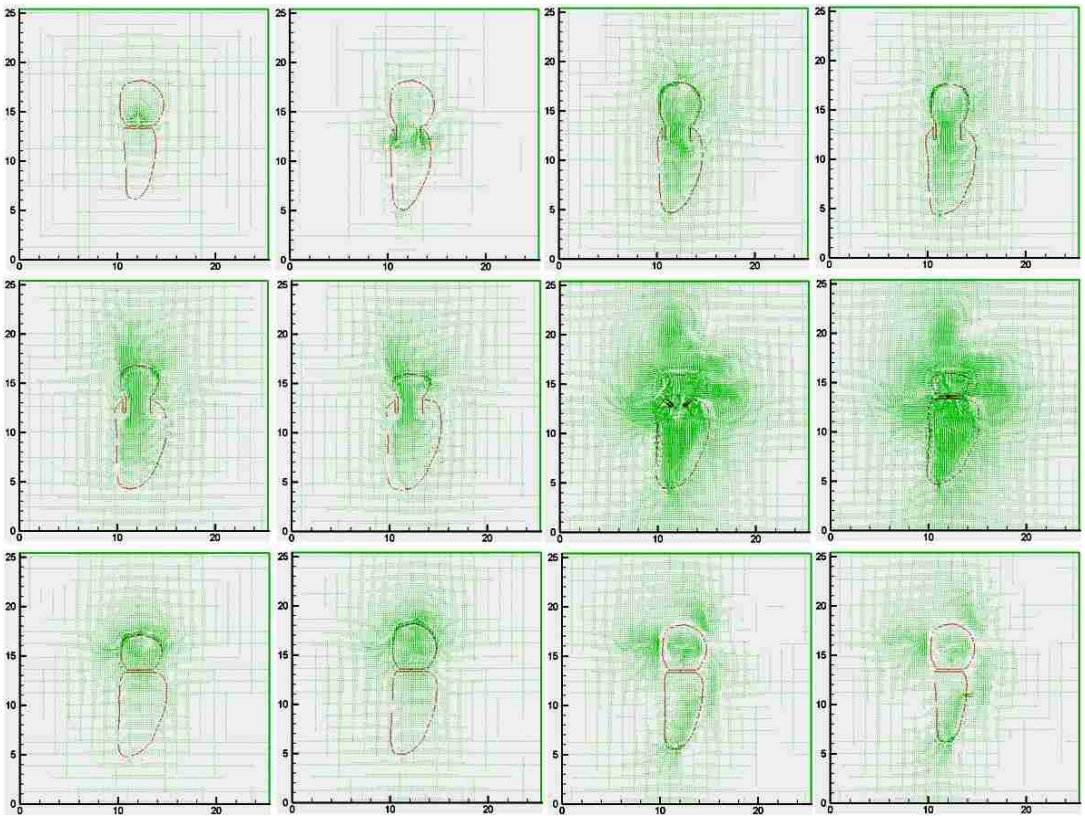

Figure 5-11 Velocity profile in the left ventricle patient 1 HR92 20 mics

There are two heart wall stresses determined in this simulation, normal stress and shear stress. Each kind of stress was calculated for five different locations of left ventricle: apex, endocardium, mitral valve, septum, and whole left ventricle for every dosages of dobutamine. The heart wall stresses will be used in the correlation models.

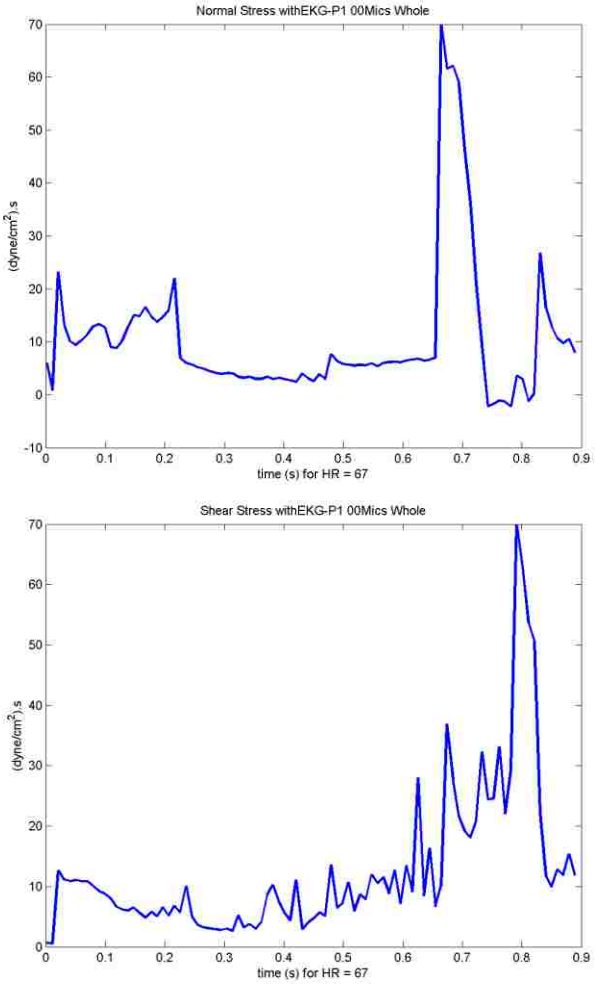

Figure 5-12 Plot of patient 1 ventricle wall stress at 0 mics

The average of normal stress and shear stress was plotted against the change of heart rate for each patient. Increasing the patient heart rate has a tendency to increase the average of normal stress and shear stress. The values for the average wall normal stresses for all patients are between 1-25 (N/m^2), whereas the average wall shear stresses for all patients are between 0.1-2 (N/m^2). However the shear stress is important as the ventricular muscles are parallel to the walls and resist the shearing force.

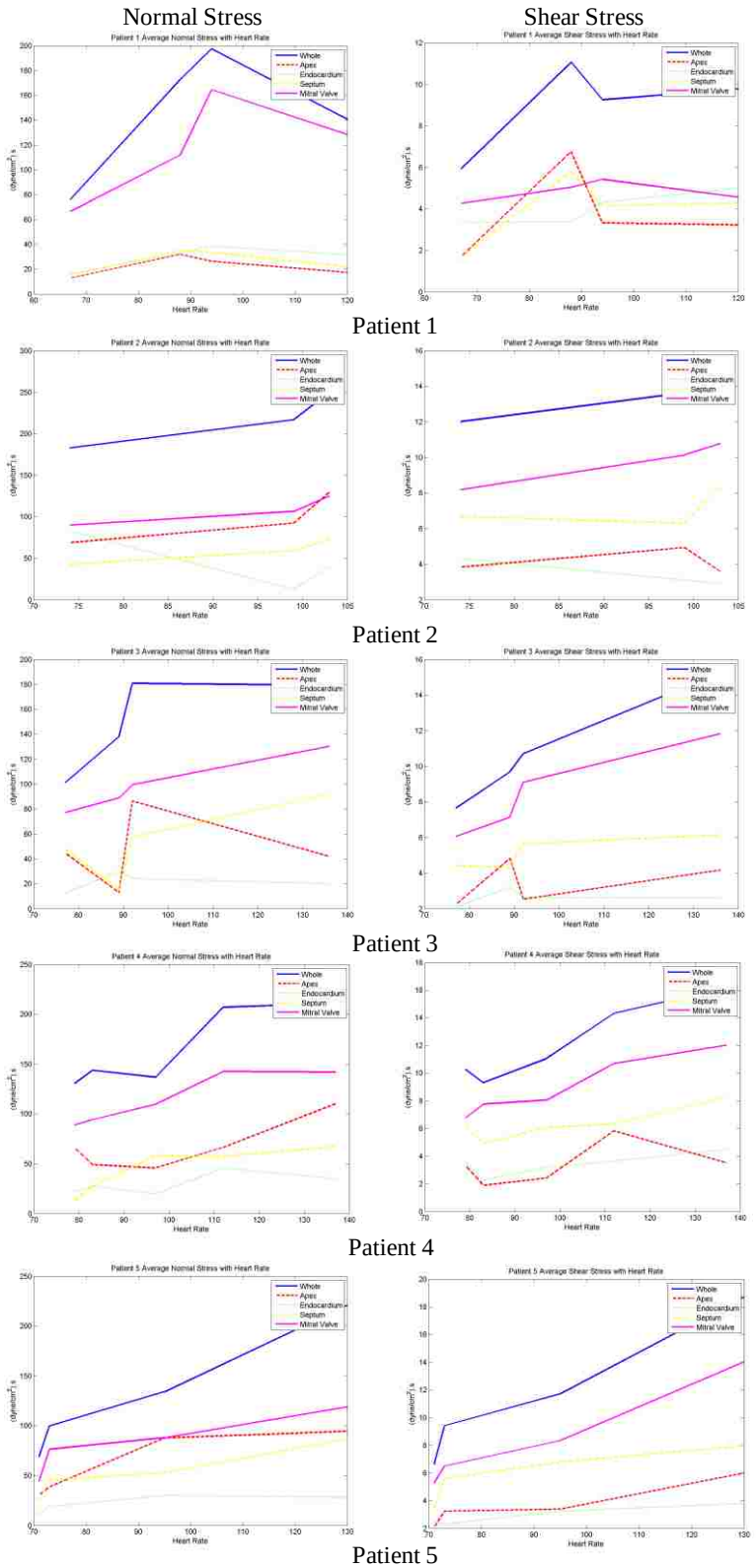

Figure 5-13 Wall stress against heart rate

5.5 Summary

In this chapter use was made of the modified moving immersed boundary numerical method to solve the flow pattern of the blood in the left ventricle. Model sensitivity of the model to errors in the mapping of the shape of the ventricle was checked and found to be satisfactory. The blood flow model in the left ventricle enabled the calculation of the systolic-diastolic volume change, blood flow pattern, blood velocity, normal heart wall stress, and shear heart wall stress. This output will be used for simulations later in the dissertation.

CHAPTER 6

Fast Fourier Transform of Electroencephalogram

In this chapter, the fast Fourier transform (FFT) was employed to examine electroencephalogram (EEG) spectral analysis.

6.1 Electroencephalogram

Electrical charge in the brain is maintained by billions of neurons. By pumping ions across their membranes, neurons are electrically charged or polarized. Neurons respond by releasing ions into the space outside the cell when the neuron receives a signal from their neighbor via an action potential. Ions with like charge repel each other, and when many ions are pushed out of many neurons at the same time, they can push their neighbors, who push their neighbors, and so on, in a wave. This process is known as volume conduction. When the wave of ions reaches the electrodes on the scalp, they can push or pull electrons on the metal on the electrodes. Since metal conducts the push and pull of electrons easily, the difference in push, or voltage, between any two electrodes can be measured by a voltmeter. Recording these voltages over time gives us the EEG.

Electroencephalography (EEG) is the recording of electrical activity along the scalp produced by the firing of neurons within the brain. In clinical contexts, EEG refers to the recording of the brain's spontaneous electrical activity in microvolt (μV) over a short period of time, usually 20 to 40 minutes, as recorded from multiple electrodes placed on the scalp. The amplitude of the EEG signals may range from 0.5 to 100 μV.

The EEG amplitudes are about 1000 times smaller than the amplitude of an action potential transmitted along an axon. EEG used to be a first-line method for the diagnosis of tumors, stroke and other focal brain disorders, but this technique now is less used because of t other more advance anatomical imaging techniques such as magnetic resonance imaging (MRI), x-ray computed tomography (CT) and positron emission tomography (PET). Scalp EEG activity shows oscillations at a variety of frequencies. Several of these oscillations have characteristic frequency ranges, spatial distributions and they are associated with different states of brain functioning such as waking and the various sleep stages. These oscillations represent synchronized activity over a network of neurons. The absence of EEG can be used to signify brain death.

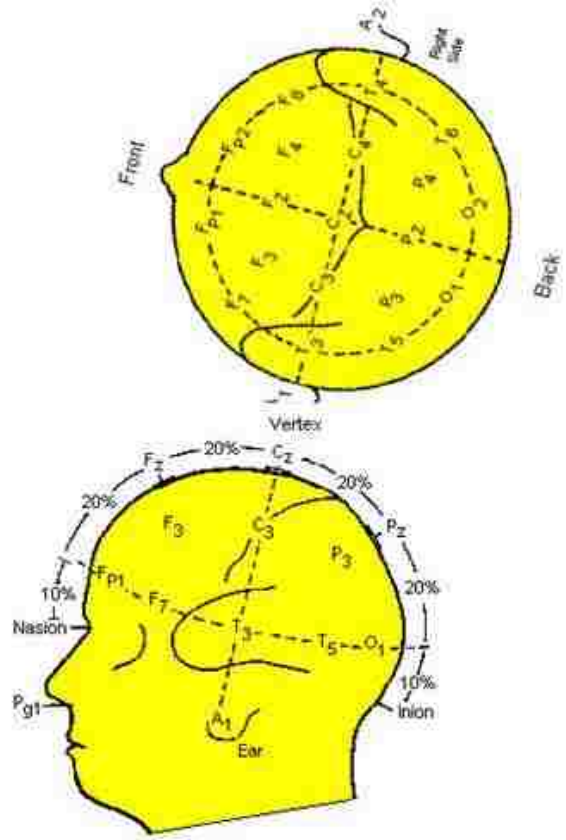

Figure 6-1 Name and lactation of electrodes

The normal EEG varies by age. The neonatal EEG is quite different from the adult EEG. The EEG in childhood generally has slower frequency oscillations than the adult EEG. EEG patterns categorized by frequency range, there are normally four types of EEG patterns, alpha wave, beta wave, theta wave, and delta wave. In common case for each EEG patterns type can predicted the commonly activity.

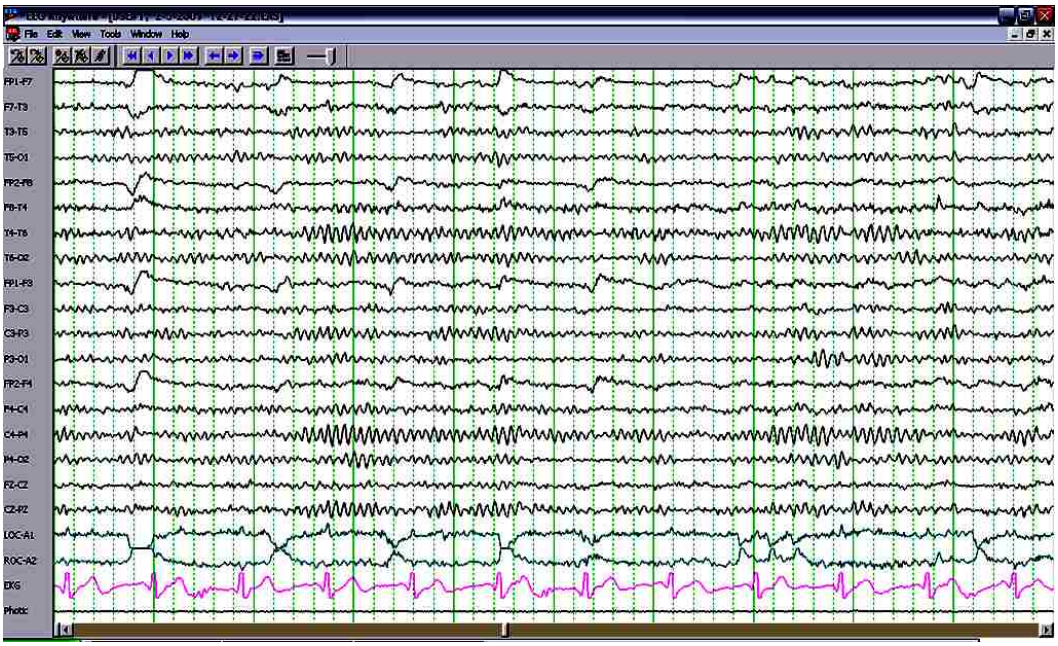

Figure 6-2 Electroencephalography recorded

A delta wave is seemingly emitted in a general pattern from the cerebral cortex. These waves have a frequency range up to 4 Hz. A delta wave tends to have the greatest amplitude and the slowest waves. It is seen normally in adults in slow wave sleep and also seen normally in a wake infant. It may occur focally with subcortical lesions (a part of the brain below the cerebral cortex) and in general distribution with diffuse EEG patterns categorized, metabolic encephalopathy hydrocephalus or deep midline lesions. The presence of delta waves in an awaked adult indicates brain damage.

Theta waves are emitted from the temporal and occipital lobes. This wave has a frequency range from 4 Hz to 7 Hz. Theta waves are seen normally in newborn infants. Theta waves may indicate drowsiness, stress or arousal in older children and adults. They also can be seen in meditation. Excess theta for age represents abnormal activity.

Alpha waves are the best recorded from the parietal and occipital regions while a person is awake and relaxed but with the eyes closed. It also emerges and attenuates with eye opening or mental exertion. These alpha waves are in the frequency range from 8 Hz to 12 Hz. In a child under age of 8 years old, the alpha frequency range from 4 Hz to 7 Hz. Hans Berger named the first rhythmic EEG activity he saw as the "alpha wave". This was the "posterior basic rhythm" (also called the "posterior dominant rhythm" or the "posterior alpha rhythm"), seen in the posterior regions of the head on both sides, higher in amplitude on the dominant side.

Beta waves are in the frequency range from 12 Hz to about 30 Hz. It is seen usually on both sides in symmetrical distribution and is strongest evident from the frontal lobes, especially the area near the precentral gyrus. Beta activity is closely linked to motor behavior and is generally attenuated during active movements. Low amplitude beta with multiple and varying frequencies is often associated with active, busy or anxious thinking and active concentration. Because these waves respond to stimuli from receptors and are superimposed on the continuous activity patterns.

Gamma waves are the frequency range approximately 30 to 100 Hz. Gamma rhythms are thought to represent binding of different populations of neurons together into a network for the purpose of carrying out a certain cognitive or motor function.

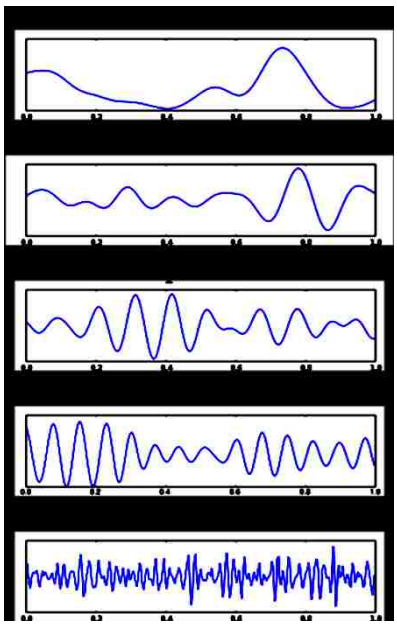

Figure 6-3 EEG patterns categorized by frequency range

6.2 Fast Fourier Transform

The Fourier transform is a mathematical prism [6-1], breaking up a function into the frequencies that compose it, as a prism breaks up light into colors. It transforms a function f that depends on time or on space into a new function $\hat{f}$, which depends on frequency. This new function is called the Fourier transform of the original function or, when the original function is periodic, it is Fourier series. A function and its Fourier transform are two faces of the same information. The function displays the time or space information and hides the information about frequencies.

The Fourier transforms display information about frequencies, but information about time or space is hidden in the phases: the displacement of the sine and cosine for each frequency. The Fourier series of periodic function concerns only those sine and cosine that are integer multiples of the base frequency.

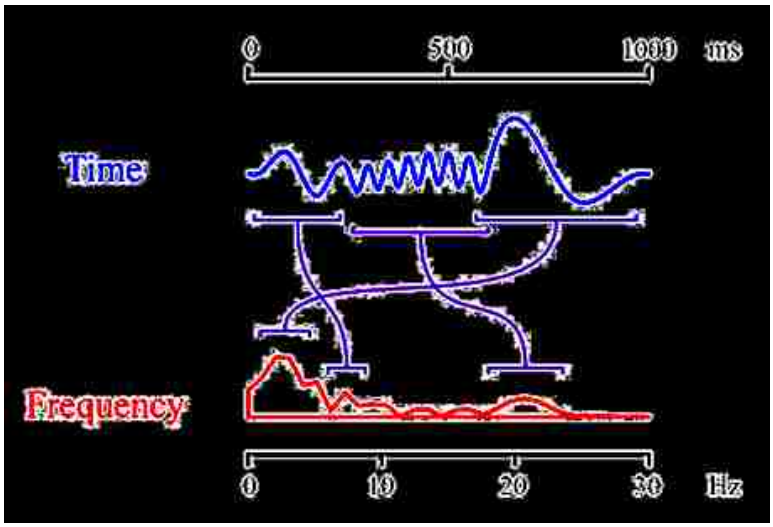

Figure 6-4 Fourier transform of time domain

The Fourier series of a periodic function f of period 1 is written:

$$f(t) = \tfrac{1}{2}a_0 + (a_1 \cos 2\pi t + b_1 \sin 2\pi t) + (a_2 \cos 2\pi 2t + b_2 \sin 2\pi 2t) + \ldots \qquad (6.1)$$

The Fourier coefficients $a_1, a_2, a_3, \ldots$ tell how much the function contains of the functions $\cos 2\pi t, \cos 2\pi 2t, \cos 2\pi 3t, \ldots$ (cosines of frequencies 1 hertz, 2 hertz, 3 hertz …) and the coefficients $b_1, b_2, b_3, \ldots$tell how much the Fourier series of a periodic function f contains of the functions $\sin 2\pi t, \sin 2\pi 2t, \sin 2\pi 3t, \ldots$ (sines of frequencies 1

hertz, 2 hertz, 3 hertz ...). A Fourier series concerns only those sines and cosines that are integer multiples of the base frequency. Formula (6-1) is more commonly written:

$$f(t) = \tfrac{1}{2}a_0 + \sum_{k=1}^{\infty}(a_k \cos 2\pi kt + b_k \sin 2\pi kt) \qquad (6.2)$$

The coefficients of a Fourier series for a function f(t), periodic of period 1, with the formulas:

$$a_k = 2\int_0^1 f(t)\cos 2\pi kt \, dt \qquad (6.3)$$

and

$$b_k = 2\int_0^1 f(t)\sin 2\pi kt \, dt$$

(6.4)

The only frequencies that contribute to the Fourier series of a periodic function are the integer multiples of the function's base frequency; the base frequency being the inverse of the period. If a function is not periodic but decreases sufficiently fast at infinity so that the area under its graph is finite, it is still possible to describe it as a superposition of sines and cosines to analyze it in terms of its frequencies. But now must compute coefficients for all possible frequencies, to compute its Fourier transform. The formulas are:

$$a(\tau) = 2\int_{-\infty}^{\infty} f(t)\cos 2\pi\tau t \, dt \qquad (6.5)$$

and

$$b(\tau) = 2\int_{-\infty}^{\infty} f(t)\sin 2\pi\tau t \, dt \qquad (6.6)$$

The fast Fourier transform (FFT) is a discrete Fourier transform algorithm which reduces the number of computations needed for N points from $2N^2$ to $2N\log_2 N$. If the function to be transformed is not harmonically related to the sampling frequency, the response of an FFT looks like a sinc function (although the integrated power is still correct). Aliasing (also known as leakage) can be reduced by apodization using an apodization function. However, aliasing reduction is at the expense of broadening the spectral response.

The FFT operates have three step, first step decomposing an N point time domain signal into N time domain signals each composed of a single point.

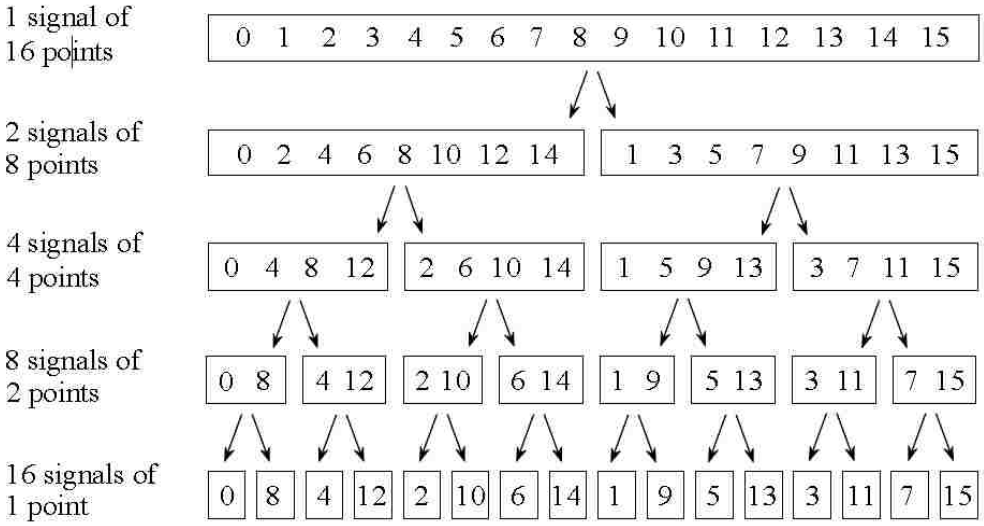

Figure 6-5 Shows an example of the time domain decomposition used in the FFT. In this example, a 16 point signal is decomposed through four.
[The Scientist and Engineer's Guide to Digital Signal Processing, Steven W. Smith, P228]

The second step is to calculate the N frequency spectra corresponding to these N time domain signals.

Sample numbers in normal order			Sample numbers after bit reversal	
Decimal	*Binary*		*Decimal*	*Binary*
0	0000		0	0000
1	0001		8	1000
2	0010		4	0100
3	0011		12	1100
4	0100		2	0010
5	0101		10	1010
6	0110	⇨	6	0100
7	0111		14	1110
8	1000		1	0001
9	1001		9	1001
10	1010		5	0101
11	1011		13	1101
12	1100		3	0011
13	1101		11	1011
14	1110		7	0111
15	1111		15	1111

Figure 6-6 The FFT bit reversal sorting. The FFT time domain decomposition can be implemented by sorting the samples according to bit reversed order.
[The Scientist and Engineer's Guide to Digital Signal Processing, Steven W. Smith, P229]

Lastly, the N spectra are synthesized into a single frequency spectrum.

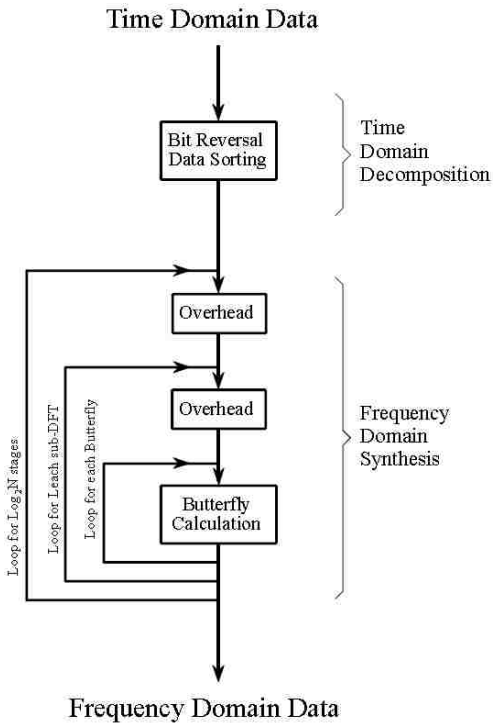

Figure 6-7 Flow diagram of the FFT
[The Scientist and Engineer's Guide to Digital Signal Processing, Steven W. Smith, P232]

6.3 Using Matlab FFT function

FFT function in Matlab Y = fft(X) returns the discrete Fourier transform (DFT) of vector X, computed with a fast Fourier transform (FFT) algorithm. If X is a matrix, fft returns the Fourier transform of each column of the matrix. If X is a multidimensional array, fft operates on the first nonsingleton dimension. The functions Y=fft(x) and y=ifft(X) implement the transform and inverse transform pair given for vectors of length N by:

$$X(k) = \sum_{j=1}^{N} x(j)\omega_N^{(j-1)(k-1)} \tag{6.7}$$

and

$$x(j) = \frac{1}{N}\sum_{k=1}^{N} X(k)\omega_N^{-(j-1)(k-1)} \tag{6.8}$$

whereas $\omega_N = e^{(-2\pi i)/N}$ is an N^{th} root of unity.

To calculate FFT for EEG, first step have to convert each channel of brain waves from EEG to a column matrix. Then used the column matrix of each channel of brain waves are as the input of matlab fft function. Finally, plot graph of each channel of brain waves return matrix.

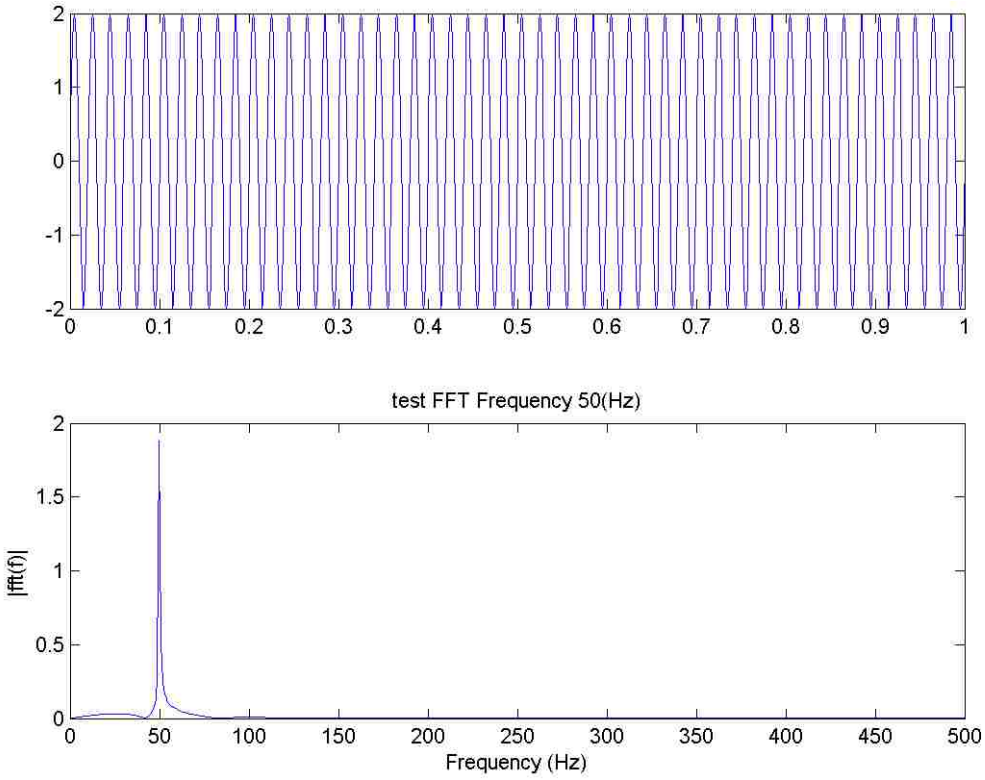

Figure 6-8 Matlab calculation FFT code result checked

To obtain confidence in the results, the matlab fft function was checked by using the generated sine wave which has known frequencies, and amplitude. The results from matlab this generated sine wave, is already know the solution. And the checked result for this matlab code is same as the actual results.

6.4 Result

The FFT of EEG for patient 1, 2, 3, and 4 has more frequency in between 10 to 15 Hz. But the FFT of EEG for patient 5 has more frequency in between 5 to 10 Hz, and sometime has more strong frequency than one region. Patient 1 has strongest FFT of EEG when patient 2 has weakest FFT of EEG. Most of strong frequencies occur at the channel of brain waves located in the back of head.

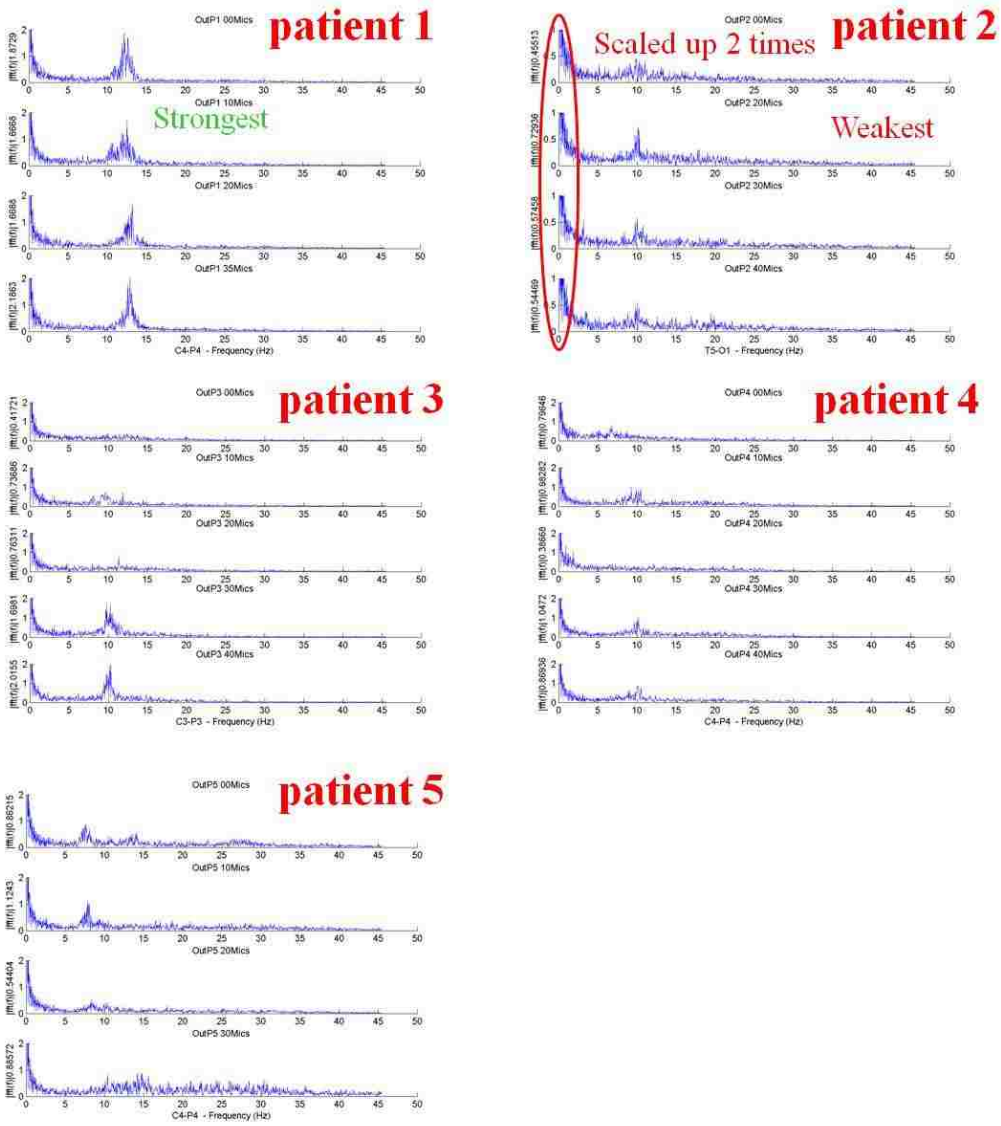

Figure 6-9 Show the strong frequency for each patient

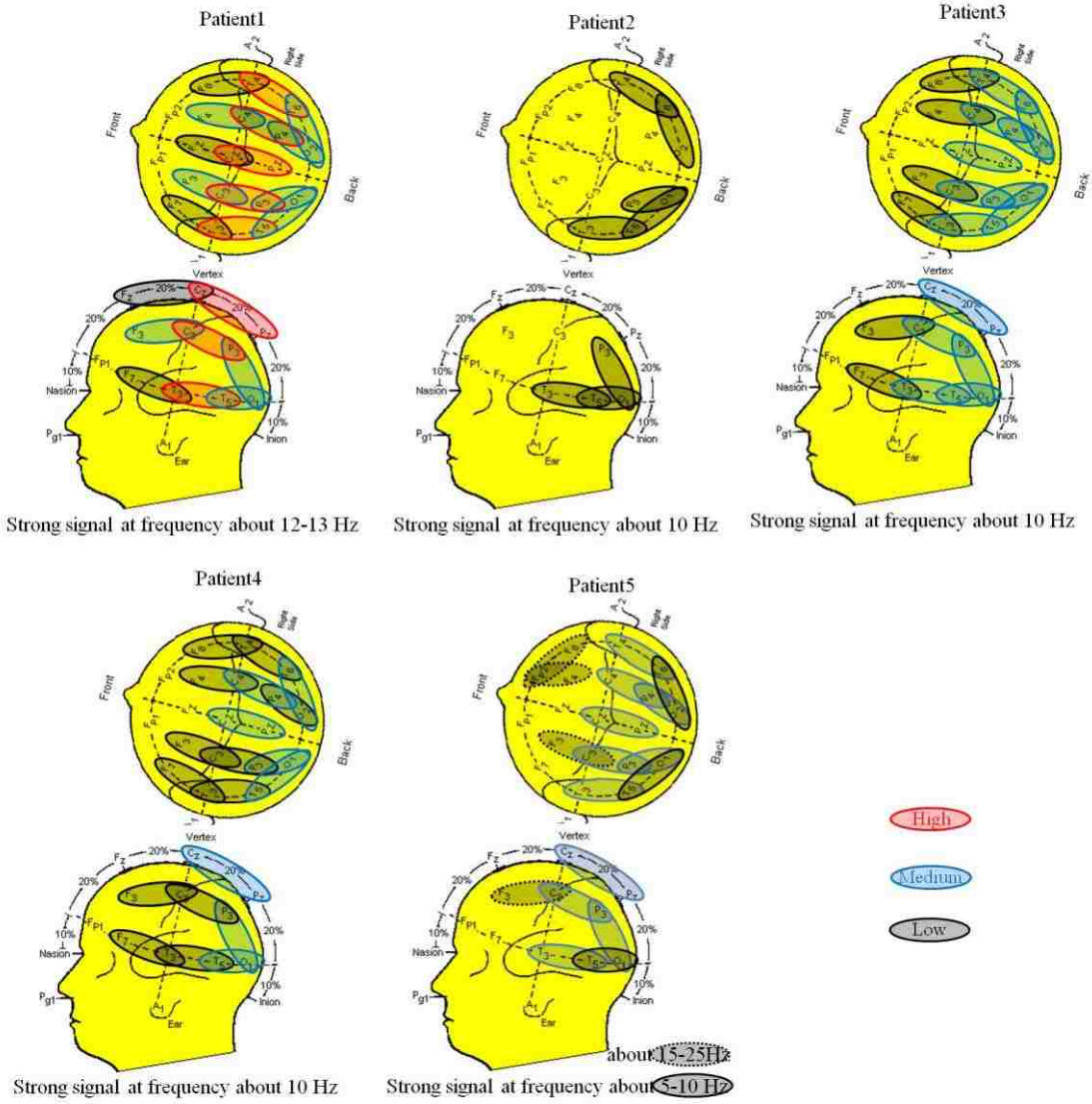

Figure 6-10 Show the location of strong frequency for each patient

6.5 Summary

For this part, the fast Fourier transform was used for determined the frequency spectrum of electroencephalogram. The strong frequency for most of patients are about 10 to 15 Hz (Alpha wave), except for patient 5, most about 5 to 10 Hz (Theta wave), sometime about 15 to 25 Hz (Beta wave). The locations of strong frequency

for all patients are found at the back side of the head. The FFT signal for patient 1 is strongest and for patient 2 is weakest, this may effect from the age of patient 1 is youngest and the age of patient 2 is oldest.

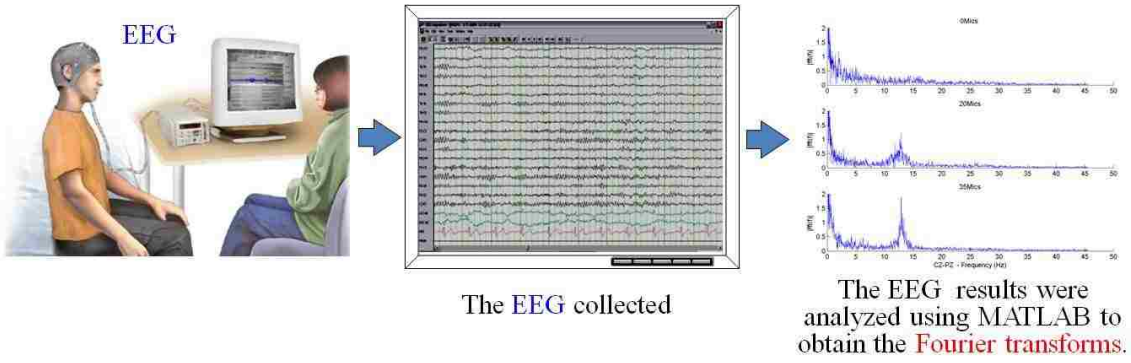

Figure 6-11 Show the EEG analyzed using MATLAB

CHAPTER 7

Wavelet Analysis of Electroencephalogram Waves

In this chapter, the wavelet transform (WLT) analysis of electroencephalogram (EEG) waves and associated spectral analysis is considered. As described earlier, the EEG waves along with the associated EKG waves for the patient were collected during the dobutamine stress test or pacing of the heart.

7.1 Wavelet Transform

Wavelet transform is mathematical manipulation that slices up data into different frequency components. Each component wavelet has a resolution matched to its scale. Wavelet transform also looks like a glass prism that breaks up white light into colors (frequencies).

Wavelet transform was developed independently in the fields of mathematics, quantum physics, engineering, and signal analytical. They have advantages over traditional Fourier methods in analyzing physical situations where the signal contains discontinuities and sharp spikes. The wavelet transform or wavelet analysis is known as the continuous wavelet transform [7-1]. More formally it is written as:

$$\gamma(s,\tau) = \int f(t)\Psi_{s,\tau}(t)\,dt \qquad (7.1)$$

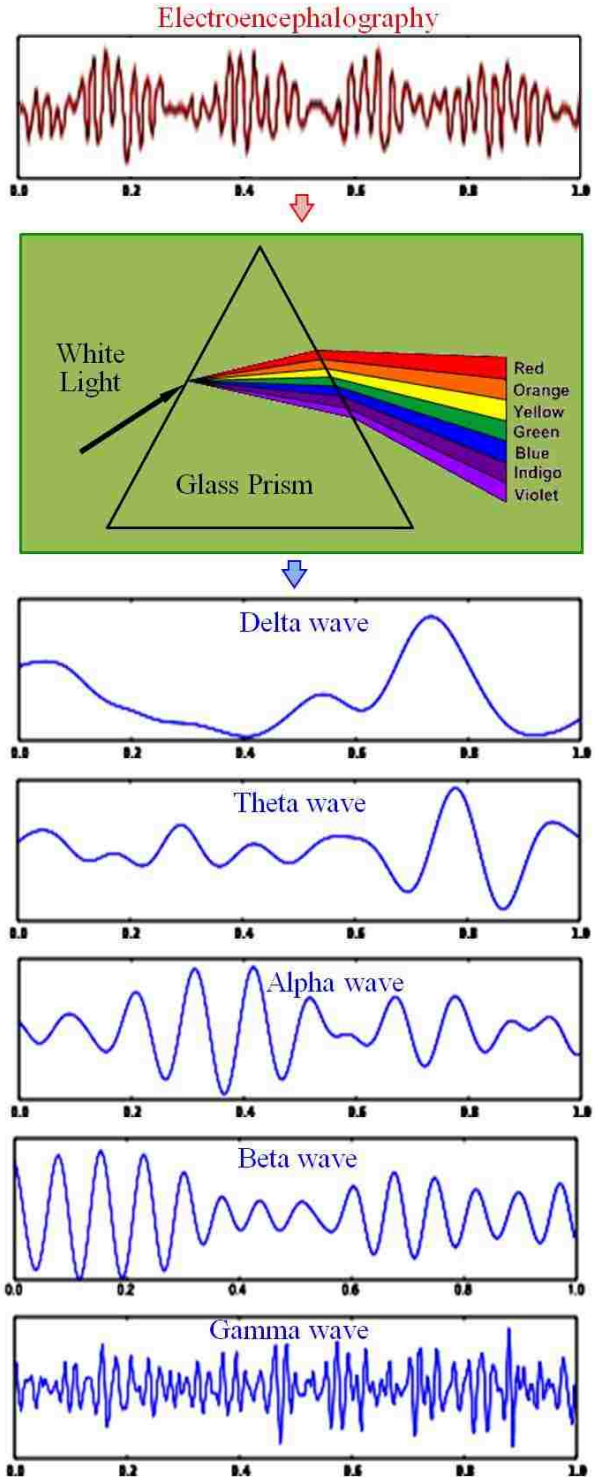

Figure 7-1 Wavelet transform cut up data into different frequency components

This equation shows how a function f(t) is decomposed into a set of basis complex conjugation functions $\Psi_{s,\tau}(t)$ called the wavelets. Whereas the variables scale s and translation τ are the new dimensions after the wavelet transform [7-1]. Therefore the inverse wavelet transform is able written as:

$$f(t) = \int\int \gamma(s,\tau)\Psi_{s,\tau}(t)\,d\tau ds \tag{7.2}$$

The wavelets are generated from a single basic wavelet $\Psi(t)$ called mother wavelet, by scaling and translation

$$\Psi_{s,\tau}(t) = \frac{1}{\sqrt{s}}\Psi\left(\frac{t-\tau}{s}\right) \tag{7.3}$$

In equation (7.3) s is the scale factor, τ is the translation factor, and the factor $\frac{1}{\sqrt{s}}$ is for energy normalization across the different scales. The most important properties of wavelets are the admissibility and the regularity conditions that square integral can be computed functions $\Psi(t)$ satisfying the admissibility condition [7-1].

$$\int \frac{|\Psi(\omega)|^2}{\omega} d\omega < \infty \tag{7.4}$$

In equation (7.4) $\Psi(\omega)$ stands for the Fourier transform of $\Psi(t)$. The admissibility condition implies that the Fourier transform of $\Psi(t)$ vanishes at the zero frequency.

$$|\Psi(\omega)|^2\Big|_{\omega=0} = 0 \tag{7.5}$$

This means that wavelets must have a band-pass like spectrum. This is a very important observation, which we will use later on to build an efficient wavelet transform. A zero at the zero frequency also means that the average value of the wavelet in the time domain must be zero.

$$\int \Psi(t)\,dt = 0 \tag{7.6}$$

In other words, $\Psi(t)$ must be a wave.

7.2 Fast Wavelet Transform Analysis

The continuous wavelet transform has some properties that make it difficult to use directly and much of the description of the process is presented as given by [7-3]. The first is the redundancy of the continuous wavelet transform. In equation (7.1) the wavelet transform is calculated by continuously shifting a continuously scalable function over a signal and calculating the correlation between the two. These scaled functions will be nowhere near satisfy orthogonal basis equation (7.6) and the obtained wavelet coefficients will be highly redundant. The second problem is that the continuous wavelet transforms have an infinite number of wavelets in the wavelet transform. The third problem is that most functions the wavelet transforms have no analytical solutions and thus they could only be calculated numerically [7-1]. The discrete wavelet transform also called fast wavelet transform, was modified to be not continuously scalable and translatable but can only be scaled and translated in discrete steps. From equation (7.3) is re-written as

$$\Psi_{j,k}(t) = \frac{1}{\sqrt{s_0^j}} \Psi\left(\frac{t - k\tau_0 s_0^j}{s_0^j} \right) \tag{7.7}$$

Where j and k are integers and $s_0 > 1$ is a fixed dilation step. The translation factor τ_0 depends on the dilation step. The effect of discretezing the wavelet is that the time-scale space is now sampled at discrete intervals. Usually, with a choice of $s_0 = 2$ so the sampling of the frequency axis corresponds to dyadic sampling.

The result of above will be a series of wavelet coefficients (wavelet series decomposition) when discrete wavelets are used to transform a continuous signal. The energy of the wavelet coefficients must lie between two positive bounds [7-3].

$$A\|f\|^2 \le \sum_{j,k} \left| (f(t), \psi_{j,k}) \right|^2 \le B\|f\|^2 \tag{7.8}$$

Where $\|f\|^2$ is the energy of f(t), and A, B are independent of f(t) for $A > 0$, $B < \infty$. When (A = B) the frame is tight and the discrete wavelets behave exactly like an orthonormal basis. When $(A \neq B)$ exact reconstruction is still possible at the expense of a dual frame. In a dual frame discrete wavelet transform the decomposition wavelet is different from the reconstruction wavelet.

The discrete wavelets can be made orthogonal to their own dilations and translations by special choices of the mother wavelet, which means:

$$\int \Psi_{j,k}(t) \Psi^*_{m,n}(t)\, dt = \begin{cases} 1 & \text{if } j = m \text{ and } k = n \\ 0 & \text{otherwise} \end{cases} \tag{7.9}$$

An arbitrary signal can be reconstructed by summing the orthogonal wavelet basis functions, weighted by the wavelet transform coefficients. And the inverse wavelet transform for discrete wavelets is able written as: [7-4]

$$f(t) = \sum_{j,k} \gamma(j,k), \psi_{j,k}(t) \tag{7.10}$$

The scaling function, as being just a signal with a low-pass spectrum, can decompose in wavelet components and express like equation (7.10).

$$\varphi(t) = \sum_{j,k} \gamma(j,k), \psi_{j,k}(t) \tag{7.11}$$

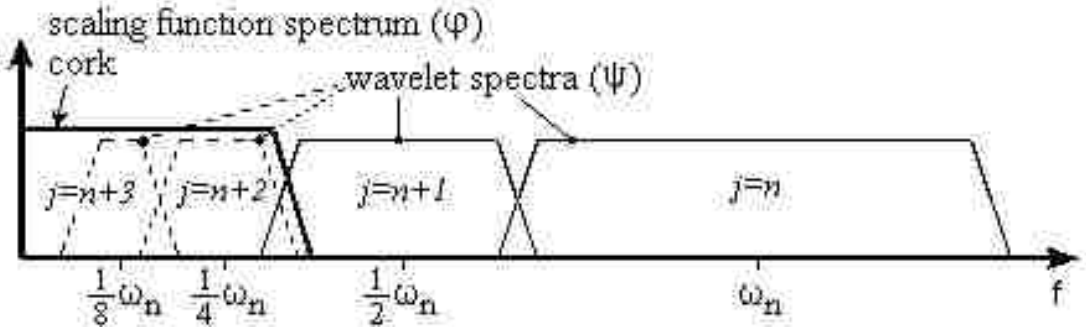

Figure 7-2 How an infinite set of wavelets is replaced by one scaling function [http://polyvalens.pagesperso-orange.fr/clemens/wavelets/wavelets.html]

Analyze a signal using the combination of scaling function and wavelets; the scaling function by itself takes care of the spectrum otherwise covered by all the wavelets up to scale j, while the rest is done by the wavelets. In this way we have limited the number of wavelets from an infinite number to a finite number. Add a wavelet spectrum to the scaling function spectrum we will get a new scaling function, with a

spectrum twice as wide as the first. Usually the number of bands is limited by for instance the amount of data or computation power available. The process of splitting the spectrum is graphically displayed in figure 7-3.Therefore all the information is contained in the second scaling function.

$$\varphi(2^j t) = \sum_k h_{j+1}(k)\varphi(2^{j+1}t - k) \tag{7.12}$$

For scaling function both wavelets scaled and wavelets translated can re-write for the wavelet at level *j*:

$$\psi(2^j t) = \sum_k g_{j+1}(k)\varphi(2^{j+1}t - k) \tag{7.13}$$

$$f(t) = \sum_k \lambda_j(k)\varphi(2^j t - k) \tag{7.14}$$

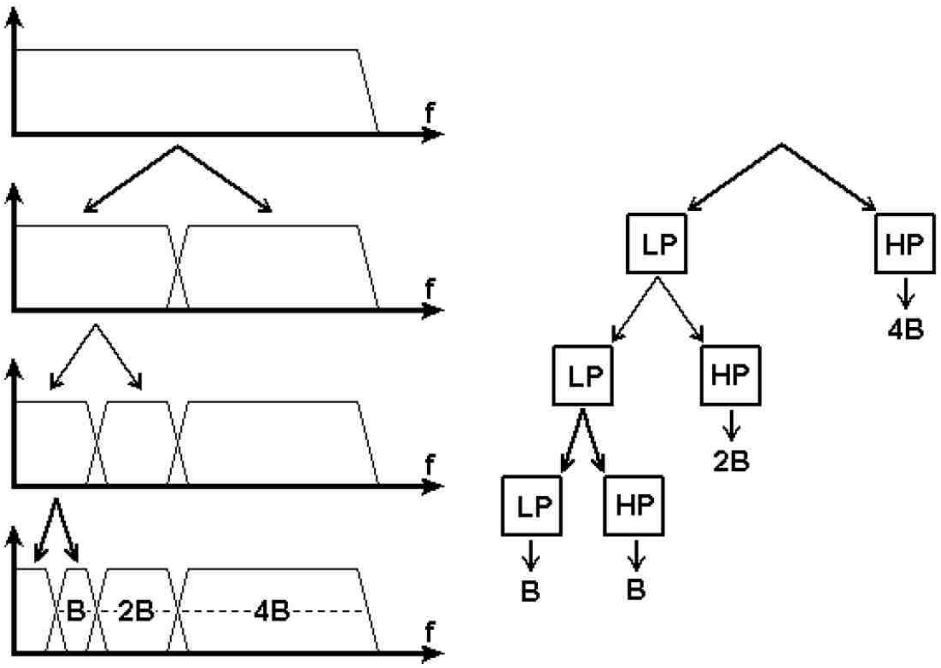

Figure 7-3 Splitting the signal spectrum
[http://polyvalens.pagesperso-orange.fr/clemens/wavelets/wavelets.html]

For step up a scale to *j*-1 have to add wavelets in order to keep the same level of detail. Therefore express the signal f(t) as:

$$f(t) = \sum_k \lambda_{j-1}(k)\varphi(2^{j-1}t - k) + \sum_k \gamma_{j-1}(k)\psi(2^{j-1}t - k) \tag{7.15}$$

There are similarities between Fourier transforms and wavelet transforms [7-5]. First, the fast Fourier transform (FFT) and the discrete wavelet transform (DWT) are both linear operations that generate a data structure that contains $\log_2 N$ segments of various lengths, usually filling and transforming it into a different data vector of length 2^N. Second, the mathematical properties of the matrices involved in the transforms are similar as well. The inverse transform matrix for both the FFT and the DWT is the transpose of the original. As a result, both transforms can be viewed as a rotation in function space to a different domain. For the FFT, this new domain contains basis functions that are trigonometric; sines and cosines. For the wavelet transform, this new domain contains more complicated basis functions called wavelets, mother wavelets, or analyzing wavelets. And the third both transforms have another similarity. The basic functions are localized in frequency, making mathematical tools such as power spectra (how much power is contained in a frequency interval) and scale grams (to be defined later) useful at picking out frequencies and calculating power distributions.

The dissimilarity between Fourier transform and wavelet transforms is that individual wavelet functions are localized in space while Fourier sine and cosine

functions are not. This localization feature, along with wavelets localization of frequency, makes many functions and operators using wavelets sparse when transformed into the wavelet domain. In figure 7-5a shows example Fourier transform plotting. The frequency is in horizontal axis and vertical axis is (unit^2)/Hz.

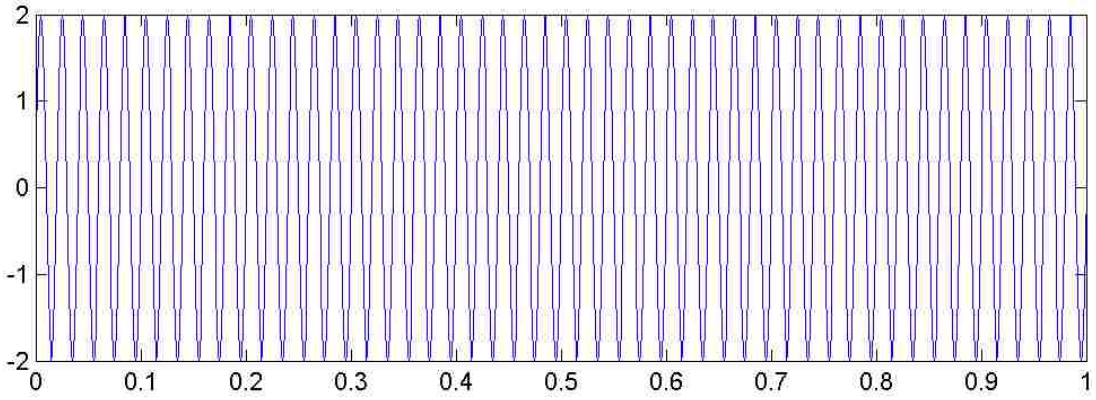

Figure 7-4 Generated 50Hz sin wave for test FFT and WLT code

Although, wavelet transforms have the windows, in order to isolate signal discontinuities, one would like to have some very short basis functions. At the same time, in order to obtain detailed frequency analysis, one would like to have some very long basis functions. A way to achieve this is to have short high-frequency basis functions and long low-frequency ones. This happy medium is exactly what one gets with wavelet transforms. Figure 7-5b shows the coverage in the time-frequency plane with one wavelet function, the wavelet.

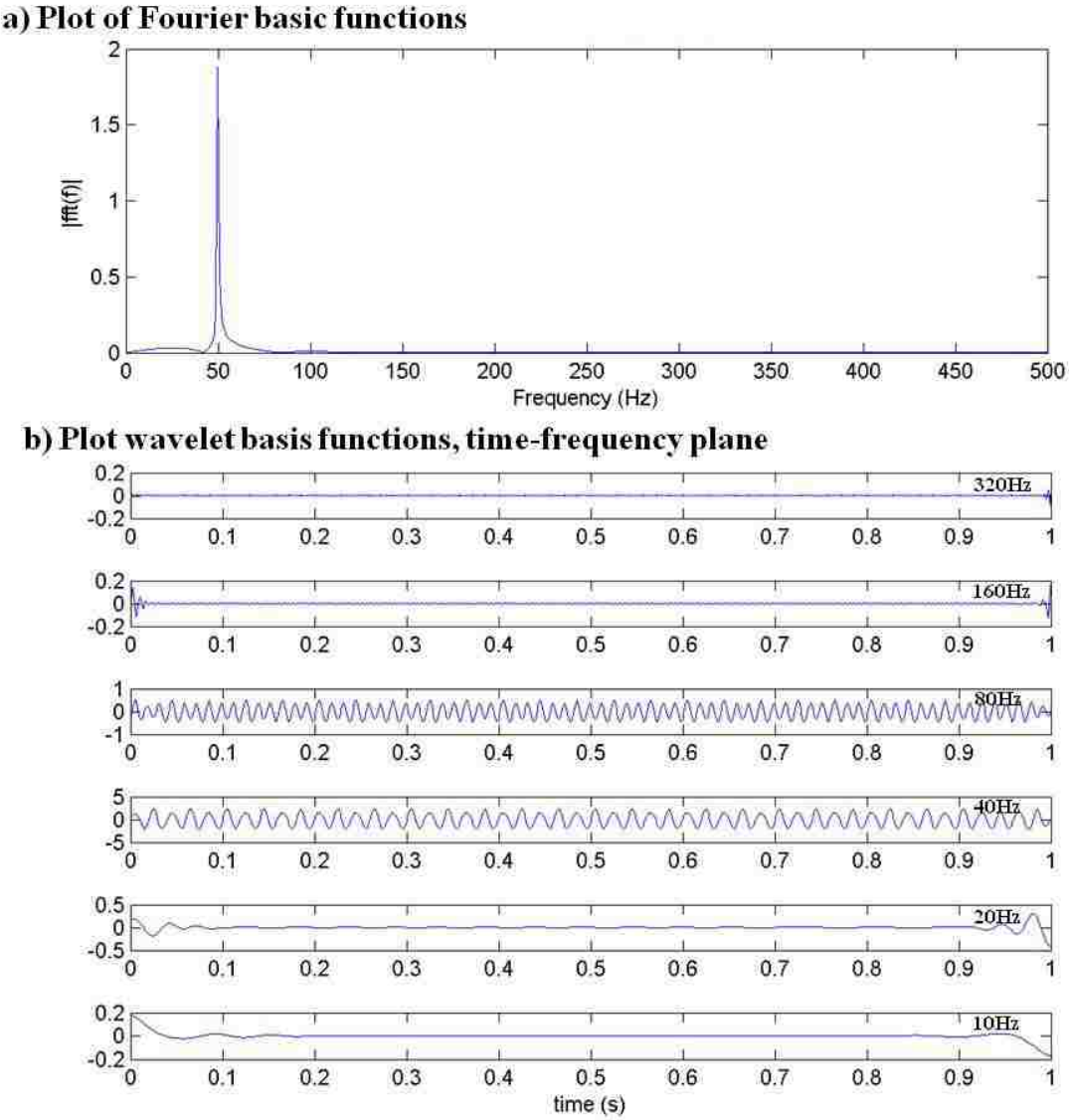

Figure 7-5 Dissimilarity between FFT and WLT result

Additionally, wavelet transforms do not have a single set of basic functions like the Fourier transform, which utilizes just the sine and cosine functions. Instead, wavelet transforms have an infinite set of possible basis functions. Thus wavelet analysis provides immediate access to information that can be obscured by other time-frequency methods such as Fourier analysis.

7.3 Wavelet Transform for Electroencephalogram

This study used the software from Matlab Uvi_Wave Wavelet Toolbox of http://www.gts.tsc.uvigo.es/. The software was modified to determine transforms for the all patients' EEG signals. Each channel of EEG signal was cut to the same time interval as one heart beat (based on data from the EKG channel). To determine the effect of delay or phase difference (equivalent of response time of the system in question) the brain wave data (EEG) was shifted pixel by pixel one pixel at a time with the EKG channel fixed and the correlations determined. The choice of one heart beat (out of two) for the correlation is indicated in the Figure below.

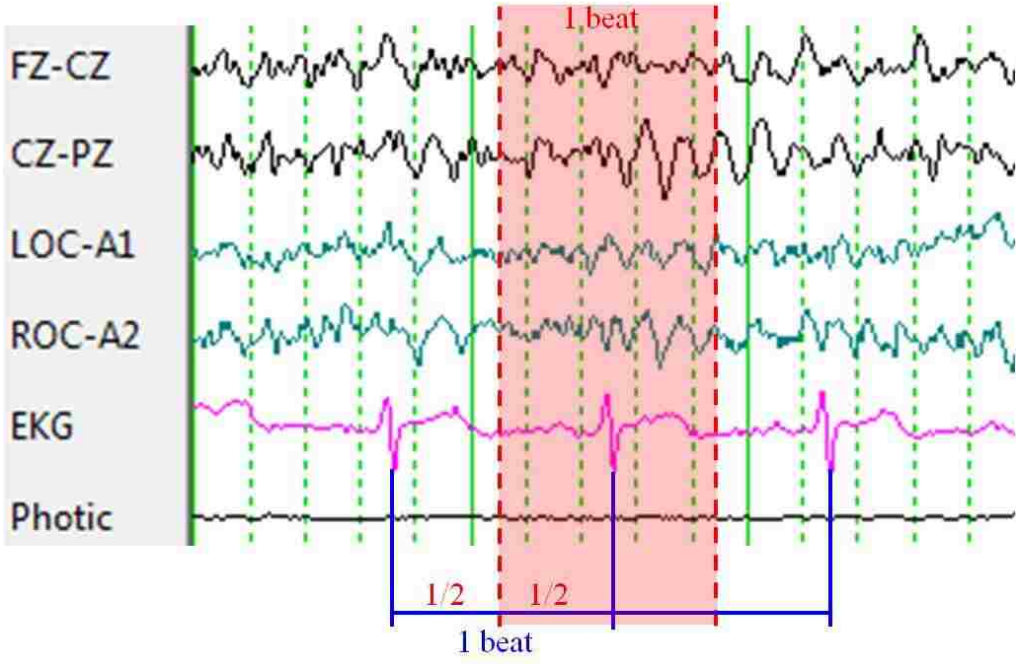

Figure 7-6 One heart beat time interval from EKG chosen to correlate to EEG

To verify the accuracy of the procedure used here, the modified of wavelet toolbox was tested for the accuracy and checked with the waveforms of various frequencies for each window. The frequency of the j^{th} window is 2^{j-1} Hz.

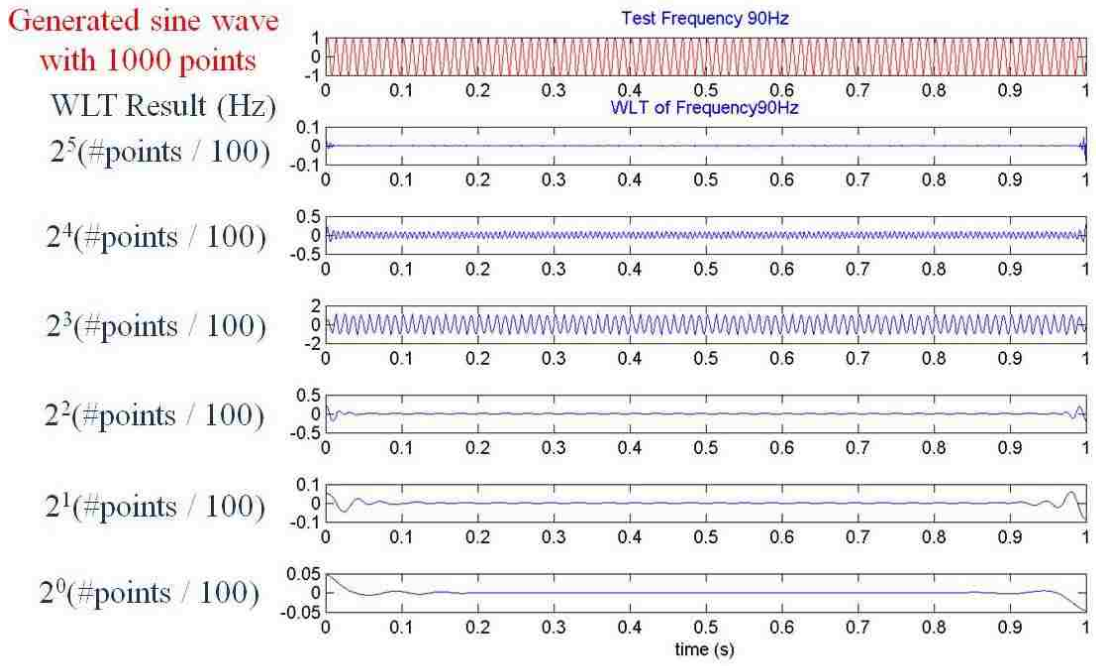

Figure 7-7 Test of wavelet transform toolbox

The combination of all wavelets gives the mother wavelet or original function back. Therefore the correct combined wavelet transforms, the combination of wavelets result must turn back mother wavelet or original function. For more confidence in the results, the modified of wavelet toolbox was compared to the reconstructed signals of the original signals. The modified of wavelet toolbox given all of reconstructed was the signals same as the original signals.

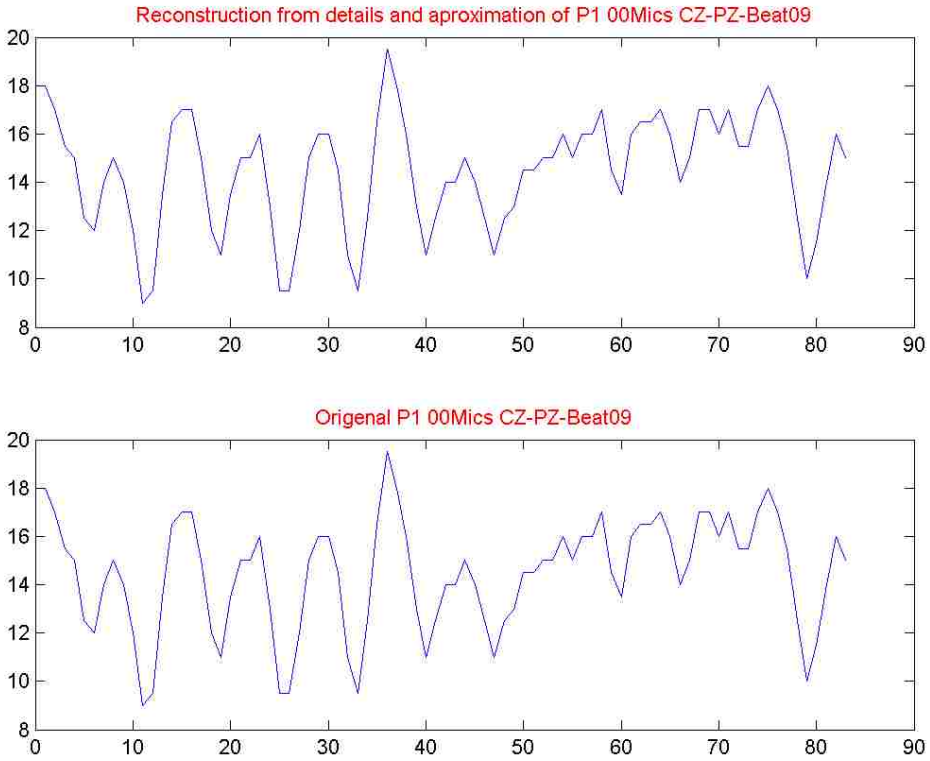

Figure 7-8 Show the compared of reconstruction signals and original signals

7.4 Results

The wavelets of each patient were found for all channels and all heart rate or dosage of dobutamine. The time intervals of all wavelets were matched with the time intervals each it's EKG.

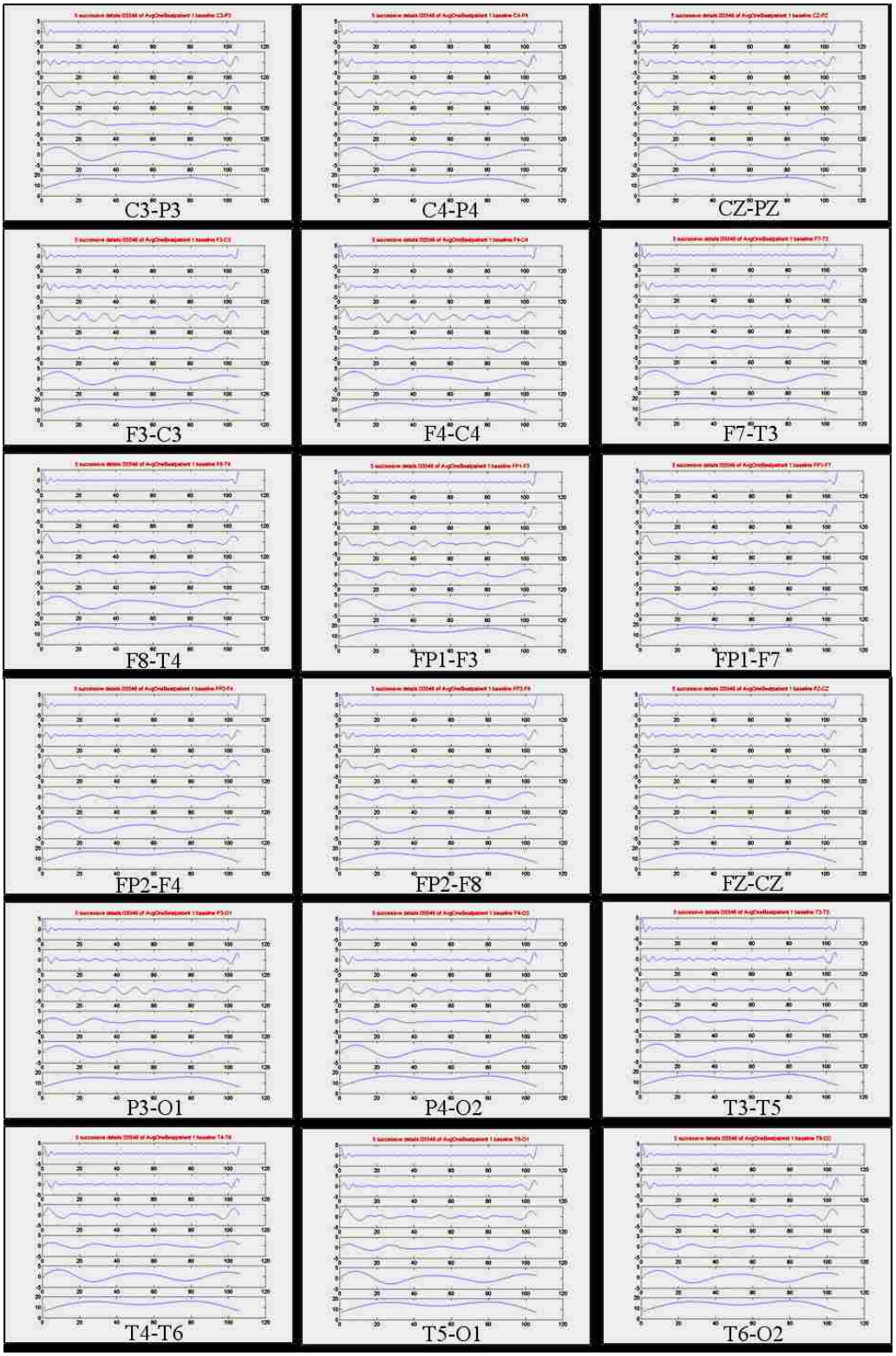

Figure 7-9 Patinet1 HR67 baseline 6 detail wavelets for all 18 channels of EEG

7.5 Summary

The modified of MATLAB wavelet toolbox was used to find the wavelet of all patients EEG channels. The wavelets for all patients EEG channel were found in the same time interval of one heart beat (out of two) because for the correlation with others result in next calculation. The reconstructed wavelet signals of the modified of Matlab wavelet toolbox was shown to reproduce the original signal. The wavelet analysis of the EEG signals during one heart beat had the following correlations of wavelet transform of EEG with EKG in chapter 8.

CHAPTER 8

Correlation of Heart and Brain Data

Based on the movement of the myocardium from the patient echocardiograms the blood flows in the heart and the associated stresses on the myocardium have been determined. Since the objective is to relate the changes in the heart function to that of the brain function, correlations between the heart wall stress, the electrical signal generation for the heart contraction, the fast Fourier transform of electroencephalogram (EEG), and the wavelet transform of electroencephalogram (EEG) have been determined. Several types of correlations are considered to bring out various anticipated and unanticipated effects. All of the correlations are considered for the same length of data, same temporal periods (i.e., for one heart beat). In some cases, phase shift effects have been brought out by temporally shifting (pixel by pixel, a few milliseconds at a time) one data set at a time and these correlation results are discussed below.

8.1 Correlation Coefficient

For many physical phenomenons, processes, or features of the phenomenon have relations between each other. For example, consider the force applied to car brake pedal to decrease of the velocity of the car. In this case, the applying force has negative relation to the car speed. In another case, when a person runs faster, normally the person's heartbeat will be increased, and also cause blood pressure increase. The body needs more energy and Oxygen for this faster metabolism and so it needs more

and faster breathing for sustaining metabolism process. Such relationships are not necessarily just between two things. For the case in point, running speed, heartbeat, blood pressure, metabolism rate, and breathing has are all related to other.

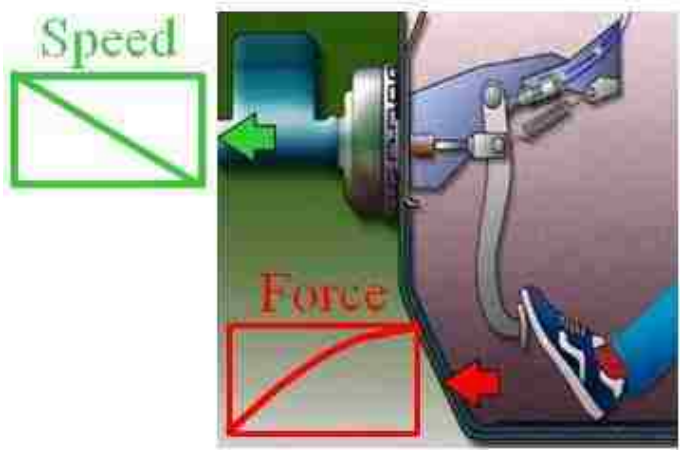

Figure 8-1 Show the (negative) relationship between speed and force

Correlation is a measure of the statistical relationships between two or more parametric variables or observed data values. Some correlations relate parameters that are tightly related temporally (with small time intervals), but other correlation coefficients are available to handle other types of data. Range of correlation coefficients is between +1.00 and -1.00 also written as Correlation coefficient value is between [-1,1]. or $-1 \le r_{X,Y} \le 1$

The correlation value of -1.00 is means the perfect negative correlation while the value of +1.00 represents a perfect positive correlation while the value of zero for correlation coefficient implies lack of correlation. Correlations are useful because they can indicate a predictive relationship that can be exploited in practice.

$$\rho_{X,Y} = \operatorname{corr}(X,Y) = \frac{\operatorname{cov}(X,Y)}{\sigma_X \sigma_Y} = \frac{E[(X-\mu_X)(Y-\mu_Y)]}{\sigma_X \sigma_Y} \qquad (8.1)$$

The correlation coefficient of a set of observations of X and Y written as $\{(x_i,y_i): i=1,..,n\}$ for least square fit is given by the formula:

$$r_{X,Y} = \frac{\sum_{i=1}^{n}(x_i - \bar{x})(y_i - \bar{y})}{\sqrt{\sum_{i=1}^{n}(x_i - \bar{x})^2 \sum_{i=1}^{n}(y_i - \bar{y})^2}} \tag{8.2}$$

where $\bar{x}$ and $\bar{y}$ are the sample means of X and Y This can also be written as:

$$r_{X,Y} = \frac{n\sum x_i y_i - \sum x_i \sum y_i}{\sqrt{n\sum x_i^2 - \left(\sum x_i\right)^2}\sqrt{n\sum y_i^2 - \left(\sum y_i\right)^2}} \tag{8.3}$$

Correlation coefficient of the Xs with the Ys is same as correlation coefficient of the Ys with the Xs, $r_{X,Y} = r_{Y,X}$. $|r_{X,Y}| = 1$if and only if the points lie exactly on a straight line. If the same constant is added to all of the Xs, the correlation coefficient is unchanged for similarly for the Ys. $r_{X,Y} = r_{X_i+C,Y}$. If all of the Xs are multiplied by a constant, the correlation coefficient is unchanged, except that the sign of the correlation coefficient is changed if the constant is negative. Similarly for the Ys. $r_{X,Y} = r_{X_i \times C,Y}$ or $-r_{X,Y} = r_{X_i \times (-C),Y}$.

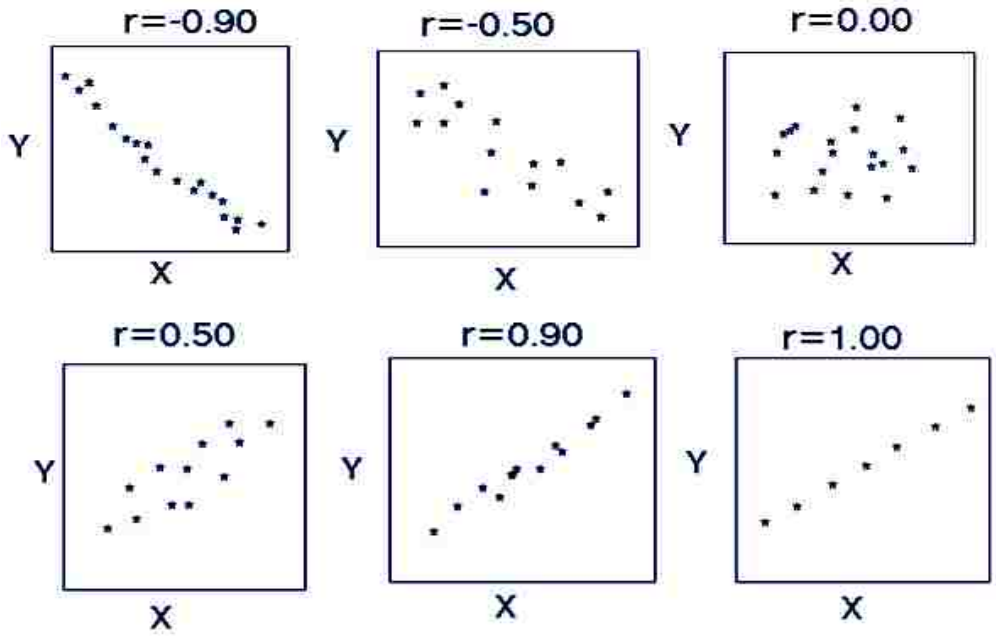

Figure 8-2 Plot of correlation coefficients of X and Y

8.2 Correlation Analysis

The analysis between all two compared properties sets of brain and heart data was employed using the function cross-correlation (corr(x,y)) on Matlab software. To calculate the correlation coefficient for each pair, output from pervious simulation the heart wall stress, the electrical signal generations, the fast Fourier transform of electroencephalogram and the wavelet transform of electroencephalogram were set up to same size matrix. The Matlab cross-correlation function (corr(x,y)) provided Pearson's correlation coefficient of matrix x and matrix y, which is essentially using equation 8.3. In the present calculations, a correlation coefficient value least than 0.5 was considered as low correlation relation which indeed is an arbitrary value. Data corresponding to the same locations for the brain, which are the same as those for EEG indicated in figure 6.1, are considered for analysis. Matlab correlation coefficient

m-code was modified for was modified for use in these calculations. To verify the procedures used here including the modified m-code, correlations between two sine waves with known amplitude, frequency, and phase shifting were calculated and verified to be correct. For the sine waves, with two identical signals in phase provide correlation coefficient equals unity. For sine wave function, phase shifting by πi radians from the original signal provides a correlation coefficient equal to negative one.

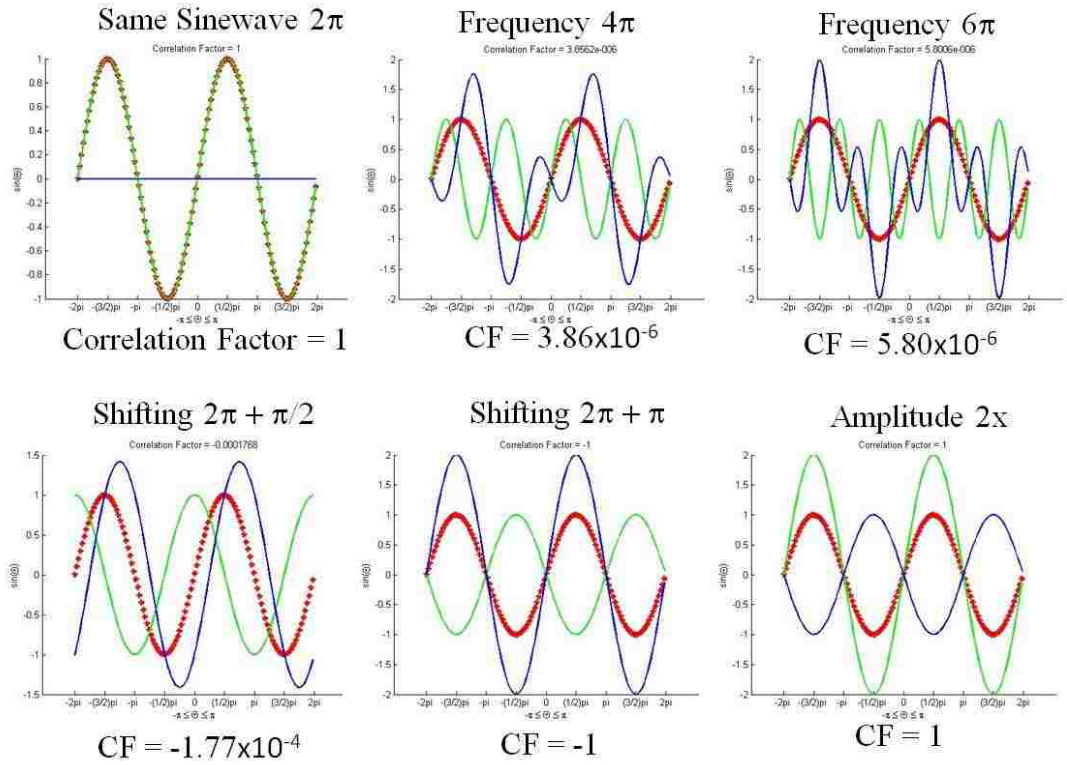

Figure 8-3 Testing matlab cross correlation coefficient code

8.3 Correlation of EKG and EEG with Heart Stresses

The myocardial wall stresses calculated in chapter three, both normal stress and shear stress were considered for correlation coefficient with the EKG. The

correlation coefficient between EKG and heart stress used the EKG from the (bottom left corner of) echocardiogram. The EKG from echocardiogram is perfectly in sync in time with the heart stress data, because the blood flow velocities and heart stress was calculated using the heart wall displacement from the echocardiogram. The analysis time for each correlation coefficient analysis was set up as the one beat (thus time is seconds will be less for a pacing heart beat). The time locations of the EKG from the echo were aligned to match the diastolic and systolic actions and the blood flow in the left ventricle.

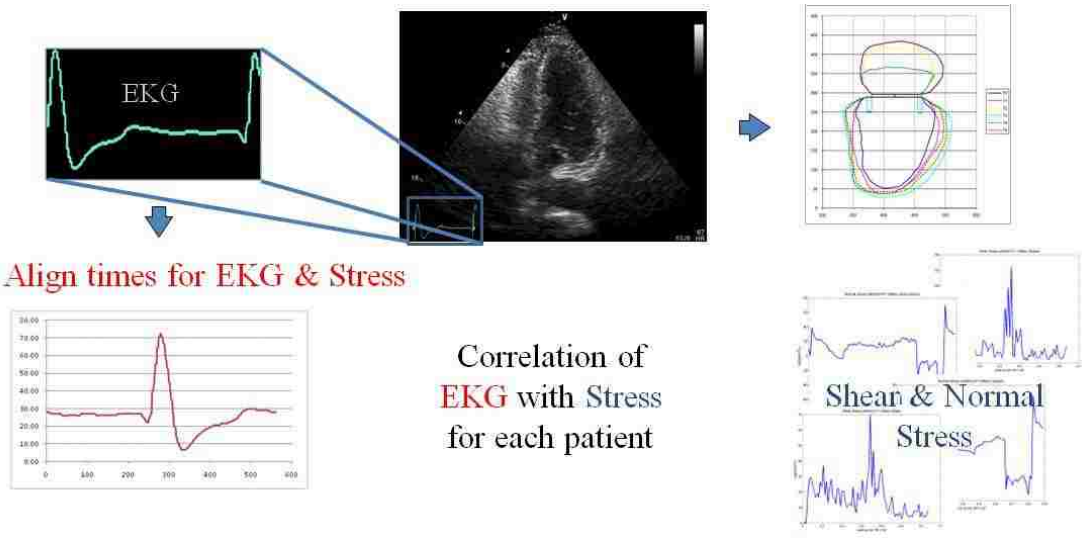

Figure 8-4 Diagram considered correlation coefficients of EKG and stress

Correlation coefficients were analyzed for all patient data as described above. The percentage of time that the correlation coefficient exceeded a value of 0.5 was evaluated. The normal stress correlated better with the EKG than the shear stress and the percentage times the correlation coefficient was significant (>0.5) was 59.28% and 40.72% respectively for normal and shear stresses. With regard to the locations of the myocardium and the corresponding percentages with coefficients larger than 0.5 are:

32.80% at mitral valve, 28.80%, at septum, 20.00%, at endocardium and 18.40% at the apex. For Patient 1, correlation coefficient value for EKG was greater than 0.5 65.79% for normal stress, and 34.21% shear stress. For Patient 2, correlation coefficient value for EKG was greater than 0.5 42.76% for normal stress, and 57.24% shear stress. For Patient 3, correlation coefficient value for EKG was greater than 0.5 77.89% for normal stress, and 22.11% shear stress. For Patient 4, correlation coefficient value for EKG was greater than 0.5 56.76% for normal stress, and 43.24% shear stress. For Patient 5, correlation coefficient exceeded 0.5 51.75% for normal stress, and 48.25% for shear stress. The correlation coefficients (% time they exceeded 0.5) at various locations of the myocardium are shown in figure 8-5.

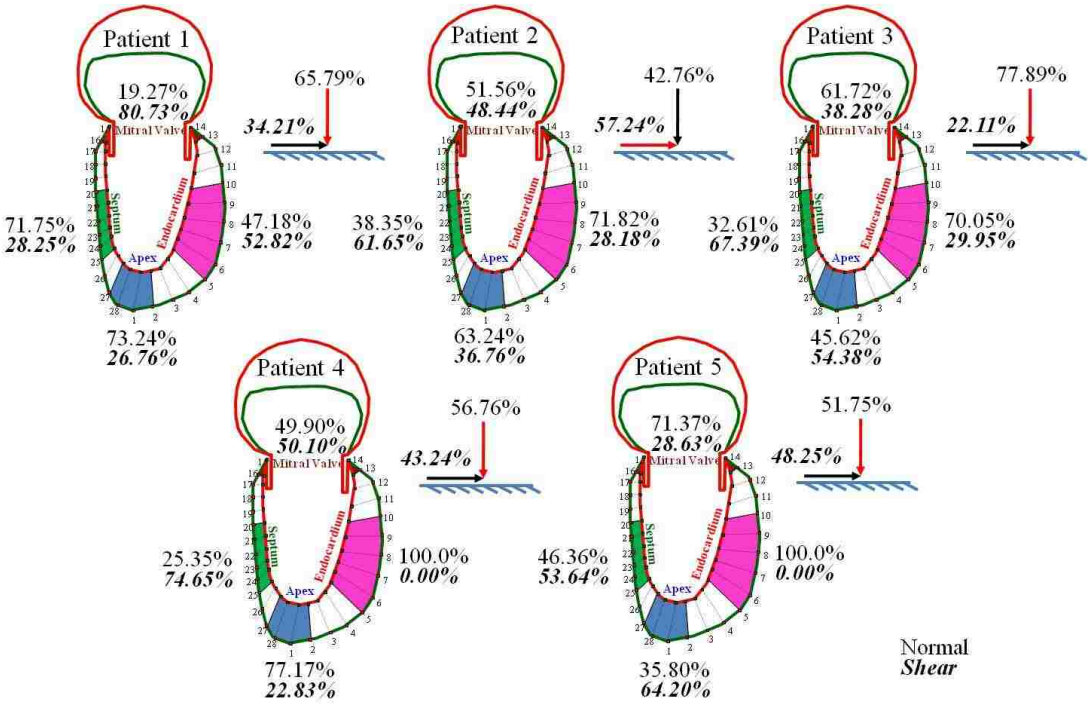

Figure 8-5 Correlation coefficients of EKG and stress results

Using a similar procedure, the correlation coefficient between the heart wall stresses and the EEG was calculated for one completed heart beat. Here the brain wave signals came from the patients' EEG records and each EEG signal from the brain was cut into time slices matching one heart beat time. To study the effects of phase change (or time delay) the correlated signal was shifted pixel by pixel for time one second. The shifting of brain wave signals provided the equivalent of response/reaction time for each Using a similar procedure, the correlation coefficient between the heart wall stresses and the EEG was calculated for one completed heart beat. Here the brain wave signals came from the patients' EEG records and each EEG signal from the brain was cut into time slices matching one heart beat time. To study the effects of phase change (or time delay) the correlated signal was shifted pixel by pixel for time one second. The shifting of brain wave signals provided the equivalent of response/reaction time for each patient. For Patient1 correlation coefficient analysis results, correlation coefficient values were greater than 0.5 at mitral valve 23.97%, at septum 37.19%, at endocardium 19.01%, and at the apex 19.83%. Similar Patient2 values were at mitral valve 39.70%, at septum 38.21%, at endocardium 8.66%, and at the apex 13.43%. Patient3 values were at mitral valve 7.32%, at septum 30.49%, at endocardium 40.24%, and at the apex 21.95%. Patient4 were at mitral valve 31.03%, at septum 37.07%, at endocardium 15.52%, and at the apex 16.38%. Patient5 values were at mitral valve 23.76%, at septum 49.72%, at endocardium 0.55%, and at the apex 25.97%.

All patients results of correlation coefficient of EKG and EEG with heart stress was also shown in the figure 8-5. The figure shows ratio in percentage of shear stress and normal stress for each patient. The figure also shows the percentage of correlation coefficient value greater than 0.5 at various locations for each patient. Response time of all patients was about 0.2-0.4 seconds. Most of strong signals were occurred at the front of the head as shown in figure 8-6 and 8-7.

Shift Time	Patient				
	1	2	3	4	5
	Percentage				
0.0 - 0.1	8.55	9.05	14.74	24.32	0.88
0.1 - 0.2	13.16	10.86	26.32	26.35	11.40
0.2 - 0.3	27.63	35.07	10.53	8.78	55.26
0.3 - 0.4	11.18	32.58	6.32	9.46	14.47
0.4 - 0.5	16.45	2.04	15.79	3.38	3.51
0.5 - 0.6	18.42	7.92	10.53	18.92	3.07
0.6 - 0.7	1.32	1.58	14.74	8.78	7.02
0.7 - 0.8	0.00	0.68	1.05	0.00	3.51
0.8 - 0.9	1.97	0.23	0.00	0.00	0.88
0.9 - 1.0	1.32	0.00	0.00	0.00	0.00

Figure 8-6 Percentage of respond time

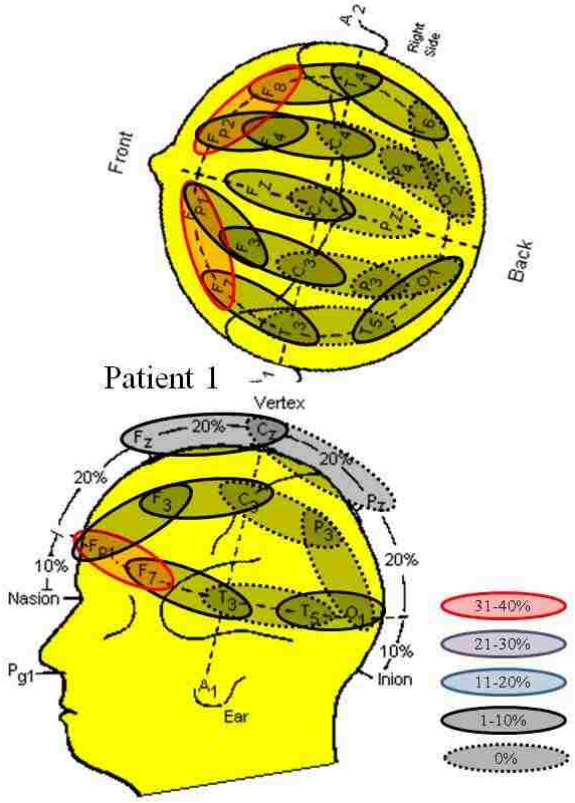

Figure 8-7 Strong correlation coefficients of EKG and stress locations

8.4 Correlation of Wavelet Transform of EEG with EKG

The wavelet transform of EEG and EKG found in chapter 7 were used for calculation correlation coefficient. The EKG signal on EEG data was sliced and matched for one completed heart beat. EEG channel dat were sliced for same length of EKG signal, EEG channels were shifted pixel by pixel for one second (to represent human response time). The strong signal correlation percentage for location, response time, dosage, and EKG matching were found.

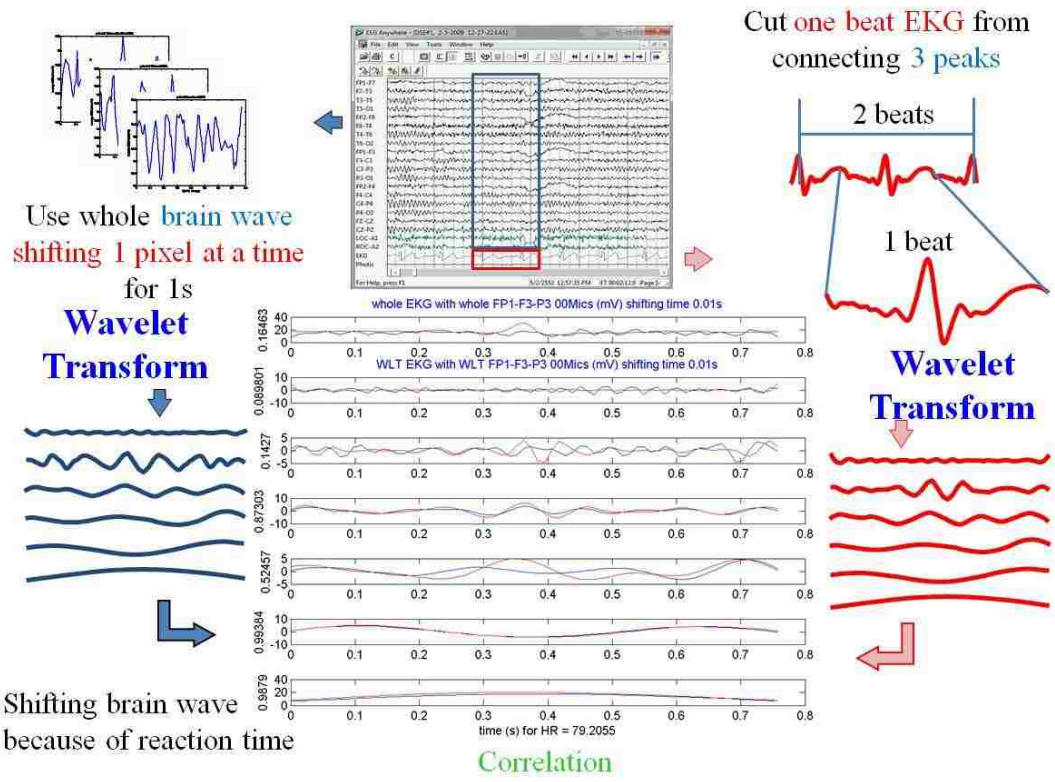

Figure 8-8 Wavelet transform of EEG and EKG correlation calculation diagram

Correlation analysis between wavelet transform of EEG and EKG for all patients resulted in larger correlation coefficients in the front head. The maximum percentages of reaction time for patient 1 to patient 5 in second were 0.2-0.3, 0.1-0.2, 0.2-0.3, 0.0-0.1, and 0.2-0.3 respectively. Higher dosages of dobutamine had stronger correlation coefficient than lower dosage. The contractions of heart (systole) had stronger correlation coefficients than the expansion of heart (diastole).

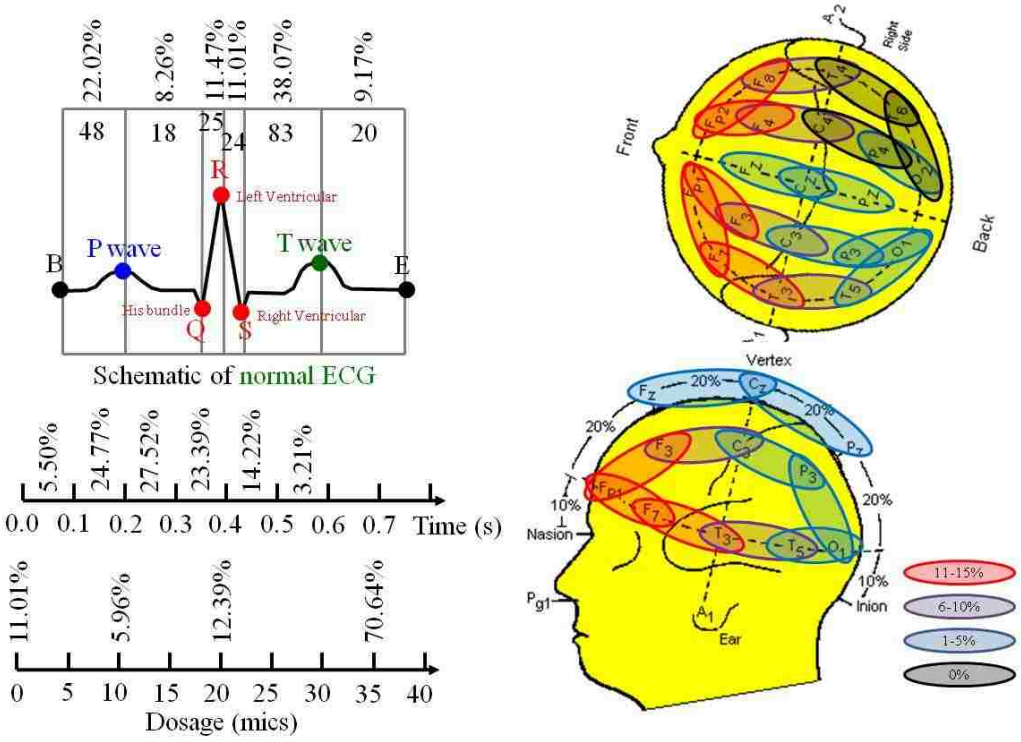

Figure 8-9 Patient 1 Wavelet transform of EEG and EKG correlation result

The correlation between wavelet transform of EEG and EKG for individual patient varied significantly, but was again larger in the front than in the back.

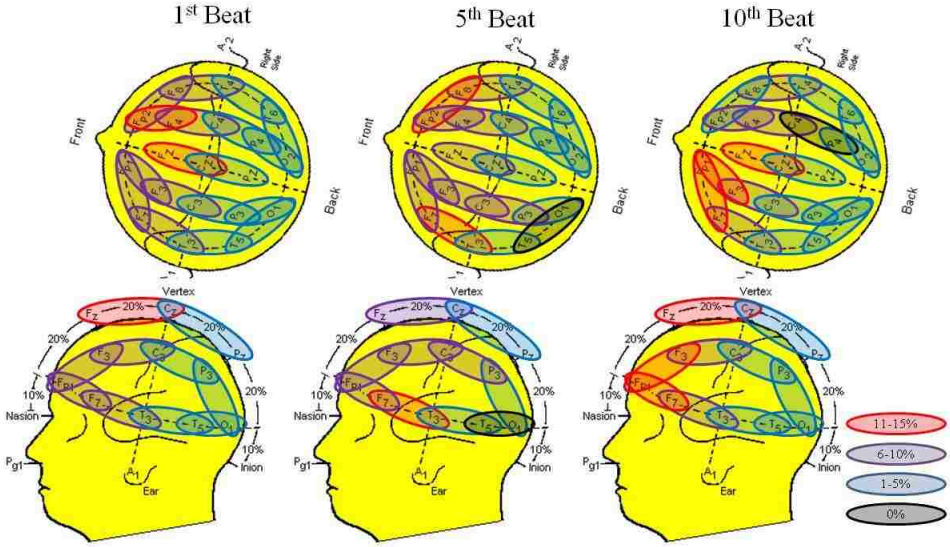

Figure 8-10 Correlation of patient 4 data for 1st, 5th and 10th heartbeat

8.5 Correlation of EEG with Electrical Signal Generated

The electrical signal generated at SA node, AV node, and Purkinji fiber found in chapter 5 were used for the calculation correlation coefficients with the EEG signal. Both EEG and generated electrical signal data were sliced in same length as before to match a complete heart beat. The EEG signal/data were shifted pixel by pixel for one second (to again represent human reaction time). The locations of strong signal correlation percentage (% for c > 0.5) for response time, dosage, and ion type were determined.

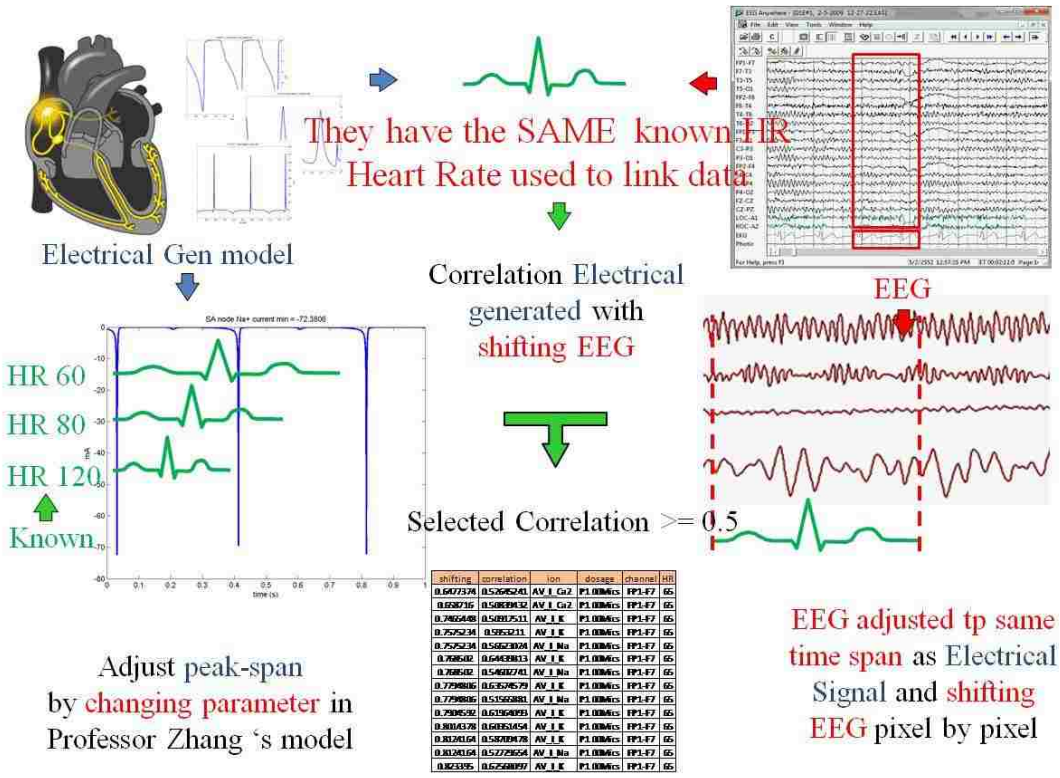

Figure 8-11 Electrical generated and EEG correlation calculation diagram

Correlation coefficient for electrical signal generated at SA node and EEG, had strong correlation with Ca^{2+} ion and K^{+} ion at SA node. There were no Na^{+} ion

correlation coefficients greater than 0.5 at SA node for any patients. At AV node the strongest correlation was for K^+ ion. At Purkinji fiber the strongest correlation was for the potential voltage. Correlations analyzed between electrical signals generated and EEG for all patients had more correlation coefficient greater than 0.5 in the front of the head.

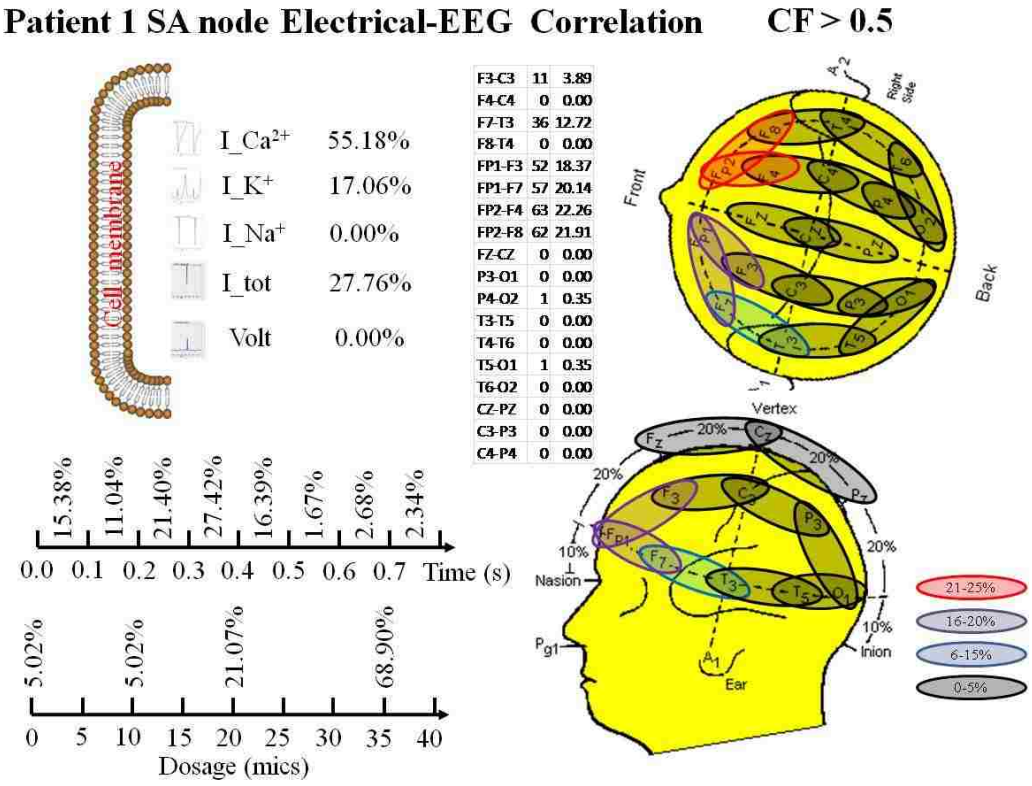

Figure 8-12 Patient1 SA electrical generated and EEG correlation result

8.6 Summary

Most of strong correlation coefficient for all patients were found near the frontal lobe of the patient. For all patients the maximum reaction times were between 0.1 to 0.4 seconds. Higher dosages of dobutamine gave higher correlation coefficients for most of calculations.

CHAPTER 9

Result and Discussion

The methods used for determining the effect of the heart function the brain has been described in some of the earlier chapters. Some of the results obtained for various aspects of the heart function and the brain function have also been presented in the earlier sections of this work. In this chapter we shall discuss the above described results in a detailed manner. Three main topics of interest here are related to the simulation of the heart function, evaluation of the corresponding brain activity and EEG data, and correlations between the heart (EKG) and brain function (EEG).

9.1 Simulation of Heart Function

In this part, for each patient, based on the echocardiogram outputs, heart functions and related parameters were calculated; these included blood flow profiles, blood velocity, blood pressure, and heart volume change. These parameters were used to evaluate the calculation of heart wall stress. This part also involved the docking of drug dobutamine into the heart β_1 adrenergic receptor that was leading to heart electrical signal generation.

9.1.1 Blood Flow and Stress in the Left Ventricle

The heart wall boundary conditions from the echocardiograms of left ventricle from echocardiogram are just two-dimensional representation of a three dimensional process that includes twist if the heart. Despite that, but the flow pattern results from the simulation of blood flow in the left ventricle of all patients looks quite reasonable

by many counts. The shear stress from successive heart beats in patient 4 at a heart rate of HR97 (Figure 3-7), were not exactly the same. This is because the successive heartbeats were not perfectly periodic functions. However, the simulations of successive beats were not significantly different. Furthermore both successive beat simulations had almost same shape and same time of peaking. This should be additional proof that the results from the simulations are reasonably good.

The systolic-diastolic volume changes for all the patients correlated well with increasing dosage of dobutamine. With increasing dobutamine dosage, the systolic-diastolic volume change increases until a maximum point, and after that the systolic-diastolic volume change decreases, (see Figure 3-10). With increased dobutamine dosage, the electrical signals that generate contraction in the heart are larger; therefore heart contracts faster and heart rate increased. As this happens fast and faster, the displaced volume decreases since the heart tissue is not completely relaxed and the ventricle is completely expanded. Therefore the systolic-diastolic volume change for all patients decreased with increased dobutamine dosage.

In figure 3-13, heart wall stress for all regions of all patients looks higher with increasing dobutamine dosage, except for patient 1. The faster contraction of heart is the reason for higher heart wall stresses. Patient 1 had only four different dosages of dobutamine yielding lesser data to be analyzed. However even for patient 1, heart wall stress increased with increased dobutamine dosage at the lower doses administered.

9.1.2 Docking of Dobutamine

Modeling and computation of the docking of dobutamine into heart b_1 adrenergic receptor is much less expensive compared to potential experiments to measure such data experimentally. The advantage of computational simulation is useful, safe, faster, and costs less although the calculated data are not as accurate as the experimental data. The bonding between atoms of dobutamine and b_1 adrenergic receptor was found from the lower free energy possible position of docking simulation. The length between bonded atoms from docking simulation was same as other general atom bonding. Bonded atoms were used as the parameters in docking of dobutamine into heart b_1 adrenergic receptor simulation model. Due to the limitations of CPU and memory of computer, number dobutamine molecules that that were simulated were around 200 dobutamine molecules for each dosage of dobutamine (Figure 4-14). Nevertheless for the 10 mics (milligrams per kg per minute) dosage of dobutamine, result shown is almost exponential as would be predicted from theory. The variations for larger dosages of dobutamine are almost linear. Thus a linear variation was assumed for the higher doses.

9.1.3 Electricals Signal Generated

The generated electrical signal lead to the contraction of heart is conducted by the action potential in sinoatrial (SA) node, action potential in atrioventricular (AV) node, and action potential in Purkinji fiber. By modifying the action potentials of rabbit models as suggested by Zhang [2-16 to 2-18], the action potential curve for human heart was derived. The results of these models compared well with measured

normal action potentials. But the amplitude of the potential was about two times bigger. This may be due using modified rabbit data (average heart rate 130-325 beats per minute). After multiplying the human potential magnitude with (human-rabbit) factor, the predicted potential amplitude of model is almost the same as the normal measured potential amplitude.

9.2 Brain Signal Analysis

Fast Fourier transform and wavelet transform were used as spectral tools for the analysis of brain waves in concert with cardiac functions.

9.2.1 Fast Fourier Transform of Electroencephalogram

The fast Fourier transform of electroencephalogram for patients 1, 2, 3, and 4 had more frequencies in alpha wave region that is typical in awake and relaxed people. The fast Fourier transform of electroencephalogram in patient 5 has more frequency in theta wave region theta wave which shown in stress or arousal person. Patient 2's EEG amplitude is weakest. This may be because of patient's age; 79 years old. All larger magnitudes of fast Fourier transforms of electroencephalogram were for in the backside of head.

9.2.2 Wavelet Transform of Electroencephalogram

Wavelet transforms of electroencephalogram used in this study were the discrete wavelet transform which is easier to use for computational calculations. However, the limit of discrete wavelet transform is that the frequency steps are 2^n apart; therefore wavelet transform of electroencephalogram is hard to calculate for all

frequencies such as say a frequency of 23Hz. Yet these discrete wavelet transform are still useful for analyzing brain wave activities and relate them to delta, theta, alpha, and beta brain waves. This activity of brain waves has frequencies in the range that almost matches with 2^n, 0 to 4 Hz, 4 to 7 Hz, 8 to 12 Hz, and 12 to 30 Hz respectively.

9.3 Correlation of Heart and Brain Data

The analysis and correlations between heart data and brain data were synchronized by heart rate. Most calculations were done for one heart beat in same period of time. Some calculations were phase shifted to evaluate the effect of phase shifting data to analyze the reaction time.

9.3.1 Correlation of EKG and EEG with Heart Stress

The study of correlation of EKG with heart stress used the shifting of EKG from echocardiogram. EKG from echocardiogram is only one beat but the heart beat is assumed to be a repeating periodic function. The phase shifting of EKG yielded results indicating a reaction time of about 0.2-0.4 seconds. That means, 0.2 to 0.4 seconds after the heart contracted, heart stress followed and corresponding changes in EEG took place.

Both correlations of EKG with heart stress and correlation of EEG with heart stress indicated that the normal stress had better correlation than shear stress. That indicates better and direct relationship to the pressure in the heart and the systolic and diastolic functions of the heart. The effect of shear stress might have been evident more clearly if the twisting of the heart was analyzed in a 3-D model. Patient 2 had a

better correlation of shear stress with heart functions; this patient may have had some problems (Figure 8-5).

9.3.2 Correlation of Wavelet Transform of EEG with EKG

EKG from the recoded EEG was used in correlation of wavelet transform of EEG with EKG calculated. EKG from the measured EEG chart permitted calculations for every heart beat.

Calculation from different beats for the same condition, gave almost the same results proving repeatability of the processes (Figure 8-12). That explains the high correlation between EEG and EKG located for many EEG channels; most of larger or better correlations of EEG were for electrodes corresponding to the front of the brain. This is not surprising knowing that in many mammals and birds some important cognitive behavior is associated with frontal lobes of the brain.

Heart contractions start at P of the wave and finish at T of the wave (Figure 8-11). The percentage of correlation between P and T of the wave were larger than those between T wave and P wave. i.e., brain waves had better correlations with heart in contracted state (systole) than heart in relaxed state (diastole).

9.3.3 Correlation of EEG with Electrical Signal Generated

Correlation of EEG with generated electrical signals from SA node, Na^+ ion and associated electrical potential had very little correlation with EEG, but better correlation with Ca^{2+} ion and K^+ ion. Na^+ ion current might just be the start of the

sharp beginning of signal and thus Na^+ ion current did not have much correlation (Figure 9-2).

Correlation of EEG with generated electrical signal from AV node, K^+ ion and electrical potential had more correlation with EEG than other ions.

Correlation of EEG with electrical signal generated from purkinji fiber, Ca^{2+} ion and electrical potential had better correlation with EEG than other ions. This may because the Ca^{2+} ion and electrical potential associated with that are the main factors that make the heart muscle contract.

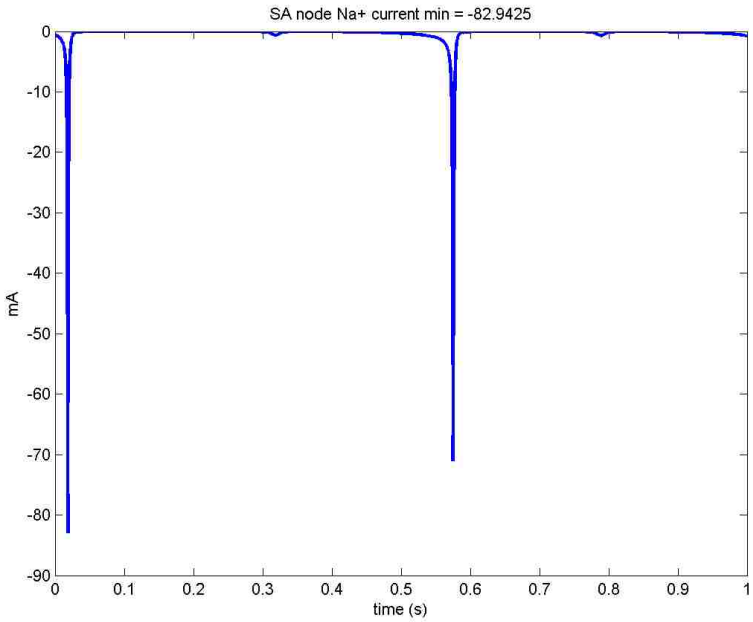

Figure 9-1 Electrical signal generated at SA node from Na^+ ion

9.4 Summay

This chapter discussed in some detail some of the results generated as part of the present work. The results included those related to the simulation of the heart

function, the analysis of the brain wave data and the relationship between the above two in the form of correlations between the heart function and brain data.

CHAPTER 10

Summary and Conclusions

The present work deals with simulation of blood flow in the heart and the stresses on the myocardium based on patient echocardiography and using the position of the myocardium from the echoes as boundary conditions. The current work also analyses the EEG brain waves using frequency and wavelet analysis and also calculates correlations between heart behavior (EKG) and brain (EEG waves). In the first part of the work, simulation and physical properties of heart have been carried out to better understand the properties of blood flow in the left ventricle, blood velocity distributions, blood pressure, and heart stresses for various heart pacing rates achieved with the use of Dobutamine in patients. In the second part of the work, brain waves (EEG, electroencephalogram waves) recorded during the Dobutamine stress tests while the heart was paced have been analyzed by wavelet transform and fast Fourier transform (FFT). In the final part of the work, both physical properties of the heart and associated waves and analysis of brain waves have been analyzed in the context of Dobutamine transport and the electrical properties of the sinus node and heart contraction.

10.1 Echocardiograms and Analysis of Heart Function

Echocardiograms consist of ultra sound based representations of the heart movement but only two dimensions. The loss of the third dimension and particularly not being able to represent the ‘twist’ of the heart is a major limitation of using

echocardiogram for measuring patient heart data. Although blood flow in the left ventricle is three-dimensional, the present computational modeling represents it as a two-dimensional body of rotation to get the whole volume. Despite the above difficulties and assumptions, it is believed that with such 2-D modeling most of the left ventricle function and physical properties of the blood flow are captured. For the present patients, the heart is paced using the drug dobutamine to test their heart functionality. The transport of dobutamine is modeled as part of this work to determine the amount of effective dobutamine. This modeling includes the evaluation of docking of dobutamine with β_1-adrenergic receptors using Autodock4 computer software and the related simulation makes several assumptions and thus are not perfect. Computational results indicate an exponential trend for the amount of dobutamine absorbed as a function of time. Since the half-life of dobutamine in the body is quite short, continued infusion at larger rates (milligrams per minute) is necessary to achieve larger doses of dobutamine in the patient. Some of the data needed for the dobutamine modeling particularly for the electrical potential modeling included some rabbit electrical potential data along with other constants, etc. The electrical signals generated as well as the overall modeling looks reasonable and have yielded good results.

10.2 Analysis of Brain Signal Data

Both wavelet transform and fast Fourier transforms have been used here for the analysis of brain (EEG) data. Fast Fourier transforms (FFT) analyzes the spectral (frequency) content of the EEG data or brain waves. The dominant frequency

displayed as a result of fast Fourier transform is useful to predict the status of patients by correlating dominant frequency with the brain waves recorded: alpha, beta, delta, and theta waves. Transformation of all channels of brain waves by fast Fourier transform also identifies location of dominant frequencies there. Wavelet transforms of brain waves also yielded spectral data but the wavelets are in the time domain.

10.3 Correlation of Heart (EKG) and Brain (EEG) Data

Most of the better correlations (larger correlation coefficients) of heart and brain data with significant correlation coefficients ($c > 0.5$) are located in the front side of the head. But some of the dominant fast Fourier transform of brain waves are located at the backside of the head too. Correlations of phase shifted brain waves with physical properties of heart provided estimates of reaction times. The reaction times calculated in this work are around 0.2 to 0.4 seconds; that means the brain waves respond about 0.2 seconds after the heart stress. For the same patient, heart rate, dosage of dobutamine, location of strong correlation of signals (% of time $c > 0.5$) had broader distribution but were larger in the front of head. In the SA node, Na^+ is the main electrical signal to make heart process run. In the same way, at the purkinji fiber, Ca^{2+} and electrical potentials are the main factors for contraction of heart muscle.

10.4 Recommendations for Future Work

The present study uses heart wall position data from the echocardiograms for the determination of blood flow and heart stresses in the left ventricle. The data used and thus the results are strictly two-dimensional. In three dimensions, the pumping of

blood by the heart not only involves contraction of the left ventricle but also a significant amount of twisting of the heart (wringing of the fluid out of the left ventricle). A three dimensional analysis of the heart and the pump in functions could shed significant new light into those cardiac phenomenon. The cardiac stresses from such an analysis will be more accurate. The docking of dobutamine, interaction with the cell and related electrical signals that generate heart function are all simulated only by computational simulation. Additional and new experimental work related to the better understand the docking of dobutamine and the electrical signals generated in the process would be welcome. Since all stronger correlations (correlations coefficients, $c > 0.5$) between heart and brain data are in the front part of the brain, much more attention should be paid to determine the next set of experiments and correlations related to brain waves in the front channels of EEG record. Correlations of a patient, at the same heart rate but for different heartbeats, can describe the variations in heartbeat and related effects and possibly deceases. Analysis of brain waves in real time by wavelet transforms or fast Fourier transforms might one day soon be helpful to cardiologists to predict and quickly decide better treatment methods.

References

[2-1] R. H. Anderson, J. Yanni, M.R. Boyett, N. J. Chandler, and H. Dobrzynski. (2009) "The Anatomy of the Cardiac Conduction System." Clin. *The Anatomical Record.* 22:99-113.

[2-2] Bertram C.D. (1995). "The dynamics of collapsible tubes". *Symp. Soc. Exp. Biol.* 49: 253– 64.

[2-3] Armitstead J.P., Bertram C.D., Jensen O.E. (1996). "A study of the bifurcation behaviour of a model of flow through a collapsible tube". *Bull. Math. Biol.* 58 (4): 611–41.

[2-4] G.A. Buxton· Nigel Clarke. (2006) "Computational Phlebology: The Simulation of a Vein Valve". *J Biol Phys* 32:507–521.

[2-5] Charles S. Peskin. (1977) " Numerical Analysis of Blood Flow in the Heart." *Journal of Computational Physics* **25**:220-252.

[2-6] C.S. Peskin., and B.F. Printz. (1992) "Improved Volume Conservation in the Computation of Flows with Immersed Elastic Boundaries." *Journal of Computational Physics* **105**:33-46.

[2-7] D.M. McQueen and C.S. Peskin (2000) " A Three-Dimensional Computer Model of the Human Heart for Studying Cardiac Fluid Dynamics" *SIGGRAPH ACM Special Interest Group on Computer Graphics and Interactive Techniques* 34(1): 56–60.

[2-8] B.D. Bursulaya, M. Totrov, R. Abagyan and C.L. Brooks (2003), "Comparative study of several algorithms for flexible ligand docking "*Journal of Computer-Aided Molecular Design* 17 (11): 755-763.

[2-9] Rosenfeld R.J. , Goodsell D.S. , Musah R.A. , Morris G.M. , and Goodin D.B. (2003), " Automated docking of ligands to an artificial active site: augmenting crystallographic analysis with computer modeling" *Journal of Computer-Aided Molecular Design* 17 (8): 525-536.

[2-10] Macpherson AK and Neti S (2004), "Blood Flow induced wall stress in the left ventricle of the heart", *Advances Fluid Mechanics V, eds M. Rahman, R.Verhoeven, C.A. Brebbla, WIT press*, Southampton, 321-331.

[2-11] Macpherson AK and Neti S (2002), "The effect of Angiotensin II on heart blood flow and hypertension", *Advances Fluid Mechanics IV, eds M. Rahman, R.Verhoeven, C.A. Brebbla, WIT press*, Southampton, 1-12.

[2-12] Macpherson AK, Neti S, Macpherson PA, Houser SR, Hari M and Marzillier J. (2005) "Mechanical Stress and Hypertrophy", *Modelling in Medicine and Biology VI, eds M. Ursino,Ca.a.Brebbia,G.Pontrelli , E.Magasso,WIT press*, Southampton, 171-179.

[2-13] Macpherson AK, Neti S (2001), "Modelling the Effects of Angiotensin Receptor Blockers on Left Ventricle Remodelling", *JRASS*, 2,1,52.

[2-14] Macpherson AK, Neti S (2001), "A Rapid Procedure for Initial Drug Evaluation", *Phys. Med. Biol*, June; **46(6)**:N139-47.

[2-15] Macpherson AK, Neti S (2004), "Simulating Physiology and Methods for Therapeutic Evaluation with Emphasis on Hypertension", *Currt Topics in Mechanical Chemistry*. **4**,461-471.

[2-16] H. Zhang ,A.V. Holden, I. Kodama, H. Honjo, M. Lei, T. Varghese and M. R. Boyett (2000), "Mathematical Models of Action Potential in the Periphery and Center of the Rabbit Sinoatrial node" *Am J Physiol Heart Circ Physiol*, **279**: 397-421.

[2-17] S. Inada, J. C. Hancox, H. Zhang, and M. R. Boyett (2009), ”One-Dimensional Mathematical Model of the Atrioventricular Node Including Atrio-Nodal, Nodal, and Nodal-His Cells” *Biophysical Journal* 97 : 2117–2127.

[2-18] Philip Stewart, Oleg V. Aslanidi, Denis Noble, Penelope J. Noble, Mark R. Boyett and Henggui Zhang (2009), “Mathematical models of the electrical action potential of Purkinje fibre cells”, *The Royal Society Publishing Subscriber Help & Services*. A 367, 2225–2255.

[2-19] Armour, J. Andrew (2004), "Cardiac neuronal hierarchy in health and disease" *Am J Physiol Regul Integr Comp Physiol*, **287**: R262-R271.

[2-20] Armour, J. Andrew (2009), "Science of The Heart: Exploring the Role of the Heart in Human Performance" *http://www.heartmath.org/research/science-of-the-heart.html, Institute of HeartMath*.

[2-21] Alkire MT (1998). "Quantitative EEG correlations with brain glucose metabolic rate during anesthesia in volunteers". *Anesthesiology* **89**, 323–333.

[2-22] Bojan Musizza, Aneta Stefanovska, Peter V. E. McClintock, Milan Palus, Janko Petrovcic, SamoRibaric and Fajko F. Bajrovic (2007), "Interactions between cardiac, respiratory and EEG-δ oscillations in rats during anaesthesia ". *J Physiol* 580(1), 315–326.

[2-23] Beatrice C. Lacey and John I. Lacey (1978), "Two-Way Communication between the Heart and the Brain Significance of Time within the Cardiac Cycle". *American Psychologist*, 99-113.

[2-24] M. Akin (2002). "Comparison of Wavelet Transform and FFT Methods in the Analysis of EEG Signals". *Journal of Medical Systems*, 26(3), 241-247.

[3-1] Chandrasekhar,S. "Principles of Stellar Dynamics", Uni. Of Chicago Press, Chicago, 1942.

[3-2] Ruth,D.W. 1972 "A Monte Carlo simulation of the impulsively started piston problem, M.S.Thesis, University of Manitoba, Dept. of Mech. Eng.,Winnipeg,Canada.

[3-3] Balescu R. Equilibrium and Non Equilibrium Statistical Mechanics ,John Wiley, New York, 1990.

[3-4] Hurlé A, Sánchez-Quintana D, Ho S.Y.,Bernabeu E, Murillo M,Climent V Capillary Supply to the sinus Node in Subjects with Long-Term Atrial Fibrillation, The annals of thoracic surgery,89,1,38-43,2010.

[3-5] Macpherson AK and Neti S 2001 "A rapid procedure for initial drug evaluation" , Phys. In Med. and Biol.46,6.

[3-6] Tsukamoto 1.T, et al "Decreased Myocardial β-Adrenergic Receptor Density in Relation to Increased Sympathetic Tone in Patients with Nonischemic Cardiomyopathy" The Journal of Nuclear Medicine,48,11,Nov 2007 177-182.

[3-7] Cheney, M., Computational predictions of Dobutamine docking using MOE software, Private Communication, 2011.

[6-1] Barbara B Hubbard. (1996) "The world according to wavelets" Editorial, Sales, and Customer Service Office, A K Peters, Ltd.

[6-2] Bertram C.D. (1995). "The dynamics of collapsible tubes". *Symp. Soc. Exp. Biol.* 49: 253–64.

[7-1] Kaiser, G. (1994) "A Friendly Guide to Wavelets" Rader, *Fishman & Grauer PLLC*, Boston: Birkhäuser.

[7-2] Amara Graps (1995). "An Introduction to Wavelets**".** *IEEE Computational Science and Engineering*, vol 2 num 2**.**

[7-3] Daubechies,I. (1992). "Ten Lectures on Wavelets". 2nd ed. Philadelphia: *SIAM*, CBMS-NSF regional conference series in applied mathematics 61.

[7-4] Sheng, Y. (1996)." Wavelet Transform" *The transforms and application handbook*. CRC Press, 747-827.

[7-5] Mallat,SG. (1989). "A Theory for Multiresolution Signal Decomposition: The Wavelet Representation" *IEEE Transactions on Pattern Analysis and Machine Intelligence*, 11(7), 674-693

Appendix A

Result

A.1 Docking of Dobutamine Result

The best possible position of dobutamine from the Autodock software is the lowest energy position.

dobutamine atom				
N	1	8.51	22.027	24.669
H	2	7.746	21.533	25.136
C	3	9.712	21.18	24.697
C	4	9.347	19.683	24.724
C	5	9.637	18.974	23.416
C	6	8.64	18.868	22.434
C	7	8.909	18.21	21.233
C	8	10.172	17.666	20.99
C	9	11.176	17.782	21.947
C	10	10.907	18.435	23.153
O	11	7.932	18.079	20.28
H	12	8.306	17.606	19.505
O	13	10.413	17.031	19.803
H	14	11.382	16.883	19.704
C	15	8.073	22.449	23.326
C	16	6.799	21.705	22.899
C	17	7.881	23.974	23.146
C	18	6.989	24.388	21.966
C	19	5.688	25.023	22.396
C	20	5.127	26.069	21.647
C	21	3.924	26.656	22.039
C	22	3.281	26.207	23.186
C	23	3.822	25.173	23.945
C	24	5.024	24.584	23.547
O	25	2.106	26.808	23.538
H	26	1.896	27.508	22.882

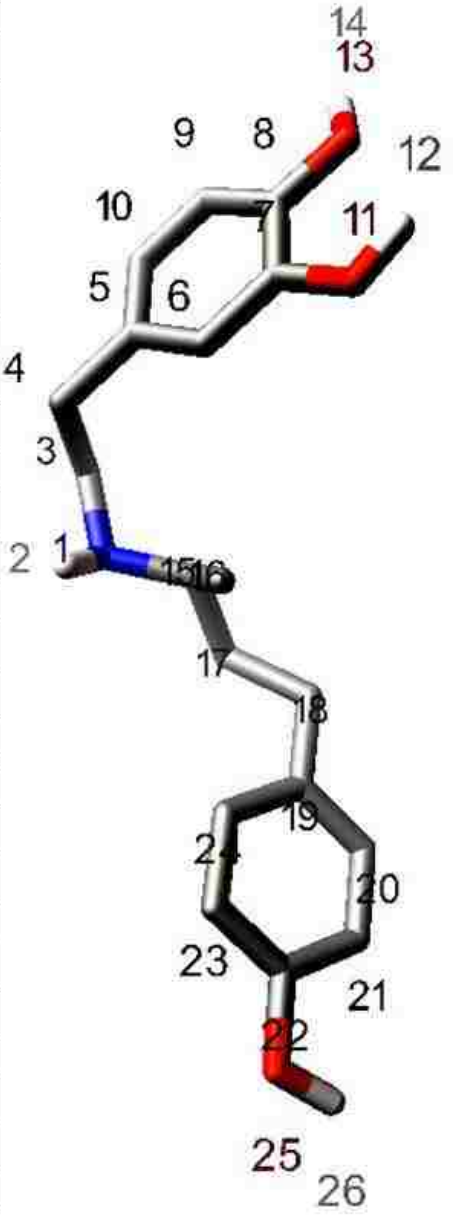

Figure A-1 The best position docked of dobutamine

Interaction Data

Ligand: hum_beta1-dobutamine.08.28.09.pdb: RECEPTOR
Receptor: hum_beta1-dobutamine.08.28.09.pdb: RECEPTOR

Heavy atoms: ligand = 22, receptor = 2960

ligand	receptor	residue	chain	type	score	dis
H 4475	O 899	GLY 98	hum_ 1	H-don	31.7%	1.5
H 4453	OD 1266	ASP 121	hum_ 1	H-don	25.3%	1.2
O 4440	OG 2706	SER 212	hum_ 1	H-don	98.2%	2.4
O 4437	OG 2755	SER 215	hum_ 1	H-don	26.0%	2.6
H 4452	OD 3947	ASN 329	hum_ 1	H-don	49.3%	1.6
O 4440	OG 2706	SER 212	hum_ 1	H-acc	98.2%	2.4
O 4437	OG 2755	SER 215	hum_ 1	H-acc	26.0%	2.6
C 4473	O 899	GLY 98	hum_ 1	weak	0.0%	3.3
C 4473	C 898	GLY 98	hum_ 1	weak	0.0%	4.3
O 4474	C 898	GLY 98	hum_ 1	weak	0.0%	3.6
C 4476	O 899	GLY 98	hum_ 1	weak	0.0%	3.4
C 4476	C 898	GLY 98	hum_ 1	weak	0.0%	4.1
C 4476	CA 895	GLY 98	hum_ 1	weak	0.0%	4.2
O 4474	CB 930	LEU 101	hum_ 1	weak	0.0%	3.5
O 4474	CG 955	VAL 102	hum_ 1	weak	0.0%	3.2
C 4454	CH 1210	TRP 117	hum_ 1	weak	0.0%	4.2
C 4455	CH 1210	TRP 117	hum_ 1	weak	0.0%	4.3
C 4457	CH 1210	TRP 117	hum_ 1	weak	0.0%	4.0
C 4462	CH 1210	TRP 117	hum_ 1	weak	0.0%	4.1
C 4462	CZ 1208	TRP 117	hum_ 1	weak	0.0%	3.9
C 4473	CH 1210	TRP 117	hum_ 1	weak	0.0%	4.2
C 4476	CH 1210	TRP 117	hum_ 1	weak	0.0%	3.7
C 4476	CZ 1206	TRP 117	hum_ 1	weak	0.0%	3.8
C 4478	CH 1210	TRP 117	hum_ 1	weak	0.0%	3.7
C 4478	CZ 1206	TRP 117	hum_ 1	weak	0.0%	3.8
C 4446	OD 1266	ASP 121	hum_ 1	weak	0.0%	4.3
C 4447	OD 1266	ASP 121	hum_ 1	weak	0.0%	3.3
C 4447	CG 1265	ASP 121	hum_ 1	weak	0.0%	4.4
C 4448	OD 1266	ASP 121	hum_ 1	weak	0.0%	3.0
C 4448	CG 1265	ASP 121	hum_ 1	weak	0.0%	4.3
N 4451	OD 1267	ASP 121	hum_ 1	weak	0.0%	4.3
N 4451	CG 1265	ASP 121	hum_ 1	weak	0.0%	3.5
N 4451	CB 1262	ASP 121	hum_ 1	weak	0.0%	4.4
C 4454	OD 1266	ASP 121	hum_ 1	weak	0.0%	3.1
C 4454	CG 1265	ASP 121	hum_ 1	weak	0.0%	4.1
C 4462	OD 1266	ASP 121	hum_ 1	weak	0.0%	3.5
C 4462	CG 1265	ASP 121	hum_ 1	weak	0.0%	4.3
C 4462	CB 1262	ASP 121	hum_ 1	weak	0.0%	4.5
C 4434	CG 1280	VAL 122	hum_ 1	weak	0.0%	4.0
C 4436	CG 1280	VAL 122	hum_ 1	weak	0.0%	4.1
O 4437	CG 1280	VAL 122	hum_ 1	weak	0.0%	4.1
O 4437	CG 1276	VAL 122	hum_ 1	weak	0.0%	3.8
C 4442	CZ 2546	PHE 201	hum_ 1	weak	0.0%	3.9
C 4442	CE 2544	PHE 201	hum_ 1	weak	0.0%	3.9
C 4444	CZ 2546	PHE 201	hum_ 1	weak	0.0%	3.7
C 4444	CE 2544	PHE 201	hum_ 1	weak	0.0%	3.7
C 4446	CZ 2546	PHE 201	hum_ 1	weak	0.0%	4.4
C 4448	CZ 2546	PHE 201	hum_ 1	weak	0.0%	4.2
C 4448	CE 2542	PHE 201	hum_ 1	weak	0.0%	4.0
C 4448	CD 2538	PHE 201	hum_ 1	weak	0.0%	4.4
C 4462	CE 2542	PHE 201	hum_ 1	weak	0.0%	4.0
C 4462	CD 2538	PHE 201	hum_ 1	weak	0.0%	4.04
O 4440	OG 2695	SER 211	hum_ 1	weak	0.0%	3.45
O 4440	CB 2692	SER 211	hum_ 1	weak	0.0%	3.73
O 4440	C 2690	SER 211	hum_ 1	weak	0.0%	3.84
C 4436	OG 2706	SER 212	hum_ 1	weak	0.0%	4.42
C 4439	OG 2706	SER 212	hum_ 1	weak	0.0%	3.22
C 4439	CB 2703	SER 212	hum_ 1	weak	0.0%	4.34
C 4439	CA 2699	SER 212	hum_ 1	weak	0.0%	4.38
O 4440	CB 2703	SER 212	hum_ 1	weak	0.0%	3.33
O 4440	CA 2699	SER 212	hum_ 1	weak	0.0%	3.16
O 4440	N 2697	SER 212	hum_ 1	weak	0.0%	3.26
C 4442	OG 2706	SER 212	hum_ 1	weak	0.0%	3.40
C 4436	OG 2755	SER 215	hum_ 1	weak	0.0%	3.92
O 4437	CB 2752	SER 215	hum_ 1	weak	0.0%	3.36
O 4440	OG 2755	SER 215	hum_ 1	weak	0.0%	3.89
C 4442	CE 3559	PHE 306	hum_ 1	weak	0.0%	4.07
C 4444	CZ 3561	PHE 306	hum_ 1	weak	0.0%	3.65
C 4444	CE 3559	PHE 306	hum_ 1	weak	0.0%	3.63
C 4446	CZ 3561	PHE 306	hum_ 1	weak	0.0%	4.05
C 4446	CE 3559	PHE 306	hum_ 1	weak	0.0%	3.99
C 4447	CZ 3561	PHE 306	hum_ 1	weak	0.0%	3.95
C 4447	CE 3559	PHE 306	hum_ 1	weak	0.0%	4.26
C 4436	CZ 3581	PHE 307	hum_ 1	weak	0.0%	4.13
C 4436	CE 3579	PHE 307	hum_ 1	weak	0.0%	4.25
O 4437	CZ 3581	PHE 307	hum_ 1	weak	0.0%	4.08
O 4437	CE 3579	PHE 307	hum_ 1	weak	0.0%	4.34
C 4439	CE 3579	PHE 307	hum_ 1	weak	0.0%	4.17
O 4440	CE 3579	PHE 307	hum_ 1	weak	0.0%	4.17
C 4442	OD 3628	ASN 310	hum_ 1	weak	0.0%	3.89
C 4447	OD 3947	ASN 329	hum_ 1	weak	0.0%	3.24
C 4447	CG 3946	ASN 329	hum_ 1	weak	0.0%	4.34
C 4448	OD 3947	ASN 329	hum_ 1	weak	0.0%	3.34
N 4451	ND 3948	ASN 329	hum_ 1	weak	0.0%	4.16
N 4451	CG 3946	ASN 329	hum_ 1	weak	0.0%	3.72
C 4454	OD 3947	ASN 329	hum_ 1	weak	0.0%	3.55
C 4454	CG 3946	ASN 329	hum_ 1	weak	0.0%	4.42
C 4455	OD 3947	ASN 329	hum_ 1	weak	0.0%	3.55
C 4455	CG 3946	ASN 329	hum_ 1	weak	0.0%	4.33
C 4456	ND 3948	ASN 329	hum_ 1	weak	0.0%	4.23
C 4456	OD 3947	ASN 329	hum_ 1	weak	0.0%	3.07
C 4456	CG 3946	ASN 329	hum_ 1	weak	0.0%	3.45
C 4456	CB 3943	ASN 329	hum_ 1	weak	0.0%	3.78
C 4457	OD 3947	ASN 329	hum_ 1	weak	0.0%	4.43
C 4473	NE 3964	TRP 330	hum_ 1	weak	0.0%	4.08
C 4476	NE 3964	TRP 330	hum_ 1	weak	0.0%	3.58
C 4478	NE 3964	TRP 330	hum_ 1	weak	0.0%	3.89

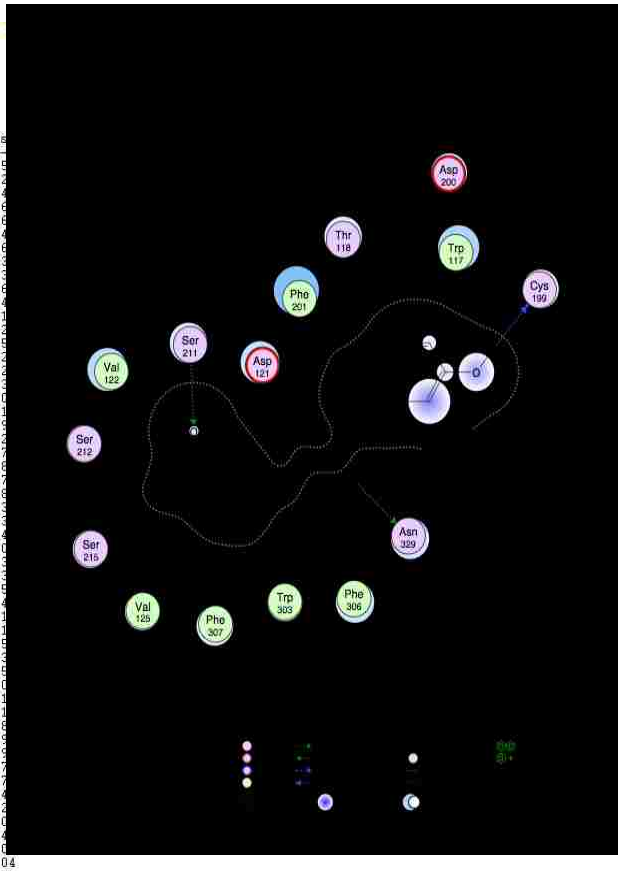

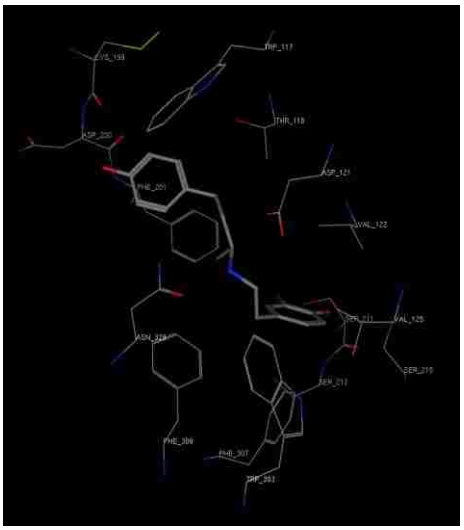

Bonding diagram

3D visualizing of bonding

Figure A-2 MOE bonding result of dobutamine on β_1 adrenergic receptor

Patient Data and Clinical Condition

Patient No.	Age	Sex	Clinical Condition
1	68	F	Normal HR 20 – 40 mics of Dobutamine, no ischemia
2	77	F	HR 134 with 40 mics of Dobutamine and 5 mcg of Atropine, no ischemia
3	58	F	Normal systolic function, no ischemia
4	58	F	Normal Dobutamine echocardiographic study
5	79	F	90% HR at 30 mics of Dobutamine, patient on O_2 during test, LV hypertrophy

Figure A-3 Patient data and clinical condition

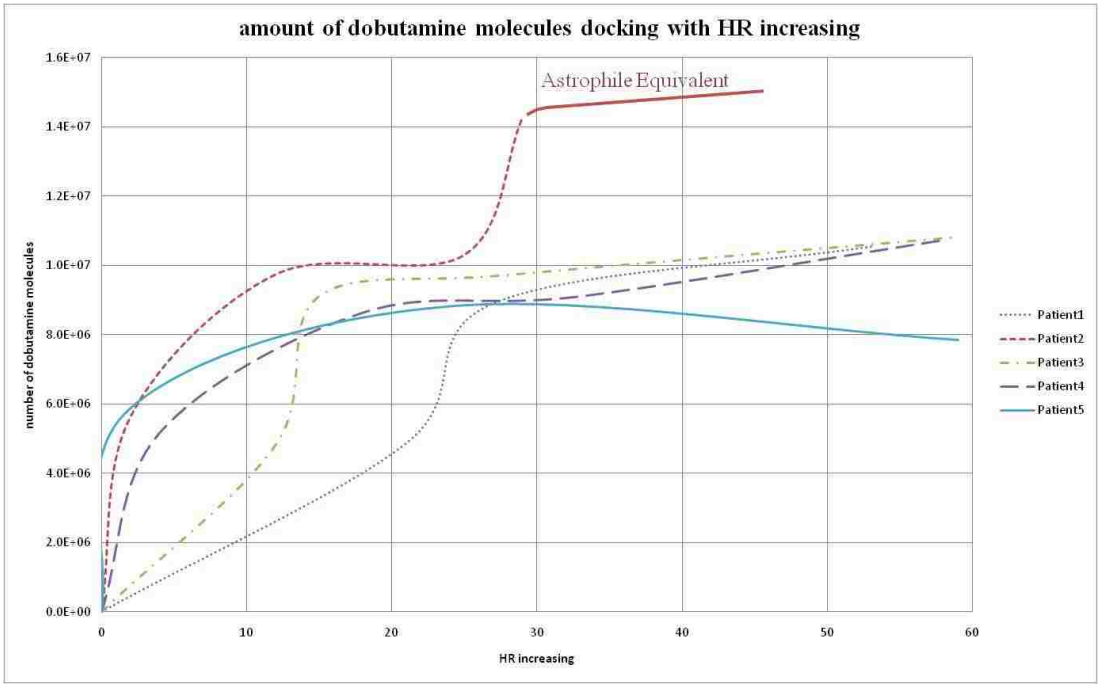

Figure A-4 Amount of dobutamine molecules docking with HR increasing

A.2 Electrical Signal Generated Result

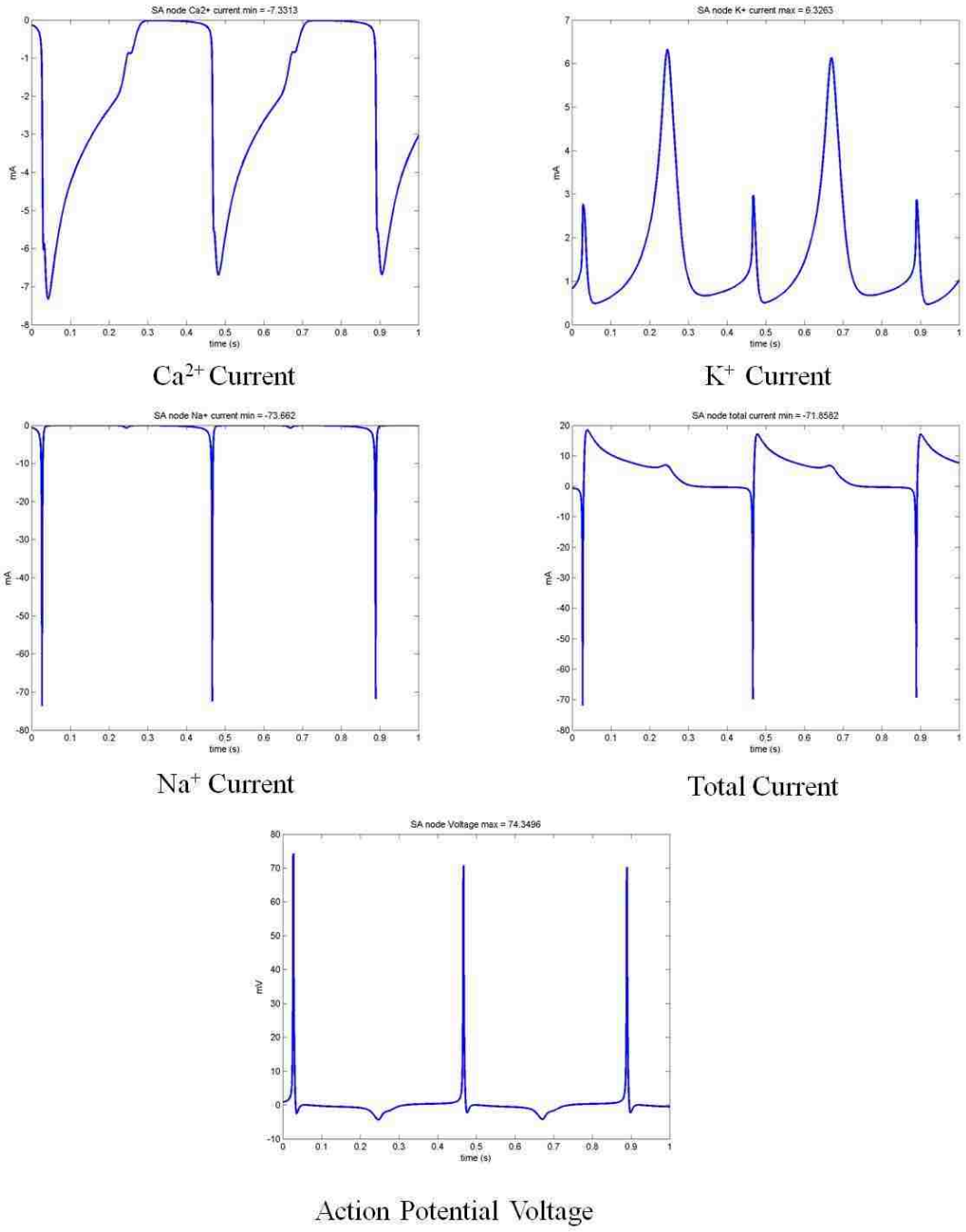

Figure A-5 Sinoatrial node currents and action potential results

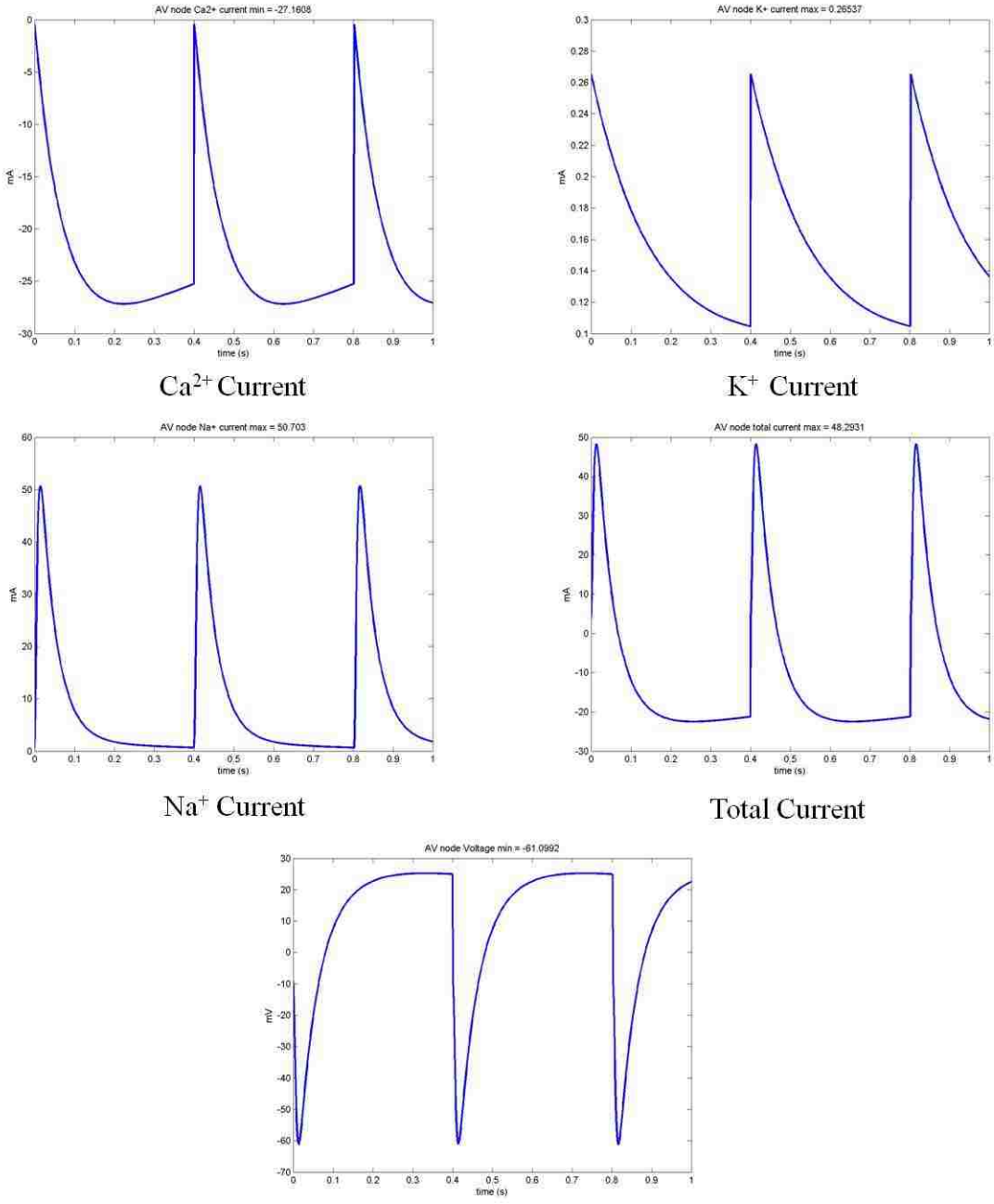

Figure A-6 Atrioventricular node currents and action potential results

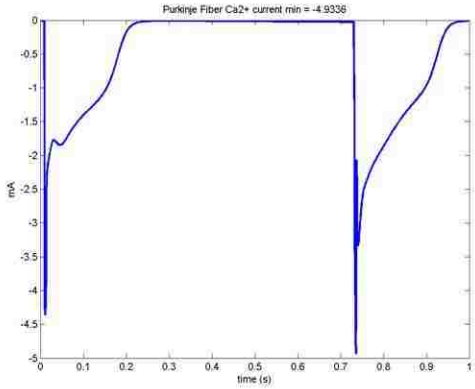

Ca^{2+} Current

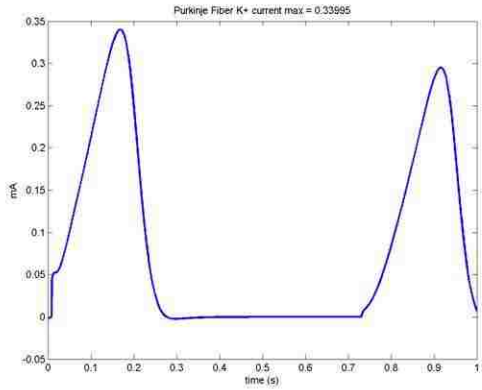

K^{+} Current

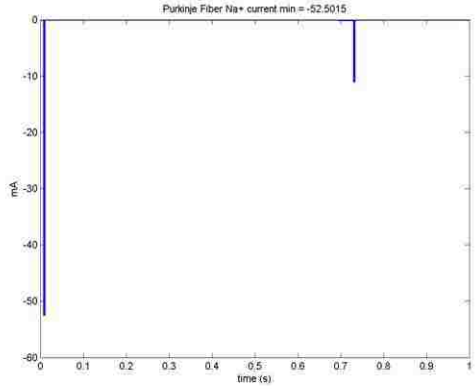

Na^{+} Current

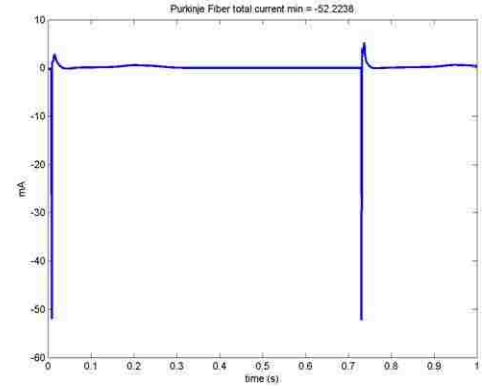

Total Current

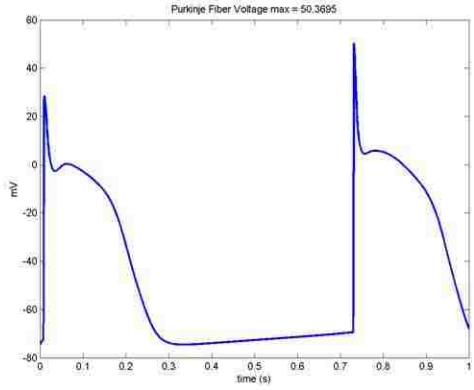

Action Potential Voltage

Figure A-7 Purkinji fiber currents and action potential results

A.3 Blood Flow and Stresses in the Left Ventricle Result

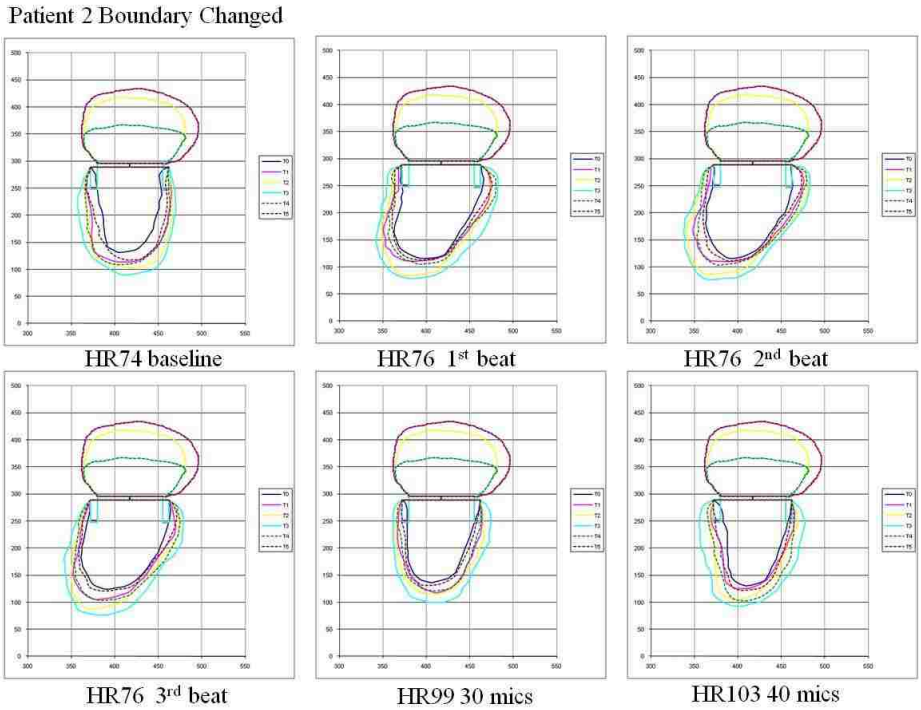

Figure A-8 Patient 1 boundary changed

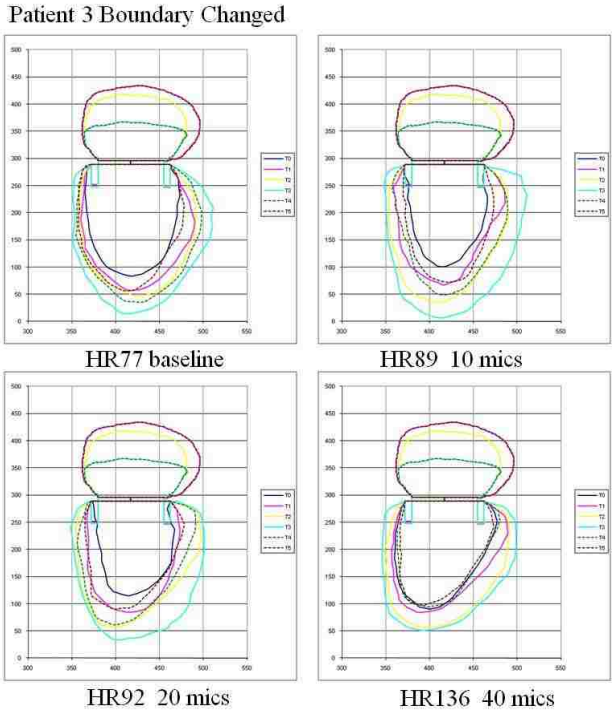

Figure A-9 Patient 2 boundary changed

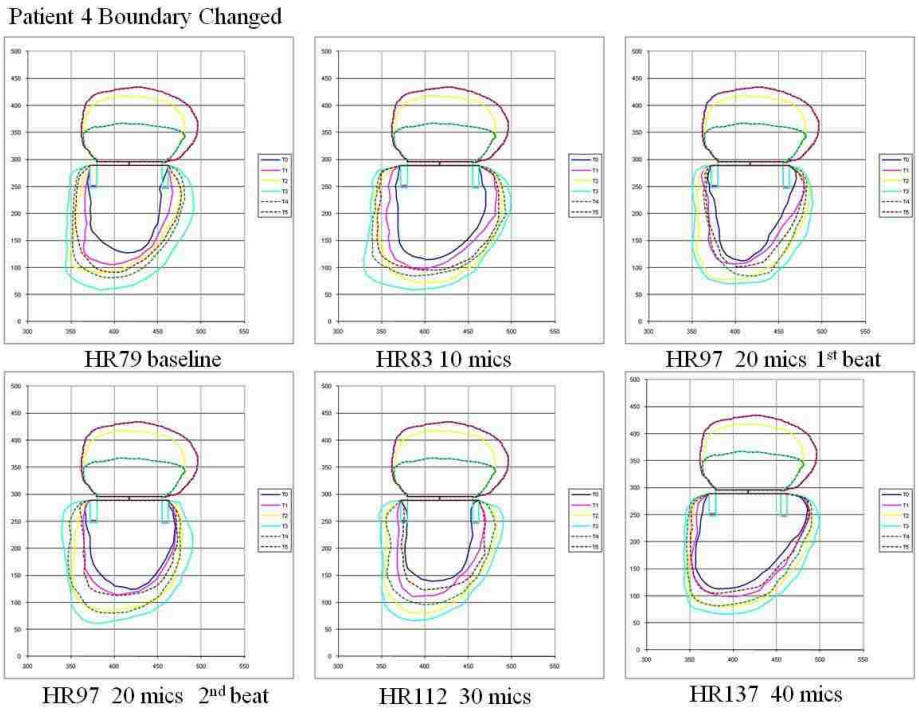

Figure A-10 Patient 3 boundary changed

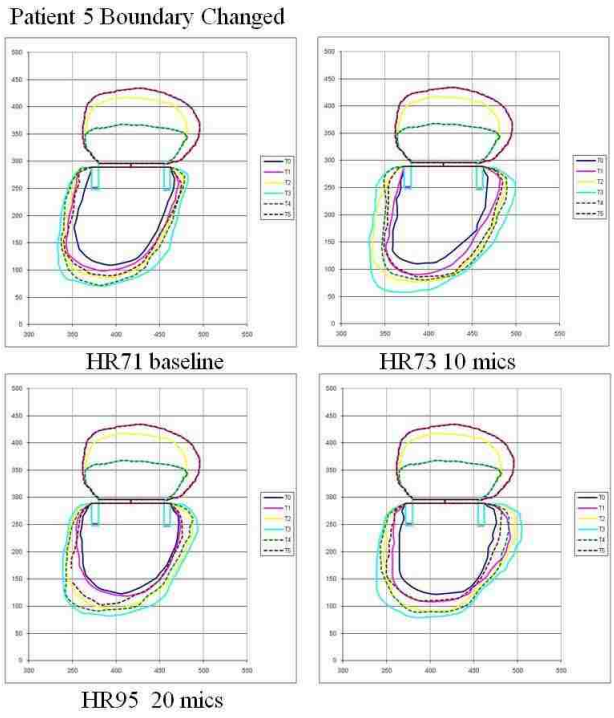

Figure A-11 Patient 4 boundary changed

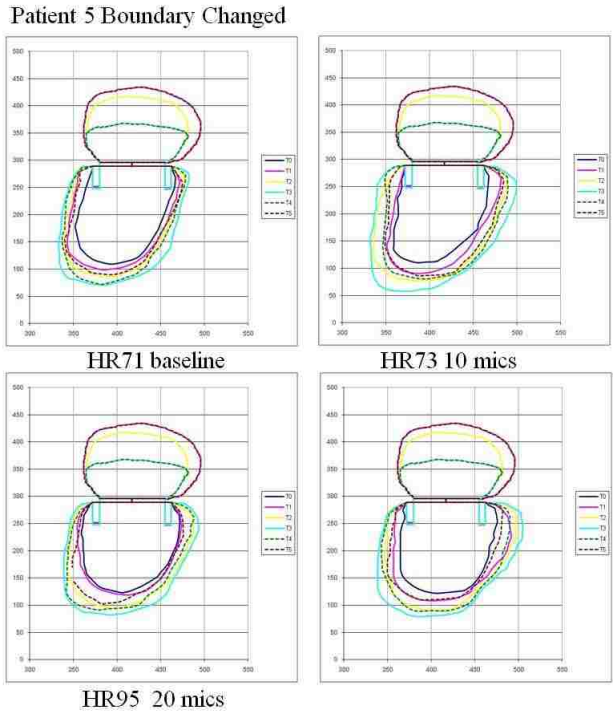

Figure A-12 Patient 5 boundary changed

mics	Patient1	Patient2	Patient3	Patient4	Patient5
0	13119.5000	9162.5000	15982.5000	16190.0000	10150.3750
10	22278.0000	9187.1667	22334.0000	16762.5000	14527.2500
20	21262.0000	8288.9161	18779.2500	16819.1535	12161.5000
30	17925.8750	7390.6655	16632.6667	15341.0000	10482.8750
35	14589.7500				
40		9348.7500	12339.5000	11563.5000	

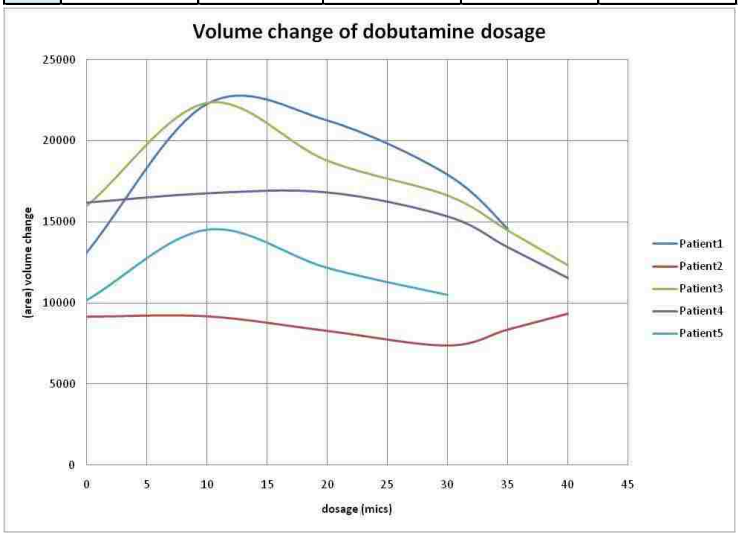

Figure A-13 Volume change with vary of dobutamine dosage

A.4 Fast Fourier Transform of Electroencephalogram Result

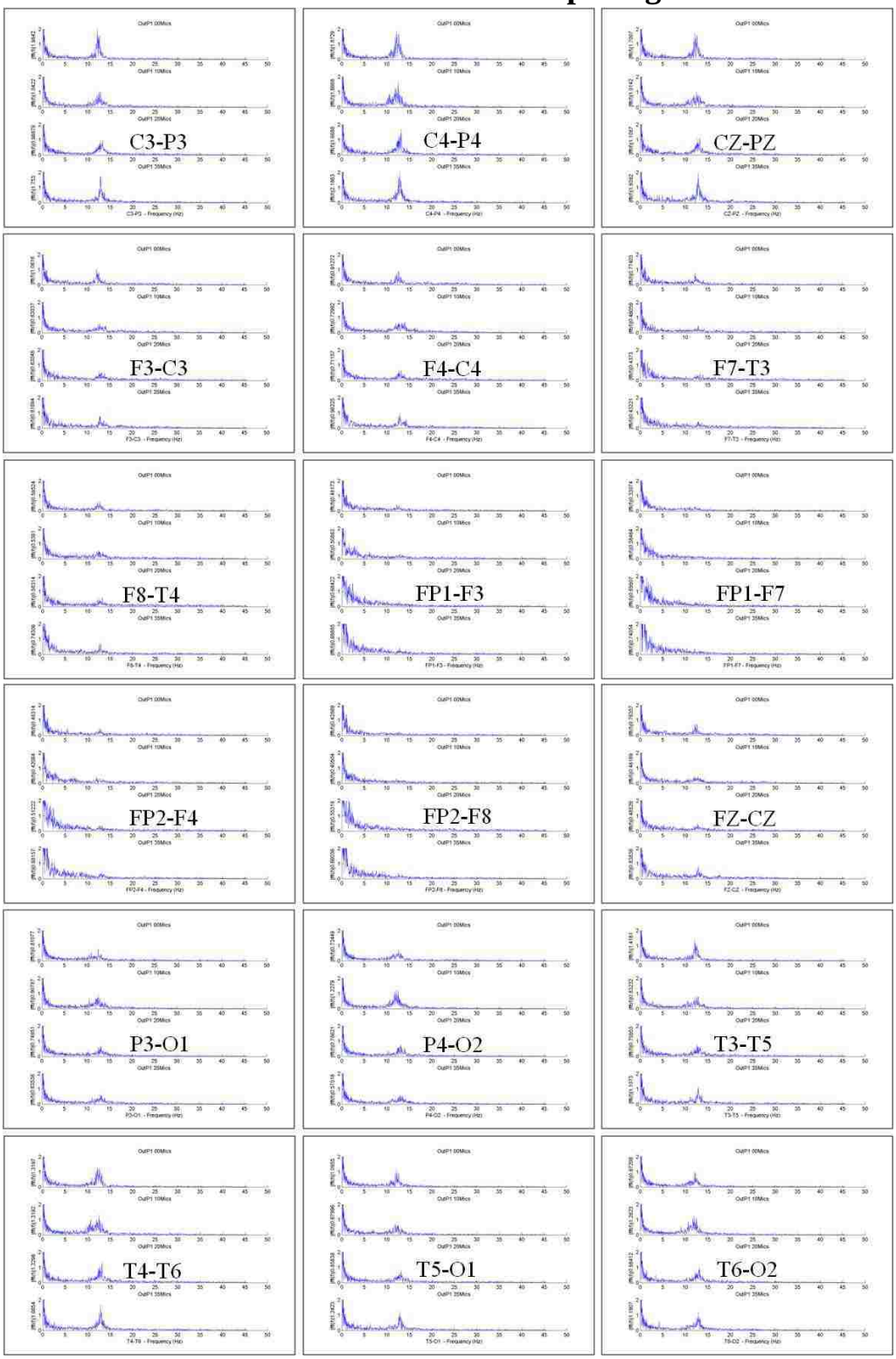

Figure A-14 Patient 1 fast Fourier transform of EEG result

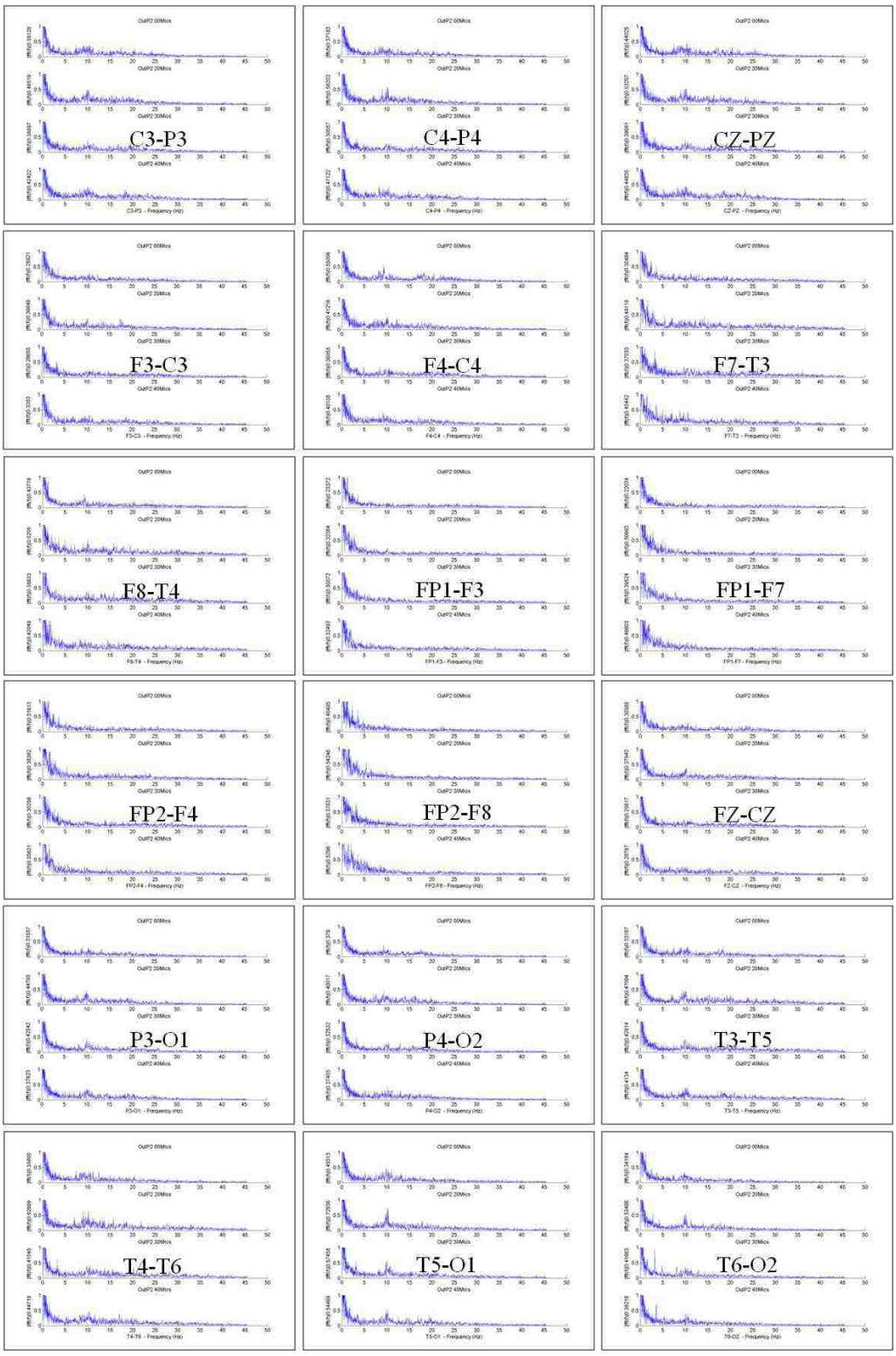

Figure A-15 Patient 2 fast Fourier transform of EEG result

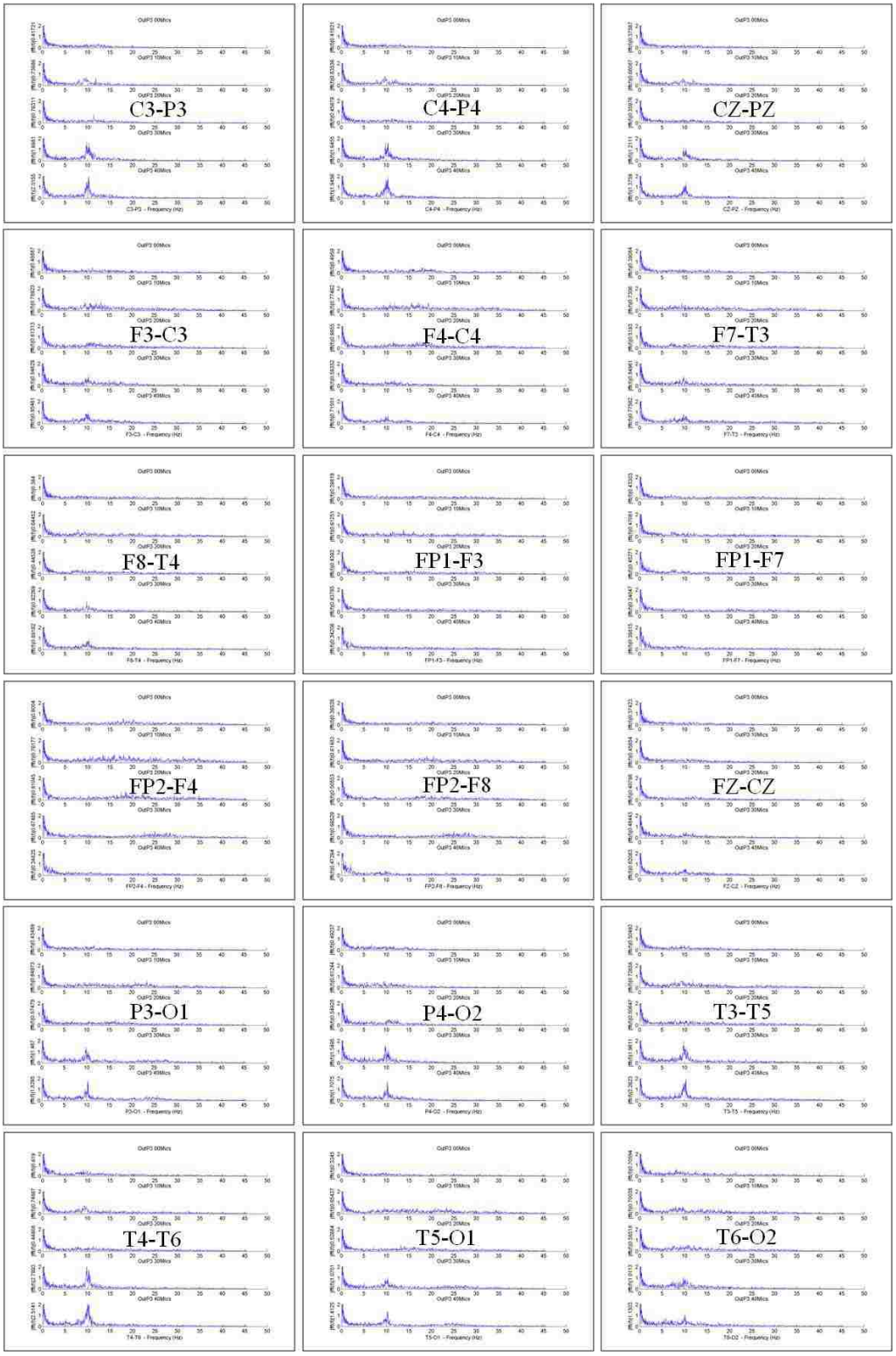

Figure A-16 Patient 3 fast Fourier transform of EEG result

Figure A-17 Patient 4 fast Fourier transform of EEG result

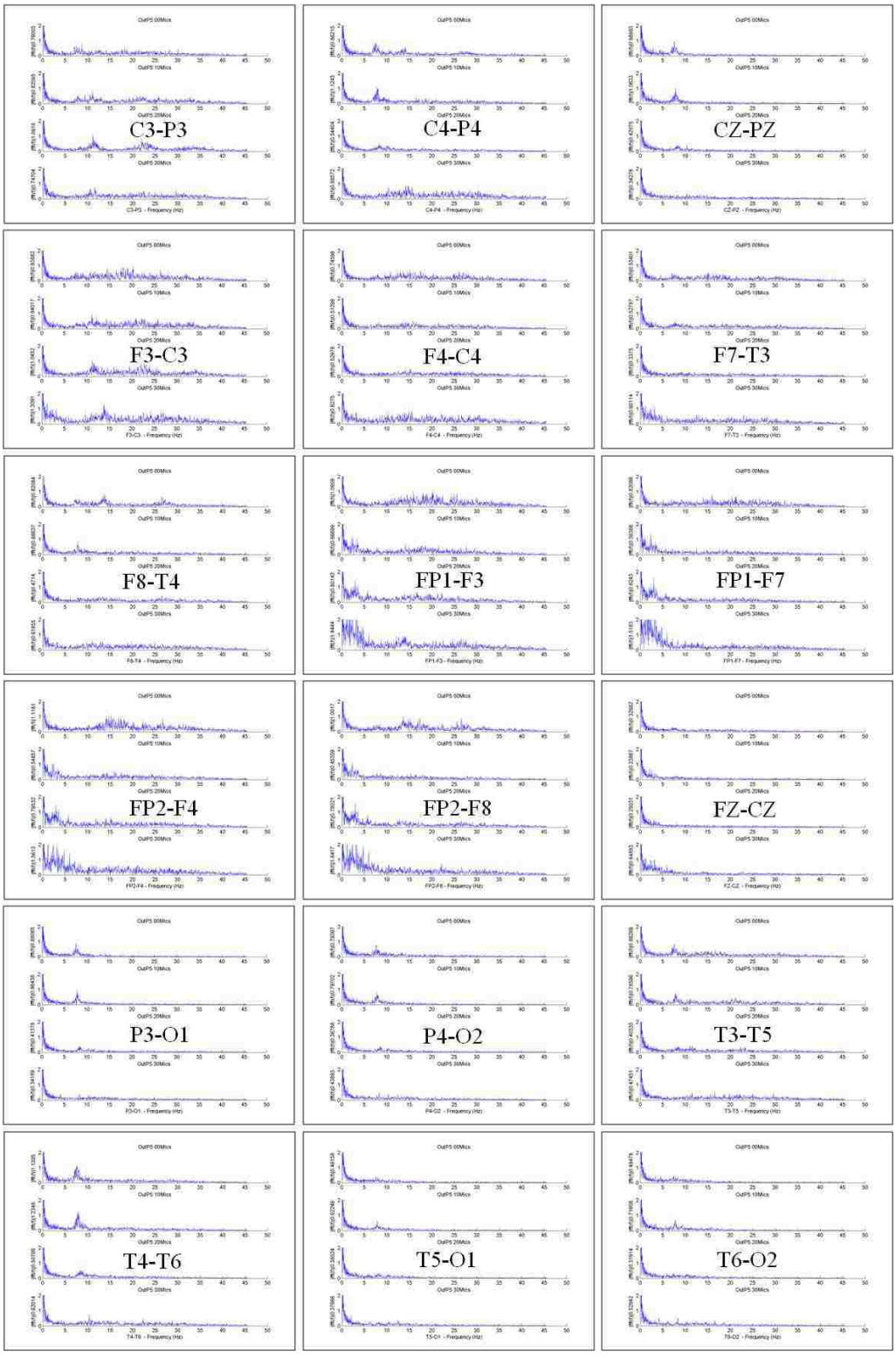

Figure A-18 Patient 5 fast Fourier transform of EEG result

A.5 Wavelet Analysis of Electroencephalogram Waves Result

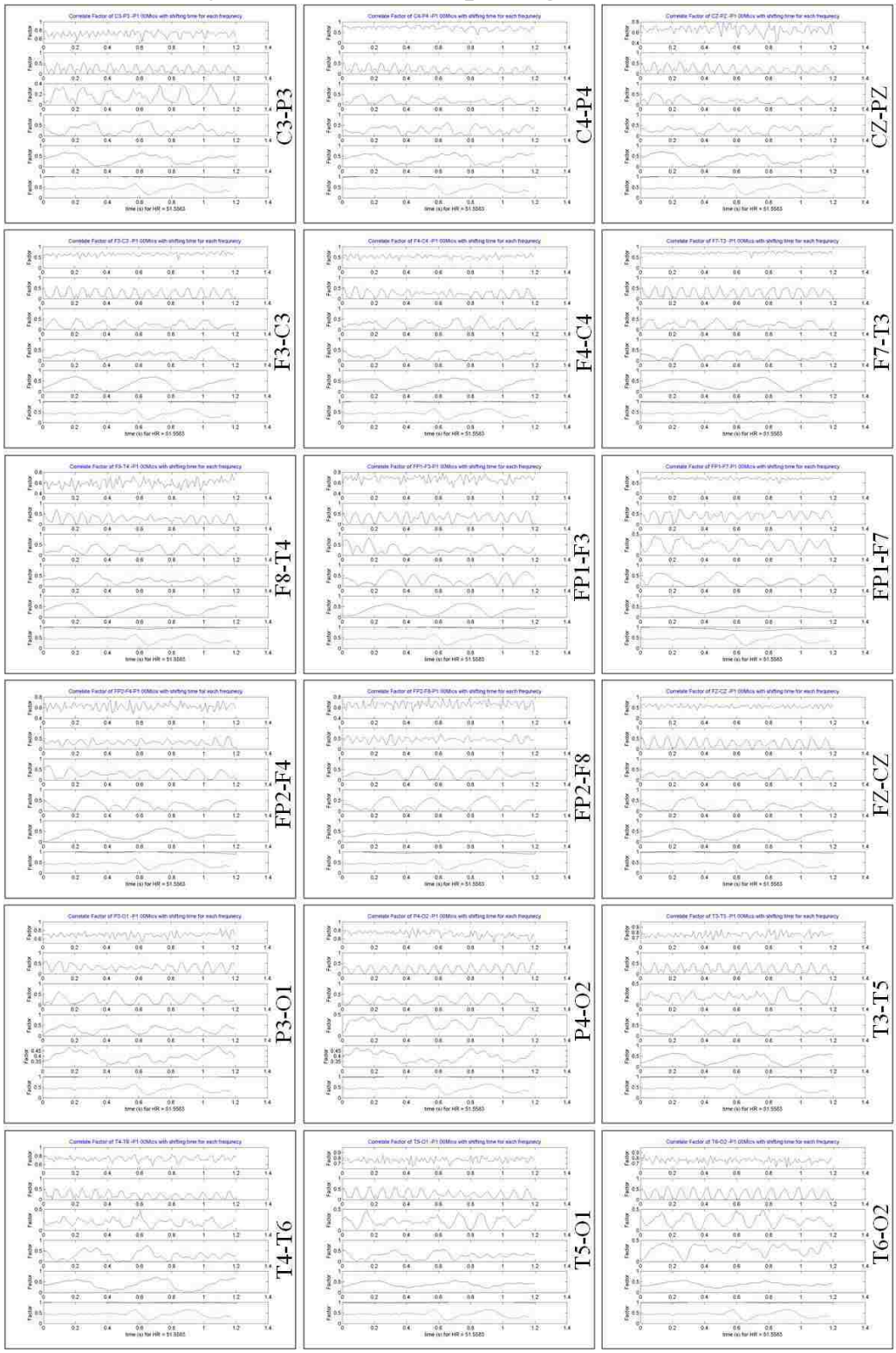

Figure A-19 Patient 1 wavelet transform of EEG with EKG correlation 0 mics

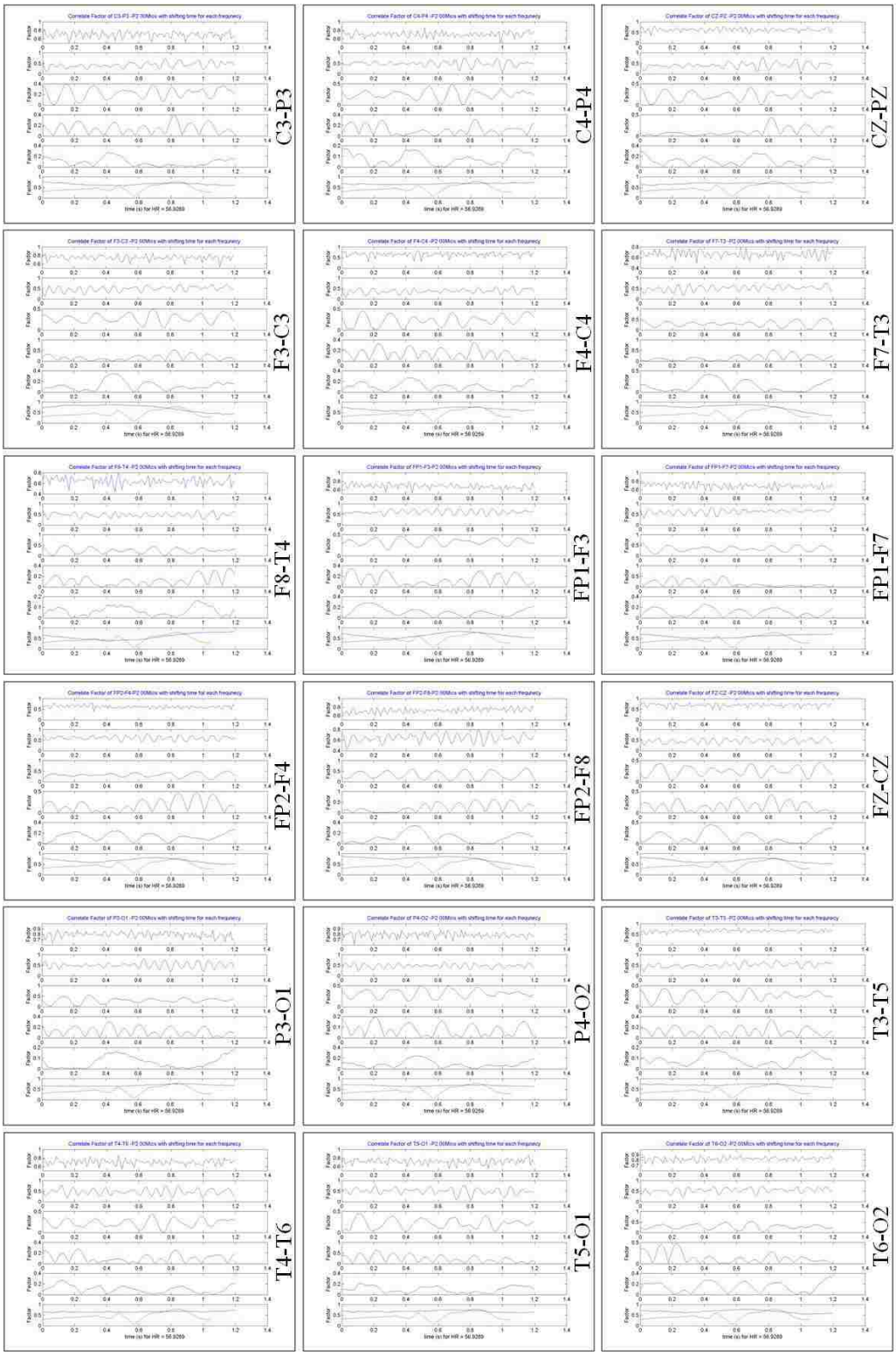

Figure A-20 Patient 2 wavelet transform of EEG with EKG correlation 0 mics

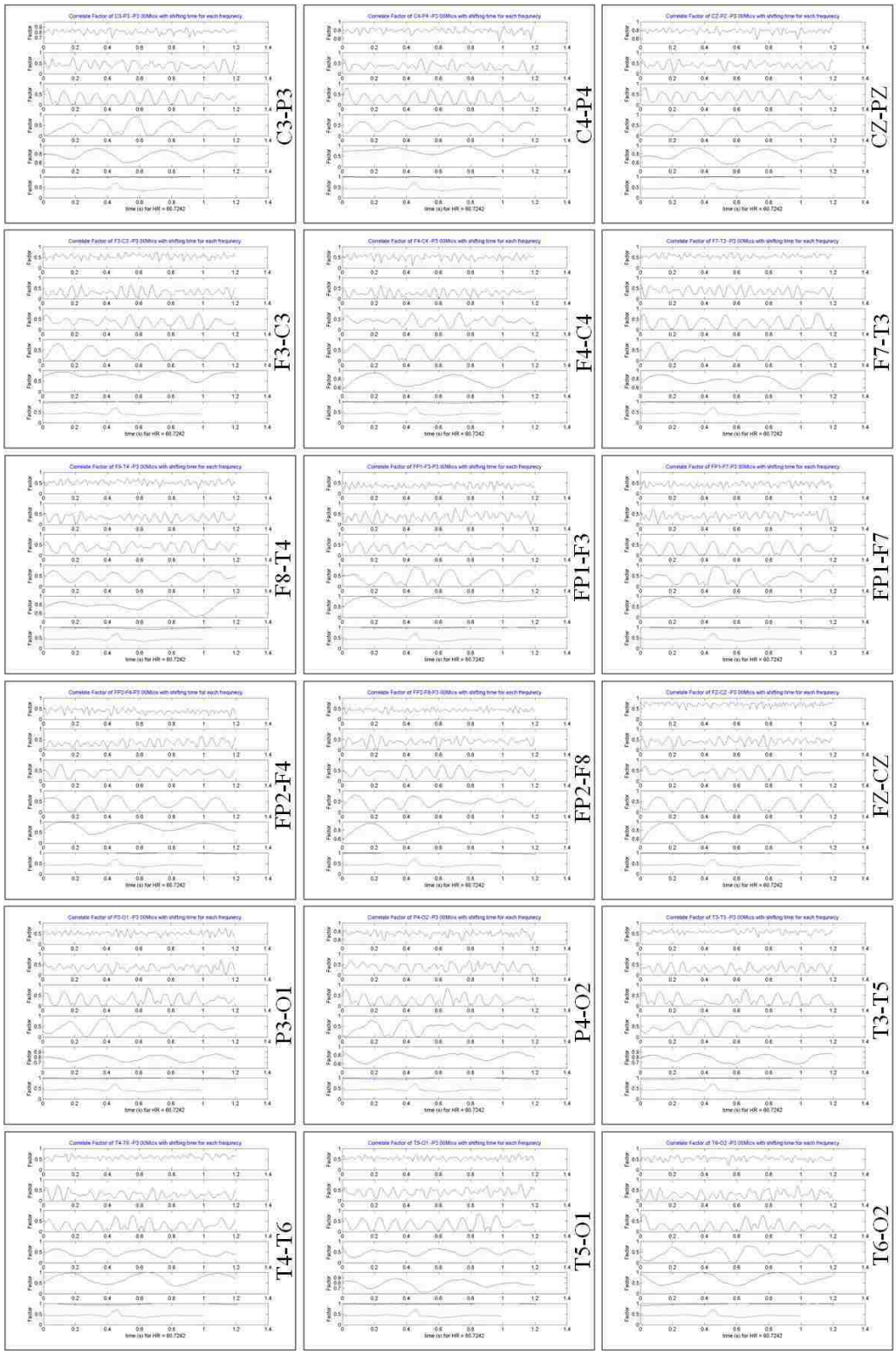

Figure A-21 Patient 3 wavelet transform of EEG with EKG correlation 0 mics

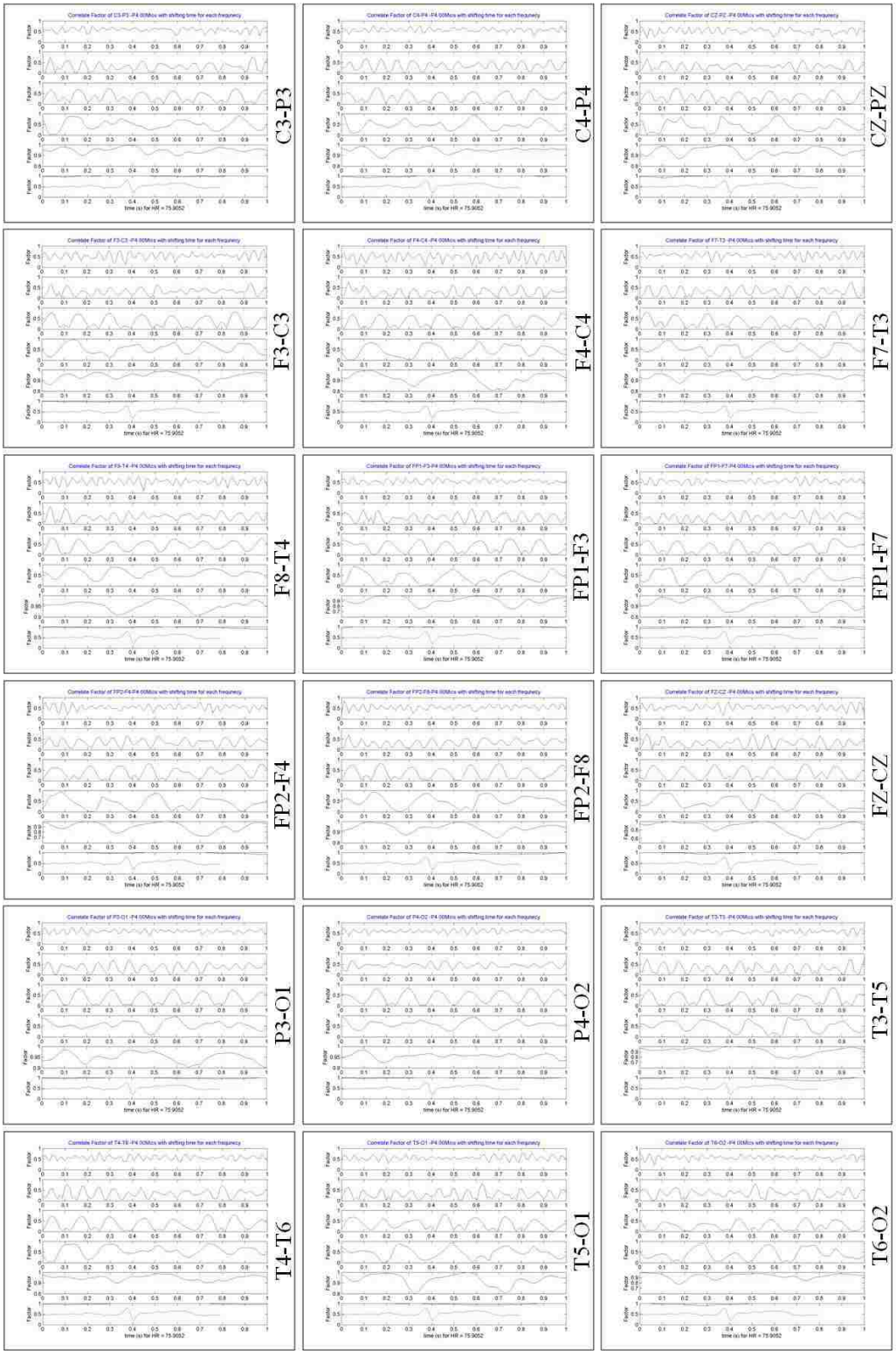

Figure A-22 Patient 4 wavelet transform of EEG with EKG correlation 0 mics

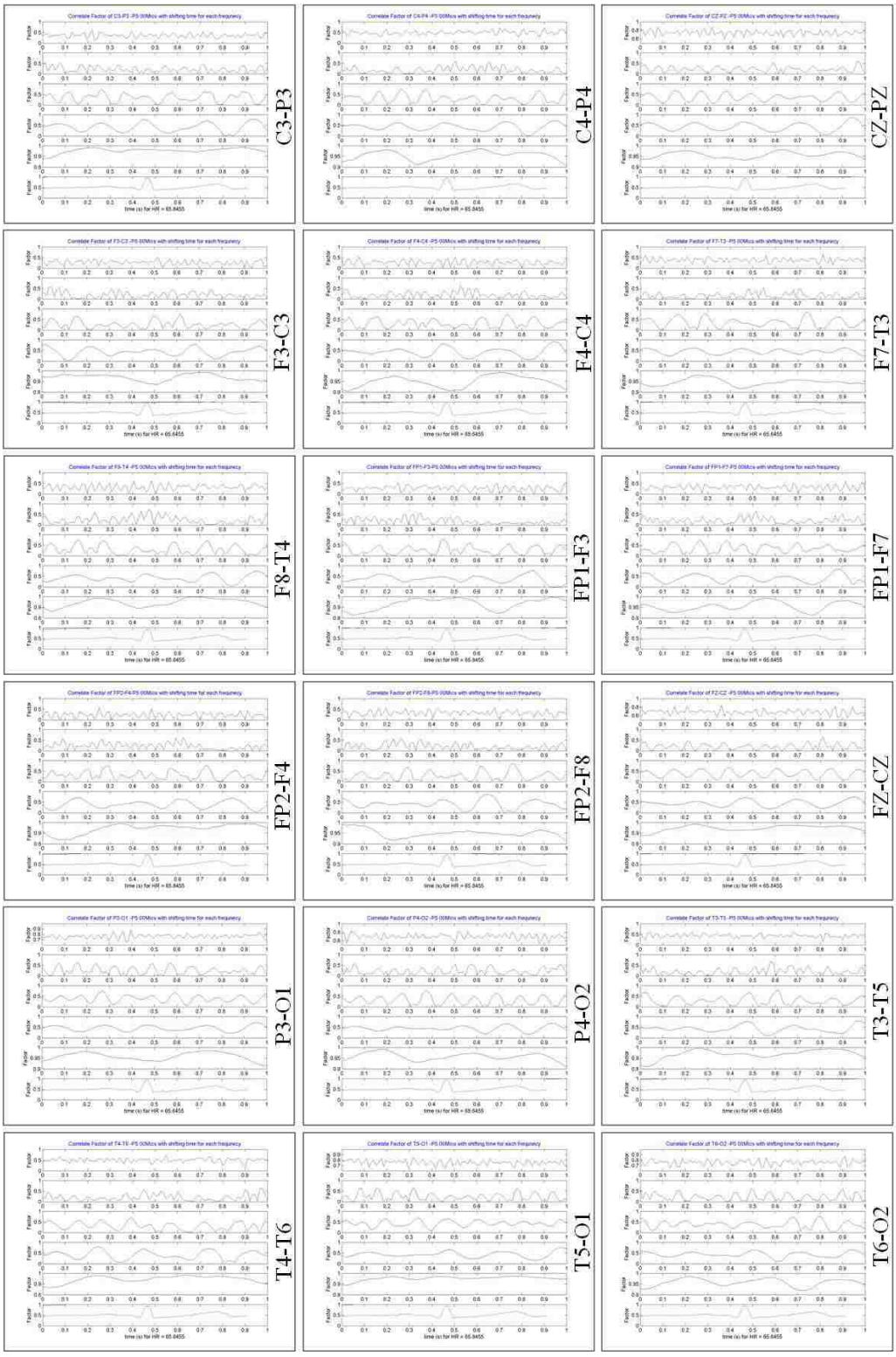

Figure A-23 Patient 5 wavelet transform of EEG with EKG correlation 0 mics

A.6 Correlation of Heart and Brain Data Result

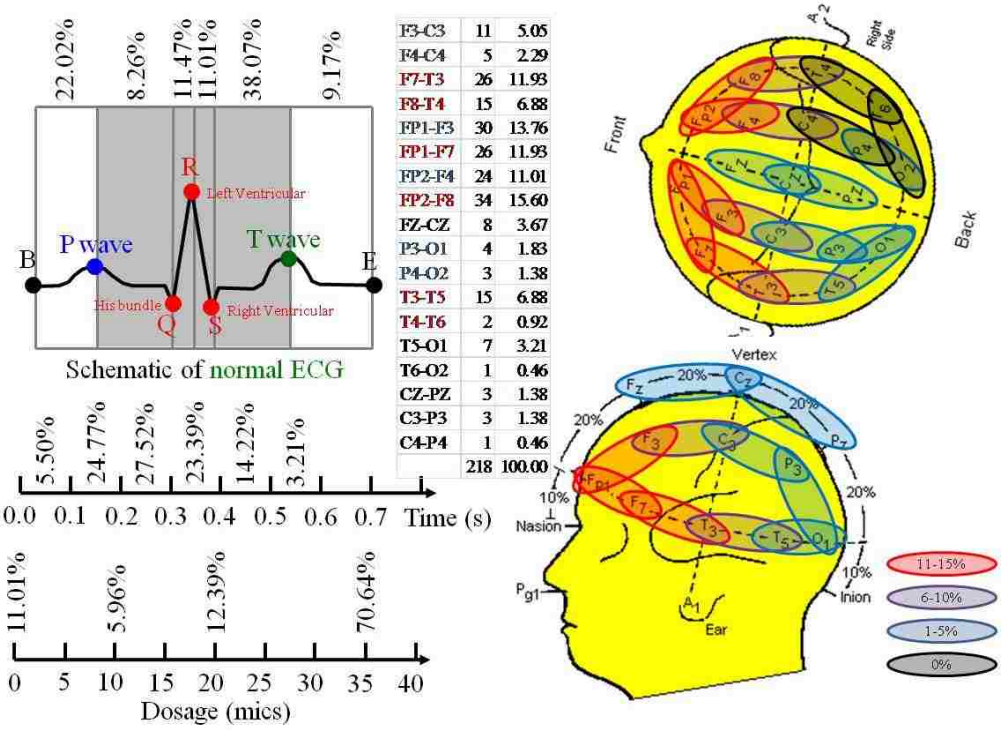

Figure A-24 Patient 1 EKG-EEG correlation result

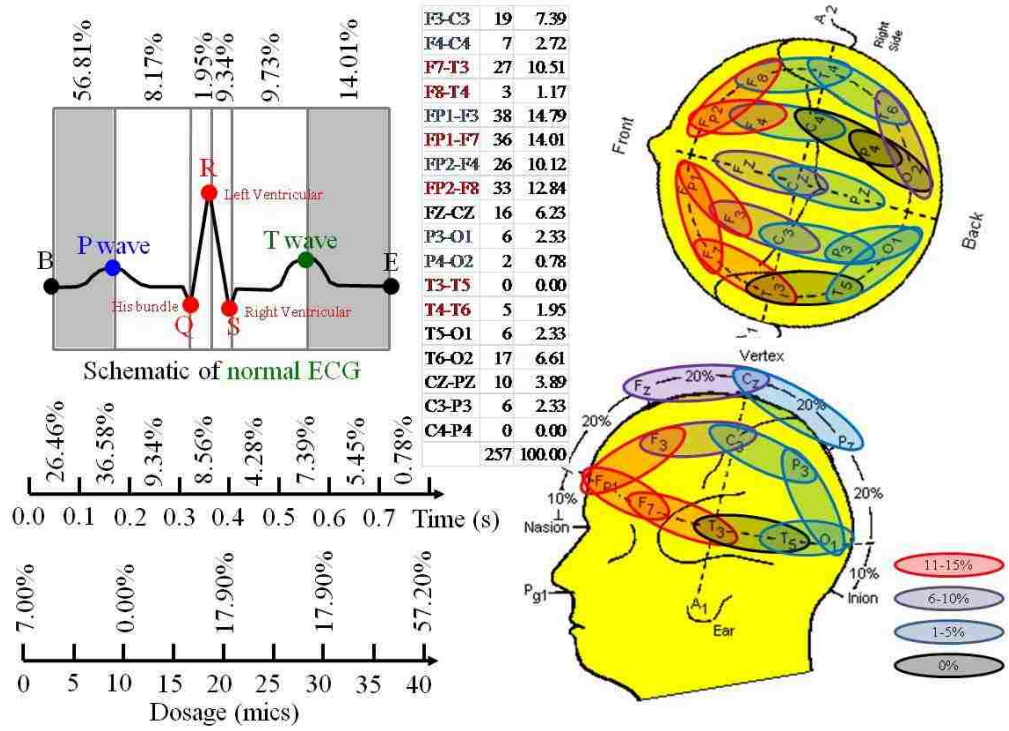

Figure A-25 Patient 2 EKG-EEG correlation result

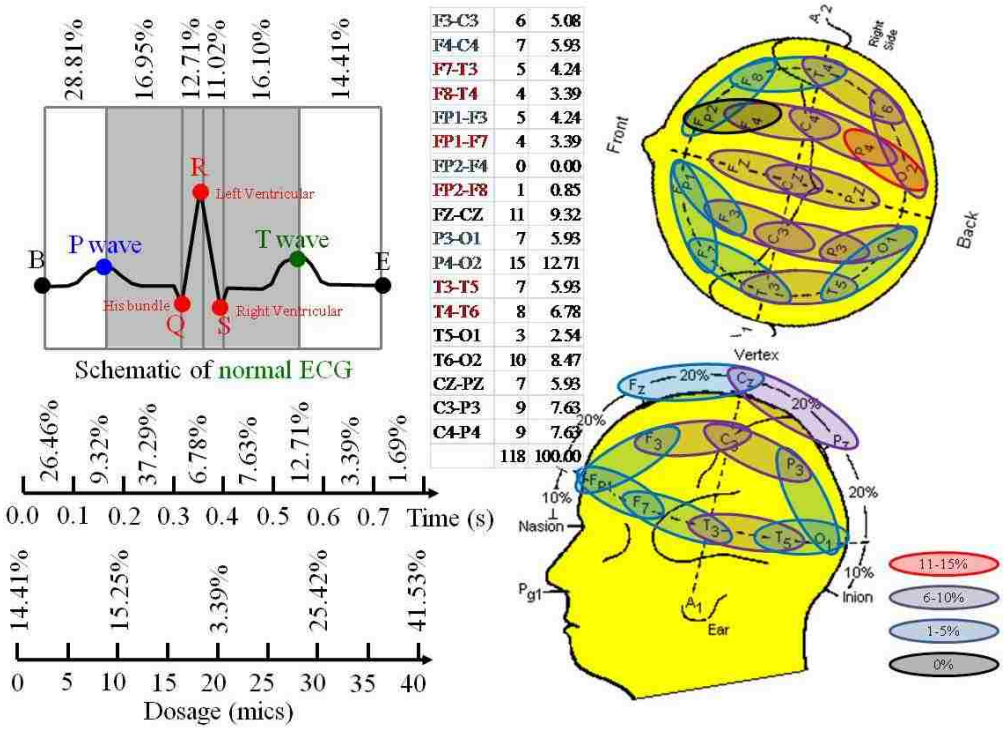

Figure A-26 Patient 3 EKG-EEG correlation result

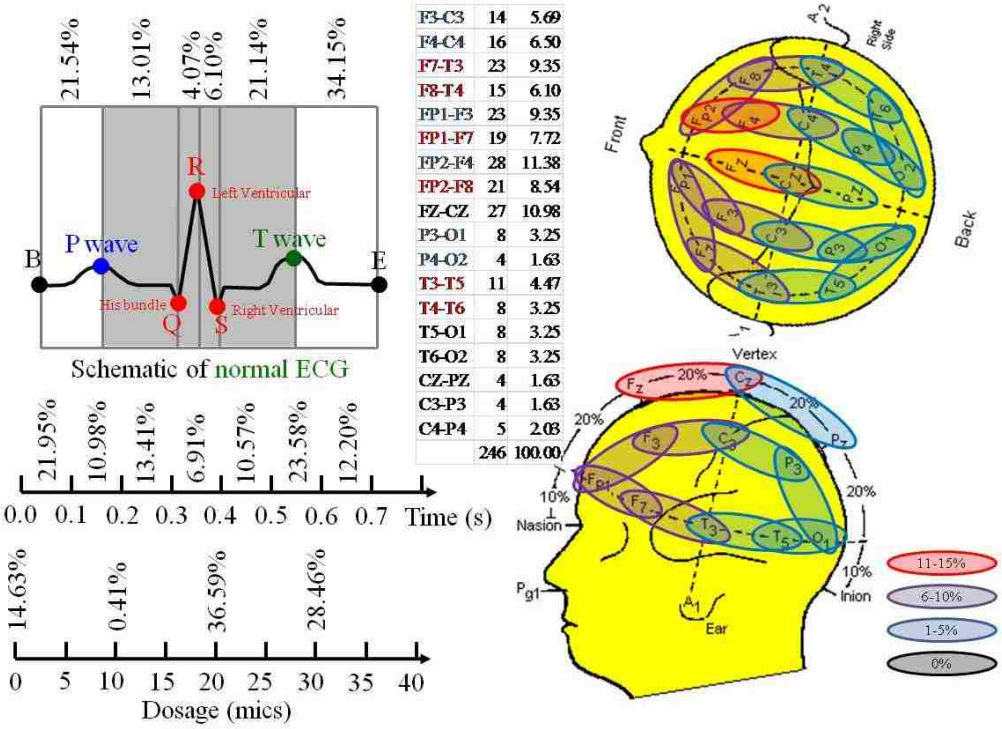

Figure A-27 Patient 4 EKG-EEG correlation result

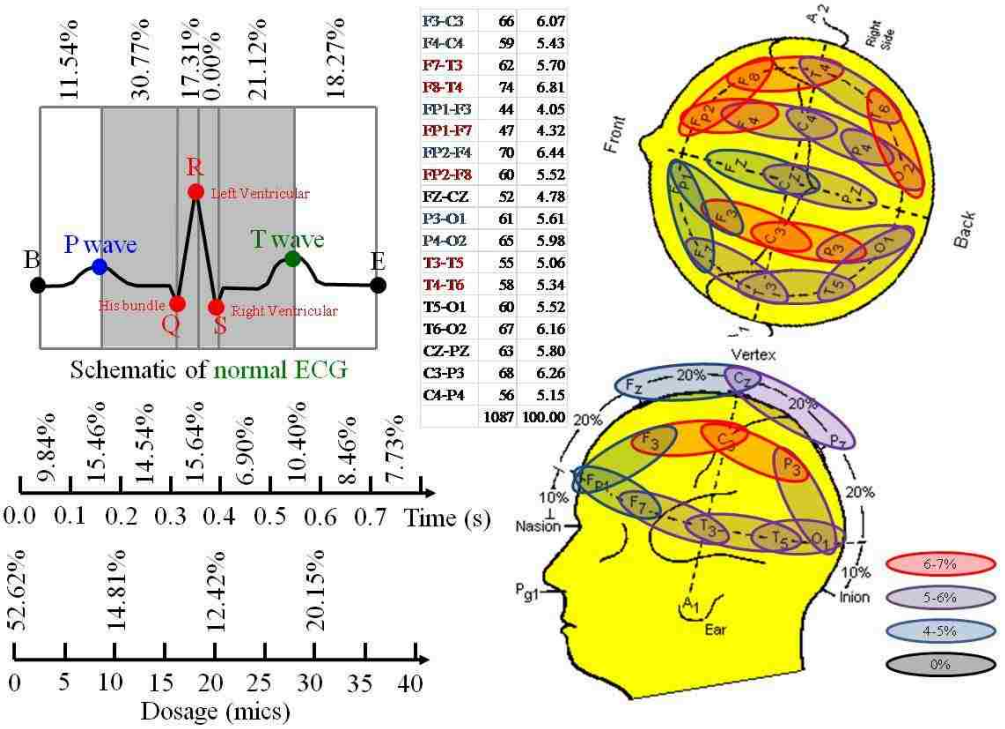

Figure A-28 Patient 5 EKG-EEG correlation result

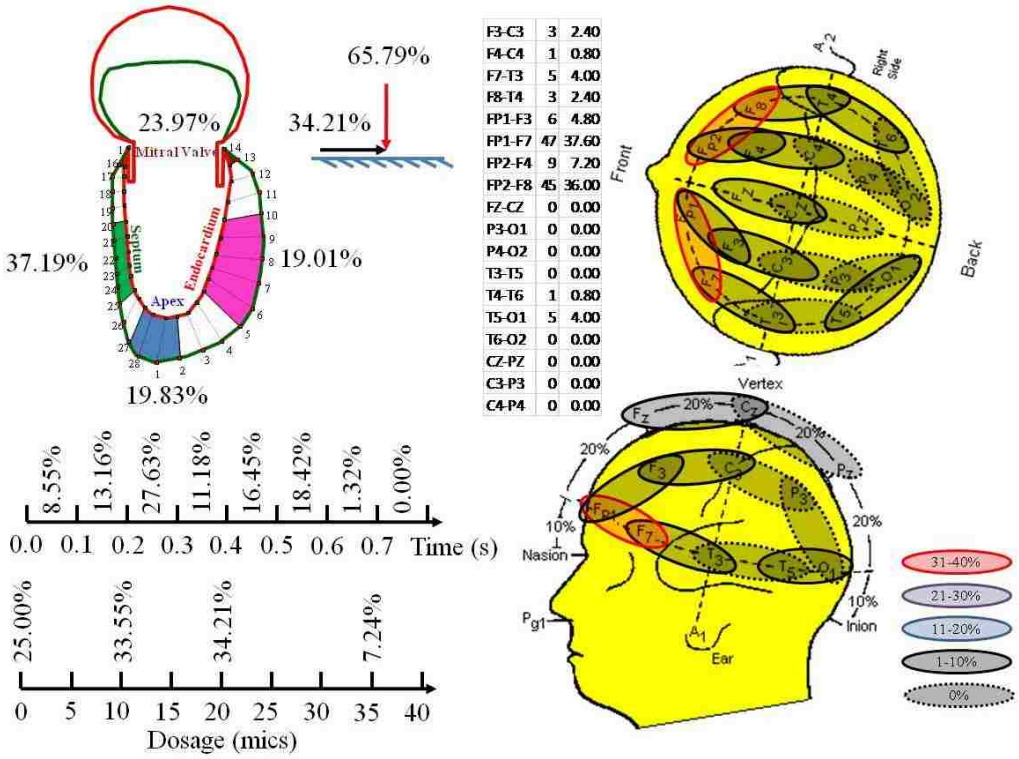

Figure A-29 Patient 1 heart stress-EEG correlation result

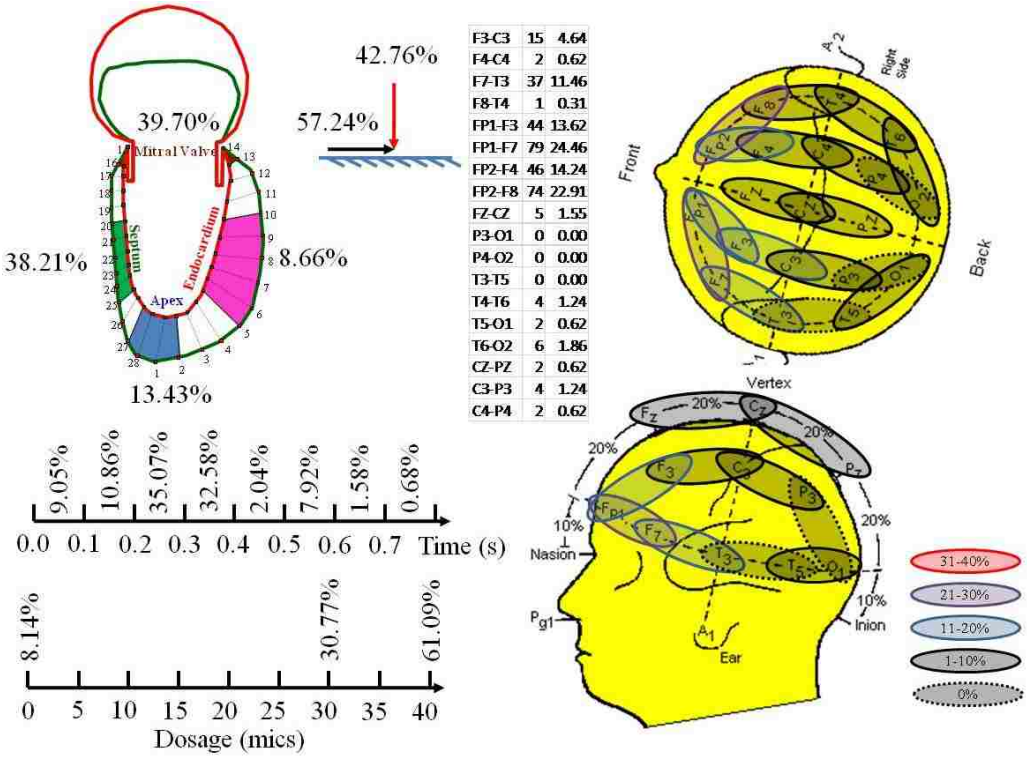

Figure A-30 Patient 2 heart stress-EEG correlation result

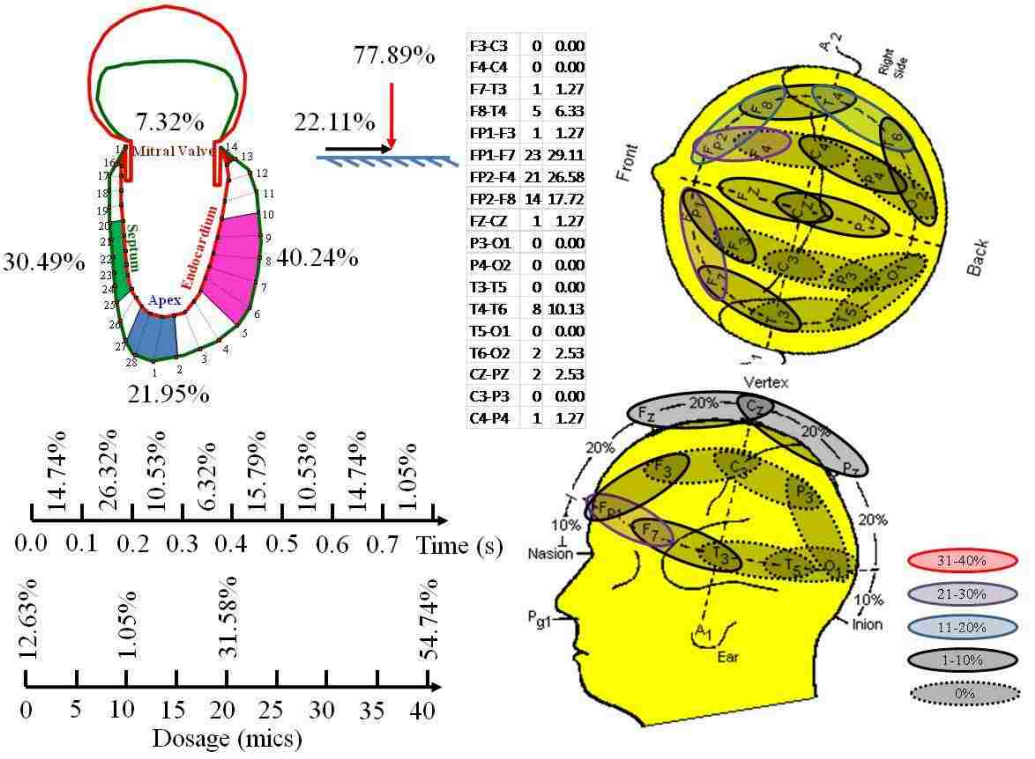

Figure A-31 Patient 3 heart stress-EEG correlation result

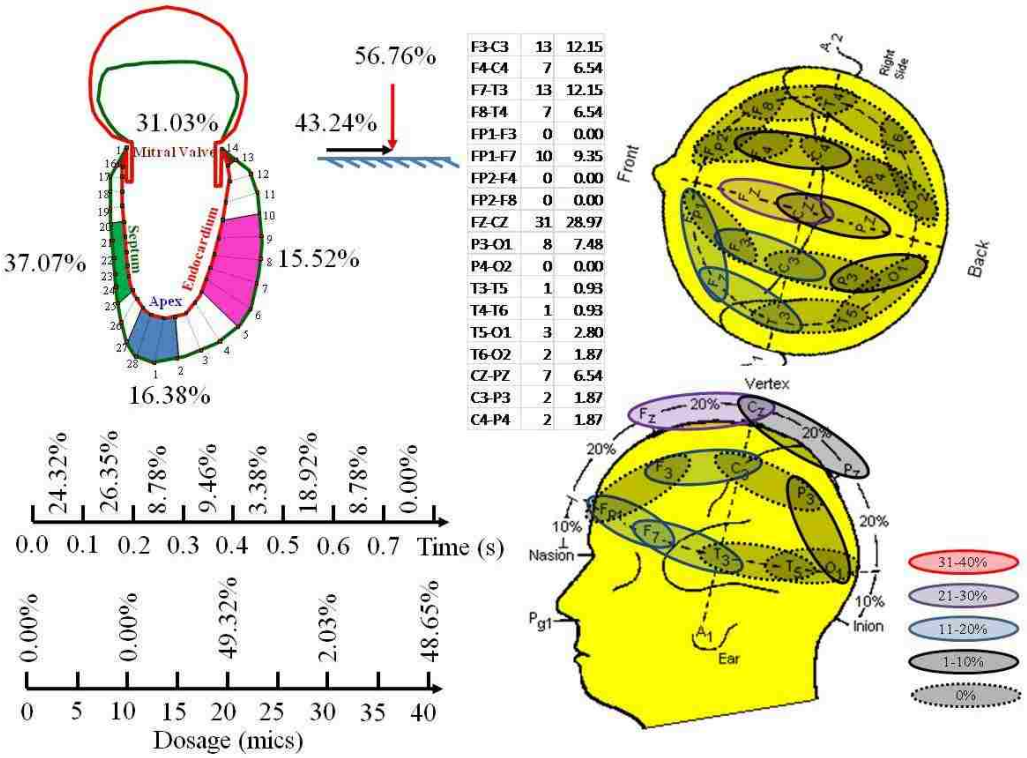

Figure A-32 Patient 4 heart stress-EEG correlation result

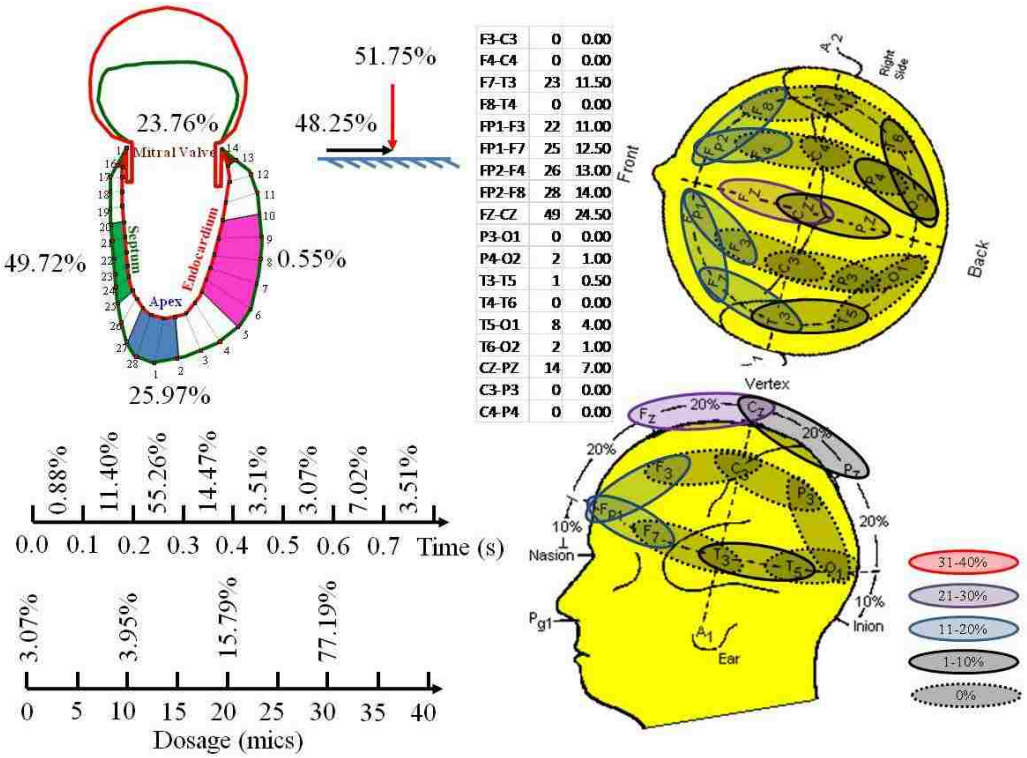

Figure A-33 Patient 5 heart stress-EEG correlation result

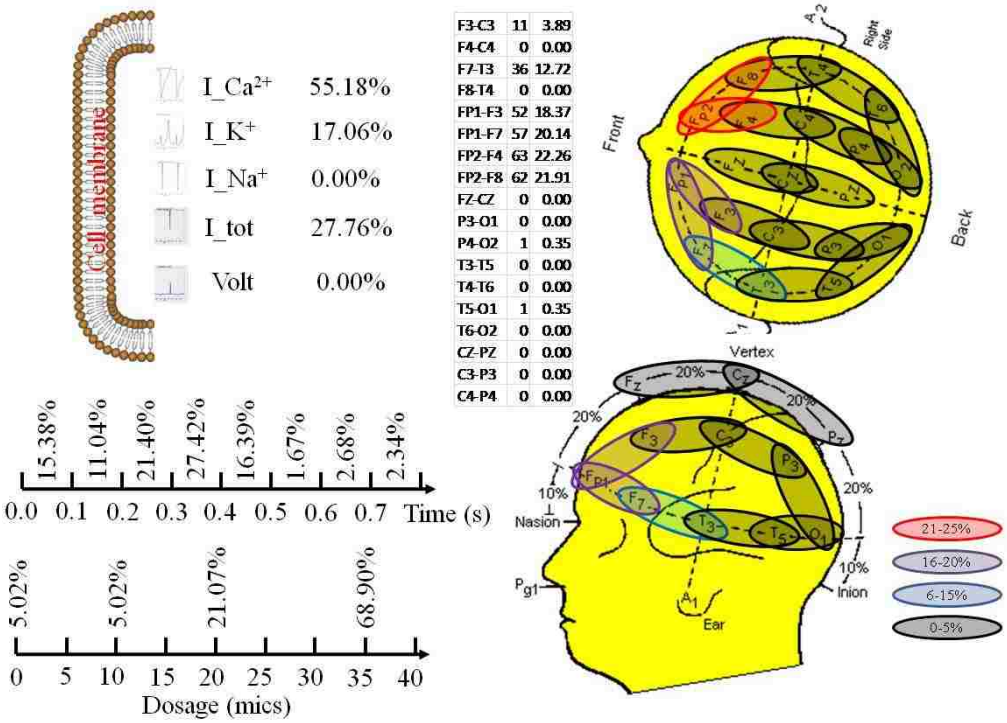

Figure A-34 Patient 1 SA node electrical-EEG correlation (CF > 0.5)

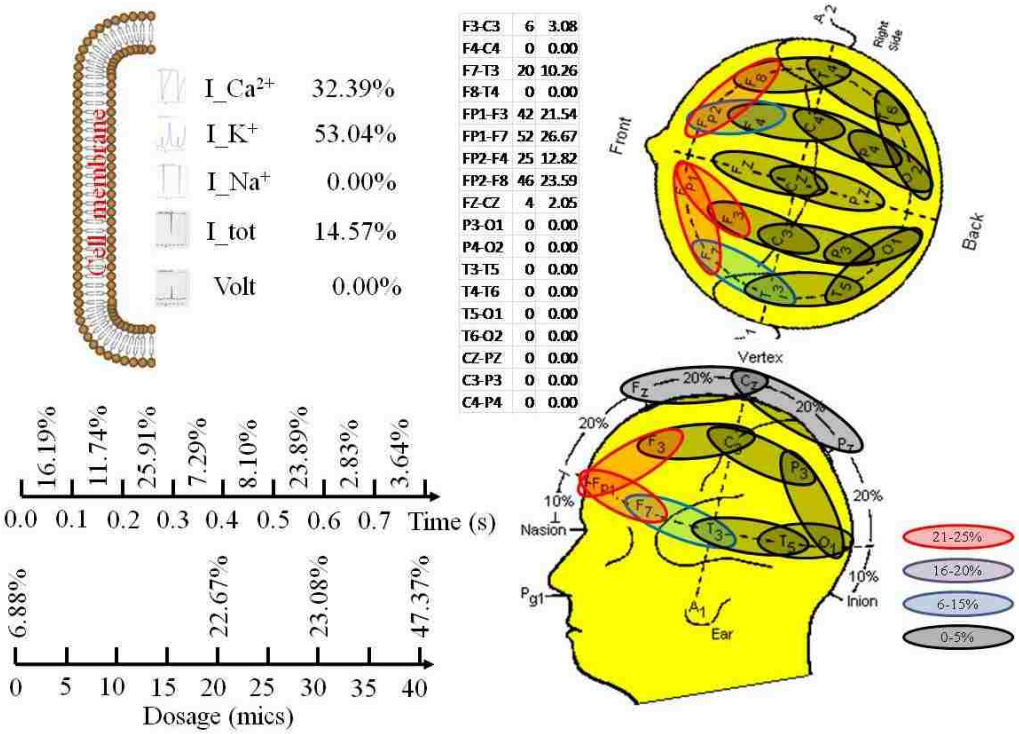

Figure A-35 Patient 2 SA node electrical-EEG correlation (CF > 0.5)

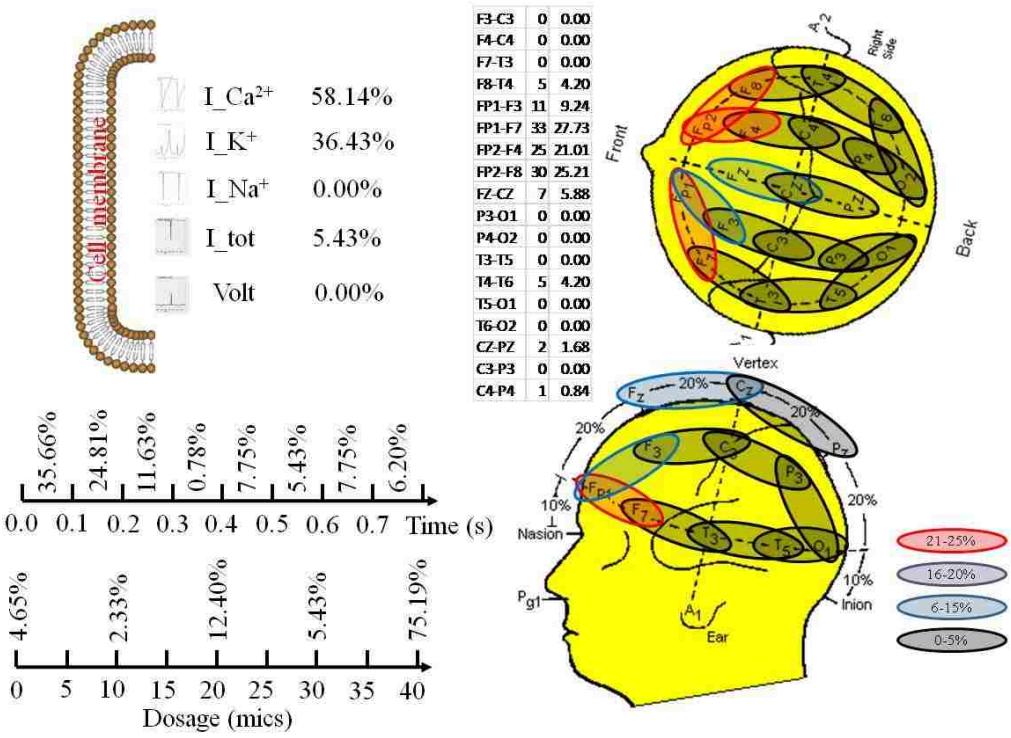

Figure A-36 Patient 3 SA node electrical-EEG correlation (CF > 0.5)

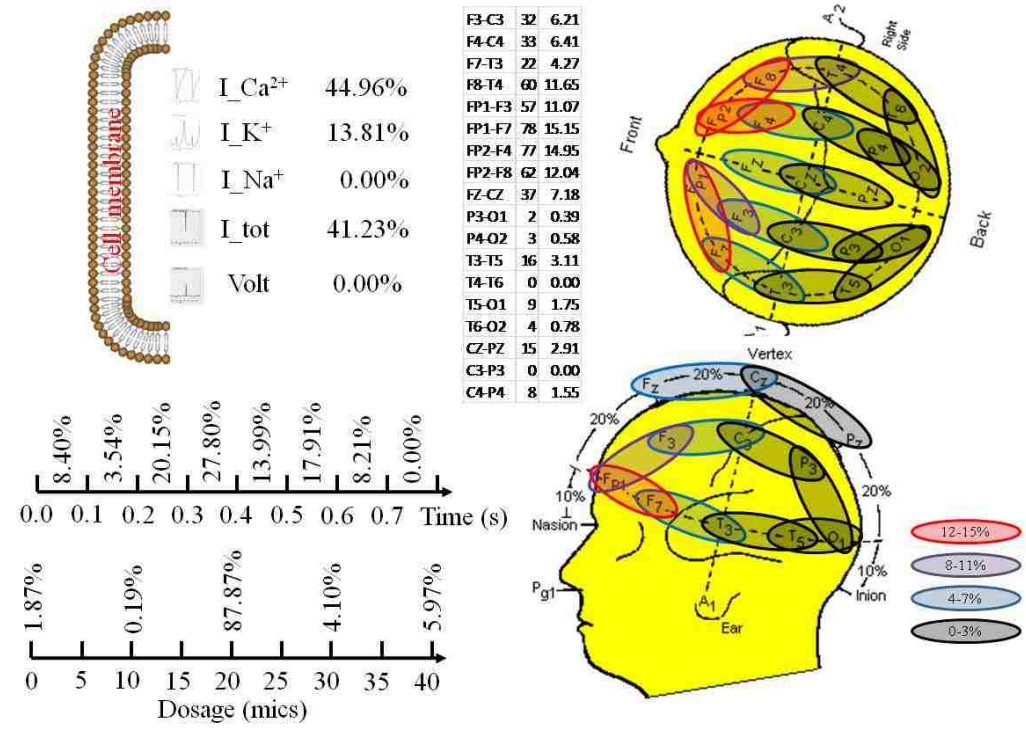

Figure A-37 Patient 4 SA node electrical-EEG correlation (CF > 0.5)

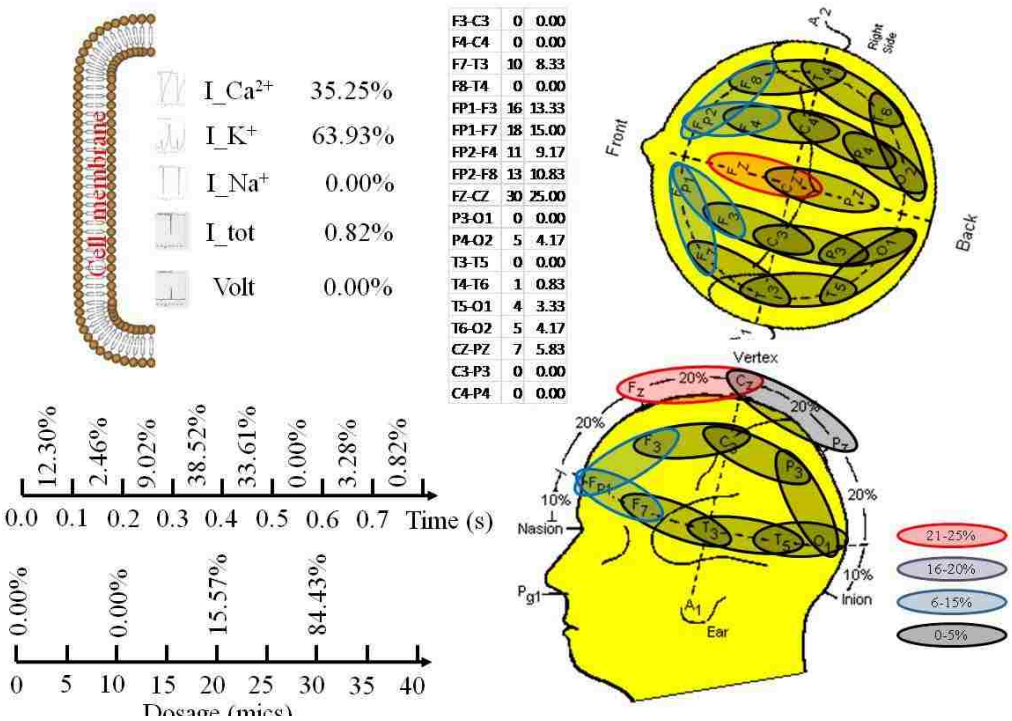

Figure A-38 Patient 5 SA node electrical-EEG correlation (CF > 0.5)

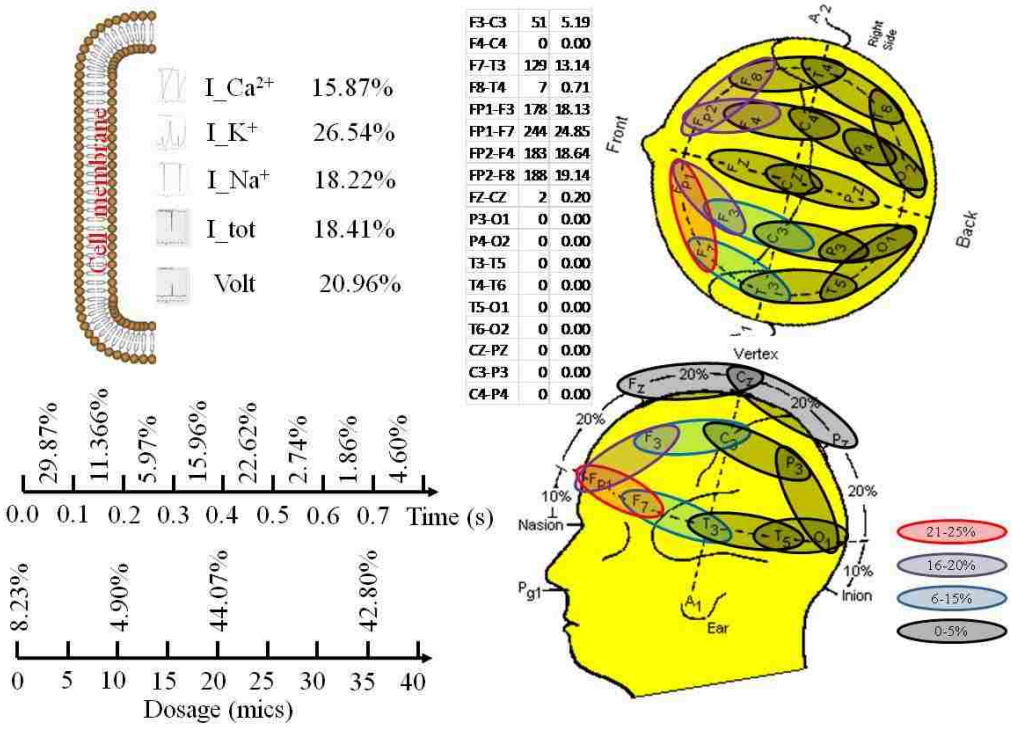

Figure A-39 Patient 1 AV node electrical-EEG correlation (CF > 0.5)

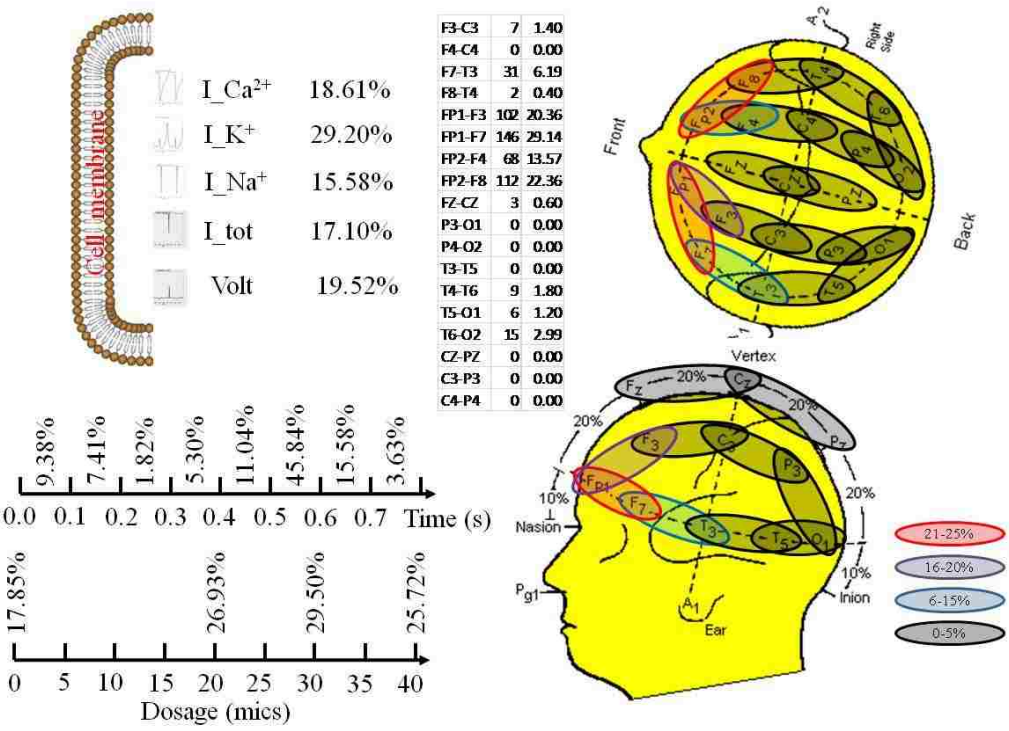

Figure A-40 Patient 2 AV node electrical-EEG correlation (CF > 0.5)

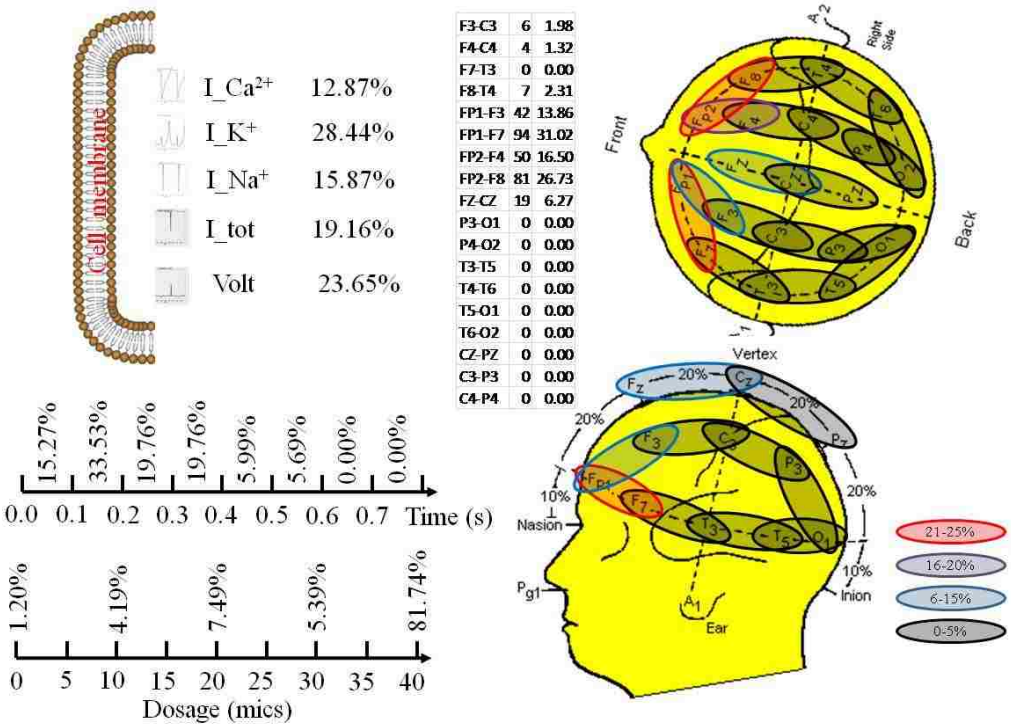

Figure A-41 Patient 3 AV node electrical-EEG correlation (CF > 0.5)

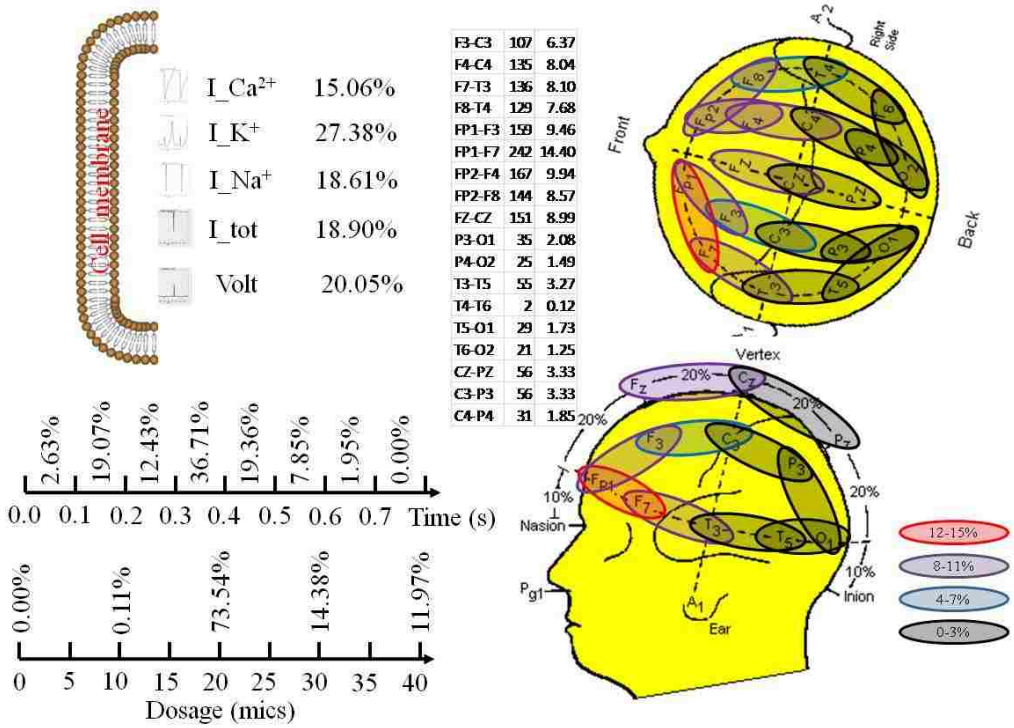

Figure A-42 Patient 4 AV node electrical-EEG correlation (CF > 0.5)

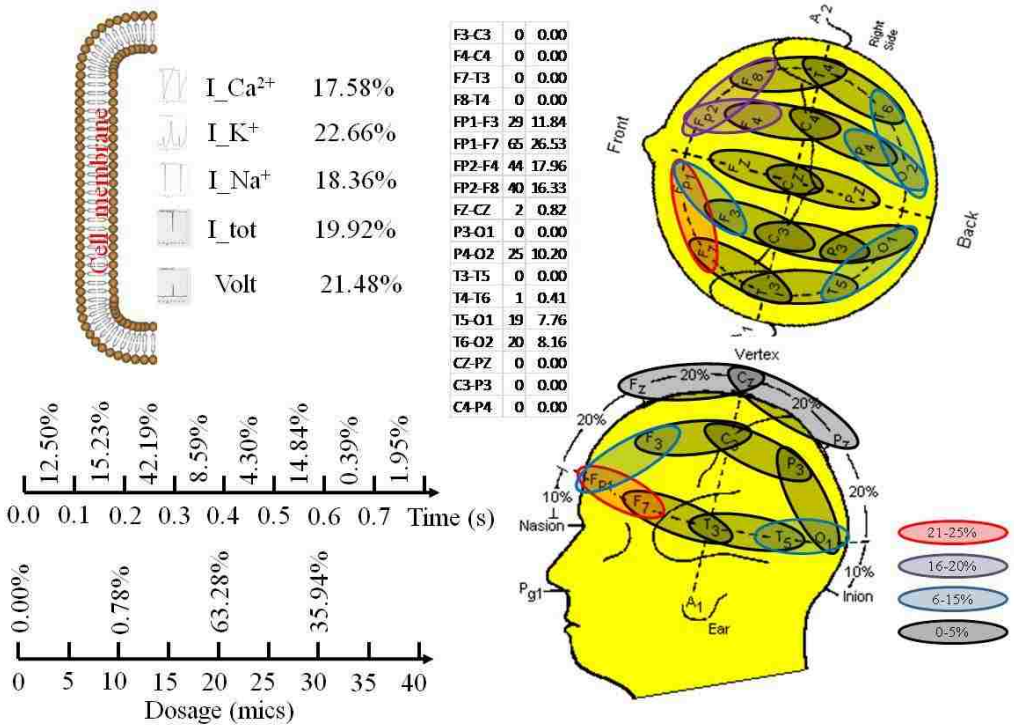

Figure A-43 Patient 5 AV node electrical-EEG correlation (CF > 0.5)

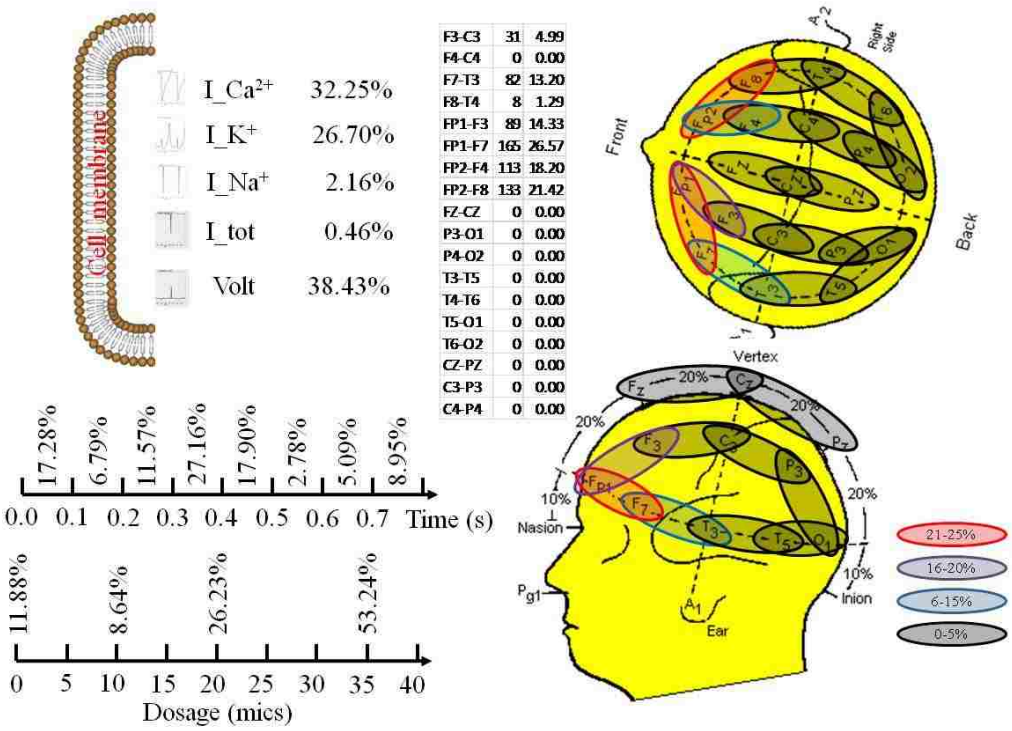

Figure A-44 Patient 1 PF node electrical-EEG correlation (CF > 0.5)

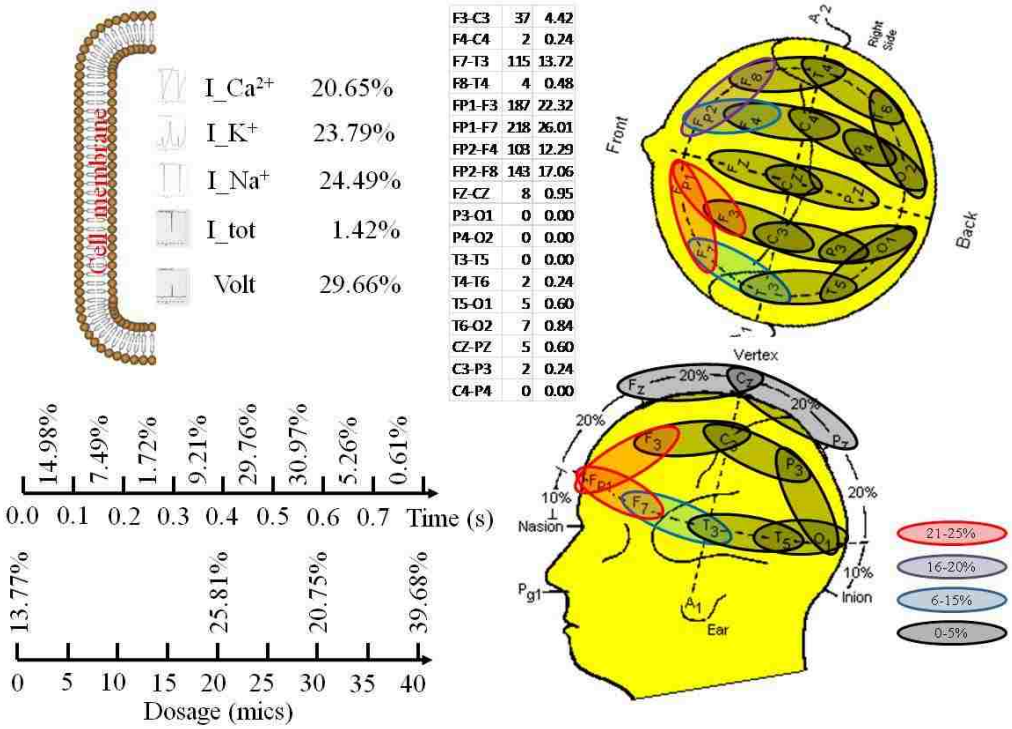

Figure A-45 Patient 2 PF node electrical-EEG correlation (CF > 0.5)

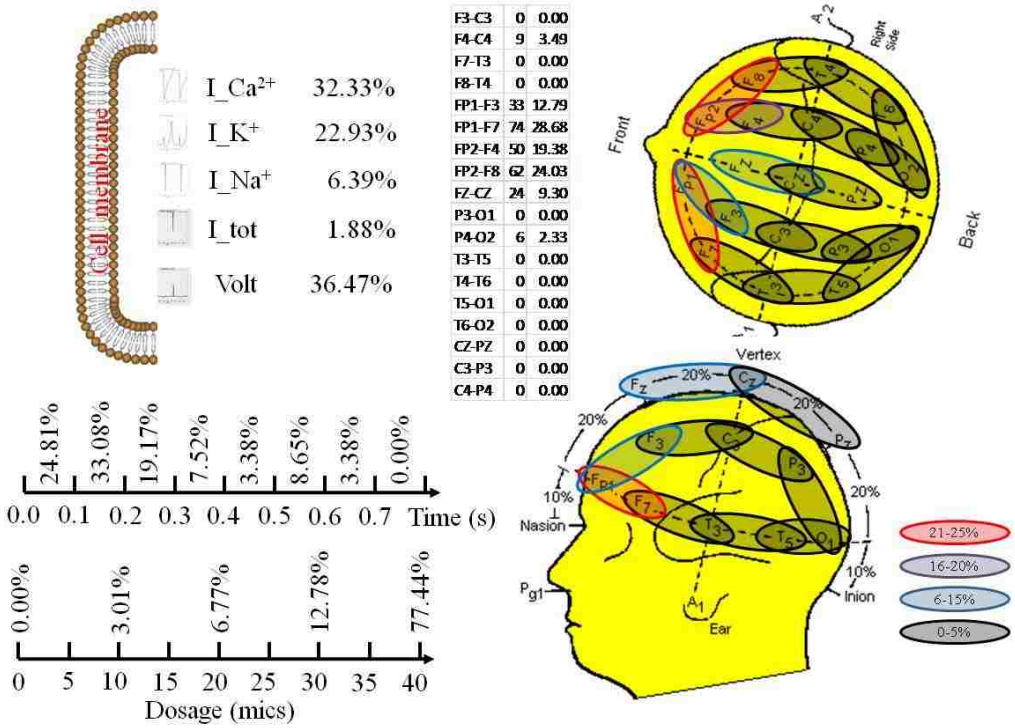

Figure A-46 Patient 3 PF node electrical-EEG correlation (CF > 0.5)

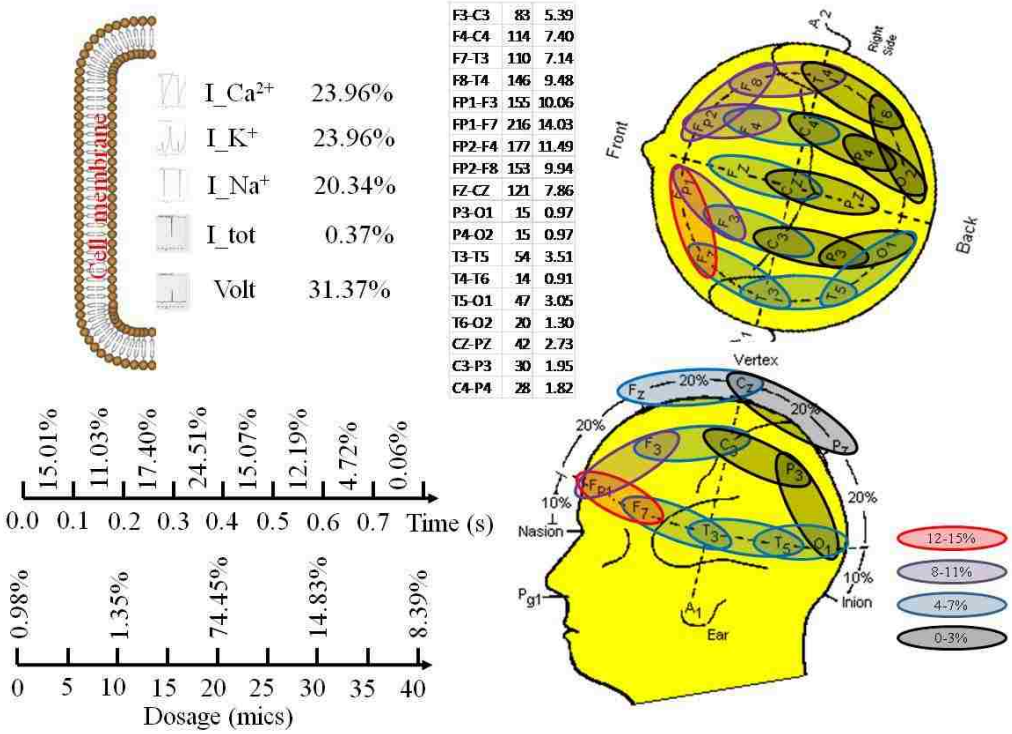

Figure A-47 Patient 4 PF node electrical-EEG correlation (CF > 0.5)

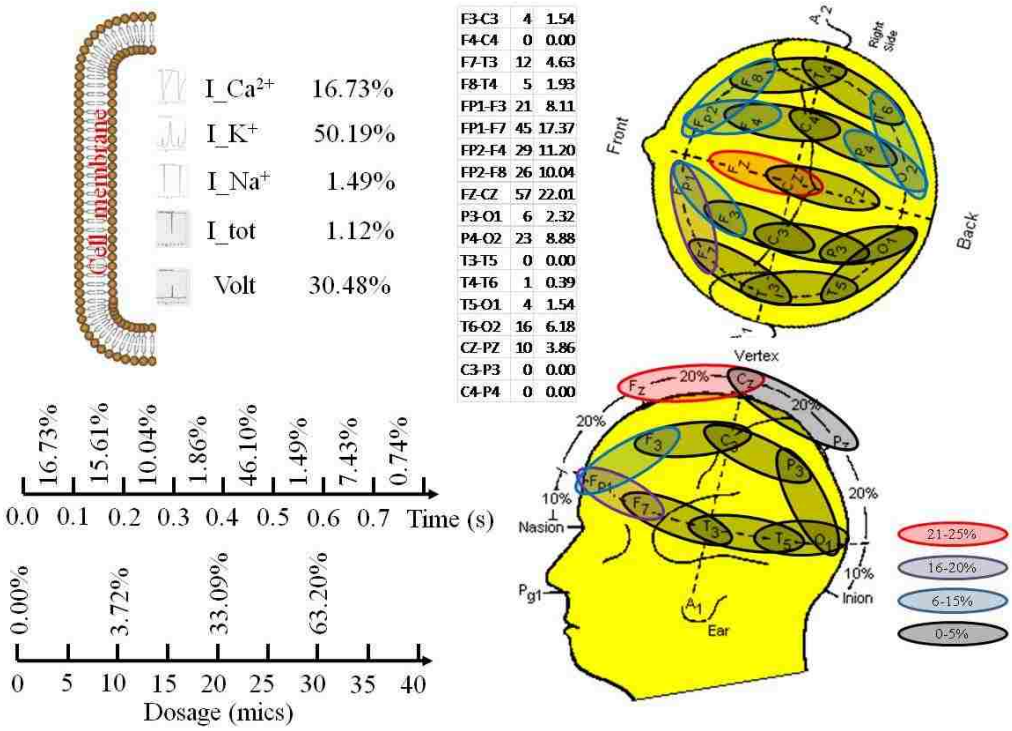

Figure A-48 Patient 5 PF node electrical-EEG correlation (CF > 0.5)

VITA

Chokchai Chutakositkanon was born in Bangkok, Thailand. He graduated from Mahidol University, Salaya, Nakorpatthom, Thailand, with a B.Eng., Mechanical Engineering, in 1997. He has been a lecturer in faculty of engineering, Mahidol University since 1997. He completed his Masters degree in M.Eng., Mechanical Engineering at Kasetsart University, Bangkhen, Bangkok, Thailand in 2004. Later, he was awarded a Royal Thai Government Scholarship and started his doctoral program in Mechanical Engineering and Mechanics department at Lehigh University in 2006.